In-Vitro Optical Assessment of Arterial Stiffness: Custom Femoral Phantoms, Blood-Pressure State Protocols, and Multimodal PPG—LDF Integration

Parmis Karimpour

1st Supervisor: Professor Panicos A. Kyriacou

2nd Supervisor: Dr James M. May

This thesis is submitted for the degree of

Doctor of Philosophy

Research Centre for Biomedical Engineering

School of Science and Technology

January 2026

To Mama & Bosh Bosh,

Abstract

Cardiovascular diseases (CVD) remain a major health challenge, affecting millions of individuals. The natural process of vascular ageing contributes to changes in the vascular system, potentially compromising cardiovascular health by causing arterial stiffness. This thesis investigates photoplethysmography (PPG) as a low-cost, non-invasive approach for vascular ageing assessment, with particular emphasis on its potential application in assessing arterial stiffness through waveform morphology and extracted features. A central contribution is the novel development of customisable vessel-tissue phantoms, mechanically characterised to replicate the properties of human femoral arteries across healthy and diseased states. These novel silicone-based phantoms were embedded within a controlled in vitro vascular system, providing a reproducible platform for evaluating PPG-derived markers of arterial stiffness.

The feasibility of PPG for assessing arterial stiffness was investigated through controlled experimental studies. For the first time, customisable vessel–tissue phantoms with tuneable mechanical properties were embedded within bilateral and single-branch in vitro vascular models to replicate vascular symmetry and progressive stiffness changes. Morphological waveform features were extracted from PPG recordings, with key metrics associated with arterial stiffness identified and analysed. A significant methodological contribution was the implementation of multimodal experiments integrating PPG and laser Doppler flowmetry (LDF) to examine the complementary discriminatory performance of combining optical modalities for vascular health assessment.

This work demonstrated the successful fabrication of novel vessel–tissue phantoms with mechanical properties representative of femoral arteries and surrounding tissue. Three phantoms were developed, for the first time, to model healthy, intermediate, and unhealthy vascular states, with Young's modulus values of 0.82 MPa, 1.48 MPa, and 2.06 MPa, respectively. Bilateral experiments confirmed the repeatability of PPG signals across identical phantoms, with no statistically significant differences ($p \geq 0.05$) in the majority of fundamental PPG features, apart from rise time. Four key waveform features, amplitude, area under the curve (AUC), median upslope–downslope ratio, and median end datum difference, showed strong correlation with arterial stiffness. Differentiation between healthy and unhealthy vessels was verified under hypertensive conditions, although classification of the intermediate state remained less distinct, with some features showing statistical similarity to the healthy state. The second derivative of the photoplethysmography signal (SDPPG) indicated that the $\frac{b}{a}$ ratio showed the clearest separation between the healthy and unhealthy phantoms under hypertensive conditions (–2.13 to –2.06). A novel multimodal approach combining PPG and LDF demonstrated complementary strengths: PPG was most effective at distinguishing unhealthy vessels from healthy and intermediate states through pulsatile blood volume changes, while LDF better differentiated the health states via LDF-derived flux. A progressive reduction in direct current (DC) mean flux was observed across the healthy, intermediate, and unhealthy phantoms, confirming the sensitivity of LDF to vascular stiffening.

This research demonstrates the significant potential of PPG as a non-invasive method for vascular ageing assessment. While integration with complementary modalities such as LDF may enhance discriminatory capability, further optimisation and validation are required before clinical implementation.

Table of Contents

Nomenclature

ABI	Ankle-Brachial Index
AC	Alternating Current
ADC	Analogue-to-Digitial Converter
AI	Artificial Intelligence
AIS	Acute Ischemic Stroke
AIx	Augmentation Index
ANCOVA	Analysis of Covariance
ANOVA	Analysis of Variance
API	Arterial Pressure-Volume Index
ASI	Arterial Stiffness Index
AUC	Area Under the Curve
AV	Atrioventricular
AVI	Arterial Velocity-Pulse Index
baPWV	Brachial-Ankle Pulse Wave Velocity
BFP	Body Fat Percentage
BMF	Blood Mimicking Fluid
BMI	Body Mass Index
BP	Blood Pressure
bpm	Beats Per Minute
CAC	Coronary Artery Calcium
CAD	Coronary artery disease
CAVI	Cardio-Ankle Vascular Index
cfPWV	Carotid Femoral Pulse Wave Velocity

CI	Compliance Index
CKD	Chronic Kidney Disease
CO	Cardiac Output
COPD	Chronic Obstructive Pulmonary Disease
CNN	Convolutional Neural Network
cPPG	Contact Photoplethysmography
CVD	Cardiovascular Disease
DC	Direct Current
DDI	Dicrotic Dilation Index
DI	Dicrotic Index
d-ICG	Dual Impedance Cardiography
DICOM	Digital Imaging and Communications in Medicine
DL	Deep Learning
DPA	Digital Pulse Wave Analysis
DVP	digital Volume Pulse
ECG	Electrocardiogram
EEI	Ejection Elasticity Index
ESRD	End-Stage Renal Disease
FEI	Finger Arterial Elasticity Index
FSI	Finger Arterial Stiffness Index
GP	General Practitioner
IBD	Inflammatory Bowel Disease
ICUs	Intensive Care Units
ID	Internal Diameter

I/M	Intima/media
iPPG	Imaging Photoplethysmography
IR	Infrared
LDF	Laser Doppler Flowmetry
LED	Light Emitting Diode
MAP	Mean Arterial Pressure
ML	Machine Learning
MRI	Magnetic Resonance Imaging
MSC	Magnitude-Squared Coherence
NIRS	Near-Infrared Spectroscopy
OD	Outer Diameter
OSI	Overnight Stiffness Index
PAT	Pulse Arrival Time
PCG	Phonocardiogram
PD	Photodetector
PDMS	Polydimethylsiloxane
PPG	Photoplethysmography
PTT	Pulse Transit Time
PWA	Pulse Wave Analysis
PWD	Pulse Wave Decomposition
PWV	Pulse Wave Velocity
RA	Rheumatoid Arthritis
RCBE	The Research Centre for Biomedical Engineering, City St. George's, University of London

RHI	Reactive Hyperemia Index
RI	Reflection Index
RMSE	Root Mean Square Error
ROC	Receiver Operating Characteristic
rPPG	Remote Photoplethysmography
SA	Sinoatrial
SDPPG	Second Derivative of the Photoplethysmography Signal
SI	Stiffness Index
SNR	Signal-to-Noise Ratio
sPLM	Single Continuous Passive Leg Movement
SpO_2	Oxygen Saturation
TAVI	Transcatheter Aortic Implantation
TKE	Turbulent Kinetic Energy
TPR	Total Peripheral Resistance
%MPA	Percentage Mean Pulse Amplitude
2D	Two-Dimensional
3D	Three-Dimensional
4D	Four-Dimensional

List of Figures

List of Tables

List of Equations

List of Publications

R. Ferizoli, P. Karimpour, J. M. May, and P. A. Kyriacou, 'A Bilateral In Vitro Model for Cardiovascular Disease Investigations Using Photoplethysmography Sensors', IEEE Biosensors Conference 2023.

P. Karimpour, J. M. May, and P. A. Kyriacou, 'Photoplethysmography for the Assessment of Arterial Stiffness', Sensors (Basel), vol. 23, no. 24, p. 9882, Dec. 2023, doi: 10.3390/s23249882.

P. Karimpour, R. Ferizoli, J. M. May, and P. A. Kyriacou, 'Customisable Silicone Vessels and Tissue Phantoms for In Vitro Photoplethysmography Investigations into Cardiovascular Disease', Sensors, vol. 24, no. 5, Art. no. 5, Jan. 2024, doi: 10.3390/s24051681.

R. Ferizoli, P. Karimpour, J. M. May, and P. A. Kyriacou, 'Arterial stiffness assessment using PPG feature extraction and significance testing in an in vitro cardiovascular system', Sci Rep, vol. 14, no. 1, Art. no. 1, Jan. 2024, doi: 10.1038/s41598-024-51395-y.

P. Karimpour, R. Ferizoli, J. M. May, and P. A. Kyriacou, 'Custom Silicone Vessels for In Vitro Investigations on Vascular Ageing using Photoplethysmography', in 2024 46th Annual International Conference of the IEEE Engineering in Medicine and Biology Society (EMBC), Jul. 2024, pp. 1–4. doi: 10.1109/EMBC53108.2024.10781560.

S. Zanelli et al., 'Developing technologies to assess vascular ageing: a roadmap from VascAgeNet', Physiol Meas, vol. 45, no. 12, p. 121001, Dec. 2024, doi: 10.1088/1361-6579/ad548e.

P. Karimpour, J. M. May, and P. A. Kyriacou, 'Feasibility of Photoplethysmography in Detecting Arterial Stiffness in Hypertension', Photonics, vol. 12, no. 5, Art. no. 5, May 2025, doi: 10.3390/photonics12050430.

P. Karimpour, R. Ferizoli, J. M. May, and P. A. Kyriacou, 'Multimodal assessment of arterial stiffness using photoplethysmography and laser Doppler flowmetry', npj Cardiovasc Health, vol. 3, no. 1, p. 19, Apr. 2026, doi: 10.1038/s44325-026-00115-8.

S. Lombardi, P. Karimpour, J. M. May, L. Bocchi, P. A. Kyriacou, 'Photoplethysmographic Signal Analysis for Vascular Ageing Assessment', Pending Publication.

Acknowledgements

This PhD journey has been one of the most defining chapters of my life, not only because of the research, but because of the people who supported me through it.

To my supervisors, Professor Kyriacou and Dr. May, whose guidance and unwavering support have been invaluable. Professor Kyriacou, your wisdom and encouragement always arrived exactly when I needed clarity. Dr. May, your knowledge and advice were of immeasurable value, and your steady presence and willingness to offer direction and support made all the difference throughout this journey.

I am thankful for my friends in the lab, where our bond went beyond work. I owe much of the joy in this journey to my friends at the Research Centre for Biomedical Engineering, who brought laughter and friendship to each day. Beyond the lab, I was lucky to have friends who were family in every way that mattered. They reminded me that even on the hardest days, there was still so much love and friendship around me.

My deepest gratitude goes to my family. To my brother, who has made my life lighter in more ways than he realises, and to my dog, Teddy, who brought joy at the exact moments I needed it most. And of course, my parents. My parents are the greatest gift I have ever been given. They left behind everything they knew, their parents, their siblings, and their home country, in the hope of giving my brother and me the chance to live freely. Everything I have been able to do rests on the sacrifices they made. Without them, none of this would have been possible.

I hold onto the belief that no injustice lasts forever. One day, the people of Iran will have the same freedom my parents sacrificed everything to find. Until then, this milestone is not just for me, it belongs to them too.

Declaration

I, Parmis Karimpour, declare that the work presented in this thesis is my work. I confirm that the work was undertaken in fulfilment of the requirements for the degree of Doctor of Philosophy in Biomedical Engineering at City St George's, University of London. I declare that this thesis has not been submitted for any other academic award or professional qualification.

Parmis Karimpour

CHAPTER 1: INTRODUCTION

1.1 Background

1.1.1 Cardiovascular Diseases and Vascular Ageing

Globally, cardiovascular disease (CVD) is the leading cause of mortality, accounting for approximately 17.9 million fatalities in 2019 [1]. CVD can emerge due to various factors, including the formation of plaque leading to atherosclerosis, which results in the accumulation of fatty substances clogging the arteries. Elevated blood pressure (BP) and high cholesterol are also recognised as contributing factors that heighten the risk of developing heart diseases. Additional risk factors include smoking, a poor diet, and excessive alcohol consumption [2].

While many of these factors are related to lifestyle choices and can be modified based on individual decisions, the ageing of blood vessels is an inevitable process. As vessels age, the heart and blood vessels undergo changes, leading to degeneration and an increased risk of CVD [3], [4]. The arterial system's ability to function may be harmed or even rendered ineffective by diseases that might develop as a result of vascular ageing. These diseases can affect vessels in both the upper and lower extremities [3].

One notable change that occurs during vascular ageing is increased arterial stiffness, which leads to volumetric, mechanical, and haemodynamic alterations in the vascular network. Arterial stiffness can restrict vessel expansion, potentially disrupting blood flow. Early detection can prevent cardiovascular death and is crucial for both asymptomatic and symptomatic patients. Advancements in technology and techniques to monitor vascular health can provide important information to avoid limb loss and other severe pathologies.

Vascular ageing can be interpreted as a gradual progression of structural and functional changes within the cardiovascular system. Although arterial stiffness is associated with increased cardiovascular risk, vascular changes occur inevitably with age, and inter-individual variability means the extent and rate of vascular decline vary among individuals [5]. Therefore, emerging vascular assessment technologies are likely to support longitudinal monitoring rather than a simple yes–no classification. In this context, relative changes from an individual's baseline over time may be more informative than absolute thresholds, as within-subject comparisons can reduce the

influence of inter-individual variability and physiological confounders. Therefore, the proposed application focused on detecting deviations from expected patterns, rather than providing a definitive binary diagnosis.

1.1.2 Monitoring Everyday Health Through Wearables

The integration of technology into wearables offers the potential to monitor vascular health seamlessly in everyday activities. Ongoing developments suggest that smart wearables could become even more prevalent in the future. The user base of wearables is experiencing rapid expansion, with projections indicating that approximately 440 million devices should be in use by 2024 [6], [7], [8].

While there are concerns about privacy and data accuracy associated with wearable devices, these devices bring forth many advantages. To begin with, they enable real-time health monitoring, allowing for continuous vascular health tracking that can be tailored to suit individual preferences. Moreover, wearables can serve as sources of motivation to enhance quality of life. For example, these portable devices can promote dietary adjustments and stimulate physical activity to postpone or even prevent the occurrence of CVD. Wearables also have the capability to support timely intervention by generating alerts when abnormal readings are detected, prompting the user or their caregiver to seek appropriate medical attention if needed. They can also serve to provide reminders for individuals to take their medications [9]. The information gathered through wearables has the potential to provide valuable insights for medical research, driving progress and innovation.

1.2 Motivation

Vascular ageing is inevitable and is accompanied by progressive increases in arterial stiffness [3]. Although arterial stiffness has been investigated extensively in vivo, in vivo measurements are inherently influenced by biological variability and confounding factors including temperature, sensor contact pressure, skin pigmentation, respiration, and inter-subject anatomical differences [10]. These sources of variability make it difficult to isolate arterial stiffness as an independent determinant of vascular signal morphology and derived markers. An in vitro model provides a controlled and repeatable environment in which arterial stiffness can be systematically manipulated while other parameters are held constant. Such a platform enables experiments that specifically

interrogate the effect of stiffness on vascular waveform behaviour and feature sensitivity, while supporting repeatability and reproducibility across defined vascular states.

In addition, an in vitro platform allows elevated BP conditions to be imposed in a controlled manner. This is clinically relevant because elevated BP is closely linked to cardiovascular risk [2]. By enabling independent control of both BP and vessel mechanical properties, an in vitro approach reduces the influence of physiological compensation and other in vivo confounders, allowing clearer attribution of observed changes to stiffness and BP changes.

A multimodal optical approach is particularly valuable in this context, as different optical techniques provide complementary information on vascular function. For example, one modality may be more sensitive to pulsatile blood volume dynamics, whereas another may reflect microvascular perfusion. Acquiring these measurements concurrently provides a stronger basis for interpreting vascular state differences and for determining whether combining modalities offers improved discrimination compared with a single measurement alone.

1.3 Aims & Objectives

Arterial stiffness is a key marker of vascular ageing and a risk factor for CVD. The primary aim of this research was to determine whether photoplethysmography (PPG) can detect controlled changes in arterial stiffness using waveform-derived metrics in an in vitro lower-body model. The rationale for selecting PPG, along with its underlying principles, is discussed in Chapter 4. Currently, the clinical assessment of vascular ageing is not readily accessible, as it typically requires referral from a general practitioner (GP) for hospital-based diagnostic procedures. This limitation may contribute to delays in detection and heightened anxiety for patients.

The first objective of this research was to critically review the current state-of-the-art technologies and techniques employed in the non-invasive detection of arterial stiffness, with the goal of outlining the direction of the research and identifying opportunities for future research. This included a review of the literature concerning the application of PPG in the screening of arterial stiffness and the assessment of vascular ageing. The intention was to highlight the limitations of existing studies and to propose methodological refinements that could address these gaps, underpinned by the premise that PPG holds

considerable promise as a tool for vascular ageing assessment. The success of this objective was defined by producing a critical review that synthesises prior findings, identifies key methodological limitations and confounders, and proposes refinements that directly informed the experimental design choices in this thesis.

Following the literature review, the feasibility of utilising PPG was examined through the development and implementation of an in vitro model replicating the physiology of the lower body. To enhance the physiological relevance of the model, a key objective was the fabrication of customisable vessel constructs designed to emulate the mechanical properties of the femoral artery. These synthetic vessels were embedded within fabricated surrounding tissue to create anatomically representative vessel-tissue phantoms. These phantoms were then integrated into the in vitro cardiovascular system, enabling a series of controlled experiments to evaluate the capability of PPG in monitoring vascular ageing. The success of fabricating customisable vessel-tissue phantoms was defined by their mechanical characterisation and their comparison of their properties with relevant in vivo values.

The experimental phase of the study was designed to systematically evaluate the feasibility and robustness of PPG as a sensing modality. The initial step involved validating the in vitro setup, configured bilaterally, by placing identical phantoms in each channel and recording PPG signals to ensure consistent and reproducible measurements. The following experiments focused on identifying specific PPG-derived features that exhibited strong correlations with arterial stiffness, with the aim of determining whether a limited set of features could reliably serve as biomarkers of vascular ageing. Success was defined by statistically significant waveform features that were consistent and reproducible across the bilateral branches under identical conditions, as well as statistically significant differences in PPG-derived features across vascular states.

An additional objective was to investigate the applicability of PPG in monitoring vascular ageing under varying haemodynamic conditions, particularly in the context of elevated BP (hypertension). The success of this was defined by stiffness-sensitive PPG features maintaining statistically significant differentiation between vascular stiffness states across imposed BP conditions. Finally, the integration of bi-modal sensing, specifically PPG and laser Doppler flowmetry (LDF), was explored to determine whether a

multimodal strategy could enhance the accuracy and reliability of vascular ageing assessments. The success was defined by whether LDF improved stiffness-state discrimination and/or reduced uncertainty relative to PPG-only assessment.

Therefore, this thesis follows a structured translational pathway from mechanism to application. Motivated by the limitations of in vivo arterial stiffness assessment, a controlled in vitro cardiovascular platform was developed in which arterial stiffness and BP could be independently manipulated. This thesis proposed a new mechanistic method for advancing understanding of arterial stiffness using PPG by investigating how controlled changes in vessel stiffness influence waveform morphology within a deterministic and reproducible in vitro environment. In addition, novel customisable vessel–tissue phantoms representative of the femoral artery and surrounding tissue were fabricated and mechanically characterised to replicate key in vivo properties. The optical assessment was further extended through a multiwavelength approach using three wavelengths, alongside evaluation across different blood mimicking fluids (BMF) and imposed BP conditions, to determine how optical and haemodynamic factors influence stiffness-related waveform behaviour. Second derivative of the photoplethysmography signal (SDPPG) analysis was also performed within the BP-modulation experiments to assess whether derivative-based metrics provided additional insight into stiffness-related waveform changes. A multimodal optical approach combining PPG and LDF was explored to evaluate the potential benefits of dual-modality assessment, and whether it improves stiffness-state discrimination. By defining clear success criteria based on repeatability through bilateral validation, stiffness sensitivity, stability across BP conditions, and whether LDF provides additional discriminatory value beyond PPG alone, this work can inform the design of future in vivo pilot studies for non-invasive vascular health assessments.

1.4 Thesis Outline

Chapter 1 of the thesis serves as a foundational introduction to the research. It articulates the motivation for the study, highlights the need for a practical vascular health monitoring tool, and outlines the aims and objectives of the research.

Chapter 2 explores the anatomy of the heart and vascular structures, with a particular focus on arterial anatomy. It outlines the physiological changes associated with arterial ageing and emphasises the potential of PPG to monitor these alterations. Finally, the chapter examines the pathologies related to vascular ageing, highlighting a range of diseases associated with this process.

Chapter 3 provides an overview of current state-of-the-art techniques and technologies used to non-invasively assess vascular ageing through the monitoring of arterial stiffness. This section covers measurements of pulse wave velocity (PWV), the use of indices, various imaging modalities, existing instruments, and computational methodologies involving algorithms and software programs. The strengths and limitations of each approach were evaluated. This chapter presents original work conducted in this thesis (published).

In Chapter 4, PPG and its recent use in assessing arterial stiffness were described. This chapter explored the use of PPG in in vivo studies and reviewed research comparing PPG-based devices with alternative assessment methods. Additionally, the chapter examined the integration of PPG with other techniques and discussed its incorporation into computational models for predicting vascular health. This chapter presents original work conducted in this thesis (published).

Chapter 5 presents the in vitro cardiovascular system model, detailing the experimental setup used in this research. The formulation and preparation of the BMFs are described, along with the technical specifications of the PPG sensors integrated into the system. Additionally, the chapter outlines the configuration of the signal processing unit and the data acquisition system used for recording and analysing the signals. This chapter presents original work conducted in this thesis.

Chapter 6 details the fabrication process of custom vessel-tissue phantoms designed to simulate physiological arterial conditions. This includes the dip-coating procedure used

to form silicone-based arterial structures and the surrounding tissue-mimicking material. The chapter presents a technical account of the mechanical characterisation process, including measurements of wall thickness and elasticity. An initial experimental study is also described to assess the feasibility of acquiring high-quality PPG signals from fabricated phantoms. Based on mechanical properties, three distinct phantoms, representing healthy, diseased, and an intermediate state of the femoral artery, are introduced and discussed. This chapter presents original work conducted in this thesis (published).

Chapter 7 describes a preliminary study in which two identical phantoms were positioned bilaterally within the in vitro cardiovascular system. The purpose of this experiment was to evaluate whether identical phantoms produced comparable PPG readings and to assess the symmetry and reliability of the in vitro setup. This chapter presents original work conducted in this thesis (published).

Chapter 8 focuses on feature engineering through pulse wave analysis (PWA), detailing the process of extracting features from PPG signals. This chapter identifies and describes key features associated with arterial stiffness, highlighting those with the greatest significance in the context of vascular ageing. Based on their relevance and statistical significance, a subset of features is selected for further analysis in the following stages of the research. This chapter presents original work conducted in this thesis (published).

Chapter 9 presents an in vitro study investigating the potential of PPG to assess vascular ageing in individuals with hypertension. In this experiment, the three phantoms, representing femoral arteries at different health states, were subjected to varying BP settings. The key features identified in Chapter 8 were analysed under these conditions. Additionally, the SDPPG was introduced, and its fiducial points were examined. This chapter presents original work conducted in this thesis (published).

Chapter 10 introduces bi-modal monitoring of vascular ageing. This chapter presents an experimental study that utilises PPG alongside LDF to assess whether combining these modalities can provide complementary information and improve the assessment of vascular ageing-related changes. The study is designed to evaluate whether PPG should be used independently or in conjunction with techniques such as LDF. This chapter presents original work conducted in this thesis.

Chapter 11 concludes the thesis by summarising the key findings and discussing the challenges and limitations encountered throughout the research. It also outlines potential directions for future work, highlighting opportunities to build upon the current findings and further advance the field of vascular health monitoring.

CHAPTER 2: ANATOMY AND PHYSIOLOGY OF VASCULAR STRUCTURES IN HEALTH AND DISEASE

2.1 Heart Structure and Function

The heart, as shown in Figure 1, is the main organ of the cardiovascular system, functioning as a muscular pump responsible for circulating blood throughout the body. Structurally, the heart is divided into four chambers: two atria and two ventricles, which serve as reservoirs and conduits for blood flow. At its base, a fibrous skeleton provides structural support and electrically insulates the atria from the ventricles [11]. The right atrium receives deoxygenated blood from the systemic circulation, whereas the left atrium receives oxygenated blood from the lung via the pulmonary veins [12]. The right ventricle pumps deoxygenated blood to the lungs for gas exchange, while the left ventricle pumps oxygenated blood into the systemic circulation to supply body tissues [11]. Four valves regulate unidirectional blood flow by opening and closing in response to pressure changes, preventing backflow during the cardiac cycle. The atrioventricular valves, comprising the right-sided tricuspid valve and the left-sided mitral valve, control flow from atria to ventricles, while the semilunar valves, pulmonary and aortic, control ejection from the ventricles into the pulmonary artery and aorta, respectively [13].

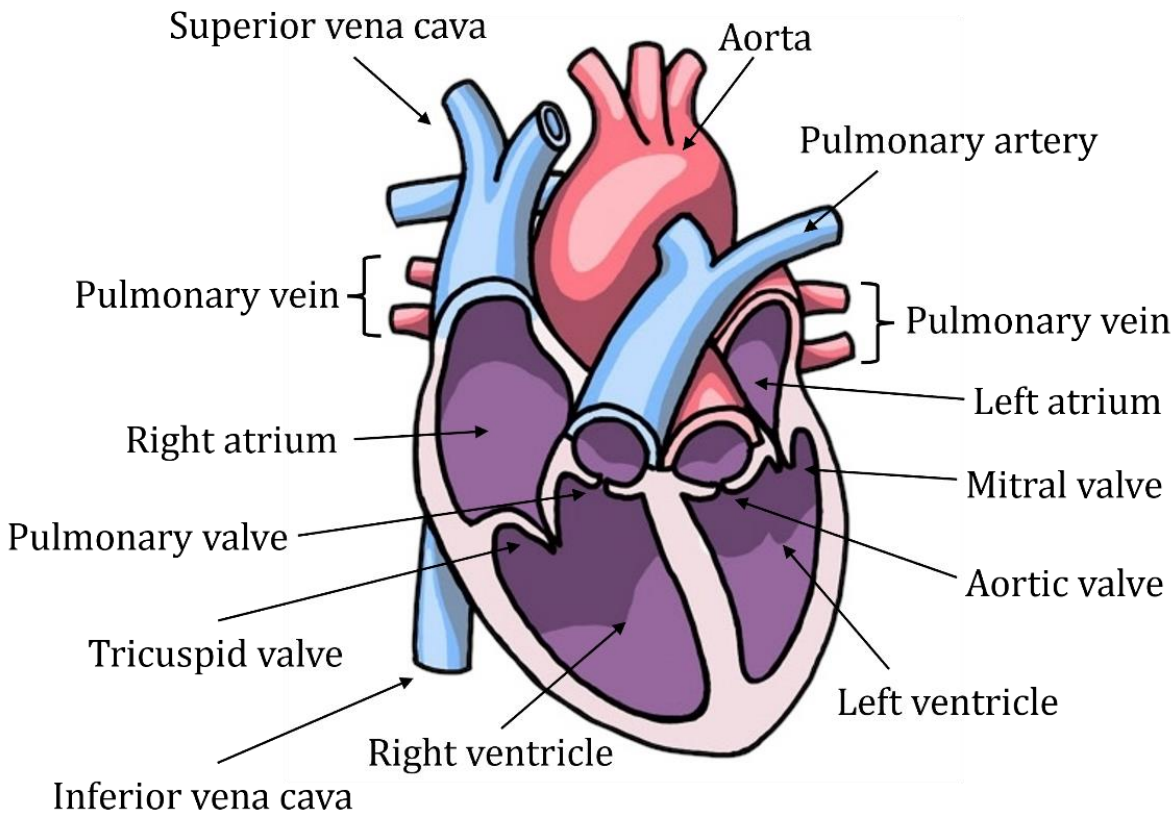

Figure 1: Anatomical illustration of the heart showing its four chambers and valves, along with the major adjacent arteries and veins. At the start of the cardiac cycle, the superior and inferior vena cava deliver deoxygenated blood into the right atrium, while the pulmonary veins return oxygenated blood to the left atrium. Adapted from Mahadevan [14].

The heart wall consists of three distinct layers, as illustrated in Figure 2. The innermost layer, the endocardium, lines the internal surfaces of the cardiac chambers and valves. It is composed of a layer of endothelial cells supported by subendocardial connective tissue, facilitating smooth blood flow and contributing to the regulation of myocardial contraction [11]. The middle layer, the myocardium, is the thickest and is primarily composed of cardiomyocytes. These muscle cells are responsible for the contractile activity of the heart, generating the force necessary for systemic and pulmonary circulation [15]. The outermost layer, the epicardium, comprises mesothelial cells, adipose tissue, and connective tissue. In addition to serving a protective role, the epicardium plays a critical part in cardiac development and contributes to tissue repair following myocardial injury [16]. Surrounding the heart, the pericardium functions as a protective sac, consisting of an outer fibrous layer and an inner serous layer [17].

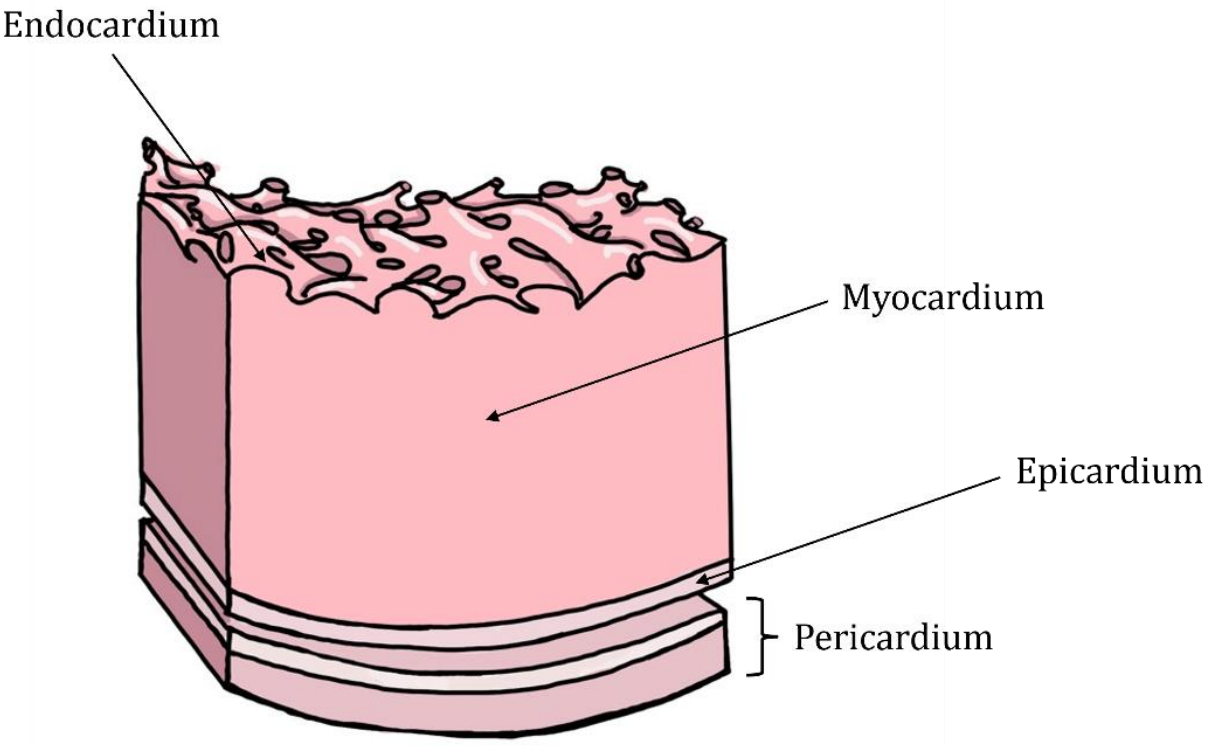

Figure 2: Illustration of the cardiac wall layers, showing the endocardium, myocardium, and epicardium. The pericardium is also shown, surrounding the heart. Adapted from Smits et al. [18].

The cardiac conduction system regulates the coordinated contraction of the heart by transmitting electrical impulses through specialised myocardial cells. The process is initiated by the sinoatrial (SA) node, located at the junction between the superior vena cava and the right atrium. From the SA node, the electrical impulse spreads across the atrial myocardium, leading to atrial contraction and thereafter reaches the atrioventricular (AV) node. The AV node is situated at the boundary between the interatrial and interventricular septa. From the AV node, the electrical impulses are transmitted through the bundle of His, which propagates the signal towards the apex of the heart. The bundle of His then branches into the left and right bundle branches within the interventricular septum, giving rise to Purkinje fibres that extend throughout the ventricular walls. These fibres facilitate synchronised ventricular depolarisation and contraction [11].

The cardiac cycle is the physiological process that drives the circulation of blood throughout the body, consisting of a coordinated sequence of atrial and ventricular contraction and relaxation. During the diastolic phase (diastole), the heart chambers are relaxed, allowing ventricular filling with blood returning from the veins. This is followed

by the systolic phase (systole), during which the chambers contract and eject blood into the arterial circulation. Filling occurs as atrial pressure exceeds ventricular pressure and the AV valves open, allowing blood to pass into the ventricles. Atrial systole then provides a final contribution to ventricular filling. Ventricular systole begins when ventricular contraction rises intraventricular pressure, closing the AV valves; once ventricular pressure exceeds that in the pulmonary artery and aorta, the semilunar valves open and blood is ejected [19]. The volume of blood ejected by each ventricle per heartbeat is referred to as the stroke volume [20]. Cardiac output (CO), defined as the total volume of blood pumped by the heart per minute, is determined by the product of stroke volume and heart rate, with the latter representing the number of heart beats per minute [21]. The PPG waveform, discussed in greater detail in Chapter 4, is directly influenced by the cardiac cycle, with its morphology reflecting the changes in blood volume driven by each heartbeat [22].

2.2 Vascular Structure and Function

The vascular network comprises a system of blood vessels that function as conduits for the circulation of blood throughout the body. This network is organised into two primary systems: the pulmonary circulation, which transports deoxygenated blood from the right ventricle to the lungs and returns oxygenated blood to the left atrium; and the systemic circulation, which conveys oxygenated blood from the left ventricle to peripheral tissues and returns deoxygenated blood to the right atrium. Blood vessels within these systems are categorised into three main types: arteries, capillaries, and veins, each with distinct structural and functional characteristics [23]. Arteries are responsible for transporting blood away from the heart. The pulmonary arteries carry deoxygenated blood from the right ventricle to the lungs, while the systemic arteries deliver oxygenated blood from the left ventricle to the peripheral tissues of the body. As blood is ejected from the ventricles, it enters large arteries, which progressively branch into smaller arteries and eventually into microscopic vessels known as arterioles, which vary from 8 μm to 60 μm. Arterioles play a crucial role in regulating blood flow into capillary networks. Capillaries, the smallest and most abundant type of blood vessel, serve as the primary sites of exchange between blood and surrounding tissue cells. Through their thin, permeable walls, capillaries deliver oxygen and nutrients to cells while collecting metabolic products, such as carbon dioxide, for removal. Following this exchange, blood flows into venules, the

smallest veins, which merge into progressively larger veins that return blood to the heart. The pulmonary veins transport oxygenated blood from the lungs to the left atrium, whereas the systemic veins return deoxygenated blood from body tissues to the right atrium [24].

The arterial wall is a muscular structure composed of smooth tissue and organised into three distinct layers: the intima, media, and adventitia, as illustrated in Figure 3. The intima, the innermost layer, lines the luminal surface and consists of a single layer of endothelial cells. The media, or middle layer, is separated from the intima by the internal elastic lamina and comprises connective tissue elements such as collagen, elastin, and other elastic fibres, along with smooth muscle cells. In healthy coronary arteries, the thickness of the media typically ranges from 125 µm to 350 µm; however, in the presence of atherosclerosis, this thickness may be significantly reduced, ranging approximately from 16 µm to 190 µm. The adventitia, the outermost layer, is predominantly composed of fibrous tissue, including elastin and collagen fibres [25].

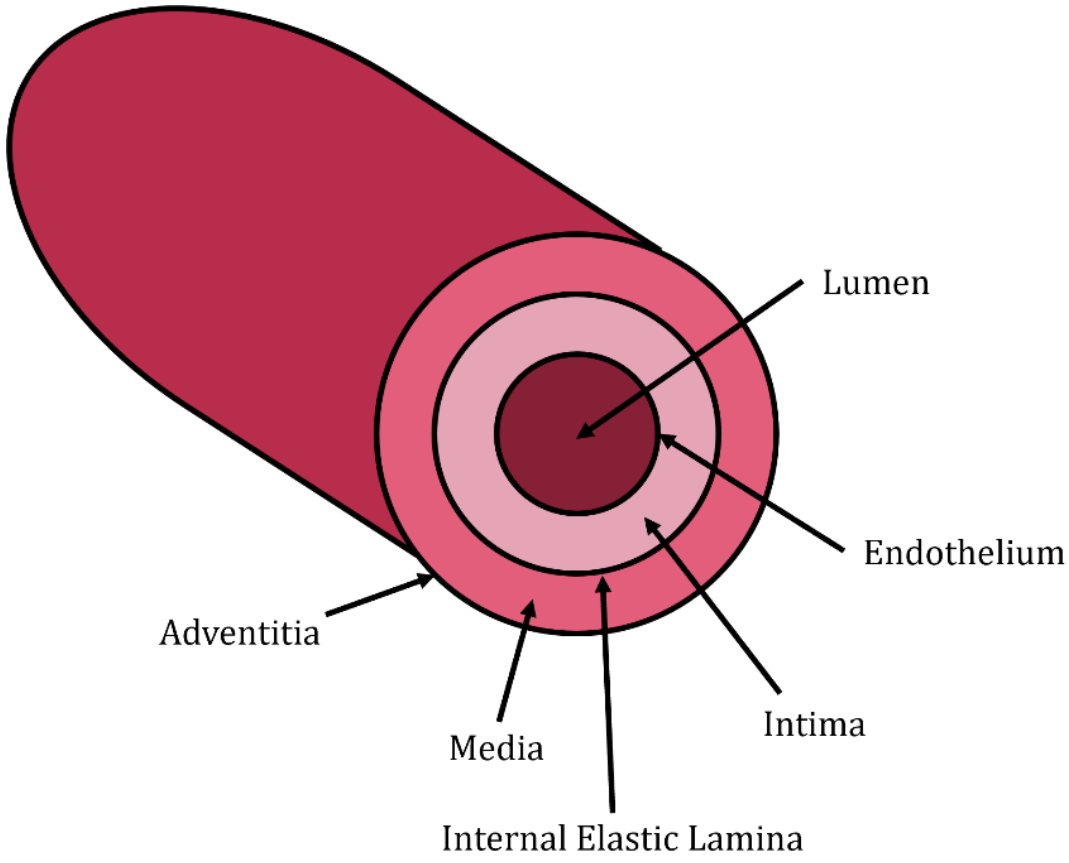

Figure 3 Cross-sectional illustration of the arterial wall structure, highlighting the three primary layers: intima, media, and adventitia (not to scale). Adapted and redrawn from Watson et al. [26].

Arteries in the human body are commonly classified into two major types: elastic arteries and muscular arteries. Elastic arteries, such as the aorta and pulmonary arteries, are located close to the heart and contain a higher proportion of elastic fibres within the tunica media compared to smooth muscle. This composition enables them to buffer the pulsatile output of the heart and maintain relatively stable BP. In contrast, muscular arteries, including vessels such as the femoral artery, have a tunica media rich in smooth muscle cells. This muscular composition allows these arteries to actively contract and relax, thereby regulating blood flow [24], [27].

Similar in structure to arteries, veins are composed of three distinct layers; however, due to the lower intravascular pressure within the venous system, their walls are thinner and less elastic. Despite this structural difference, veins can accommodate large volumes of blood at low pressures. Additionally, unidirectional valves within the venous system facilitate the return of blood to the heart by preventing backflow [24]. The movement of blood from the peripheral veins back to the heart is referred to as venous return. This process is primarily driven by a pressure gradient between the peripheral veins and the right atrium, with peripheral venous pressure being higher [28]. Several physiological mechanisms assist venous return. One such mechanism is the skeletal muscle pump, which enhances venous return during physical activity by compressing nearby veins, thereby driving blood toward the heart. During muscle relaxation, venous valves prevent reverse flow [29]. Respiratory activity also plays a role in venous return. Increased rate and depth of respiration elevate CO, largely due to changes in right atrial pressure. During inspiration, the expansion of the thoracic cavity and the downward displacement of the diaphragm lead to lung expansion. This results in a reduction in intrathoracic and right atrial pressures, which enhances the pressure gradient and thereby promotes venous return. During expiration, the gradient is reduced [30].

Vessel elasticity refers to the ability of a blood vessel to expand and contract in response to changes in pressure, while compliance describes the change in vessel diameter per unit change in pressure [31]. With ageing, blood vessels progressively lose elasticity, primarily due to a decline in elastin fibres and an increase in collagen content within the arterial wall, thereby increasing arterial stiffness [32], [33]. In addition, aged or unhealthy arteries typically exhibit an increased internal diameter (ID), which alters peripheral resistance and can lead to reduced pressure as a consequence of diminished

flow resistance [34]. Since PPG can detect pulsatile changes in blood volume, alterations in vessel stiffness, and the resulting changes in vascular expansion, are expected to be reflected in the morphology of the PPG waveform.

2.3 Vascular Physiology and Haemodynamics

Haemodynamics refers to the dynamics of blood flow within the vascular system and is fundamentally governed by the relationship between intravascular pressure, vascular resistance, and flow rate. Blood flow is primarily driven by pressure gradients, while vascular resistance acts to oppose this movement. Laminar flow is characterised by the orderly movement of fluid particles in parallel layers, with minimal mixing between them. Elastic arteries are capable of expanding and contracting in response to pulsatile CO, which modulates pulsatile haemodynamics rather than inducing turbulent flow. Turbulent flow is defined as irregular, non-linear fluid motion involving mixing, in contrast to the organised structure of laminar flow [35], more likely to occur under pathological conditions, such as stiff or diseased vessels. Figure 4 illustrates these concepts by comparing a healthy, elastic vessel with an unhealthy, stiff vessel, showing the associated differences in flow profiles. In the healthy vessel, flow streamlines illustrate the velocity distribution across the vessel radius, a pattern arising from shear stress at the vessel wall. Frictional forces between the blood and the endothelial surface reduce flow velocity near the vessel wall and increase it towards the centre, producing a parabolic velocity profile [3], [35].

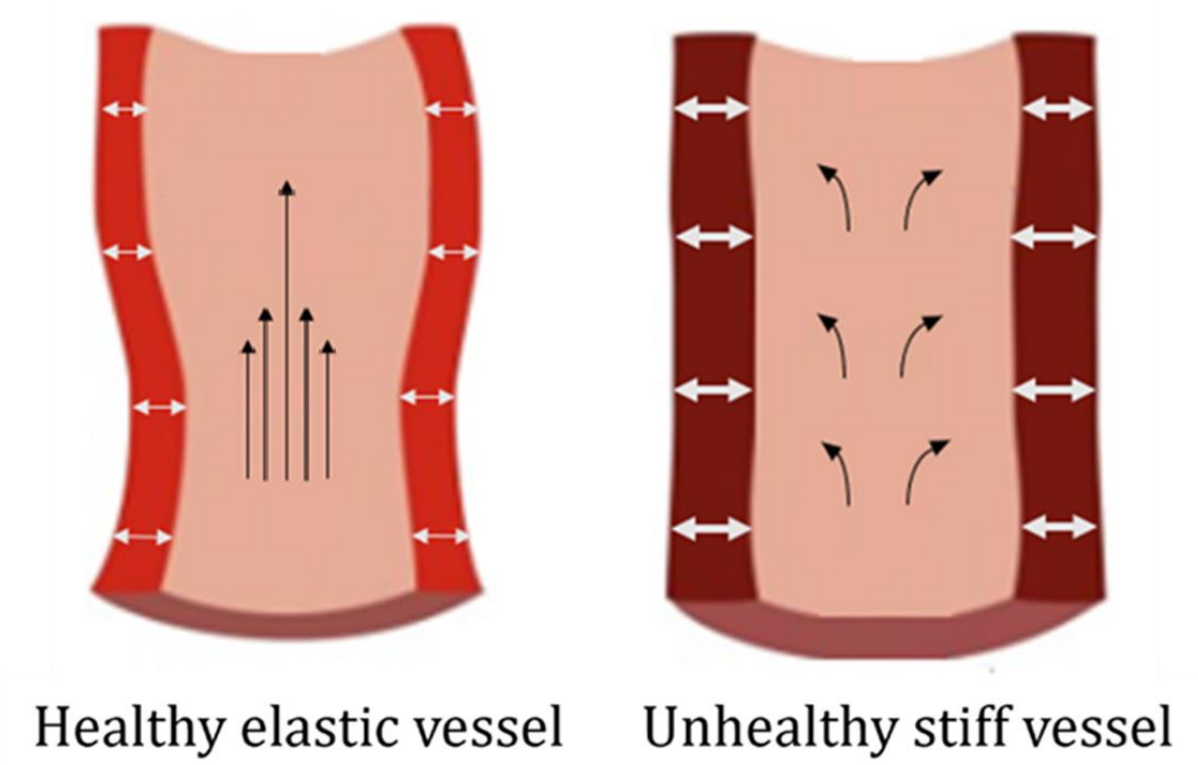

Figure 4: Comparison between a healthy, elastic artery (left) and an aged, stiffened artery (right) [3]. Adapted from LaRocca et al. [36]. Laminar flow is depicted by smooth, parallel streamlines, while turbulent flow is illustrated by curved lines.

Given that elevated BP is a recognised risk factor for CVD, it is important to outline the underlying concept [2]. BP, measured in millimetres of mercury (mmHg), refers to the force exerted by circulating blood on the walls of the arteries, generated primarily by the contraction of myocardial fibres during the cardiac cycle. The relationship between BP, CO, and total peripheral resistance (TPR) can be described using an analogy to Ohm's Law, as expressed in Equation 1. In this context, BP is the product of CO and TPR, where TPR represents the overall resistance to blood flow imposed by the systemic vasculature. This relationship also defines the mean arterial pressure (MAP), which represents the average arterial pressure throughout one cardiac cycle [37].

Equation 1: Ohm's Law in the context of blood pressure (BP).

$$BP = CO\ X\ TPR$$

The arterial pressure waveform, shown in Figure 5, represents the cyclical changes in pressure that occur with each heartbeat. It is characterised by distinct features, including the systolic and diastolic pressures, as well as the dicrotic notch, which highlights the

transition from systole to diastole [38]. Systolic pressure corresponds to the arterial pressure during ventricular contraction, while diastolic pressure reflects the pressure during the relaxation phase between heartbeats.

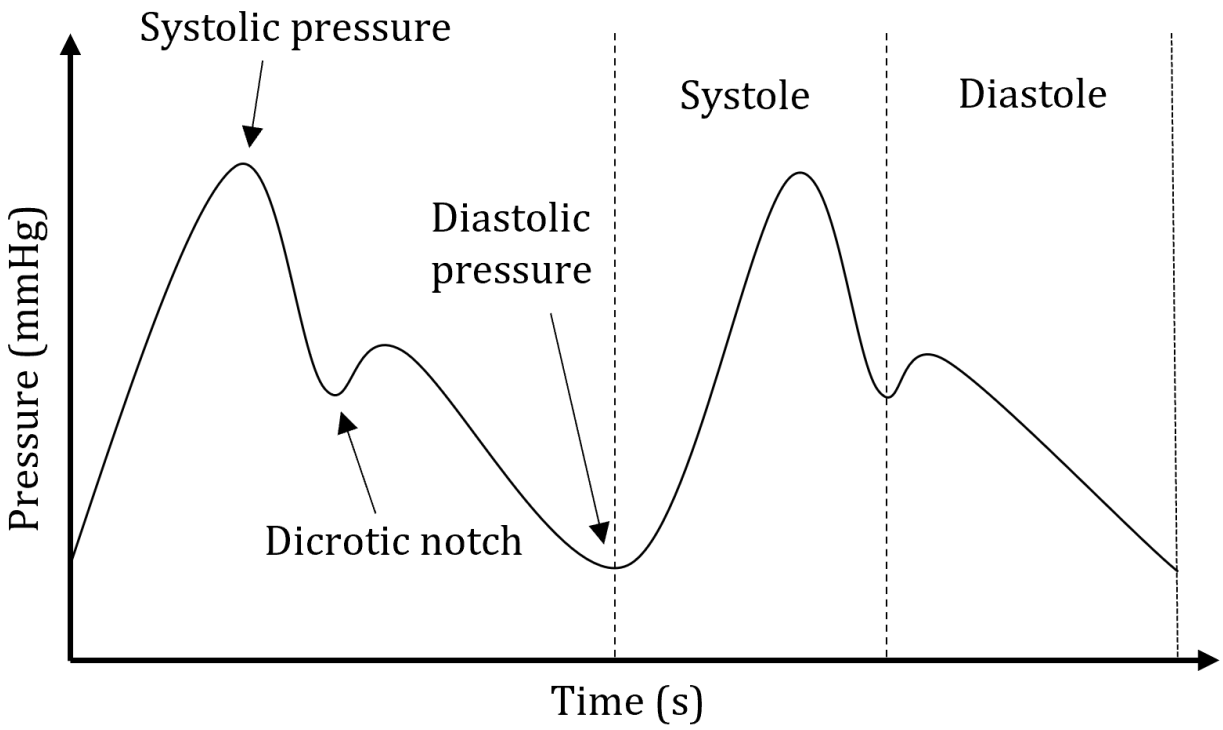

Figure 5: Graphical representation of the arterial pressure waveform. The systolic and diastolic pressures are highlighted, along with the dicrotic notch. The pressure peaks reflect the systolic and diastolic phases of the cardiac cycle. Adapted from Nguyen and Bora [38].

Vascular ageing is not only associated with volumetric changes but is also hypothesised to contribute to haemodynamic alterations. As arterial stiffness increases with age, it is commonly observed that pulse pressure, defined as the difference between systolic BP and diastolic BP, increases due to a decline in diastolic pressure and a rise in systolic pressure [39]. The reduction in diastolic pressure can impair coronary perfusion, given that coronary blood flow predominantly occurs during diastole [40]. This can be explained by Poiseuille's Law, which describes the volumetric flow rate, F, as being proportional to the pressure gradient between arterial pressure, P_a, and venous pressure, P_v, and inversely proportional to the viscous resistance, R, assuming laminar flow, as shown in Equation 2. The resistance, R, depends on both the length of the vessel, L, and the viscosity of the blood. The viscosity, μ, defined as the friction opposing fluid motion,

contributes to flow resistance along with vessel geometry, as shown in Equation 3, where r denotes the vessel radius [41].

Equation 2: Poiseuille's Law assuming laminar flow [41].

$$F = \frac{P_a - P_v}{R}$$

Equation 3: Resistance to flow in a tube (vessel) [41].

$$R = \frac{8\mu L}{\pi r^4}$$

In cases where turbulent flow occurs, often due to pathological conditions, the relationship between pressure and flow is no longer linear. Similarly, pulsatile flow, as opposed to steady laminar flow, introduces additional resistance [42]. According to Poiseuille's Law, stiffened, aged vessels are expected to exhibit lower flow rates due to increased resistance, in contrast to young, healthy vessels that demonstrate lower arterial stiffness and, consequently, reduced resistance. These younger vessels serve as a physiological baseline. It is important to investigate whether the progression of vascular ageing can be characterised as a deviation from this baseline, as it may be associated with altered haemodynamic patterns that impair tissue perfusion and potentially damage downstream organs [3].

2.4 Vascular Pathologies

An increasing body of evidence indicates a strong association between vascular ageing and the onset of various neurological and cardiovascular conditions. As the vasculature deteriorates with age, the risk of CVD and cerebrovascular disease, including stroke, dementia, and cerebral small vessel disease (SVD) increases [43], [44]. It is suggested that vascular ageing may contribute to the development of these conditions, particularly among individuals with comorbidities such as hypertension. The remainder of this section explores vascular pathologies associated with the ageing of the vasculature.

2.4.1 Arterial Stiffness

Arterial stiffness is a core indicator of vascular ageing and is characterised by the progressive loss of elasticity within the arterial walls, impairing their ability to expand and recoil in response to pulsatile blood flow [45]. This stiffening arises from structural and functional changes within the arterial wall, including reduced elastin and increased collagen, which shift the vessel towards a more rigid state. This loss of compliance alters the haemodynamic environment by disrupting the efficient distribution of blood throughout the vascular system. As arterial stiffness increases, the capacity for volumetric expansion diminishes, leading to changes in overall cardiovascular performance [46]. Mechanisms such as endothelial dysfunction and chronic inflammation contribute to the initiation and progression of arterial stiffness. Endothelial dysfunction arises from damage to the vascular endothelium, which reduces the arteries' ability to dilate [47]. Chronic inflammation promotes arterial stiffening through the release of pro-inflammatory cytokines, which contribute to arterial wall damage [48]. Arterial stiffness may be further increased by arterial calcification; although calcification and stiffness are distinct processes, they can mutually reinforce one another [49]. Therefore, while these processes are considered independent, the ability to detect arterial stiffness is of significant value, not only as a marker of vascular ageing and CVD, but also as an indicator of other processes that contribute to progressive arterial hardening.

One of the most widely used indicators of arterial stiffness is PWV, which measures the speed at which the arterial pulse wave generated by the cardiac cycle travels between two sites [50]. Elevated PWV has been associated with increased arterial stiffness, as the loss of elasticity results in faster transmission of pulse waves through stiffened arteries [51]. Another commonly used indicator of arterial stiffness is the augmentation index (AIx), an index expressed as a percentage. It is calculated by dividing the augmentation pressure, which is the difference between the second and first systolic peaks of the arterial pressure waveform, by the pulse pressure, defined as the difference between systolic and diastolic BP [52]. A higher AIx value is indicative of increased arterial stiffness, as it reflects that a greater proportion of the pressure wave is returning from the peripheral arteries due to reduced vascular compliance. The measurement techniques for arterial stiffness are discussed in more detail in Chapter 3 and Chapter 4.

2.4.2 Atherosclerosis, Coronary Artery Disease, and Arterial Thrombosis

Atherosclerosis, as depicted in Figure 6, is a chronic inflammatory disease characterised by the build-up of fatty deposits on the inner walls of arteries, leading to their hardening. It accounts for approximately 50% of deaths in Western societies. The condition is primarily initiated by the accumulation of low-density lipoprotein and activation of inflammatory processes within the arterial walls. This results in lipid retention in the intima layer, forming arterial lesions and further aggravating chronic inflammation. Atherosclerosis is predominantly asymptomatic in its early stages and is regarded as a major cause of CVD [53]. Over time, it can progress to coronary artery disease (CAD), where atherosclerotic plaque builds up within the arterial lumen, leading to narrowing or blockage of the coronary arteries and reduced blood flow to the heart [54].

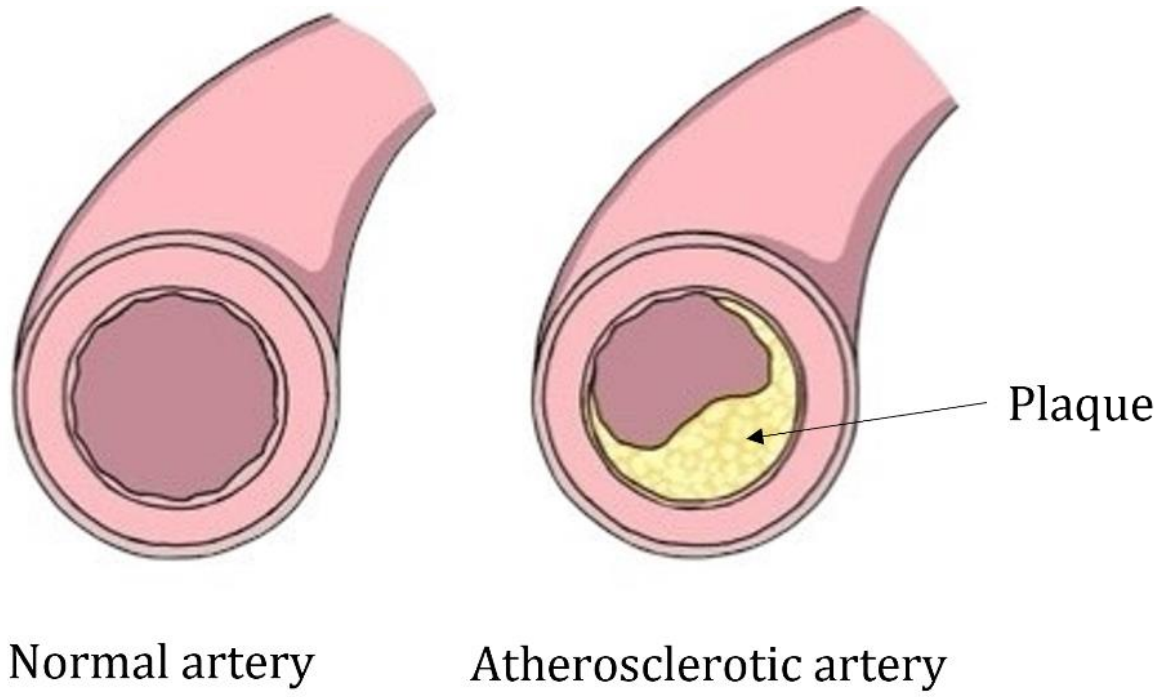

Figure 6: Illustration of atherosclerotic artery (right) compared with a healthy artery (left). The atherosclerotic artery shows plaque accumulation within the intimal layer and lumen, resulting in arterial narrowing. Adapted and modified from Pahwa and Jialal [53].

The initial stage in the development of atherosclerosis, and ultimately CAD, involves the formation of fatty streaks due to the accumulation of lipids within the arterial wall. Over time, these fatty streaks can progress into fibrous plaques, characterised by a lipid-rich necrotic core covered by a fibrous cap composed of connective tissue, including collagen and smooth muscle cells. If this fibrous cap becomes thin or ruptures, the plaque is exposed to the bloodstream, potentially triggering thrombus (clot) formation. This can

obstruct blood flow and lead to clinical events such as myocardial infarction or stroke [53], [54]. The obstruction of blood flow in CAD affects the haemodynamic function of the cardiovascular system. The narrowing of the arteries can lead to restricted blood flow, resulting in inadequate tissue perfusion. This impaired perfusion can cause common symptoms such as chest pain or shortness of breath [54].

Arterial thrombosis refers to the formation of a blood clot within an artery, leading to partial or complete obstruction of blood flow. This typically occurs following the rupture of an atherosclerotic plaque, which exposes thrombogenic material to the bloodstream. Platelets are rapidly recruited to the site of rupture, where they become activated, adhere to the endothelium, and aggregate to form a thrombus [58]. As with other vascular pathologies discussed, arterial occlusion due to thrombosis can impair perfusion and restrict blood supply to downstream organs, potentially resulting in tissue damage or organ dysfunction.

2.4.3 Peripheral Arterial Disease

Around 20% of people in the United Kingdom (UK) aged between 55 and 75 suffer from peripheral arterial disease (PAD), which is a narrowing of the artery vessels due to factors such as wall thickening or the accumulation of fatty deposits [55], [56]. PAD patients typically have no outward symptoms, making early detection difficult. In extreme cases, this may necessitate even an amputation because in the absence of treatment, cardiovascular death may occur [57]. Cardiovascular death can occur due to a lack of blood reaching the organs/tissues when the arteries become narrow or obstructed, a state known as gangrene. Affected limbs may have decreased perfusion and hence suffer from oxygen starvation, immobility, and increased discomfort [58]. Early detection (facilitated by wearable devices) has the potential to prevent cardiovascular death, especially in asymptomatic patients and further advances in technology and techniques to monitor vascular health can provide important information to avoid limb loss.

Similar to atherosclerosis and CAD, the accumulation of fatty deposits within the arterial walls can lead to arterial stiffening and luminal narrowing, both of which cause reduced blood flow [57]. This arterial stiffness impairs the ability of blood vessels to undergo normal vasodilation and vasoconstriction, thereby compromising overall vascular function [45]. Asymptomatic PAD poses a silent risk, potentially leading to severe

conditions if undetected [3], [59]. However, when assessing PAD, particularly using bilateral signals, such as those from both lower limbs, it is important to account for potential asymmetry between the signals. Such asymmetry may arise because PAD can affect one limb or multiple limbs, and thus should be carefully considered during measurement and interpretation to avoid diagnostic inaccuracies [60].

CHAPTER 3: CURRENT STATE-OF-THE-ART TECHNIQUES AND TECHNOLOGIES IN VASCULAR AGEING

The contents of this chapter are adapted from my published paper in Sensors, titled 'Photoplethysmography for the Assessment of Arterial Stiffness', and have been updated to reflect developments up to the present date.

3.1 Introduction

This section outlines the latest methods and innovations for assessing arterial stiffness, along with their respective advantages and disadvantages. Furthermore, compelling evidence indicating a recent growth in research focused on assessing arterial stiffness using PPG is presented in Chapter 4, to propose PPG as a potential tool for assessing vascular ageing. Numerous techniques have been investigated to assess arterial stiffness, some of which are currently used in commercial medical devices and some, such as PPG, of which still remain in the research space.

The primary aim of this review was to cover the current state-of-the-art technology and approaches in detecting arterial stiffness and monitoring vascular ageing. The review aimed to evaluate current trends and to offer suggestions for future research. The concept of using non-invasive measuring techniques to evaluate vascular stiffness is presented along with the benefits and drawbacks of the available modalities.

Non-invasive imaging techniques such as ultrasound and Magnetic Resonance Imaging (MRI) are common in clinical practice. Angiography, a more invasive technique that is radiation-based and involves the injection of a contrast agent into the vessel [61], is also utilised. These techniques, while routinely used, are perhaps not ideal when rapid and early screening might be the desirable way forward. Such techniques can be cumbersome, expensive, operator-dependent, and sometimes invasive. In addition, patients must be referred by a GP for hospital-based screening, which might delay detection and increase patient concern. The use of non-invasive sensing modalities for the assessment of vascular disease has attracted a lot of attention from researchers throughout the years [3], [62]. Despite many efforts, a quick and relatively simple screening method that is clinically acceptable is not yet available.

As discussed in Chapter 4, PPG is an optical technology that has risen in popularity. It is suggested that PPG can be a solution when developing novel techniques for assessing vascular ageing. Arterial stiffness can cause haemodynamic, mechanical, and volumetric changes. In aged vessels, the unhealthy vessels become stiff and thicken, becoming less elastic and making it more difficult for blood to pass through. Blood flow is altered in ways that can damage downstream organs. A higher pulse pressure results from higher systolic arterial pressure and lower diastolic arterial pressure. Unhealthy vessels experience blood volume changes as a result of having less pulsatile expansion than healthy vessels. These changes can influence the PPG signal. Therefore, it is suggested that PPG-based technology has the potential to evaluate viscoelastic properties of arteries, including monitoring haemodynamic and pulsatile blood volume changes, and hence evaluate vascular ageing.

The current methods utilised in clinical settings to evaluate vascular health have limitations. This literature review explores state-of-the-art non-invasive techniques for assessing vascular ageing through measurements of arterial stiffness. By examining prior research conducted in in vitro and in in vivo settings, while emphasising key discoveries and outcomes along with the strengths and weaknesses of each technique, this review proposes recommendations for assessing vascular health in the future. While existing methods are inconvenient for GP-level screening, PPG has the potential to provide a non-invasive optical solution for assessing vascular ageing. PPG has gathered attention for its ability to assess viscoelastic properties, monitor haemodynamic changes, and detect pulsatile changes in blood volume. As a result, it offers promise in assessing vascular health by addressing the shortcomings of existing techniques. Nonetheless, further research is crucial for understanding the full scope of the capabilities and limitations of PPG before its widespread adoption in clinical practice. The findings from the literature review have been structured to present studies related to PPG in Chapter 4, while other relevant techniques and technologies are covered in Chapter 3.

3.2 Methodology

Literature was identified through searches conducted in PubMed, Embase, Scopus, Web of Science, and Cochrane Library. Keywords including “vascular ageing”, “non-invasive”, and “arterial stiffness” were used in assessing the titles and abstracts. Several permutations of “photoplethysmography” were also employed. An example query for Embase was: (vascular ageing or vascular aging or arterial stiffness).ti. and (non-invasive or PPG or photoplethysmography or photoplethysmogram).ab. A full list of the keywords along with the search strings can be found in Appendix (Table 25). Only publications from 1990 to June 2025 were included to assess the shift from traditional to recent technologies. Papers published in the English language were only included in the search. This yielded a total of 620 papers from all the databases. Studies involving in vivo and in vitro experiments met the inclusion criteria. A total of 294 duplicate papers were eliminated. Furthermore, 254 papers were omitted because their titles and/or abstracts were unrelated to the study. Therefore, 72 papers were included for analysis by meeting the inclusion criteria (Figure 7). The searches were performed in June 2025.

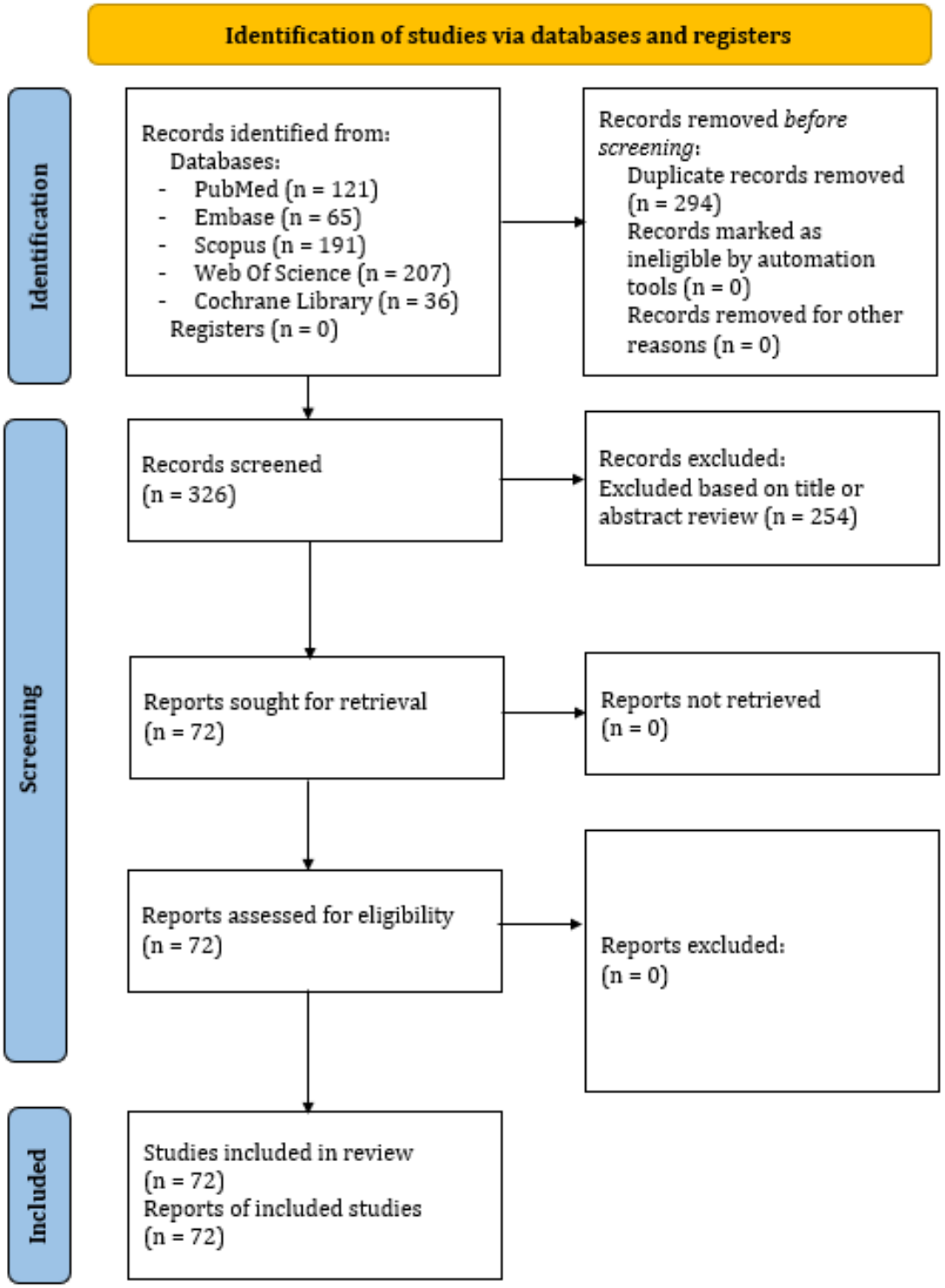

Figure 7: Flow diagram from PRISMA [63] illustrating the search strategy for the literature review procedure [3]. The PRISMA flow diagram facilitated study selection. It was used to present the review clearly, mapping the number of papers and eliminating duplicates in databases. Records deemed irrelevant based on title or abstract were excluded from the screened total. Subsequently, 72 papers underwent eligibility assessment, all of which have been included in the review, as presented in Chapter 3 and Chapter 4.

Out of the 72 studies reviewed, 38 evaluated arterial stiffness using PPG-based methods, which are discussed in Chapter 4. Another 34 studies concentrated on alternative measurement techniques. Two PPG-based studies found in the search overlapped with another method; they have been included in the overall count for PPG-based procedures. The split for the mean number of publications found per decade can be seen in Figure 8. Between 2010 and 2019, demand rose for arterial stiffness measurement techniques, particularly those using PPG-based methods, compared to the period from 2000 to 2009. The search and inclusion criteria revealed a lack of interest in arterial stiffness assessment techniques from 1990 to 1999; nevertheless, studies from this decade may not have been captured if alternative terminology was used during this period.

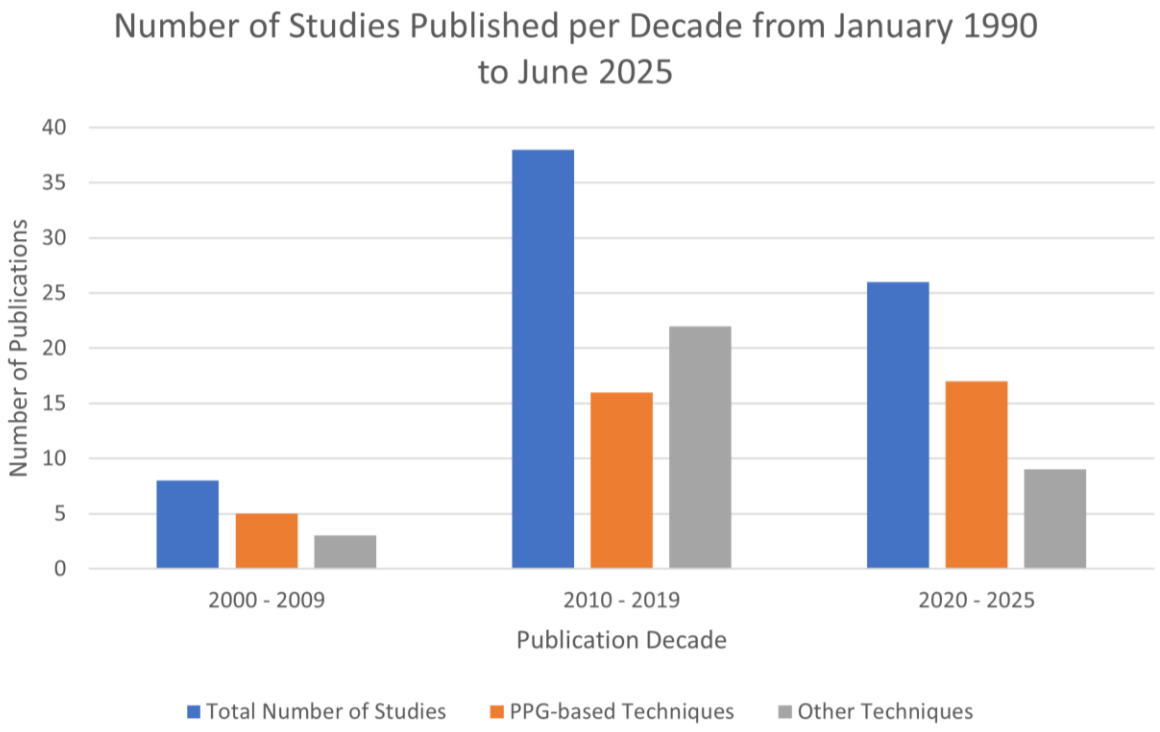

Figure 8: Bar chart showing the mean number of publications released per decade for the years between 2000 and 2025 that met the inclusion criteria. The total number of publications has been split between PPG-derived methodologies and other techniques used. No relevant studies were found for the years between 1990 and 1999, which may be due to alternative terminology used during this period [3].

3.3 Measurements of Pulse Wave Velocity

PWV is considered the gold standard for assessing arterial stiffness. PWV assesses the speed at which arterial pressure waves move through the aorta and large arteries. Recently, different techniques have been employed to analyse PWV in the assessment of arterial stiffness. Research has been conducted in areas linking arterial stiffness to body fat percentage (BFP), aortic valve replacement, children and adolescents with inflammatory bowel disease (IBD), and coronary stenosis. The use of impedance cardiography in assessing arterial stiffness using PWV has also been explored.

Gong et al. [64] conducted a study to examine the relationship between BFP and arterial stiffness. Eligible patients were categorised into four groups based on gender and arterial stiffness, and carotid femoral PWV (cfPWV) was measured. Each patient's BP, height, waist circumference, and body weight were also recorded. The study concluded that it was challenging to confirm a cause-and-effect relationship between BFP and cfPWV. PWV Tonometry-based devices were also utilised to measure the cfPWV prior to this investigation. Ji et al. [65] used cfPWV measurements to assess arterial stiffness. The study focused on the operator's placement, the distance being measured, and the tonometer position. Manual measurements were made of the distances between the suprasternal notch and the remote detection site (femoral artery), the distance between the sternal notch and the proximal (carotid artery) detection point, and the distance between the femoral artery and the carotid artery detection point (cf-distance). Western nations make extensive use of cfPWV, and the study's tonometry-based apparatus is frequently used to assess aortic PWV. The device allowed for the measurement of central BP; however, questions over the accuracy of doing so with non-invasive methods remain.

Cantürk et al. [66] investigated the severity of aortic stenosis after an aortic valve replacement. The patients were between the ages of 43 and 75. PWV was measured at baseline and six months after having an aortic valve replaced. However, a limited sample size was employed, and the study's methodology was different from that of earlier research, making comparison challenging. A larger investigation is needed for more conclusive results.

The arterial stiffness of children and adolescents with IBD has also been examined. Based on the carotid artery and the femoral artery, the Vicorder device (Skidmore Medical

Limited, Bristol, UK) was used to take cfPWV measurements. A causal interpretation of the findings was constrained because it was a cross-sectional study of a relatively small and heterogeneous sample. Additionally, no comparison groups were available, meaning the outcomes had to be interpreted in relation to pre-determined reference values. Future research on the long-term effects of CVDs in patients with IBD should make use of bigger sample numbers [67].

Liu et al. [68] used multidetector computed tomography angiography to determine coronary stenosis using brachial-ankle PWV (baPWV). Although only elastic arterial stiffness should be recorded, one limitation of baPWV is that the parameter captures both muscle and elastic arterial stiffness. In another study, PWV was examined to determine whether it reflects central or peripheral arterial stiffness. However, one of the study's shortcomings was that a longitudinal follow-up was not conducted to examine subsequent CVD occurrences. The results' applicability to other populations is also uncertain despite the sample size being rather large [69]. In another study, Yufu et al. [70] measured the aortic PWA and percent mean pulse amplitude (%MPA). These tests were performed on 33 patients at the right brachial artery on both sides of the ankle. However, the study omitted the consideration of additional factors impacting %MPA beyond aortic stiffness, such as femoral stiffness.

Scudder et al. [71] recorded dual impedance signals using a spot electrode arrangement on 78 adults aged 19 to 78. The pulse transit time (PTT), which was obtained by measuring the aortic flow onset and arrival times of peripheral pulse waveforms, was used to calculate PWV. PTT has an inverse relationship to PWV and represents the amount of time it takes for a pulse wave to travel a known distance. The study had drawbacks despite the authors' claim that dual impedance cardiography (d-ICG) is a reliable approach to measure arterial stiffness, reasonably inexpensive, and easy to use due to minimal expertise being required. Firstly, the sample size was small and comprised, mostly, young healthy adults. Secondly, because of the longer pulse trajectory through distal arteries, such as the tibial artery, d-ICG was unable to provide direct assessments of central aortic stiffness (as with most non-invasive measures of PWV). Furthermore, it was advised that specific software configurations needed to be changed in order to collect the whole signal range and use the first derivative to determine timing characteristics.

3.4 Arterial Stiffness Index Calculations

The use of indices for measuring arterial stiffness has been studied by numerous researchers. This section summarises the recent utilisation of different indices, including the cardio-ankle vascular index (CAVI), ambulatory arterial stiffness index, AIx, arterial velocity–pulse index (AVI), arterial pressure–volume index (API), compliance index (CI), arterial stiffness index (ASI), and ankle-brachial index (ABI).

In order to determine arterial stiffness, Miyoshi and Ito [72] used the CAVI, which measured the distance from the origin at the aorta to the ankle and calculated the time it took for the pulse pressure wave to travel from the aortic valve to the ankle in order to obtain the PWV from the heart to the ankle. Additionally, the brachial artery in the upper arm was used to gauge BP. Following that, the Bramwell–Hill formula was applied to express the link between the PWV and change in volume. The fact that the CAVI can analyse arterial characteristics by splitting them into BP and arterial stiffness is one of its advantages over other methods for measuring arterial stiffness. Additionally, it measures the ascending aorta, suggesting that the arterial stiffness measurement may be more closely related to cardiac function. The CAVI has the potential to be helpful in clinical settings because of its relative simplicity and flexibility, though more research is needed.

In recent years, Darroudi et al. [73] assessed the CAVI alongside PWV, central aortic pressure, and central AIx. The study included 363 healthy participants, 266 individuals with self-reported but unconfirmed CVD symptoms, and 292 individuals who had experienced major cardiovascular events. Multivariate regression analysis revealed that PWV was significantly higher among those with confirmed CVD. However, no significant associations were observed between CAVI and traditional cardiovascular risk factors such as hypertension and obesity. Individuals with diabetes exhibited lower central AIx, although no other significant associations between central AIx and additional risk factors were identified. The authors highlighted the need for longitudinal follow-up, as the cross-sectional design limited the study to single-time-point measurements.

Souza-Neto et al. [74] evaluated the ambulatory arterial stiffness index for the measurement of arterial stiffness in heart transplant patients. It was determined that the ambulatory arterial stiffness index presented a non-invasive way to indicate hypertension. However, the index was not compared with standard methods such as

PWV or AIx. In rheumatoid arthritis (RA) patients, Klocke et al. [75] used radial PWA to determine AIx. The subjects were between the ages of 18 and 50, and the results were contrasted with that of a healthy control group. Despite this, validation is still needed from larger research that might examine further elements of the illness. Investigations into known physiological factors that can affect the AIx are also necessary. As an illustration, it was stated that AIx was lower in men and that it negatively correlated with height and heart rate and positively correlated with age and peripheral BP; however, these results must be investigated further.

Zhang et al. [76] measured AVI and API to evaluate early atherosclerosis. As stated in Table 1, baPWV was unable to predict the presence of early atherosclerosis. However, this could be explained as, according to Vlachopoulos et al. [77], baPWV is the average arterial stiffness between the brachial and ankle arteries, which reduces sensitivity in detecting changes in central arterial stiffness. Despite this, the study had some drawbacks, including a sample comprising a high proportion of patients who had taken cardiovascular medications such as anti-hypertensive medications. The effects of such medications remain unknown [76]. Wang et al. [78] used a digital volume pulse (DVP) approach (also reported by Millasseau et al. [79]) to compare clinical features in patients with chronic kidney disease (CKD) using measurements of arterial stiffness in various arteries; however, similar to Zhang et al. [76], medication effects were not considered. To assess local vascular stiffness, CI was utilised to analyse the correlation between volume and pressure changes at the fingertip. The study included 186 CKD patients and 46 healthy subjects. The study had limitations in terms of the types of cardiovascular risk factors and, as mentioned earlier, the medications examined; not all risk factors were considered. Furthermore, because it was a cross-sectional study, causality could not be established.

Table 1: Studies that used state-of-the-art techniques and technologies to assess vascular ageing [3].

Study	Year	Device(s)/Techniques	Measurement(s)	Number of Subjects	Major Findings
Gong et al. [64]	2023	Complior (Alam Medical, Saint-Quentin-Fallavier, France)	Carotid femoral pulse wave velocity (cfPWV)	2603	In women over 60 years, body fat percentage (BFP) and cfPWV were correlated. There was no correlation detected for men or women under the age of 60. BFP was calculated using a mathematical equation rather than measured directly.
Ji et al. [65]	2018	Not stated	cfPWV	Not stated	The method was able to successfully assess aortic pulse wave velocity (PWV) and measure central blood pressure (BP) using a non-invasive tonometry-based device to record cfPWV and pulse wave analysis (PWA). The protocol emphasised standardisation of operator positioning, distance e measurements, and tonometer placement to improve reproducibility.

Study	Year	Device(s)/Techniques	Measurement(s)	Number of Subjects	Major Findings
Cantürk et al. [66]	2017	Not stated	PWV	38	The mean PWV improved in 20 individuals, as indicated by an absolute decrease in PWV detected 6 months after having aortic valve replacement compared to a baseline, and deteriorated in the other 18 subjects. Generally found that aortic valve replacement had no effect on PWV mean and that aortic stenosis was related to baseline PWV.
Lurz et al. [67]	2017	Vicorder device (Skidmore Medical Limited, Bristol, UK)	cfPWV	25	All subjects were found to have a normal cfPWV, suggesting that cfPWV does not change in subjects under 18 years of age. Most participants (68%) were in clinical remission and had no clinical evidence of cardiovascular disease (CVD).
Liu et al. [68]	2011	Computed tomography angiography	Brachial-ankle PWV (baPWV)	654	In 127 patients, there was at least one coronary artery that was stenotic. In comparison to the

Study	Year	Device(s)/Techniques	Measurement(s)	Number of Subjects	Major Findings
			Coronary Artery Calcium (CAC) score		normal control group, the stenotic group's mean baPWV and mean CAC were considerably greater. The study found a link between coronary atherosclerosis and baPWV.
Tsuchikura et al. [69]	2010	Automated device	PWV	2806	In comparison to heart-carotid PWV, heart-brachial PWV, and femoral-ankle PWV, it was discovered that baPWV had the strongest association with heart-femoral PWV. According to the findings, baPWV exhibited central stiffness as opposed to peripheral arterial stiffness.
Yufu et al. [70]	2004	Not stated	Aortic PWA Percent mean pulse amplitude (%MPA)	33	Higher arterial stiffness was indicated by a low %MPA. The %MPA was suggested as a novel atherosclerosis marker by the authors. It was discovered that the %MPA was lower in subjects with coronary artery stenosis than in

Study	Year	Device(s)/Techniques	Measurement(s)	Number of Subjects	Major Findings
					those without it. The findings showed that brachial %MPA offered prognostic values for coronary atherosclerosis in people at risk for CVD.
Scudder et al. [71]	2021	Dual impedance cardiography	PWV Pulse transit time (PTT)	78	Measurements of PWV showed a considerable positive connection with advancing age. PWV was derived using impedance signals collected from the thorax and calf. PWV demonstrated strong test-retest reliability over several days and high inter-rater reliability.
Miyoshi and Ito [72]	2016	Not stated	Cardio-ankle vascular index (CAVI)	Not stated	The study found that CAVI allows for the quantitative evaluation of disease progression, with higher CAVI values indicating a worse prognosis compared to lower CAVI values. CAVI was independent of BP at the time of measurement (unlike PWV) and indicated the

Study	Year	Device(s)/Techniques	Measurement(s)	Number of Subjects	Major Findings
					overall stiffness of the artery from the aortic origin to the ankle. The study concluded that CAVI was a better identifier of disease severity than baPWV.
Darroudi et al. [73]	2025	SphygmoCor XCEL (AtCor Medina, Sydney, Australia)	PWV CAVI Central augmentation index (AIx) Central aortic pressure	881	PWV was higher in individuals with confirmed CVD. No significant association was observed between CAVI and cardiovascular risk factors such as hypertension and obesity. Central AIx was lower in participants with diabetes.
Souza-Neto et al. [74]	2016	Not stated	Ambulatory arterial stiffness index	85	The study found that those with a risk factor such as hypertension would have arterial stiffness. It was shown that arterial stiffness was substantially correlated with diabetes, hypertension, peripheral arterial disease (PAD), and coronary artery disease (CAD). Gender did

Study	Year	Device(s)/Techniques	Measurement(s)	Number of Subjects	Major Findings
					not appear to impact arterial stiffness. Contrary to popular belief, age did not seem to be associated with arterial stiffness.
Klocke et al. [75]	2003	Not stated	AIx	14	The findings suggested that rheumatoid arthritis (RA) and increased arterial stiffness were related. Arterial stiffness was assessed using radial artery PWA, and participants with RA demonstrated a higher AIx than the control group.
Zhang et al. [76]	2017	Oscillometric device	Arterial velocity–pulse index (AVI) Arterial pressure–volume index (API) BaPWV	183	It was discovered that baPWV, which was measured separately, was unable to foretell the existence of early atherosclerosis. BaPWV was found to be comparable to AVI in predicting CAD.
Wang et al. [78]	2011	Not stated	Compliance index (CI)	232	Measurements were made for both CI derived from digital volume pulse (DVP) and PWV-DVP;

Study	Year	Device(s)/Techniques	Measurement(s)	Number of Subjects	Major Findings
					chronic kidney disease (CKD) patients had lower CI-DVP and greater PWV-DVP values than the healthy control group. Additionally, it was discovered that patients with late-stage CKD had lower CI-DVP levels than those with early-stage CKD. The more cardiovascular risk factors there were, the lower the CI-DVP was, according to the data.
Choy et al. [80]	2010	Oscillometric automated digital BP instrument	Arterial stiffness index (ASI) Ankle-brachial index (ABI) Arterial wave pattern	895	The risk of stroke was six times higher when the ASI was abnormal. Both ABI and arterial wave pattern showed strong correlations with stroke. However, there was a synergistic impact when assessing the risk of stroke when all three parameters were considered.
Naessen et al. [81]	2023	Ultrasound	Common carotid artery	63	It was discovered that compared to healthy subjects, patients with pulmonary arterial

Study	Year	Device(s)/Techniques	Measurement(s)	Number of Subjects	Major Findings
			Intima thickness Intima/media (I/M) thickness ratio Intima–media thickness		hypertension had an intima that was 56% thicker and an I/M ratio that was 128% higher. Patients with pulmonary arterial hypertension showed a thicker intima and greater I/M ratios than those with left ventricular heart failure with a reduced ejection fraction.
Li et al. [82]	2016	Real-time shear wave elastography	Longitudinal elasticity modulus PWV	179	PWV and systolic and diastolic BP were observed to be higher in acute ischemic stroke (AIS) patients than in the control group. It was demonstrated that shear wave elastography could accurately and non-invasively measure the arterial wall's longitudinal elastic modulus and assess arterial stiffness.
Bjällmark et al. [83]	2010	Conventional and Ultrasonographic strain measures	Common carotid artery elasticity	20	It was concluded that 2D strain imaging through ultrasonography was proven superior to traditional vascular stiffness measurements for

Study	Year	Device(s)/Techniques	Measurement(s)	Number of Subjects	Major Findings
					determining the elastic characteristics of the common carotid artery.
Arnold et al. [84]	2024	2D Speckle tracking	Circumferential strain Peak strain rate	47	Following transcatheter aortic implantation (TAVI), both peak circumferential strain and overall circumferential strain showed improvement, suggesting a reduction in arterial stiffness of the common carotid artery.
Kang et al. [85]	2011	Cardiac magnetic resonance imaging (MRI)	Pulmonary artery distensibility index	35	The study aimed to determine whether the pulmonary artery stiffness estimated based on right heart catheterisation and Cardiac MRI-derived pulmonary artery distensibility corresponded.
Ha et al. [86]	2018	4D Flow MRI	Aorta's turbulent kinetic energy (TKE)	42	The study examined the extent and degree of turbulent blood flow in a healthy aorta and determined whether age has an impact on the turbulence level. TKE was a measurement of

Study	Year	Device(s)/Techniques	Measurement(s)	Number of Subjects	Major Findings
					turbulence intensity. All the healthy subjects experienced turbulent flow in the aorta, and both groups' aortas were similar overall. However, when compared to the younger participants, the older subjects had 73% greater total TKE in the ascending aorta. This was associated with age-related dilation of the ascending aorta, which increases the volume available for the generation of turbulence. It was determined that age-related geometric changes influenced the development of turbulent blood flow in the aortas of healthy subjects.
Sorelli et al. [87]	2018	Periflux 5000 Laser doppler flowmetry (LDF) system (Perimed, Järfälla, Sweden)	Peripheral pulse Microvascular perfusion	54	A multi-Gaussian decomposition approach was applied to the LDF signals, and the algorithm proved effective at reconstructing the shape of the LDF pulses. It was concluded that the model

Study	Year	Device(s)/Techniques	Measurement(s)	Number of Subjects	Major Findings
					could accurately reconstruct the pulse waveform shape.
Rogers et al. [88]	2023	Near-infrared spectroscopy (NIRS) vascular occlusion testing	Age-related metabolic and microvascular function changes	34	It was concluded that the microvascular hyperaemic response and skeletal muscle metabolism decline with age for women. Test-retest reliability was investigated, with reliability higher in younger women than in middle-aged and older women.
Silva et al. [89]	2021	Mobil-O-Graph 24 h PWA Monitor Device Dual energy X-ray absorptiometry	Body composition PWV AIx Pulse Pressure Amplification Index Central Pulse Pressure	124	It was determined that arterial stiffness in the elderly is directly correlated with BFP. The findings could be related to an increased risk of CVD. It was also suggested that lower muscle mass is associated with greater arterial wall stiffness.

Study	Year	Device(s)/Techniques	Measurement(s)	Number of Subjects	Major Findings
Perrault et al. [90]	2019	SphygmoCor-Px System (AtCor Medina, Sydney, Australia) VP-1000 system (Omron Healthcare, Hoffman Estates, IL, USA) EndoPAT 2000 system (Itamar Medical, Franklin, MA, USA)	PWV AIx Reactive hyperemia index (RHI)	40	A comparison was made between the three devices. A high level of PWV reliability was attained for both the VP-100 and SphygmoCor, as shown by a low coefficient of variation. AIx had a larger coefficient of variation when using the SphygmoCor or EndoPAT than PWV. The lack of association between RHI and AIx suggests that endothelial and artery parameters have different functional properties.
Markakis et al. [91]	2021	SphygmoCor-Px System Mobil-O-Graph 24 h PWA Monitor Device	Peripheral BP Central BP PWV Artificial Intelligence (AI)	57	Both devices were compared with patients experiencing hemodynamic shock in intensive care units (ICUs). The results showed that a lack of extra-vascular diseases made invasive procedures more reliable. However, the authors concluded that non-invasive techniques are practical and can be employed as extra monitoring techniques for shock patients. With

Study	Year	Device(s)/Techniques	Measurement(s)	Number of Subjects	Major Findings
					the Mobil-O-Graph 24 h PWA Monitor Device and the SphygmoCor, full haemodynamic evaluations were successful in 48 patients and 29 patients, respectively. However, across the two devices, variations in the PWA were found.
Costa et al. [92]	2019	SphygmoCor-Px System	PWV	151	The PWV mean was observed to be higher in hypertensive patients. This finding suggests a clear relationship between arterial stiffness and increased PWV in the presence of hypertension. It was also discovered that arterial stiffness was more common in males who were older and had more risk factors than females.
Sridhar et al. [93]	2007	PeriScope (M/S Genesis Medical Systems, Hyderabad, India)	cfPWV baPWV	3969	Patients with RA had the highest heart rates whereas those with end-stage renal disease (ESRD) had the highest systolic BP. The PWV was discovered to be higher among people at

Study	Year	Device(s)/Techniques	Measurement(s)	Number of Subjects	Major Findings
					higher risk of developing CVD, including those with CAD, diabetes mellitus, ESRD, and RA, compared to the healthy control group.
Komine et al. [94]	2012	Oscillometric BP device Form PWV/ABI vascular diagnostic device SonoSite 180 Plus (SonoSite Inc., Washington, DC, USA)	BP baPWV cfPWV Carotid arterial compliance	173	The study demonstrated that arterial stiffness can be assessed solely through cuff pressure oscillometric BP measurement. Similar to cfPWV and carotid arterial compliance, the estimated API had repeatability.
Hoffmann et al. [95]	2019	Oscillometric BP monitor	Heart rate Peripheral BP Central BP PWV	8	Long-term space flight's vascular ageing biomarkers were assessed at baseline, 4 days, and 8 days post a 6-month International Space Station mission. Heart rate rose significantly 4 days after the return, but not on day 8, in comparison to the baseline. Additionally, central systolic BP also increased 4 days post-return versus the baseline measurement. PWV had an

Study	Year	Device(s)/Techniques	Measurement(s)	Number of Subjects	Major Findings
					insignificant increase from baseline 4 days post-return and remained elevated on day 8. Overall, no clinically significant changes in early vascular ageing biomarkers were found in the evaluated cosmonauts.
Juganaru et al. [96]	2019	Anteriograph instrument	Waist-to-hip ratio	313	The device was able to identify patients at cardiovascular risk before any clinical indicators found arterial stiffness. The study suggested that a high waist-to-hip ratio could be a risk factor for increased vascular stiffness.
Osman et al. [97]	2017	Anteriograph instrument NICOM (Cheetah Medical, Portland, OR, USA)	Arterial stiffness PWV AIx Cardiac output Stroke volume	33	Ultrasound scans were taken at five gestational windows between 11 and 40 weeks of pregnancy. It was discovered that normal pregnancy is associated with significant alterations in the maternal cardiovascular system. Arterial stiffness changes were

Study	Year	Device(s)/Techniques	Measurement(s)	Number of Subjects	Major Findings
			Total peripheral resistance		observed in all measurements during healthy pregnancy, and the aortic PWV showed a significant variation during pregnancy.
Kostis et al. [98]	2021	Computational algorithm	Arterial stiffness 1 Arterial stiffness 2	14097	Both indices were able to predict the occurrence of strokes. The study found that the indices derived from pulse pressure were more accurate at predicting the occurrence of stroke than pulse pressure or chronological age alone.
Negoita et al. [99]	2018	Computational algorithm: semi-automatic vendor-independent software Vivid E95 ultrasound (GE Healthcare, Illinois, US)	PWV	12	The study successfully developed software to trace the luminal diameter and blood velocity in the human ascending aorta by drawing from ultrasound images. The technique could calculate the PWV in the ascending aortas of adults.

The ASI, which was used to quantify arterial distensibility, ABI, and the arterial wave pattern using an oscillometric automated digital BP instrument, was studied by Choy et al. [80]. The subjects were split into two groups: 266 newly diagnosed stroke patients, ranging in age from 26 to 98, and a control group of 629 volunteers, all of whom were older than 30. A greater ASI indicated a higher likelihood of stroke incidence. However, ASI was determined based on BP readings, which can change depending on the participant's health at the time of the examination. Subjects who had previously experienced a transient ischemic attack or a mild stroke may not have been detected despite efforts to rule out past stroke experience based on a questionnaire. Additionally, the effects of medications on ASI were not investigated.

3.5 Imaging Techniques

3.5.1 Ultrasonography

One of the key techniques for assessing vascular age is ultrasound, an acoustical imaging modality, which uses high-frequency sound waves. Researchers have employed ultrasound to assess arterial stiffness, yielding promising results. However, ultrasound methods tend to be expensive and require expertise to operate.

Naessen et al. [81] conducted a study involving 30 healthy individuals (median age, 62; range, 27 to 82), 19 patients with pulmonary arterial hypertension (median age, 53; range, 27 to 84), and 14 patients with left ventricular heart failure with a reduced ejection fraction (median age, 67; range, 48 to 82). The healthy subjects were non-smokers and had no prior history of heart or arterial disorders. Additionally, the subjects were not taking any medications that would have impacted the arterial wall. The study disproved the common belief that vascular changes in pulmonary arterial hypertensions are only related to lung vasculature.

Li et al. [82] utilised ultrasound imaging techniques to assess arterial stiffness in patients with acute ischemic stroke (AIS) using real-time shear wave elastography to measure longitudinal elasticity modulus. With this technology, 50,000 images could be captured every second. Furthermore, radio frequency ultrasonography technology was used to calculate the PWV of the bilateral carotid arteries. The results demonstrated that shear wave elastography can be used in vascular applications. Future research is necessary to

evaluate risk factors and assign various weights to arterial stiffness in longitudinal and circumferential directions because the study was unable to analyse all deviations.

Age-dependent elasticity variations in the common carotid artery elasticity served as the foundation for the comparison between conventional and ultrasonographic strain measures in a study conducted by Bjällmark et al. [83]. The evaluation involved 10 younger subjects, between the ages of 25 and 28, and 10 older subjects, between the ages of 50 and 59. The conclusion drawn was that two-dimensional (2D) strain imaging exhibited greater accuracy compared to traditional measurements. However, concerns arose regarding the stiffness indices, as these were derived from BP and lumen diameter measurements obtained at different sites, casting doubt on the accuracy of the variables.

Echocardiography, a form of ultrasonography, has been used to assess arterial stiffness by tracking the motion of the vessel wall, particularly in the common carotid artery, using 2D speckle tracking. Arnold et al. [84] investigated arterial stiffness in a cohort of 47 patients aged between 73 and 86 years who were undergoing transcatheter aortic valve implantation (TAVI). The analysis focused on circumferential strain, defined as the maximum deformation of the vessel wall, and peak strain rate, representing the highest rate of change of circumferential strain over time. The study reported an improvement in common carotid artery stiffness following TAVI. However, the authors noted that further validation is required in larger cohorts, as technical limitations and measurement quality issues restricted the sample size to 47 participants.

3.5.2 Magnetic Resonance Imaging

MRI, which uses magnetic fields to create images, has also been investigated by researchers for the assessment of arterial stiffness.

The study conducted by Kang et al. [85] used cardiac MRI to calculate the pulmonary artery distensibility index to assess pulmonary artery stiffness. However, the study had certain limitations. Firstly, despite the disease being rare, the subject group was small. Secondly, among the thirty-five patients under observation, only three were noted to have severe pulmonary regurgitation, which can suggest that the pulmonary artery distensibility index would have been overestimated.

The impact of age on turbulent blood flow was assessed by Ha et al. [86] using four-dimensional (4D) flow MRI. As stated in Table 1, all subjects experienced turbulent flow in the aorta. However, this was based on a small sample size of twenty healthy males aged between 67 and 74 and twenty-two healthy males aged between 20 and 26. Although MRI does not expose patients to radiation, some may experience claustrophobia, rendering it inappropriate for a general evaluation of vascular ageing.

3.6 Optical Techniques

In the context of arterial stiffness assessment, optical modalities including LDF, near-infrared spectroscopy (NIRS), and PPG have been investigated.

The medical technique of LDF is based on the Doppler shift principle, whereby changes in the frequency of laser light are used to assess microvascular blood flow. In this technique, the tissue surface is illuminated, and the backscattered light is collected using an LDF probe. When the incident laser light interacts with moving red blood cells, a frequency shift occurs, forming the basis of the Doppler effect used by the method [100]. This principle is discussed in greater detail in Chapter 10. Sorelli et al. [87] assessed vascular ageing using the Periflux 5000 LDF system (Perimed, Järfälla, Sweden). On the right hallux pulp of the individuals, microvascular perfusion was recorded. A supervised classifier was trained and validated using over 20,935 models of pulse waves. Although using LDF is less expensive than using other imaging techniques, it can have signal processing and motion artefact issues [101].

The analytical technique, NIRS, uses a broad spectrum of near-infrared light to illuminate the region of interest and measures the light that is absorbed, transmitted, reflected, or scattered. Age-related metabolic and microvascular function changes were assessed by Rogers et al. [88] using NIRS vascular occlusion testing. NIRS signals were recorded from 17 younger and 17 middle-aged and older women. The Framingham risk calculator was used to determine a 10-year risk. Due to the cross-sectional nature of the study, it was not possible to evaluate the causal temporal relationship between age and the results. Additionally, the thickness of the adipose tissue was not assessed, which might have reduced the absolute NIRS signals. Finally, the melanin levels were not considered, which might have affected the NIRS signal.

PPG measures pulsatile changes in blood volume via light–tissue interactions and has been investigated as an optical approach for assessing arterial stiffness [3]. Studies that employ PPG for arterial stiffness assessment are discussed in greater detail in Chapter 4.

3.7 Existing Commercial Devices

Commercial devices which measure arterial stiffness do exist. These devices include the Mobil-O-Graph 24 h PWA Monitor Device, SphygmoCor-Px System (AtCor Medina, Sydney, Australia), VP-1000 system (Omron Healthcare, Hoffman Estates, IL, USA), EndoPAT 2000 system (Itamar Medical, Franklin, MA, USA), PeriScope (M/S Genesis Medical Systems, Hyderabad, India), Form PWV/ABI vascular diagnostic device (Omron Healthcare, Kyoto, Japan), SonoSite 180 Plus (SonoSite Inc., Washington, DC, USA), Anteriograph, and NICOM (Cheetah Medical, Portland, OR, USA).

The Mobil-O-Graph 24 h PWA Monitor Device was used by Silva et al. [89] to evaluate the link between body composition and arterial stiffness. Dual-energy X-ray absorptiometry on a Hologic bone densitometry machine (Model Discovery A, Waltham, MA, USA) was used to obtain the body compositions of the participants. However, the study was constrained because it was carried out in a single location with community elders, lacking applicability to a broad and diverse population. Additionally, the study ignored the individuals' usage of medications such as anti-hypertensives, which would have affected the central circulation parameters.

Although there are instruments that can distinguish between healthy and unhealthy vessels, no device is ideal. Perrault et al. [90] compared the measurement capabilities of the SphygmoCor-Px System, the VP-1000 system, and the EndoPAT 2000 system in healthy subjects ranging in age from 23 to 71. The outputs of the instruments differed numerically, making it difficult to compare the outcomes. Furthermore, because there is a lack of knowledge regarding changes to the parameters in relation to illness progression, it makes it difficult to track disease progression or the efficacy of a particular intervention. Markakis et al. [91] evaluated the SphygmoCor-Px System and the Mobil-O-Graph 24 h PWA Monitor Device in terms of feasibility. Invasive and non-invasive measurements were performed within 24 h of admission and again 48 hours later for comparison purposes on patients experiencing haemodynamic shock in intensive care units (ICUs). It was concluded, as illustrated in Table 1, that non-invasive procedures can

be used as part of an additional monitoring method while invasive techniques are more trustworthy. However, the results of the study are questioned because of the small sample size. The SphygmoCor-Px has also been used in studies to assess vascular ageing by acquiring the PWV. Costa et al. [92] used the SphygmoCor-Px in a study conducted on individuals with arterial hypertension. Chi-square analysis was performed as the primary statistical analysis. Despite the small size representing a community and the requirement for a larger size, the study was able to demonstrate its ability to measure arterial stiffness non-invasively using a gold-standard instrument.

Sridhar et al. [93] used the PeriScope to measure arterial stiffness by obtaining the PWV of 988 healthy controls and 2988 who had a high risk of developing CVD. Using an oscillometric approach, the PeriScope simultaneously assessed the cfPWV and baPWV. It was concluded that those with a higher risk of developing CVD had a higher PWV than the healthy control group. In another study, Komine et al. [94] used an oscillometric BP device to evaluate arterial stiffness. An inflatable cuff was used to assess the BP of the individuals, and the Form PWV/ABI vascular diagnostic device was used to obtain the baPWV and cfPWV. The SonoSite 180 Plus was used in the study to obtain images using ultrasound. It should be noted that the study did have restrictions. For instance, the oscillometric cuff pressure was used to take an indirect measurement of arterial volume. Between the brachial blood vessel and cuff, the size of the muscle and fat has unknown effects on the arterial volume. To determine whether the technique could be utilised to measure arterial stiffness when illnesses are present, more research is needed. In a more recent study, Hoffmann et al. [95] used a oscillometric BP monitor to assess early vascular ageing biomarkers in cosmonauts, aged between 41 and 51 (7 males and 1 woman), undergoing long-term space flights. To summarise, it was found that the cosmonauts had not undergone any clinically significant changes despite comparisons to the baseline measurements (represented by 65 to 90 days prior to the flight). Long-term flights in deep space should reportedly be looked upon in the future. Due to the study's limited sample size, it is recommended to conduct a follow-up examination several years later. The current follow-up duration in the study was deemed too short to adequately identify any delayed onset of vascular diseases.

Juganaru et al. [96] collected arterial stiffness parameters from 184 males and 129 females, ranging in age from 18 to 53, using the Anteriograph instrument. According to

the study, a high waist-to-hip ratio may be a vascular stiffness risk factor. The early asymptomatic detection of vascular atherosclerosis could be aided by screening healthy people with high waist-to-hip ratios. Despite the device's non-invasiveness, quick deployment, and repeatability in assessing artery stiffness parameters, incorrect cuff positioning can produce false findings. Osman et al. [97] evaluated arterial stiffness changes in low-risk pregnant women using the Arteriograph. Non-invasive evaluations were performed on low-risk pregnant women. A cuff was placed on the right arm over the brachial artery to use the Arteriograph. The NICOM was also used in the study for measurements including those of CO, stroke volume, and TPR. Advantageously, the Arteriograph instrument has been extensively utilised in pregnancy research and has been validated in invasive and non-invasive measurements in non-pregnant populations. Additionally, to reduce bias in the results, only one expert who was trained on using both the Arteriograph and NICOM made the recordings. The authors were able to identify developments or changes in arterial stiffness over a longer length of time because the longitudinal investigation was based on five distinct occasions. This study was based on a small number of participants; however, a larger population is required in future studies.

3.8 Computational Algorithms

Over the years, researchers have created various computational algorithms to predict arterial stiffness. Computational algorithms navigate around the challenges associated with gathering extensive in vivo datasets along with the associated time and costs [102]. Kostis et al. [98] predicted arterial stiffness from pulse pressure using an algorithm. To test whether arterial age predicted stroke better than chronological age, two indices of arterial stiffness were created by the algorithm and adjusted for specified demographics. The study was constrained, nevertheless, because the algorithms had been demographically adjusted and hence could not be applied to other datasets. As a result, the approach could not be used with different datasets that included, for instance, different age and gender groupings. Having said that, and according to the authors, the approach may be used to design and carry out new randomised clinical trials.

To assess local arterial stiffness, a semi-automatic vendor-independent software was created by Negoita et al. [99] using a Vivid E95 ultrasound (GE Healthcare, Illinois, US) to collect images. The edges of the luminal arterial walls (M-mode) and blood velocity were determined by the software, and diameter and velocity waveforms were extracted from

the ultrasound images. The study was assessed on healthy volunteers aged between 22 and 32, with four of them being females. The technique was vendor-independent; therefore, it could be used to analyse ultrasound images of diameter and velocity recorded on any ultrasound machine as long as they have been saved in the Digital Imaging and Communications in Medicine (DICOM) format.

3.9 Summary of Chapter 3

The measurement and detection of vascular ageing is important, whether it be in a hospital setting, a GP clinic, or even a home setting. Early detection and guidance to individuals can offer patients time to change their lifestyles and to postpone the onset and progression of diseases such as atherosclerosis or PAD. Unfortunately, no device has yet been proven ideal. It is important that a future device should be relatively inexpensive, non-invasive, accurate, and user-friendly. As such, an easy-to-use measuring tool can allow for measurements to take place at home without the need to be referred by the GP to a clinical setting for a trained specialist to take readings, saving time and resources.

Predominantly, imaging techniques used to assess vascular ageing are expensive, often impractical, and require a specialist. Procedures such as MRI and angiography must be carried out in a hospital setting where qualified professionals are on hand to take images and recordings. Despite the fact that these methods exist, patients still rely on GP referrals, which might delay the detection of vascular ageing and cause patients' concern, especially in more remote areas where GP access might be difficult in the first place. Unfortunately, there is not a single imaging technique that can accommodate all patients; although MRI is inappropriate for claustrophobic patients, other methods can expose patients to radiation, and certain imaging modalities, such as angiography, are more invasive. Home monitoring is gaining popularity as wearable devices expand. Therefore, to continuously monitor vascular ageing in real time, it is crucial to have a practical, expert-independent, relatively inexpensive diagnostic instrument that can be integrated into smart homes or wearable technology.

There are commercially available instruments to assess arterial stiffness, such as the SphygmoCor-Px System and the Mobil-O-Graph 24 h PWA Monitor Device; however, their use has certain limits. Nonetheless, potentially, there is a possibility of using

commercially available tools at home to monitor progress on a frequent basis while, if necessary, maintaining the option to go to a clinical setting for more precise monitoring.

CHAPTER 4: USING PHOTOPLETHYSMOGRAPHY FOR ARTERIAL STIFFNESS ASSESSMENT

The contents of this chapter are adapted from my published paper in Sensors, titled 'Photoplethysmography for the Assessment of Arterial Stiffness', and have been updated to reflect developments up to the present date.

4.1 Photoplethysmography

PPG is a widely used non-invasive optical technique. It aids in studying and monitoring pulsations associated with changes in blood volume in a peripheral vascular bed. Over the last thirty years, the number of published articles on PPG has significantly increased, covering both basic and applied research. Throughout these publications, PPG has been praised as a non-invasive, low-cost, and simple optical technique for measuring physiological parameters applied at the surface of the skin.

The popularity of this topic can be attributed to the realisation that PPG has important implications for a wide range of applications [103], [104]. Amongst many, it aids in blood oxygen detection, cardiovascular assessment, and vital sign monitoring. In addition, the significant contribution of PPG in wearable devices has exponentially elevated the popularity and usability of PPG.

Currently, there exists a large body of literature that contributes new knowledge on the relationship between PPG pulse morphology, PWA, and pulse feature extraction with the physiological status of peripheral blood vessels. This encompasses aspects such as ageing, stiffness, BP and compliance, and microvascular disease, amongst others. There are also significant efforts in the utilisation of the PPG for the detection of heart arrhythmias such as atrial fibrillation. Researchers are continuing to strive to combine the PPG sensory capabilities of wearables, such as smartwatches, with Artificial Intelligence (AI) in delivering ubiquitous health monitoring solutions that go beyond the current available heart rate wearables [103], [105].

PPG sensors comprise Light Emitting Diode(s) (LEDs) and photodetector(s) (PD). The emitted light, which is made to transverse the skin, is reflected, absorbed, and scattered in the tissue and blood. The modulated light level, which emerges, is measured using a suitable PD. For example, it is possible for the hand to be directly transilluminated where

the light source, usually in the broad region of 450 nm to 960 nm, is on one side of the skin and the detector is on the other side. This method, also called the transmission mode, is limited to areas such as the finger, the ear lobe, or the toe. However, when light is directed into the skin, a proportion is backscattered, emerging near the light source. The light source and the PD can be positioned side by side. This method, also called the reflection mode, allows measurements on virtually any skin area. The intensity of reflected and backscattered light reaching the PD in either reflection or transmission mode is measured. The variations in the PD current are assumed to correlate to blood volume changes beneath the probe. These variations are electronically amplified and recorded as a voltage signal called the photoplethysmogram (Figure 9) [105].

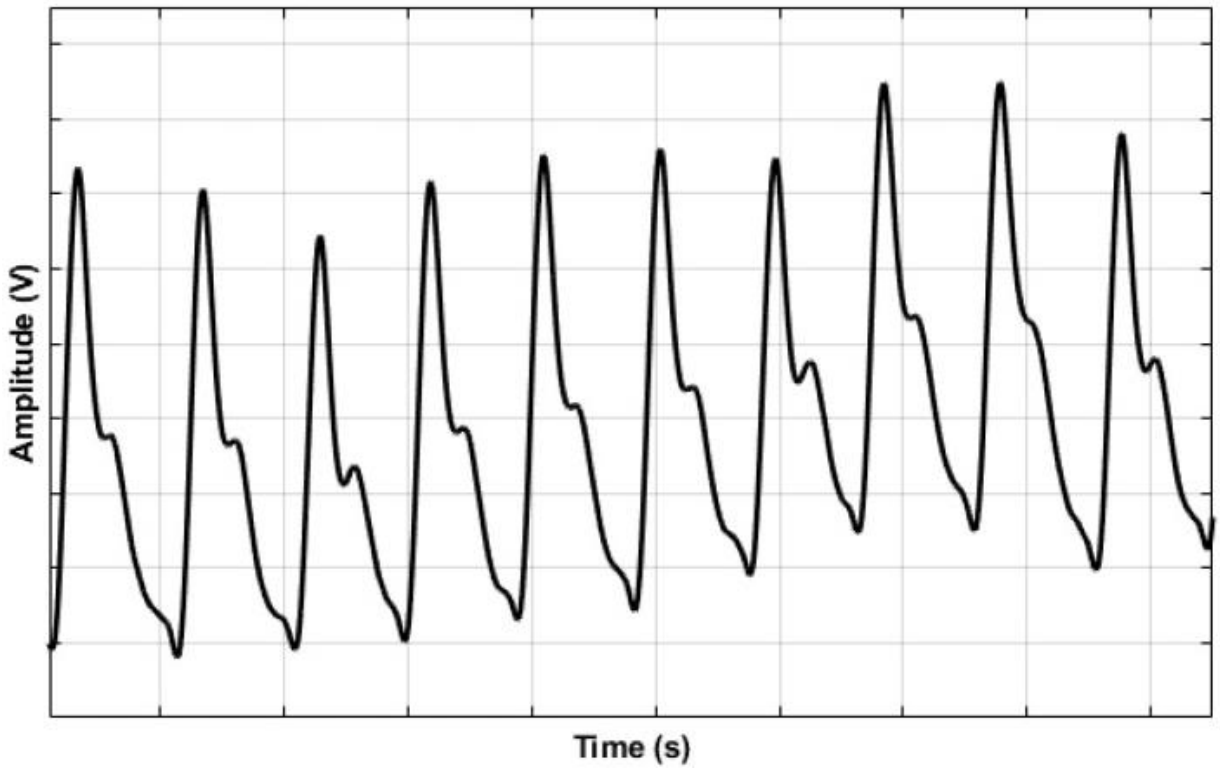

Figure 9: An example photoplethysmogram depicting the systolic and diastolic peaks with a dicrotic notch [105].

The PPG signal can be impacted by a number of variables such as temperature variations, the measurement site, perfusion status, and motion artefacts. As mentioned earlier, the transmittance or reflectance mode of the PPG sensor can differ depending on the anatomical measurement site, as shown in Figure 10. Thus, the wavelength of the light source(s) must be accounted for depending on the mode and distance that the light must penetrate. For example, red and infrared (IR) light reaches deeper than green light.

Peripheral vasoconstriction can cause low-quality signals while good skin contact has demonstrated high-quality signals [8], [106].

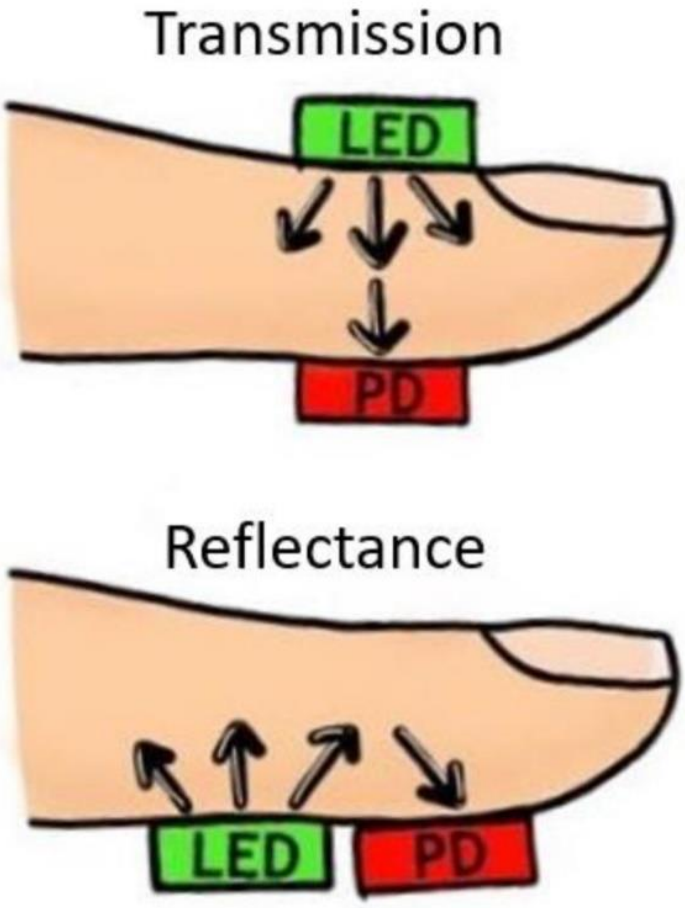

Figure 10: Photoplethysmography (PPG) sensor configuration modes [3]. Transmittance mode configuration (top image) shows light source (LED) and photodetector (PD) placed on opposite sides of the body site. In reflectance mode (bottom image), the LED and PD are adjacent.

Understanding the constraints of PPG monitoring holds significance. Since PPG detects light, it faces drawbacks such as susceptibility to interference from ambient sources, impacting measurement accuracy. Motion artifacts also pose challenges [107], though utilising post-processing algorithms can mitigate the interferences. Additionally, variations in skin tones can impact the signal as PPG relies on light–tissue interactions. Considering these factors is crucial when developing PPG-based sensors for experiments, whether in vivo or in vitro.

The evaluation of arterial stiffness using PPG has recently become popular. Many researchers have attempted to understand arterial stiffness using PPG in in vivo settings. Some in vivo research focuses on specific conditions including pregnancy, obesity, and diseases such as CAD [108], [109]. Studies have also compared PPG-based devices to one

another and to other modalities to assess the viability of using PPG-based devices. This chapter provides a review of the existing literature on the use of PPG for assessing arterial stiffness.

4.2 Existing Photoplethysmography-Based Devices

PPG is a well-established optical technology; many researchers have adopted or developed new PPG-based devices, including systems developed in university laboratories. Some researchers have conducted in vivo studies to distinguish between healthy and unhealthy patients either bilaterally (such as between healthy and PAD subjects) or by obtaining pulse waveforms from a single measuring site (such as the left index finger). This section introduces novel and existing PPG-based devices in further detail.

One of the earliest PPG research studies was conducted by Allen and Murray [110] on a group of healthy people. PPGs were recorded bilaterally from six peripheral sites (that is, the left and right ears, left and right thumbs, and left and right toes). To validate the electronic matching of right-to-left channels, a set of validation data was first gathered. Physiological measures derived from the PPGs included the root mean square error (RMSE), which measured the differences between the right and left side, and cross-correlation analysis, which measured the degree of similarity. Allen and Murray [110] found that in healthy individuals, the right and left sides of the body were highly correlated, as perhaps expected. This work paved the way for further research by Bentham et al. [60]. While it was already proven that in healthy individuals the PPGs from the right and left were highly correlated, Bentham et al. [60] obtained multi-site finger and toe PPG recordings from 43 healthy control patients and 31 PAD subjects to carry out another bilateral study. Beat-to-beat normalised amplitude variability and pulse arrival time (PAT) were assessed in the frequency domain using magnitude-squared coherence (MSC) and in the time domain using two statistical approaches. In contrast to healthy subjects, patients with PAD had a different signal on one side of the body compared to the other. The work conducted by Bentham et al. [60] highlighted the possibility of distinguishing between healthy and PAD subjects. However, the clinical demographic dataset that was gathered for the study was nonetheless limited.

Brillante et al. [111] used PPG to non-invasively measure arterial stiffness from the left index finger in healthy participants aged 18 to 67, examining the effects of age, gender, and race on indices including stiffness index (SI) and reflection index (RI) using simple correlation, Spearman's correlation, and multivariate regression. Although comparisons were reported, healthy adults over 65 were underrepresented. Similarly, Jannasz et al. [112] reported no gender differences in arterial stiffness-related outcomes, supporting the notion that gender had no bearing on the likelihood of developing atherosclerosis; however, the sample was predominantly female, which may have influenced the findings. Tąpolska et al. [113] stratified participants by age, gender, and weight and used the Pulse Trace PCA 2 device (Micro Medial, Rochester, UK) on the index finger to evaluate SI, concluding that SI was more useful than RI, although both may be used in clinical practice.

Chen et al. [114] used the PulseTrace PCA2 (CareFusion, San Diego, CA, USA) to obtain PPG-derived ASI from fingertip pulse waveforms and applied multivariable Cox proportional hazards models to assess differences between elderly (65–69 years) and non-elderly (40–64 years) individuals. The study concluded that ASI monitoring may be more relevant in individuals under 65; however, participants under 40 were not included and the cohort lacked ethnic diversity, comprising exclusively individuals of European backgrounds, limiting generalisability. Future research should include younger age groups and more diverse populations.

Tanaka et al. [115] analysed PPG signals from an occluded finger, supporting the feasibility of assessing small artery and arterioles. Bland–Altman plots were used to evaluate the agreement between the finger arterial stiffness index (FSI) and finger arterial elasticity index (FEI), alongside regression, linear, and bi-logarithmic analyses. The findings increased confidence in measuring arterial stiffness in smaller vessels.

Wowern et al. [109] conducted an in vivo trial in participants of varying ages and genders, including pregnant women, using the SphygmoCor-Px System and Meridian digital pulse wave analysis (DPA) (Salcor AB, Uppsala, Sweden) to assess the repeatability of DPA-derived arterial stiffness parameters. Measurements were obtained from the left index finger, with PPG waveforms analysed using second-derivative wave reflection features, and Bland–Altman plots used for statistical analysis. Although DPA was suggested as a valuable tool for gauging vascular health, none of the DPA variables demonstrated

optimal repeatability, indicating further validation is required. In another in vivo study, Djurić et al. [116] used a PPG sensor to estimate blood flow using scalar coefficients and reported encouraging differentiation between age groups above and below 50 years, suggesting potential utility for vascular ageing assessment. However, the findings were preliminary, based on a limited sample size, and restricted to healthy volunteers.

Huotari et al. [117] tested a transmission-probe-based PPG device developed in a university laboratory, in which captured pulse waveforms were mathematically decomposed to estimate the arterial stiffness. However, the complexity of haemodynamic features made it challenging to derive arterial stiffness indices and to link PPG-derived indices with those obtained from pressure and flow pulses.

Hellqvist et al. [118] collected finger PPG recordings using a sleep diagnostic device to derive the overnight stiffness index (OSI) in 79 patients who also completed ambulatory BP monitoring. OSI was calculated as body height divided by the time interval between the first and second pulse peaks, and was found to correlate with the ambulatory arterial stiffness index, a well-established cardiovascular risk marker. However, sleep duration and timing was self-reported, making it unclear to what extent recordings were acquired specifically during sleep. Additionally, the cohort included a higher proportion of men than women, which may limit generalisability.

4.3 Use of Photoplethysmography on Specific Conditions

Researchers have implemented PPG-based techniques to assess arterial stiffness in patients with specific health conditions, such as CAD, heart transplantation, diabetes, hypertensia, and obesity, and high-risk patients. Pregnancy and cerebral pulsatility have also been investigated by researchers.

Zekavat et al. [119] evaluated the association of ASI with BP and CAD. Multivariable COX proportional hazards and additive linear regression were among the analysis models used. The results led to a lack of confidence that PPG-derived ASI could predict CAD risk, leaving a gap for future research. Arterial stiffness changes in heart transplant patients have been compared by Sharkey et al. [120]. The study was conducted on 20 children with heart transplantation and on a healthy control group of 161 children. Data were collected bilaterally from the ear lobes, index fingers, and great toes. The PPG signal collected from the children with heart transplants was normalised and compared to the

normalised PPG signal from the control group. For statistical analysis, multivariate (that is, binary logistic regression) and univariate analyses (that is, the Mann–Whitney U test) were performed. This study suggested the possibility to measure arterial stiffness at different body sites. Research has also been conducted on diabetic patients whereby there is a possibility to distinguish between diabetic and non-diabetic individuals using an arterial stiffness monitoring system based on PPG technology [121]. Furthermore, the SDPPG has been investigated as a potential indicator of arterial stiffness. In a study conducted on 260 patients, it was found that the arterial stiffness progression differed in the diabetic and non-diabetic stages [122].

The SDPPG and the PWV were compared in a study by Bortolotto et al. [123] that examined vascular ageing evaluation in hypertensive participants. The study involved 524 patients with hypertension and 140 with atherosclerosis alteration, which included coronary heart disease, peripheral vascular disease, and abdominal aortic aneurysm. The SDPPG was suggested as a potential tool for assessing vascular ageing in hypertensives. The length of the vascular segment may have been overstated by the PWV approach, which should be considered despite the fact that PWV was a better indicator of the presence of atherosclerosis alteration than the SDPPG.

Jeyashree et al. [124] investigated arterial stiffness in prehypertensive and normotensive individuals. The study reported higher ASI values in the prehypertensive group compared to normotensive participants. However, the findings were based on a small sample comprising 20 male participants (10 normotensives and 10 pre-hypertensives), with individuals diagnosed with CVDs excluded from the study.

Korneeva and Drapkina [125] investigated the possibility of using PPG on obese patients with high BP by assessing arterial stiffness. The main objective was to provide statins, namely atorvastatin and rosuvastatin, to these patients and track the development of vascular stiffness. In an additional effort, Drapkina and Ivashkin [126] used a PPG device attached to a finger to conduct a pulse wave study on arterial stiffness in obese and high-BP patients. Prior to this research, Drapkina [127] used a finger PPG device to examine arterial stiffness in high-risk patients with high BP. The study was carried out similarly to that by Korneeva and Drapkina [125], albeit for high-risk patients. Both sets of results

supported one another, noting that high-risk or obese patients had increased arterial stiffness.

Other circumstances, such as pregnancy-related circumstances, have also been analysed using PPG. The study conducted by Wowern et al. [108] involved PPG signals being collected from the left index fingers of healthy pregnant women. For analysis, linear and polynomial mixed effects were used to account for gestational age, and analysis of variance (ANOVA) and analysis of covariance (ANCOVA) were used to account for age influences. Yet, there was uncertainty and a lack of trust in the ability to identify pathological haemodynamic changes during pregnancy, thus postulating the necessity to investigate pathological changes that can occur during pregnancy.

In two independent acute interventions (a cold pressure test and one involving mild lower-body negative pressure), Lefferts et al. [128] investigated the effects of cerebrovascular pulsatility in terms of acute increases in arterial stiffness in middle-aged and young adults. A mean BP reading was acquired using PPG for continuous BP monitoring. Cerebrovascular haemodynamics at rest, during the cold pressure test, and during the lower-body negative pressure intervention were evaluated in 15 middle-aged people between the ages of 47 and 61 and in 15 young adults with genders matched to the middle-aged. The measurements, however, were not evaluated constantly, resulting in a little variation in the timings of the measurements. The middle-aged adult group also included a small number of participants who had CVD risk factors, such as obesity and anti-hypertensive medication usage, which could have improved validity but affected the findings. Future research should involve older subjects, as the study only focused on those under 61 years of age.

4.4 Comparing Current Photoplethysmography-Based Instruments and Other Measurement Methods

While some researchers have used custom-made PPG-based instruments, others have compared commercial devices, including Complior (Alam Medical, Saint-Quentin-Fallavier, France), PulsePen (DiaTecne, Milan, Italy), and PulseTrace (GP Supplies, Borehamwood, UK). PPG and measurement indices that gauge arterial stiffness, such the ABI, ASI, SI, and AIx, have also been examined. Additionally, imaging PPG (iPPG) and contact PPG (cPPG) have been compared.

Salvi et al. [129] compared commercial PPG devices, namely Complior, PulsePen, and PulseTrace. In contrast to Complior and PulsePen, which used aortic PWV based on the interval between carotid and femoral pressure waves, PulseTrace was evaluated using SI measures. The authors highlighted an ongoing need to standardise PWV measurements and establish reference values through cross-device comparisons. Djeldjli et al. [130] compared iPPG with cPPG in healthy participants. For cPPG, two probes were used, one on the right earlobe and the other on the index finger. However, the sample covered a limited age range and skin type, restricting generalisability; larger-scale studies are needed to assess the impact of measuring site.

Kock et al. [131] compared the ABI with PPG-based measures of arterial stiffness in elderly patients, using bivariate and multivariate linear regression, the Shapiro–Wilk test, and winsorisation. The study concluded that ABI did correlate with PPG indicators, and that further work is needed to establish standardised vascular assessment procedures. Using a fingertip PPG device, Murakami et al. [132] compared ASI with baPWV and, using the Wilcoxon rank sum test, Receiver Operating Characteristic (ROC) curve, and the Area under the Curves (AUCs), showed that the device could assess arterial stiffness in agreement with baPWV. To evaluate discrimination of cardiovascular risk, Clarenbach et al. [133] compared PPG-derived SI with AIx obtained via radial tonometry in 62 individuals with chronic obstructive pulmonary disease (COPD) or obstructive sleep apnea, and 21 healthy controls (aged 18-75). Whilst both devices were effective, PPG-derived SI better distinguished between intermediate and high-risk people, rendering it more effective in clinical settings.

4.5 Photoplethysmography in Computational Models

Researchers have incorporated PPG into computational models to predict vascular health, as well as analysing incident and reflected waves from the PPG waveform. The advantages and disadvantages of using PPG in computational models are discussed.

Machine learning (ML) and deep learning (DL) were applied to the PPG signals of a database in a study conducted by Dall'Olio et al. [134]. The approach involved pre-processing data on the raw PPG signals, through steps such as detrending, demodulating, and denoising. The DL employed the entire signal to predict healthy vascular ageing (by bypassing the feature extraction stage), whereas the ML relied on known extracted features from the PPG signal. For DL, it was possible to bypass the feature extraction stage as several convolutional neural networks (CNNs) were applied to the entire PPG signal as an input. Although CNNs with 12 hidden layers or fewer showed good performance, more complicated structures cannot be trained on a common laptop; subsequent research should explore more complex structures using a feasible technique. Due to the black-box approach being used, the study was restricted in its ability to compare its findings to those of other ML methodologies. In a study conducted by Shin et al. [135], DL was applied to the PPG pulses of individuals ranging in age from 20 to 80. DL offers an advantage over manually recognising features during the assessment of vascular ageing since it has the potential to produce features from PPG waveforms automatically. It is anticipated that more databases will become accessible in the future, resulting in the DL approach performing better in the assessment of vascular ageing. Nonetheless, the employment of computational models in wearable technology raises additional issues such as the computing power that may affect the ability to obtain an immediate diagnosis. Resolving computation model issues, such as determining the optimal number of hidden layers or the trade-off between the number of parameters and the volume of training data, is crucial [134].

Park and Shin [136] evaluated vascular ageing using an artificial-neural-network-based regression model to analyse incident and reflected waves from a PPG waveform. Their study reported that a trustworthy single PPG-based technique for assessing arterial stiffness had not yet been developed. The Gaussian mixture model was used to deconstruct each waveform into incident and reflected waves after the recorded PPG signals were segmented for each beat. Since the measurements were based on nasal PPG

rather than the more typical finger PPG measurements, it was challenging to generalise the findings. It is unclear how this has an impact on the findings. Future research is needed to understand the effects of various measurement sites. Assessing the model's performance in relation to risk factors that hasten vascular illnesses such as atherosclerosis, which were not considered in the study, is imperative. Similarly, Abrisham et al. [137] utilised a dataset of 4374 healthy adults aged 25 to 75 years, collecting PPG signals from the radial and digital arteries. Four distinct neural network models were employed to predict vascular ageing using PPG. This study was likewise limited by the exclusive inclusion of healthy individuals, excluding those with cardiovascular conditions, which may reduce the generalisability of the findings. Additionally, the models were not evaluated using real-world data, which could introduce factors such as noise, motion artefacts, and ambient light variability.

Chen et al. [138] extracted 58 potentially relevant features from a single-channel PPG signal to investigate their relationship with arterial stiffness. An interaction factor was initially computed to assess the degree of interaction and redundancy among the features. Based on this, a feature selection algorithm was developed, and ML techniques were then applied to estimate arterial stiffness.

In recent years, researchers have also shown interest in remote health monitoring, particularly through wearables [139]. This is driven by the ageing population, which was projected in 2023 to increase by 10% within five years [140]. Remote PPG (rPPG), monitoring cardiovascular activity via facial video, has gained attention. Despite being labelled non-invasive and low-cost, rPPG faces challenges such as a low signal-to-noise ratio (SNR). Lian et al. [141] proposed employing signal processing methods to enhance rPPG by reducing noise and improving accuracy. This involved data fusion, region of interest selection, and heart rate estimation. Furthermore, rPPG attracts attention for fatigue detection. Zhao et al. [142] utilised CNN for rPPG-based learning fatigue classification through multi-source feature fusion. However, the study used a self-collected dataset and lacked confirmation on enhancing fatigue detection accuracy with a larger sample size using DL. Previous research explored rPPG for estimating blood oxygen saturation (SpO_2). Casalino et al. [143] credited rPPG as being portable, enabling continuous SpO_2 monitoring. However, while rPPG is gaining popularity, it has not yet been applied rigorously in any large studies relating to vascular ageing.

4.6 Combining Photoplethysmography with Other Modalities

Some researchers have attempted to fuse PPG with other modalities, such as an electrocardiogram (ECG) and phonocardiogram (PCG), to overcome some of the current drawbacks. In the same respect, the novel device known as the single continuous passive leg movement (sPLM) has been assessed as a possible screening technique using PPG technology.

By combining multi-site PPG and ECG, Perpetuini et al. [144] performed an in vivo assessment of vascular stiffness. Ten ECG leads and eight PPG probes were used to collect signals. Signals could be simultaneously gathered from numerous places using various PPG probes. The ECG served as a reference for single-pulse PPG evaluation and averaging. Pressure cuffs were offered to ensure robust optode-to-skin connection. Given that the PPG–ECG system could record back-reflection signals at a significant inter-optode distance, it was hypothesised that PPG signals could be collected from large arteries. Additionally, numerous sites were monitored at once due to the large number of probes used. However, the results were not always interpretable when collecting multiple PPG signals, and significant computing resources may be required [145].

To obtain PWV measurements, Margain et al. [146] combined PCG and PPG. The measurements acquired included cfPWV and carotid-toe PWV in a sample of 63 healthy volunteers. Both cfPWV and carotid–toe PWV were found to correlate with age; however, the PCG-based carotid–toe PWV demonstrated less consistency, suggesting reduced reliability compared to cfPWV. Nonetheless, the findings are limited in their generalisability due to the exclusive inclusion of healthy participants.

PPG was used in a study by Hydren et al. [147] in an effort to evaluate sPLM. All subjects were male and were split into two groups consisting of 12 younger and 12 older subjects. The instructions provided by Gifford and Richardson [148] for using the sPLM were followed. Although it is highlighted in Table 2 that a decline in vascular function brought on by ageing is sensitive to sPLM, further studies are required with larger samples prior to labelling the sPLM as a clinical tool for monitoring vascular ageing [147].

Table 2: PPG-based studies for the assessment of arterial stiffness [3].

Study	Year	Device(s)/Technique	Parameters Measured	Number of Subjects	Major Findings
Allen and Murray [110]	2000	Bilateral photoplethysmography (PPG) study	Waveform of the pulses from six peripheral sites (including ears, thumbs, and big toes).	40	The system validation data showed low levels of root mean square error (RMSE), indicating good right-to-left channel matching. According to the bilateral study, normal patients' pulses from their right and left sides were highly correlated at every segmental level (that is, the ears, thumbs, and toes).
Bentham et al. [60]	2018	Bilateral multi-site finger and toe PPG study	Multi-site finger and toe PPG	74	It was shown, using time-domain analysis, that those with PAD had lower normalised amplitude variability and significantly higher pulse arrival time (PAT) variability at the toe sites. In the frequency domain analysis, patients with PAD had

Study	Year	Device(s)/Technique	Parameters Measured	Number of Subjects	Major Findings
					noticeably decreased magnitude-squared coherence (MSC) values across a variety of frequency bands. It was discovered that the right toe had a different signal from the left toe while comparing the left and right sides of the body for the ear, finger, and toe. This resulted in the conclusion that PAD was at least present in one leg.
Brillante et al. [111]	2008	PPG	Peak to peak Stiffness index (SI) Reflection index (RI)	152	Age was found to significantly correlate with SI and RI, with race serving as an independent predictor of SI. At the same age, it was discovered that men had higher BP than women. There were no discernible differences between men and women in any of the arterial stiffness measures.

Study	Year	Device(s)/Technique	Parameters Measured	Number of Subjects	Major Findings
Jannasz et al. [112]	2023	SphygmoCor XCEL	Central and regional PWV cfPWV	118	cfPWV was discovered to be more reliable than regional PWV in determining arterial stiffness. There was insufficient evidence that gender affected the risk factors for atherosclerosis.
Tąpolska et al. [113]	2019	Pulse Trace PCA 2 device (Micro Medial, Rochester, UK)	SI RI	295	Patients between the ages of 40 and 54 showed the greatest benefit from SI. The authors concluded that since SI and RI can be assessed non-invasively, they have the potential to be used in routine clinical practice to identify individuals who are at risk of developing future cardiovascular problems. Though RI can still be used as a supplementary measurement, it was found that it seemed to be less useful than SI.

Study	Year	Device(s)/Technique	Parameters Measured	Number of Subjects	Major Findings
Chen et al. [114]	2025	PulseTrace PCA2 (CareFusion, San Diego, CA, USA)	ASI	127045	The non-elderly group (aged 40–64 years) showed more pronounced age-related trends in ASI compared to the elderly group (aged 65–69 years). Higher ASI was also associated with a greater increase in risk of major adverse cardiovascular events in the non-elderly than in the elderly over long-term follow-up (median 11.7 years).
Tanaka et al. [115]	2011	PPG	Finger arterial elasticity index (FEI) Finger arterial stiffness index (FSI)	199	The indices were gathered by occluding the finger, supporting the feasibility of assessing stiffness in small arteries and arterioles using these measures. FSI was able to differentiate arteriosclerotic patients from healthy participants.

Study	Year	Device(s)/Technique	Parameters Measured	Number of Subjects	Major Findings
Wowern et al. [109]	2015	SphygmoCor-Px System Meridian digital pulse wave analysis (DPA) (Salcor AB, Uppsala, Sweden)	PPG signals DPA Ejection Elasticity Index (EEI) Dicrotic Index (DI) Dicrotic Dilation Index (DDI)	112	It was discovered that the EEI should be used for large artery stiffness estimation while the DI and DDI should be used for small artery stiffness estimation. DPA parameters correlated more strongly with the AIx than with PWV.
Djurić et al. [116]	2023	PPG sensor	Blood flow Scalar coefficients	117	The study allowed for the analysis of amplitude changes in blood pulse waves. The scalar coefficient ratios declined with age, distinguishing between those above and below 50 years of age.
Huotari et al. [117]	2009	Transmission probe-based PPG device	Pulse waveforms from the left index finger and second toe	Not stated	It was discovered that PPG waveform analysis, as opposed to ultrasound analysis, offered greater details about artery structure and function. This

Study	Year	Device(s)/Technique	Parameters Measured	Number of Subjects	Major Findings
					was based on mathematically decomposing the signals into the percussion wave and four reflected components.
Hellqvist et al. [118]	2025	SOMNOcheck micro CARDIO (Löwenstein Medical Technology GmbH, Hamburg, Germany)	Overnight stiffness index (OSI)	79	OSI was found to correlate well with the ambulatory arterial stiffness index. Participants with higher OSI had higher cardiovascular risk scores and higher ambulatory arterial stiffness index values.
Zekavat et al. [119]	2019	Finger PPG-derived ASI	ASI PPG BP	Approximately 500,000	It was determined that PPG-derived ASI was an inappropriate proxy for CAD risk but a genetically causal risk factor for BP. Mendelian randomisation supported a directional effect of ASI on BP traits.

Study	Year	Device(s)/Technique	Parameters Measured	Number of Subjects	Major Findings
Sharkey et al. [120]	2018	Bilateral PPG setup	Electrocardiogram (ECG) PPG PAT	181	A reduced PAT and thus higher arterial stiffness were discovered in heart transplant patients. Paediatric heart transplant recipients showed significantly shorter segmental PAT compared with healthy controls.
Wei et al. [121]	2013	PPG Radial pulse	cfPWV Spring constants	70	The PPG-based spring constant was able to distinguish between normal and pathological characteristics in both non-diabetic and diabetic individuals. The spring constant showed a strong inverse correlation with cfPWV.
Park [122]	2023	SA-3000P (Medicore Co., Seoul, Republic of Korea) VS-1000 (Fukuda Denshi, Tokyo, Japan)	Second derivative of the photoplethysmography signal (SDPPG) CAVI	276	The SDPPG, requiring a single transducer, proved simpler and yielded results in under 2 minutes. It

Study	Year	Device(s)/Technique	Parameters Measured	Number of Subjects	Major Findings
					was concluded that CAVI could not replace the SDPPG.
Bortolotto et al. [123]	2000	Complior (Colson, Garges les Gonesses, France) Fukuda FCP-3166 (Fukuda, Tokyo, Japan)	cfPWV SDPPG	664	In patients over 60 with atherosclerosis, PWV and the SDPPG remained higher, whereas in patients aged 60 with atherosclerosis, only PWV remained greater. While the index of the SDPPG was correlated with age and other atherosclerosis risk factors, PWV was associated with age and arterial hypertension. The study found that aortic PWV more accurately captured changes in arterial compliance caused by ageing, high BP, and atherosclerosis than the SDPPG.

Study	Year	Device(s)/Technique	Parameters Measured	Number of Subjects	Major Findings
Jeyashree et al. [124]	2024	PPG	ASI	20	It was found that individuals with prehypertension had higher ASI values compared to normotensive individuals. ASI showed a positive correlation with BP measures, although these correlations were not statistically significant.
Korneeva and Drapkina [125]	2015	PPG-based device	SI RI AIx Systolic BP	82	Obese patients with high BP showed vascular stiffness; based on pulse wave characteristics of the PPG signal, both treatments improved the arterial stiffness parameters, reducing SI and RI. Nonetheless, it was noted that compared to atorvastatin, rosuvastatin reduced the AIx.
Drapkina and	2014	PPG-based device	SI RI	82	The study found increased arterial stiffness in obese patients with high

Study	Year	Device(s)/Technique	Parameters Measured	Number of Subjects	Major Findings
Ivashkin [126]			AIx Systolic BP		BP according to PWA. Following satin therapy, PWA-derived arterial stiffness parameters improved overall, indicating reduced vascular stiffness after treatment.
Drapkina [127]	2014	PPG-based device	SI RI AIx Systolic BP	82	The study found increased arterial stiffness in high-risk patients with high BP. Rosuvastatin was reported to significantly improve PWA-derived arterial stiffness parameters.
Wowern et al. [108]	2019	PPG	DPA	139	It was concluded that DPA reflects longitudinal changes in arterial compliance in normal pregnancy. In uncomplicated pregnancy, it was found that arterial stiffness changes in both large and small arteries significantly with gestational age.

Study	Year	Device(s)/Technique	Parameters Measured	Number of Subjects	Major Findings
Lefferts et al. [128]	2021	PPG Tonometry Ultrasound Doppler	BP cfPWV Carotid stiffness Blood velocity pulsatility index	30	Despite younger adults having larger carotid dilations, pulsatile damping decreased in both middle-aged and young adult groups. According to the study's findings, the carotid diameter and cerebrovascular pulsatility are altered differently in young and middle-aged adults. The study suggested that changes in intracranial cerebral pulsatility could be slowed down by cerebrovascular characteristics.
Salvi et al. [129]	2008	Complior PulsePen (DiaTecne, Milan, Italy) PulseTrace (GP Supplies, Borehamwood, UK)	Aortic PWV SI	50	Complior and PulsePen were found to be accurate at estimating PWV via Bland–Altman analysis whereas PulseTrace was found to be an unsuitable substitute for PWV. This highlights inter-device differences and

Study	Year	Device(s)/Technique	Parameters Measured	Number of Subjects	Major Findings
					the need for standardisation across PWV measurements.
Djeldjli et al. [130]	2021	Imaging PPG (iPPG) Contact PPG (cPPG)	16 features of the pulse wave relating to arterial stiffness and BP	12	A comparison was made between the iPPG and cPPG, whereby cPPG recorded signals using contact probes and iPPG used a quick camera to record signals remotely. High agreement between the results and the features captured by the reference sensors was observed. The contact and contactless PPG features (from two separate sites) were found to share strong correlations. The non-invasive iPPG approach provided quantitative data on the underlying mechanisms of waveform shape from various body sites and allowed for a

Study	Year	Device(s)/Technique	Parameters Measured	Number of Subjects	Major Findings
					remote means to evaluate waveform features.
Kock et al. [131]	2019	ABI PPG	Peak to peak time	93	The results showed that ABI was not related to PPG indicators. However, this may be attributed to the fact that the participants were less likely to have PAD, as the median age was relatively low.
Murakami et al. [132]	2019	Rossmax International LTD SB200 pulse oximeter (Taiwan, China)	ASI baPWV	18	The fingertip PPG device was found to be capable of measuring arterial stiffness in line with the baPWV.
Clarenbach et al. [133]	2012	PPG Radial tonometry	SI AIx	83	Both devices distinguished between people with high and low cardiovascular risk accurately. However, unlike AIx, SI could also distinguish between people at intermediate and high risk, making it

Study	Year	Device(s)/Technique	Parameters Measured	Number of Subjects	Major Findings
					potentially more effective in sizable clinical research. Low failure rates were present in both devices.
Dall'Olio et al. [134]	2020	Machine learning (ML) Deep learning (DL)	Raw PPG signal	4769	It was discovered that individuals do not age at the same rate. The study reported that women had better health than men in terms of vascular ageing.
Shin et al. [135]	2022	DL	PPG pulse signals	752	The model outperformed earlier models at the time without the requirement for an additional feature detection process. It was found that waveform regions around the systolic peak contributed most strongly to age estimation.
Park and Shin [136]	2022	Artificial neural network-based regression model	Incident and reflected waves from PPG waveform	757	It was determined that the reflected wave's features may be used to assess

Study	Year	Device(s)/Technique	Parameters Measured	Number of Subjects	Major Findings
					vascular ageing, with the amplitude-related feature of the reflected wave being more favourable than the time-related feature in doing so.
Abrisham et al. [137]	2024	PPG	Pulse waveforms	4374	Four neural network models were compared using PPG recorded from the radial and digital arteries. The VGG-16 model outperformed other models, although its performance is limited when applied to large datasets and under time constraints.
Chen et al. [138]	2024	Single-channel PPG	baPWV	392	The proposed feature selection algorithm identified interactions between features that enhanced the accuracy of arterial stiffness prediction. Using the selected interacting feature set, baPWV

Study	Year	Device(s)/Technique	Parameters Measured	Number of Subjects	Major Findings
					estimation achieved strong agreement with the reference values.
Lian et al. [141]	2023	3 Lead ADS1292 ECG (Texas Instruments, Dallas, TX, USA) Remote PPG (rPPG)	ECG Heart rate	30	ECG signals were obtained as reference values. Video recordings from the rPPG were transferred for analysis; however, the results were limited to the Han ethnicity, lacking diversity.
Zhao et al. [142]	2023	700-MAX-ECG MONITOR (Maxim Integrated, San Jose, CA, USA) rPPG	ECG Heart rate	12	The study proposed an rPPG-based fatigue-detection approach using multi-source feature fusion. Unlike PPG and ECG, which may cause skin irritation and discomfort, rPPG offers a solution by eliminating adherence to the body.
Casalino et al. [143]	2023	rPPG	Blood oxygen saturation (SpO_2)	10	Experimental results showed no significant differences with slight head

Study	Year	Device(s)/Technique	Parameters Measured	Number of Subjects	Major Findings
					movements. Further work is needed to explore potential light-condition impacts on real-time measurements.
Perpetuini et al. [144]	2019	Multi-site ECG and PPG	baPWV	78	It was discovered that the results were age-sensitive and had high signal quality since cross-talk effects were absent. The baPWV was found to be consistent when the results were compared to those from a commercial pulse sensor device, Enverdis Vascular Explorer (Düsseldorf, Germany).
Margain et al. [146]	2025	PPG Phonocardiogram (PCG) Femoral pressure cuff	cfPWV Carotid-toe PWV	63	It was determined that both cfPWV and carotid-toe PWV correlated with age. However, the PCG-based carotid–toe PWV demonstrated lower consistency compared to cfPWV.

Study	Year	Device(s)/Technique	Parameters Measured	Number of Subjects	Major Findings
Hydren et al. [147]	2019	Finger PPG-based device (Finapres Medical Systems, Amsterdam, The Netherlands) Doppler ultrasound	BP Single continuous pass leg movement (sPLM) Leg blood flow Leg vascular conductance	24	It was found that age-related decline in peripheral vascular function was found to be susceptible to sPLM. It was concluded that sPLM simplified the process and reduced the amount of equipment needed to just perform a Doppler ultrasound as compared to a standard passive leg movement.

4.7 Summary of Chapter 4

Researchers are increasingly turning to PPG-based technology, which might provide an answer when developing and inventing novel devices to evaluate vascular ageing and arterial stiffness. Due to PPG's simplicity of use, longitudinal studies could be performed to understand whether vascular ageing treatments can alter arterial stiffness and whether a PPG-based device can detect vascular ageing over time. PPG can easily be incorporated into devices and wearable technology, as has already been proven. PPG is suited for universal screening since it is easy to use, is relatively inexpensive, and does not need special training to operate. Another consideration, when creating novel technologies, should be the utilisation of a multi-sensor approach. Combining various sensors with PPG should be considered, as relying solely on PPG may not be the optimal solution. Employing a multimodal approach has the potential to address the challenges associated with PPG and result in a more reliable sensor technology for assessing vascular ageing.

To acquire more conclusive results from in vivo investigations, it is recommended that future studies use bigger sample numbers. Longitudinal studies should also be conducted to assess novel methodologies over the long term. Within study protocols, and as part of the recommended application of PPG devices, a strong contact pressure should be established because measurements can be affected by the quality of the contact [106]. A contact pressure between 20 mmHg and 30 mmHg is typically recommended [149]. Future research should focus on standardising measuring methods, expanding the databases accessible to computational models, and understanding the potential impacts of medications such as anti-hypertensive medications. Additionally, the use of an in vitro system that simulates the mechanical dynamics of the vascular system in a controlled environment is recommended. This way, pathologies can be introduced to imitate CVD disorders to verify the accuracy of novel devices. A key gap in the field remains the fabrication of novel, customisable vessel-tissue phantoms that can be mechanically characterised to replicate healthy and diseased vessels for integration within an in vitro setting. Given that CVD is the main cause of mortality worldwide, it is only a matter of time before cost-effective, reliable screening based on PPG is needed.

CHAPTER 5: IN VITRO CARDIOVASCULAR SYSTEM CONFIGURATION

Some of the work presented in Chapter 5 was completed in collaboration to develop an in vitro model replicating the lower body; however, the additional work presented in this chapter beyond the collaboration was undertaken solely as part of this thesis and includes the integration of multi-wavelength PPG sensors and the exploration of multiple BMFs. Accordingly, this chapter focuses on the in vitro cardiovascular model, the optical sensors used within this research, and the selection and preparation of the BMFs.

5.1 Design and Development of the In Vitro Model

The in vitro vascular system model was developed to replicate the vasculature of the lower body, beginning at the aorta, and branching into the femoral arteries. The lower body is a common site for PAD, with the femoral artery being the most frequent location for embolic events [57], and hence the chosen vessel for investigation in this research. In the initial stages of design, the model incorporated bilateral branching to simulate the lower limbs, as illustrated in Figure 11. This configuration was adopted in the experimental study described in Chapter 7. The study conducted in Chapter 7 employed a pulsatile pump (Model 1423 PBP, Harvard Apparatus, US), capable of replicating the human cardiac cycle by inducing pulsatile flow within the system, thereby generating PPG waveforms. The pump allowed control over parameters such as stroke volume, heart rate, and the systolic-to-diastolic time ratio. Care was taken to ensure that the in vitro bilateral system was symmetrical. Chapter 7 presents a validation study demonstrating bilateral symmetry by showing that statistically similar PPG signals were obtained from both branches when identical vessel-tissue phantoms were inserted. The vessel-tissue phantom fabrication process is described in greater detail in Chapter 6.

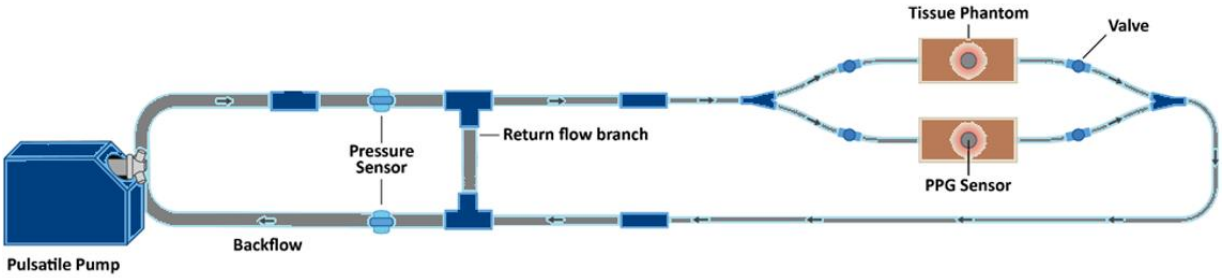

Figure 11: Schematic illustration of the initial in vitro cardiovascular model, which was also employed in the study described in Chapter 7. The vascular system replicates the lower body circulation, beginning at the aorta and branching into the femoral arteries. This configuration enabled the simultaneous insertion of two vessel–tissue phantoms for parallel signal acquisition.

The vascular system was assembled using clear silicone tubing (Hilltop Products Limited, Warrington, UK), forming a network designed to replicate the vasculature of the human lower body. The tubing was selected for its mechanical properties, which approximate those of human blood vessels. Pressure sensors (PendoTech, Princeton, NJ, USA) were integrated into the system to enable monitoring of internal pressure. In the initial experimental studies (Chapters 6 through 8), the pressure sensors were positioned downstream of the vessel–tissue phantoms to provide a reference measurement for validating the PPG-derived signals. In the study presented in Chapter 9, the pressure sensor was relocated upstream of the vessel–tissue phantom because the primary objective was to assess the feasibility of PPG monitoring across a range of imposed BP conditions; therefore, it was necessary to monitor the pressure entering the phantom. This upstream configuration was retained for the final experimental study (Chapter 10), and the pressure sensor remained positioned upstream of the vessel-tissue phantom. To accommodate variations in tubing diameter and to allow integration of instrumentation such as pressure sensors, curved and angled Y-connectors, along with luer lock fittings, were incorporated. A pulsatile pump was employed to drive fluid through the system, simulating the human heartbeat and generating pulsatile flow within the system to produce PPG waveforms [150]. Across all experiments, the heart rate was set between 60 and 66 beats per minute (bpm). The fabrication of customisable vessels and tissue phantoms, as well as the acquisition of PPG signals from these phantoms, is described in Chapter 6.

For the experimental studies, excluding the one presented in Chapter 7, a different pulsatile pump was utilised due to its enhanced suitability for the in vitro cardiovascular system. The PD-1100 Pulsatile Pump System (BDC Laboratories, Wheat Ridge, CO), shown in Figure 12, was used as the source of pulsatile flow for the experimental studies detailed in Chapter 6 and Chapters 8 through 10.

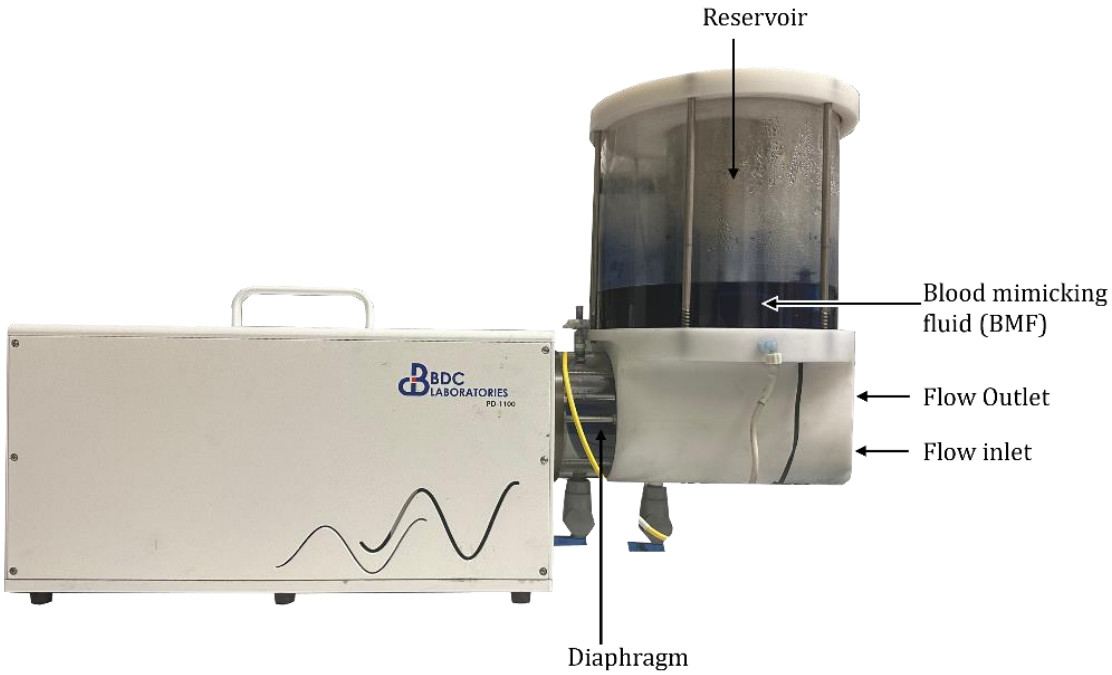

Figure 12: PD-1100 Pulsatile Pump System (BDC Laboratories, Wheat Ridge, CO). The pulsatile pump system was used to generate pulsatile flow within the in vitro vascular system.

The experimental studies presented in Chapter 6 and Chapters 8 through 10 utilised a slightly modified in vitro vascular system. The original bilateral branching was replaced with a single-branch configuration, allowing vessel–tissue phantoms to be inserted individually, as illustrated in Figure 13. A one-way valve, used the setup, was included to maintain unidirectional flow, and prevent backflow.

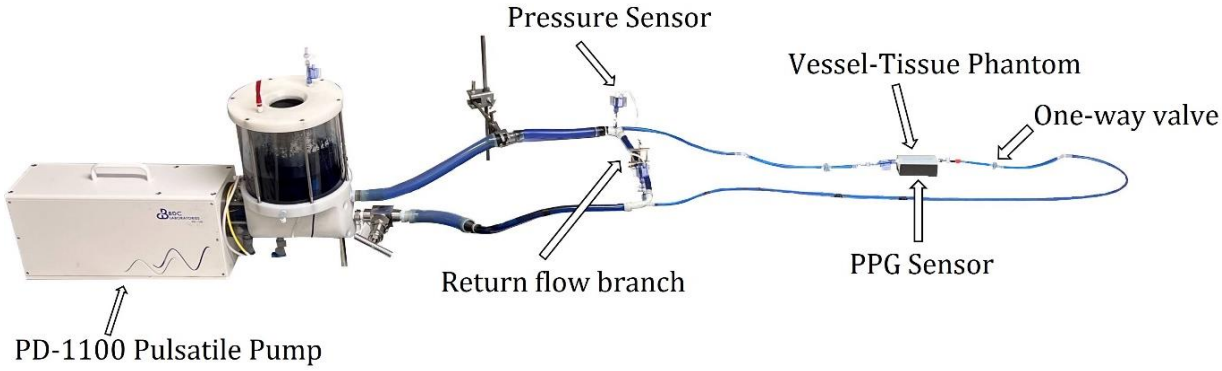

Figure 13: In vitro vascular configuration simulating the lower body, incorporating the PD-1100 Pulsatile Pump System. A PPG sensor was positioned beneath the vessel–tissue phantom to capture raw PPG signals. The diagram illustrates a single-branch lower limb design, allowing vessel–tissue phantoms to be integrated into the setup individually. This configuration was employed in the experimental studies described in Chapter 6 and Chapters 8 through 10 [150].

In the final experiment, described in Chapter 10, the setup remained the same, with the integration of an LDF device (moorVMS-LDF, Moor Instruments Ltd, Devon, UK). The PPG sensor and the LDF probe were positioned alternately to obtain readings, and to minimise cross-talk, data were collected sequentially. All experimental studies in which PPG or LDF recordings were obtained, as presented in Chapters 6 to 10, were conducted in a darkened room, and completed on the same day to minimise the influence of ambient lighting on the recorded signals and to reduce variability arising from environmental conditions.

5.2 Blood-Mimicking Fluid

The fluid circulating through the system and driven by the pulsatile pump was formulated to optimise the quality of the signals by enhancing light absorption at the wavelengths relevant to the optical sensors used, including both PPG and LDF sensors. Throughout the research, the BMF was repeatedly reformulated and adapted to ensure consistent and high-quality signal acquisition. Table 3 provides a summary of the BMF formulations and pulsatile pump systems used in each experimental study presented in this thesis.

Table 3: Summary of the blood-mimicking fluid (BMF) formulations and pulsatile pump systems used in the experimental studies presented across chapters. In the study described in Chapter 10, scattering agents were introduced into the BMF, consisting of either LPFS (Moor Instruments Ltd, Devon, UK), which contained OptiBind™ polystyrene microspheres (Seradyn Inc., Indianapolis, IN, USA) and the non-ionic surfactant Tween 20 (Sigma-Aldrich, St. Louis, MO, USA), or oil-in-water emulsions prepared using vegetable oil and lecithin (Product Code: 10494501, Thermo Fisher Scientific Inc, Waltham, MA, USA).

Experimental studies described in Chapter	**Pulsatile Pump**	**Blood-Mimicking Fluid (BMF)**
6	PD-1100 Pulsatile Pump System (BDC Laboratories, Wheat Ridge, CO)	Methylene blue powder (Thermo Fisher Scientific, Waltham, MA, USA) Deionised water
7	Pulsatile pump (Model 1423 PBP, Harvard Apparatus, US)	Methylene blue powder Deionised water
8	PD-1100 Pulsatile Pump System	Methylene blue powder Deionised water
9	PD-1100 Pulsatile Pump System	Indian ink (Jackson's Art Supplies, London, UK) Wright stain (Thermo Fisher Scientific Inc, Waltham, MA, USA) Congo red powder (BDH Chemicals LTD, Poole, UK) Deionised water
10	PD-1100 Pulsatile Pump System	Indian ink Wright stain Congo red powder Deionised water Scattering agents

For studies described in Chapter 6 through 8, the fluid circulating within the system was a simple BMF, created by blending methylene blue powder (Thermo Fisher Scientific, Waltham, MA, USA) with deionised water. This mixture increased absorption in the red and IR regions of light, improving the PPG signal quality [151], [152].

To simulate blood flow, a fluid mixture consisting of deionised water, Indian ink (Jackson's Art Supplies, London, UK), Wright stain (Thermo Fisher Scientific Inc, Waltham, MA, USA), and Congo red powder (BDH Chemicals LTD, Poole, UK) was circulated throughout the system during the experimental study described in Chapter 9 [59].

For the experimental study described in Chapter 10, scattering agents were introduced into the BMF to accommodate the use of the LDF probe. The base BMF formulation used in Chapter 9 was utilised, with the addition of either LPFS (Moor Instruments Ltd, Devon, UK) or oil-in-water emulsions prepared using vegetable oil and lecithin (Product Code: 10494501, Thermo Fisher Scientific Inc, Waltham, MA, USA), following the fabrication principles described in [153]. The LPFS, which contained non-ionic surfactant Tween 20 (Sigma-Aldrich, St. Louis, MO, USA) and OptiBind™ polystyrene microspheres (Seradyn Inc., Indianapolis, IN, USA) was added at a concentration of 0.25% of the total BMF volume. In contrast, a 30% oil-in-water emulsion was incorporated into the BMF. These scattering agents were added separately to different BMF batches, and signals were recorded for each batch to determine which mixture provided better in vitro PPG and LDF signal acquisition. The comparison was based on extracted waveform features, visual assessment of signal quality, and statistical analysis of differences between vascular states within each mixture.

5.3 Photoplethysmography Sensor Specifications

In the experimental studies described in Chapters 6 through 8, a dual-wavelength PPG sensor was positioned beneath the customised phantoms, using an existing research probe from the Research Centre for Biomedical Engineering, City St. George's, University of London (RCBE). This probe comprised red and IR LEDs with wavelengths of 640 nm and 900 nm, respectively. Additionally, a photodiode, a type of PD, with a peak sensitivity of 900 nm (BPW34, Osram, Munich, Germany) was incorporated to measure the reflected light [150]. The dual-wavelength PPG sensor is shown in Figure 14, where the photodiode and LEDs are placed adjacent to one another, forming a PPG sensor operating in reflectance mode.

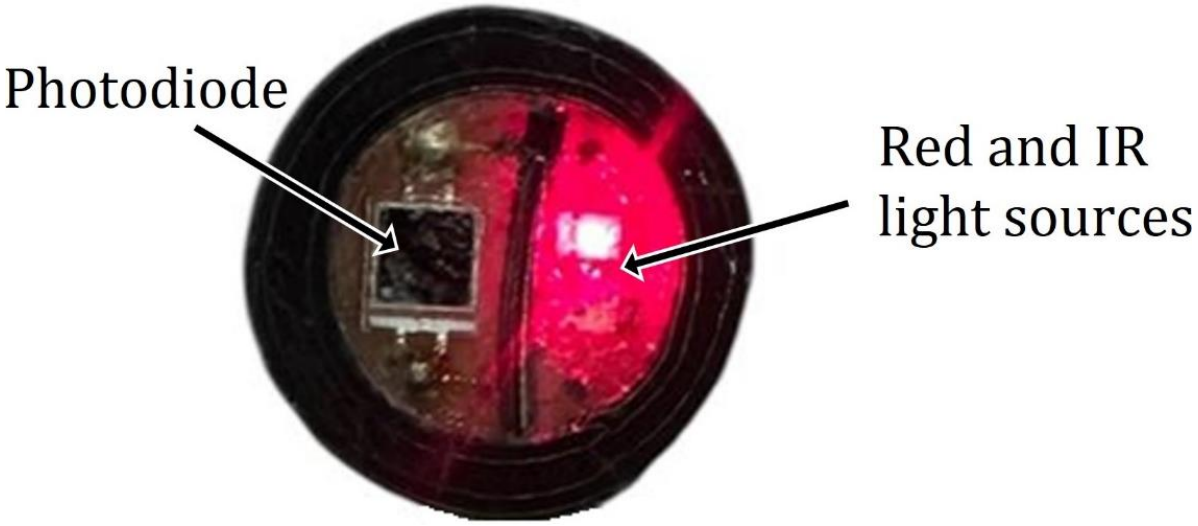

Figure 14: Cross-sectional image of the dual-wavelength PPG sensor, comprising a photodiode, and two light-emitting diodes (LEDs) with wavelengths of 640 nm and 900 nm, corresponding to red and infrared (IR) light, respectively, which serve as the optical sources.

For the experimental studies described in Chapter 9 and Chapter 10, a multi-wavelength PPG sensor previously fabricated as a research prototype within RCBE was used. The PPG sensor, shown in Figure 15, operated in reflectance mode and was equipped with three wavelengths (green at 530 nm, red at 655 nm, and IR at 940 nm). The fabricated sensor also incorporated three PDs, each with a different source-detector separation distance that could be selected using a switch. The separation distances were adjustable to 2.5 mm, 5 mm, or 8 mm. It was positioned above the phantom to capture the signals [59].

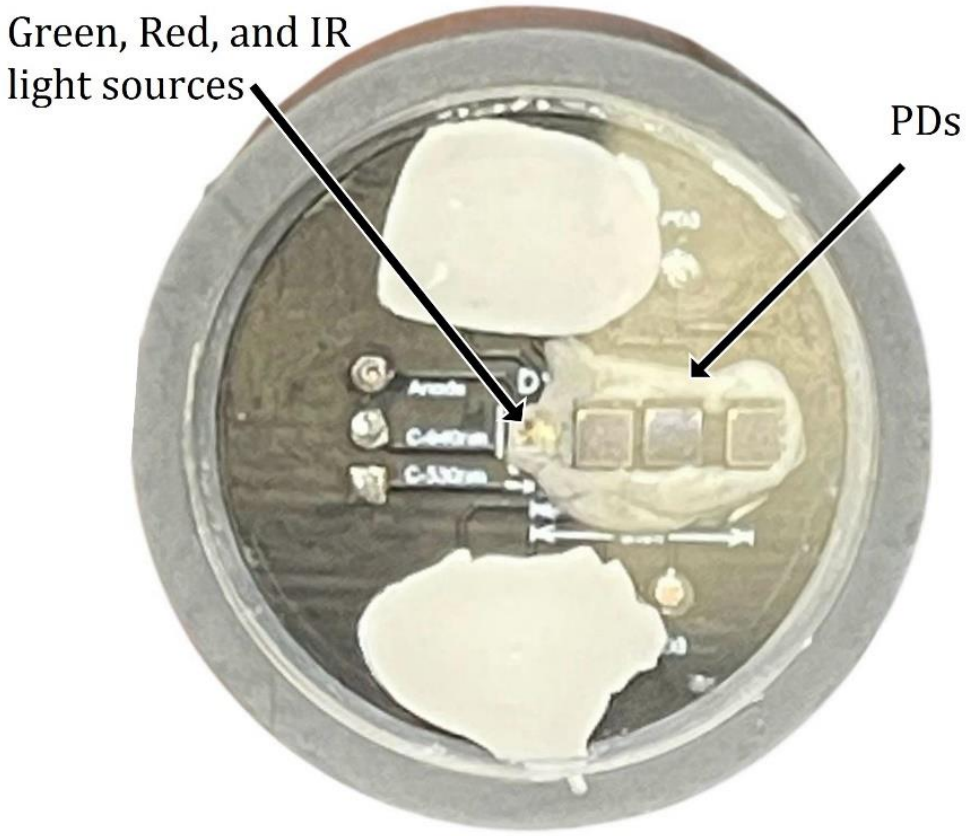

Figure 15: Cross-sectional image of the multi-wavelength PPG sensor, comprising three PDs and three LEDs with wavelengths of 530 nm, 655 nm, and 940 nm, corresponding to green, red, and IR light, respectively, which serve as the optical sources.

5.3.1 Signal Processing Unit and Data Acquisition

To acquire and process the signals detected by the sensors, a signal processing unit was connected to the PPG sensors. A ZenPPG device, set to a sampling rate of 2000 Hz and developed at the RCBE [154], was used in the experimental studies involving the dual-wavelength PPG sensor described in Chapters 6 through 8. The ZenPPG is a dual-channel system capable of recording raw PPG signals at two distinct wavelengths [154]. However, as it does not support more than two wavelengths, a different signal processing unit was utilised for the studies described in Chapter 9 and Chapter 10, which utilised the multi-wavelength PPG sensor comprising three wavelengths.

The second signal processing unit, used in the experimental studies described in Chapter 9 and Chapter 10, was also developed at the RCBE [155] and was designed to process signals from multi-wavelength PPG sensors at a sampling rate of 2000 Hz. This hardware-based PPG processing system provided power to the sensor, multiplexed the

three wavelengths by switching current sources to activate specific LEDs on the sensor, and performed de-multiplexing, since light from the three LEDs was detected by a single PD. During de-multiplexing, the PD current was converted into a voltage signal. Additionally, the processing unit filtered and amplified the signals to prepare them for analysis [155].

The signal was then transmitted from the signal processing unit to a data acquisition card (NI USB-6162, National Instruments, TX, USA), which interfaced with a computer to convert the analogue signals into digital data suitable for analysis. The computer, running LabVIEW software (National Instruments, Austin, TX, USA) was used to display and record the signals. Each recording lasted four minutes.

For consistency across recordings, the gain of the signal processing unit remained fixed throughout all recordings. However, minor adjustments to LED intensity were made where necessary to optimise signal quality and prevent saturation. As comparisons were performed only within individual experiments, and not between experiments conducted under different LED intensity settings, relative amplitude analyses were not affected by these adjustments. Absolute voltage amplitudes were therefore dependent on the acquisition configuration.

5.3.2 Signal Pre-Processing of Photoplethysmography Signals

The recorded PPG signals were pre-processed prior to feature extraction to reduce noise and support pulse detection. Signals were sampled at 2000 Hz and segmented into non-overlapping windows for analysis. Within each window, the signals were bandpass filtered to attenuate baseline drift and high-frequency noise while preserving the physiological frequency content of the cardiac waveform. For the studies in Chapters 6 through 9, a fourth-order Chebyshev Type II bandpass filter with cut-off frequencies of 0.5 Hz and 6 Hz was applied using zero-phase forward–backward filtering to avoid phase distortion. In Chapter 10, a second-order Chebyshev bandpass filter was used. Following bandpass filtering, a moving average was computed and used to identify zero-crossings. Peaks and troughs were then identified within these regions and used as fiducial points for pulse segmentation, after which feature extraction was performed on the filtered pulse waveforms [156].

5.4 Summary of Chapter 5

This chapter details the design and implementation of an in vitro cardiovascular system replicating the human lower body vasculature from the aorta to the femoral arteries. Two vascular configurations were used: an initial bilateral branching model (with the experiment described in Chapter 7) and a modified single-branch model (used in the experimental studies described in Chapters 6 and Chapters 8 through 10). Both configurations incorporated components including a pulsatile pump to simulate the cardiac cycle, one-way valves to maintain unidirectional flow, and pressure sensors for monitoring intra-system pressure. Customisable vessel-tissue phantoms (described in Chapter 6), fabricated to match the human mechanical properties, were integrated into the system.

BMFs were formulated with absorption and scattering agents to enhance signal quality across different optical sensing modalities. Methylene blue solutions were used in the early studies (Chapters 6 through 8), while the experiment in Chapter 9 employed a BMF containing Indian ink, Wright stain, Congo red. In Chapter 10, scattering agents such as LPFS with polystyrene microspheres or oil-in-water emulsions were added to the BMF to support LDF measurements.

For optical sensing, dual-wavelength and multi-wavelength PPG sensors were used. The dual-wavelength sensor (Chapters 6 through 8) incorporated red (640 nm) and IR (900 nm) LEDs. The multi-wavelength sensor (Chapter 9 and Chapter 10) included green (530 nm), red (655 nm), and IR (940 nm) LEDs. Signal acquisition and processing relied on two different systems developed at the RCBE. The ZenPPG device, sampling at 2000 Hz, recorded dual-channel PPG signals for the dual-wavelength sensor. For the multi-wavelength sensor, a second processing unit multiplexed the three wavelengths by activating specific LEDs and de-multiplexed the combined signals into voltage outputs. Signals were digitised via a data acquisition card and displayed or recorded on a computer using LabVIEW software.

CHAPTER 6: DEVELOPMENT OF VASCULAR TISSUE PHANTOMS

Most of the content in this chapter is adapted from my published paper in Sensors, titled 'Customisable Silicone Vessels and Tissue Phantoms for In Vitro Photoplethysmography Investigations into Cardiovascular Disease'. The material presented in part of Section 6.4.2, and the majority of Sections 6.6 and 6.6.1, is taken from my published paper in Photonics, titled 'Feasibility of Photoplethysmography in Detecting Arterial Stiffness in Hypertension'.

While some of the work presented within Chapter 6 was completed in collaboration to produce a wide range of customisable vessel-tissue phantoms, my contribution exceeded this collaborative work by developing customisable vessel–tissue phantoms that were mechanically characterised to represent healthy and diseased femoral arteries, as well as an intermediate state. Furthermore, compliance testing was completed on the fabricated femoral artery phantoms.

6.1 Introduction

Given that vascular ageing contributes to the development of CVD and involves a progressive increase in arterial stiffness [32], [33], [157], the measurement and assessment of arterial stiffness are valuable in indicating vascular ageing.

Current non-invasive assessment techniques, such as PTT, vascular ultrasound, and MRI, are confined to clinical settings due to the expertise required for the imaging techniques or the need for multiple measurement points, as in the case of PTT [158], [159]. More precise methods, such as angiography and computerised tomography angiography, require the injection of contrast agents [61]. While these procedures are accessible within clinical environments, referrals by a GP may introduce delays in cardiovascular health assessment. Therefore, the demand for more innovative technologies capable of the accurate and non-invasive assessment of vascular ageing is clear.

In vitro studies simulating vascular ageing in a controlled environment offer a promising path for developing new non-invasive technologies and signal processing algorithms. Previously, in Chapter 4, it was discussed that PPG sensor technology has the potential to provide information that is directly related to vascular ageing [3]. Researchers have previously created artificial vessels through techniques such as three-dimensional (3D) bioprinting [160], [161], [162], microfluidics based on laminar flow [163], [164], and

coaxial scale-up printing [165]. Although these approaches have shown encouraging results, they have limitations. For example, they often rely heavily on specific types of inks for printing, and the technology involved in laminar flow-based microfluidics can be complex [166].

This chapter describes the fabrication and mechanical testing of custom novel silicone vessels and tissue phantoms, utilising silicone additives to simulate the human vascular system in the in vitro setup, described in Chapter 5. This builds upon previous methods outlined by the RCBE. Previously, polydimethylsiloxane (PDMS) (Sylgard 184) (Dow Silicones, Barry, Wales, UK) was explored to create the initial vessels [167]. While this was successful, the formulations in PDMS silicone cannot be adjusted for customisable vessel elasticity. In this study, vessel fabrication and mechanical testing were performed using PlatSil Gel-10 (Polytek Development Corp., Easton, PA, USA) silicone, which demonstrated greater versatility in modifying vessel properties. Furthermore, unlike PDMS, this silicone contains a scatterer, which diffuses light from the sensor in a manner more similar to that in human tissue. This study aimed to investigate the effectiveness of the PlatSil elastomer in vessel stiffness customisation to determine the precision of formulation adjustments and the range of elasticities possible. Mechanical tests on the fabricated vessels, including hardness, thickness, and elasticity measurements were conducted. The fabricated custom vessels were embedded within silicone to mimic the surrounding tissue, creating vessel–tissue phantoms. The resulting phantoms were then integrated into the in vitro model for an initial PPG measurement and statistical analysis [168].

6.2 Materials and Methods

6.2.1 Fabrication of Custom Vessels

To fabricate the custom vessels, PlatSil Gel-10 elastomer was used, and silicone was chosen for its durability. In contrast to latex, silicone maintains its form and can withstand high temperatures [169], a crucial quality for the curing stage of the dip-coating process (described in Section 6.2.2). The mixture comprised two parts: Part A and Part B. Initially, Part A and Part B were individually weighed using a digital precision scale (Scout, Ohaus, Parsippany, NJ, USA). Once equal amounts were added, they were mixed thoroughly. To prevent premature curing, a retarder was added, extending the pour time. The addition of a 1% retarder of the total weight doubled the pour time [170].

Depending on the application, different softness and hardness of the elastomer solutions can be achieved by adding Smith's Deadener (Polytek Development Corp., Easton, PA, USA) or hardener, respectively. The silicone was then mixed and placed in a vacuum chamber (Applied Vacuum Engineering, Bristol, UK) for three minutes to remove air bubbles, before being utilised in the dip-coating process.

6.2.2 Dip-Coating Process

To construct the vessels, the elastomer mixture was poured into a silicone pot. The dip-coating method was set up as illustrated in Figure 16 and followed the methodology created by Nomoni et al. [171]. The commercial silicone tubing, employed as the form for the custom vessels, was positioned on pulleys and threaded through a heating element by the Precision Dip Coater (Qualtech Products Industry, Denver, CO, USA). One end of the form was attached to a tension weight, while the other side was secured to the dip-coater arm. The heating element was activated for three minutes, reaching a temperature of 275 °C. The elastomer was then poured into the silicone pot, and a coating layer of the elastomer mixture was applied by pulling up the form at a fixed speed of 40 mm/min, enabling the tubing to pass through without premature curing. The heating element was deactivated once the arm had reached its highest point, and the dip-coated tubing was left to cure. The internal form was carefully separated from the cured custom vessel.

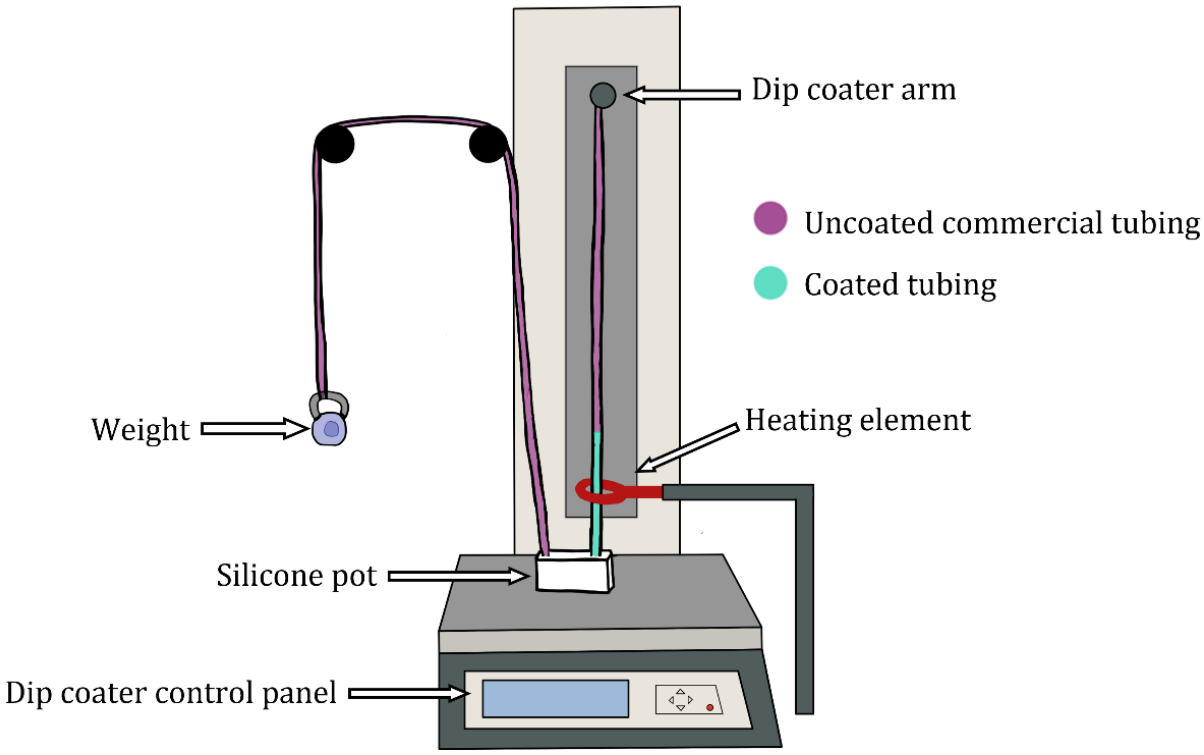

Figure 16: Schematic diagram of the dip-coating stage to produce customised vessels [152]. The form was threaded through the silicone pot and heating element and attached to the dip coater arm. The dip coater arm pulled the form to apply a layer of elastomer from the silicone pot. Once cured, the form was separated, isolating the silicone coating as the custom vessel.

The formulation of the mixture in the dip pot was adjusted by varying the amounts of retarder to generate vessels with different wall thicknesses, using a form with a total outer diameter (OD) of 3 mm. Similarly, deadener and hardener were incorporated to produce vessels with varying elasticities, using a form with OD of 2.6 mm.

6.2.3 Vessel-Tissue Phantoms Fabrication

The surrounding tissue was formulated by combining equal amounts of Part A and Part B of Gel-00 (Polytek Development Corp., Easton, PA, USA). Gel-00, softer than Gel-10, was selected to achieve tissues with a Shore hardness of OO 30, in line with the mechanical properties of the surrounding tissue [172]. The mixture was then placed in a vacuum chamber to eliminate air bubbles before being poured into 3D-printed moulds (Figure 17), resulting in the creation of vessel–tissue phantoms (Figure 18).

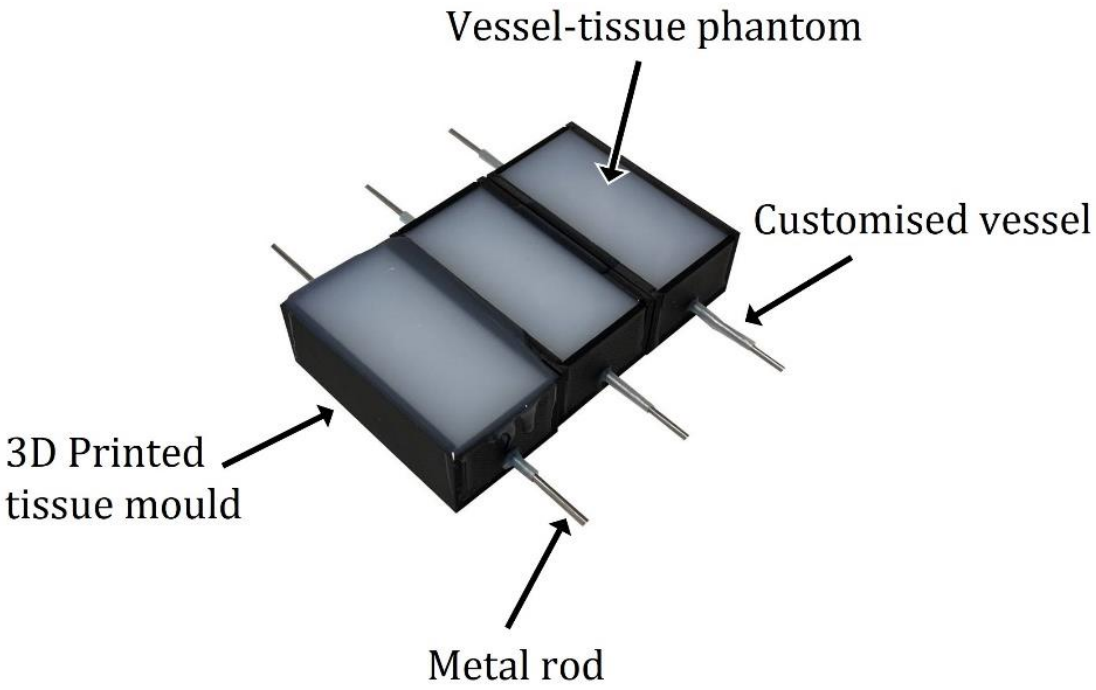

Figure 17: Diagram illustrating the construction of the vessel-tissue phantoms. A metal rod is threaded through the customised vessel and incorporated into the three-dimensional (3D) printed tissue moulds. The tissue elastomer was then poured into the mould and left to cure. Once cured, the vessel-tissue phantoms were removed from the moulds [150].

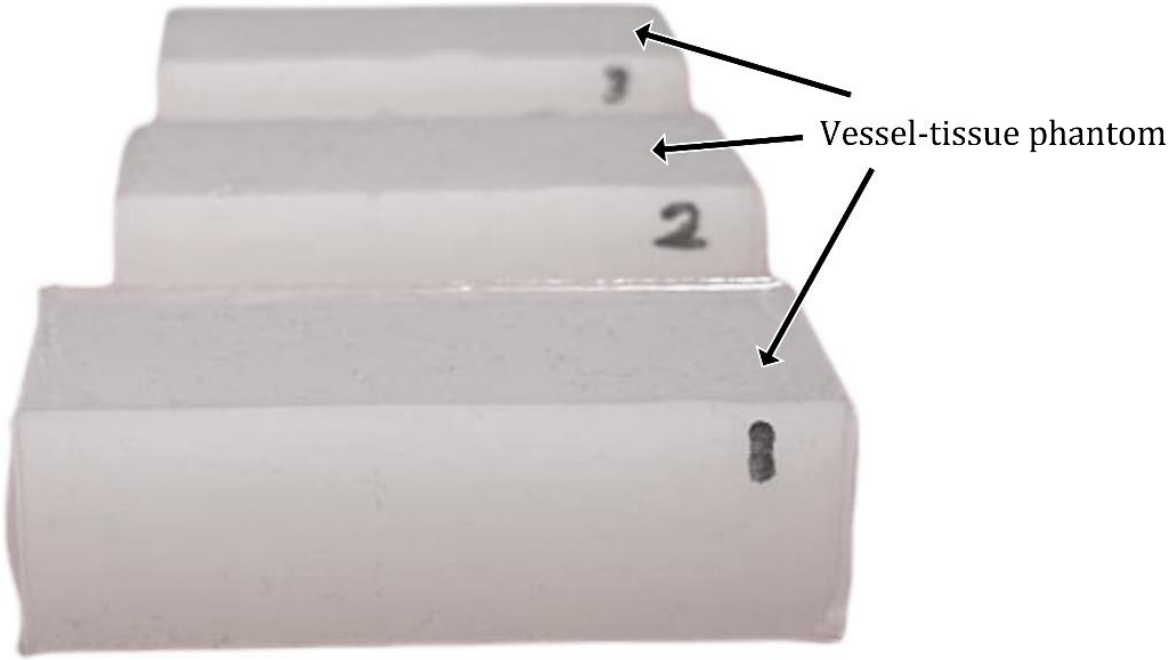

Figure 18: Cured vessel-tissue phantoms after removal from the 3D printed moulds. The fabricated custom vessels are embedded within the surrounding tissue. Labels 1, 2, and 3 represent vessel–tissue phantoms with vessels of varying mechanical properties.

6.3 Mechanical Testing

6.3.1 Measuring Thickness

To investigate the impact of the formulations on the vessel wall thickness, sections of the constructed vessels, each 1 mm in length, were sliced from both ends. These sections were then stained with black paint to enhance viewing contrast and examined under a digital microscope (Celestron, Torrance, CA, USA) for wall thickness measurements, as illustrated in Figure 19. The sample size comprised three stained cross-sections from each side of the vessel, totalling six cross-sections for each vessel. Still pictures were captured using Celestron MicroCapture Pro software version 2.5 (Celestron, Torrance, CA, USA). The wall thickness of each section was measured four times and averaged. The mean value for each vessel was determined by finding the average between both ends of the vessels. The same process was employed to determine the ID. The OD was calculated based on ID by adding the thickness on each side of the vessel wall.

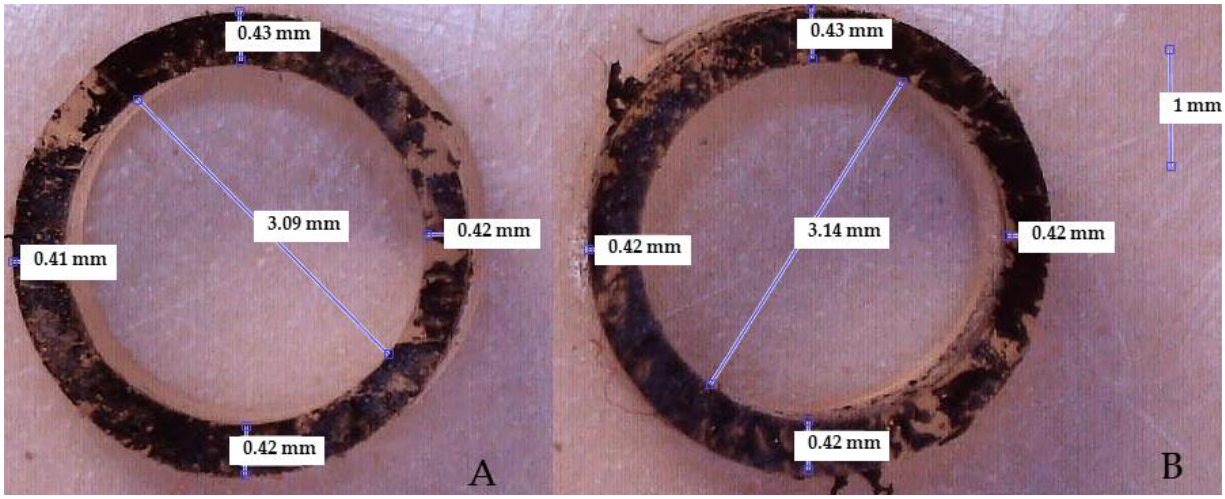

Figure 19: Cross-sectional image of a stained vessel during wall thickness measurement [152]. (A) represents one end of the vessel and (B) represents the other end. For each cross-section, internal diameter (ID) and wall thickness were measured four times and averaged. The ID and wall thickness mean values were calculated by averaging the results from both ends. Outer diameter (OD) was then derived from the ID by adding twice the mean wall thickness.

6.3.1.1 Thickness, Internal Diameter, and Outer Diameter Measurements

Measurements of the wall thickness of the vessels made with varying amounts of retarder are presented in Figure 20. The findings indicate that increasing the retarder concentration reduced the wall thickness until stabilising at 3.0% and 3.5%. The ID ranged from 2.55 mm to 2.78 mm, and the OD ranged from 3.20 mm to 3.77 mm.

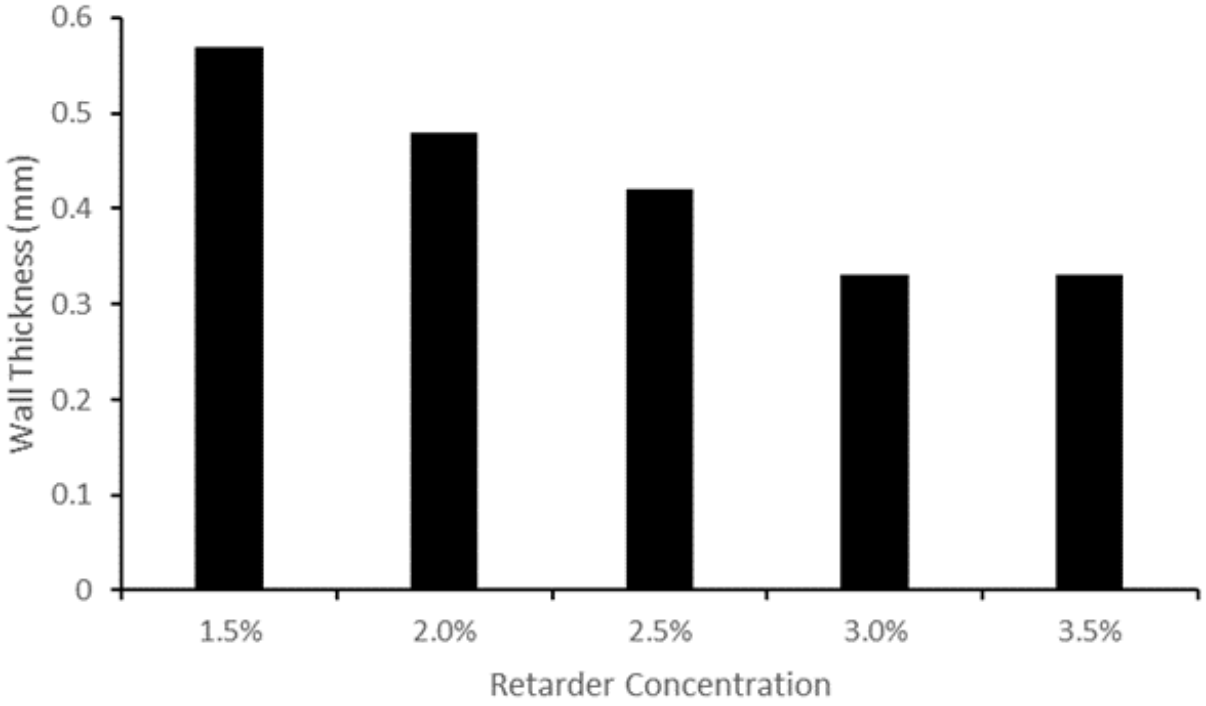

Figure 20: Bar chart displaying the change in wall thickness measurements for varying retarder concentrations. Wall thickness decreased with increasing retarder concentration [152].

Increasing the retarder concentration reduced the thickness of the custom vessels until reaching a plateau at concentrations above 3%. This change in thickness is linked to the cure time, which is determined by the retarder level. When the retarder concentration was increased, the silicone coating had more time to descend, resulting in a thinner dip-coated vessel before curing.

Table 4 and Table 5 respectively outline the wall thickness, ID, and OD values obtained when varying the deadener and hardener ratios within the elastomer. The wall thickness remained between 0.50 mm and 0.58 mm. This outcome was anticipated, as the amounts of deadener and harder should not affect the thickness of the vessel; instead, they influence its softness and hardness [170]. For both datasets, the retarder concentrations were maintained at 1.5%. The OD ranged from 3.96 mm to 4.04 mm for the deadener dataset, whereas in the hardener dataset, the OD ranged from 3.96 mm to 4.09 mm. For both the deadener and hardener experiments, equal amounts of Part A and Part B were used with varying amounts of Part D (deadener) and Part H (hardener). Deadener experiments are represented with the ratio A:B:D, up to a limit of 0.6 D, and hardener with A:B:H, up to 1 H.

*Table 4: Thickness, internal diameter, and outer diameter measurements for varying deadener ratios. * Ratio of Part A:Part B:deadener [152].*

Mixture Ratio (* A:B:D)	Wall Thickness (mm)	Internal Diameter (mm)	Outer Diameter (mm)
1:1:0	0.53	3.00	3.96
1:1:0.2	0.58	2.82	4.00
1:1:0.4	0.57	2.90	4.04
1:1:0.6	0.58	2.85	4.00

*Table 5: Thickness, internal diameter, and outer diameter measurements for varying hardener ratios. * Ratio of Part A:Part B:hardener [152].*

Mixture Ratio (* A:B:H)	Wall Thickness (mm)	Internal Diameter (mm)	Outer Diameter (mm)
1:1:0	0.53	3.00	3.96
1:1:0.2	0.54	2.98	4.06
1:1:0.4	0.50	3.02	4.02
1:1:0.6	0.51	2.95	3.97
1:1:0.8	0.53	2.96	4.01
1:1:1	0.52	3.02	4.09

6.3.2 Measuring Elasticity

The Universal Testing System (Instron 5944, Norwood, MA, USA) was used in a tensile test configuration to measure the Elastic Modulus of each custom vessel, as shown in Figure 21. This involved two grips holding a vessel with a length of 15 cm in place and vertically drawing the sample apart with a drawing speed of 500 mm/min until the material reached its breaking point. This procedure was set in accordance with the ASTM D412-16 standard [173]. Along with the previously calculated vessel diameter and thickness measurements, each vessel was universally loaded with a force of 0.10 N to

calculate Young's modulus using Bluehill Universal software version 4.42 (Instron, Norwood, MA, USA). This process was repeated for each vessel to observe differences in elastic properties with varying levels of retarder, deadener, and hardener. For the tissue samples, the system was set to the compression test configuration (as seen in Figure 21) to measure the Elastic Modulus of each tissue phantom. Each tissue phantom measured 50 × 20 × 20 mm (L × W × H). The phantoms were placed on a flat metal plate and compressed to calculate Young's modulus. A drawing speed of 12 mm/min was set in accordance with the ASTM D575-91 standard [174].

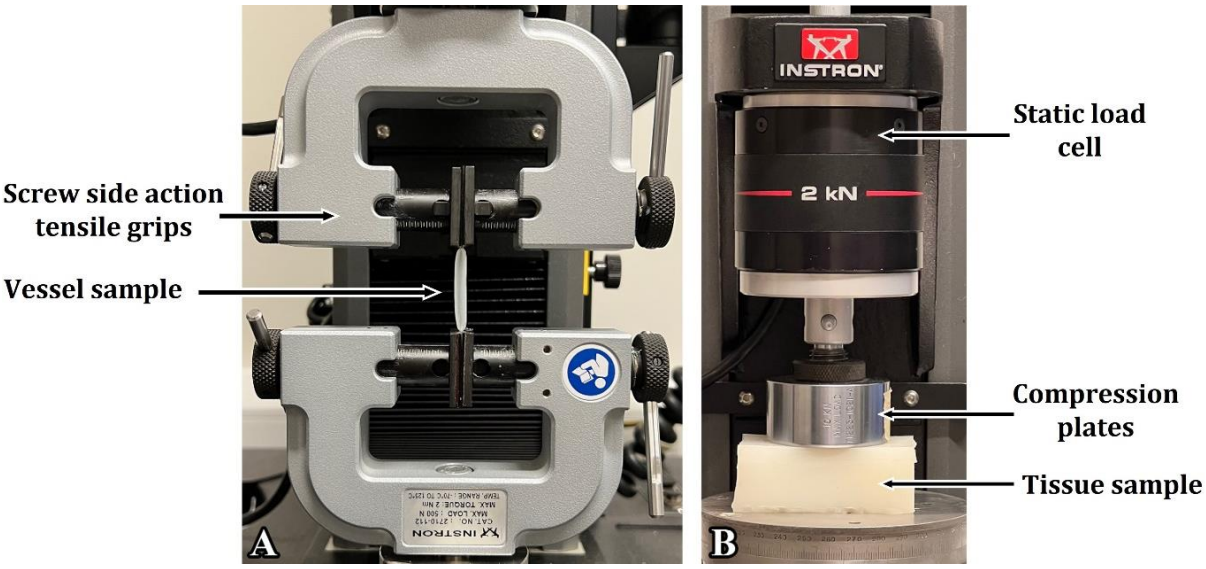

Figure 21: Universal Testing System for Elastic Modulus measurement of custom vessels through tensile testing (A) and compression testing of silicone tissue samples (B) [152].

6.3.2.1 Elasticity Measurements

The Young's modulus measurements recorded during the tensile test of the custom vessels made with varying amounts of retarder are presented in Figure 22. The resulting Young's modulus ranged from 0.42 MPa to 0.61 MPa with retarder concentrations of 1.5% to 3.5%, respectively. It should be noted that the retarder level had an impact on vessel elasticity, as explained by the change in thickness. It was found that the Young's modulus was thickness-dependent; as the thickness decreased due to increasing retarder levels, the Young's modulus increased [175].

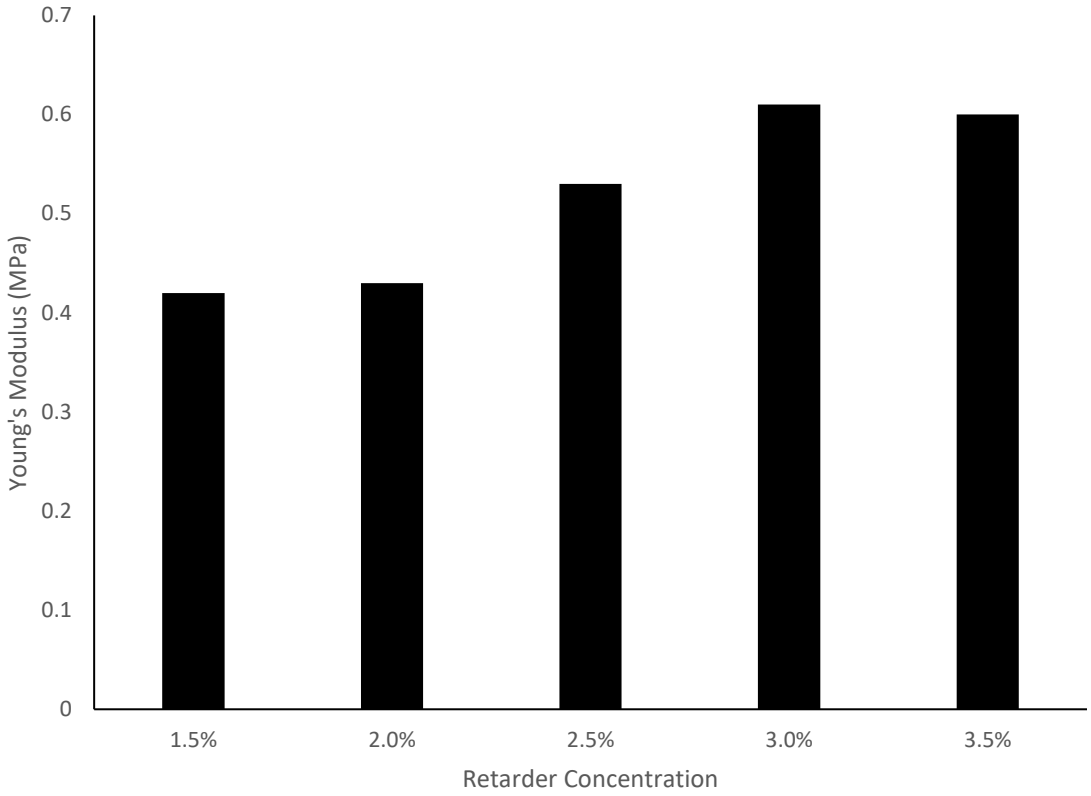

Figure 22: Bar chart displaying the Young's modulus measurements for varying levels of retarder concentrations [152].

The Young's modulus calculations on vessels with varying amounts of deadener and hardener are shown in Table 6 and Table 7, respectively. Deadener was used to produce softer and more elastic vessels, simulating the properties of healthy human blood vessels. As the ratio of deadener increased, the resulting Young's modulus values decreased from 0.52 MPa to 0.20 MPa, indicating an increase in elasticity. As expected, the wall thickness remained between 0.53 mm and 0.58 mm (Table 4), showing that the deadener primarily impacted the material's stiffness. When creating stiffer materials, hardener was utilised to decrease elasticity, mimicking unhealthy vessels. As the ratio of hardener increased, the Young's modulus increased from 0.52 MPa to 1.22 MPa, indicating a reduction in elasticity. Again, the wall thickness did not alter significantly with the hardener, remaining between 0.50 mm and 0.54 mm (Table 5). Figure 23 displays these elasticity trends between the deadener and hardener and shows the Young's modulus of a healthy femoral artery for the adventitia and radial strain [176].

Table 6: Young's modulus measurements of custom-made silicone tubing with varying levels of deadener [152].

Mixture Ratio (A:B:D)	Young's Modulus (MPa)
1:1:0	0.52
1:1:0.2	0.46
1:1:0.4	0.28
1:1:0.6	0.20

Table 7: Young's modulus measurements of custom-made silicone tubing with varying levels of hardener [152].

Mixture Ratio (A:B:H)	Young's Modulus (MPa)
1:1:0	0.52
1:1:0.2	0.64
1:1:0.4	0.78
1:1:0.6	0.82
1:1:0.8	0.92
1:1:1	1.22

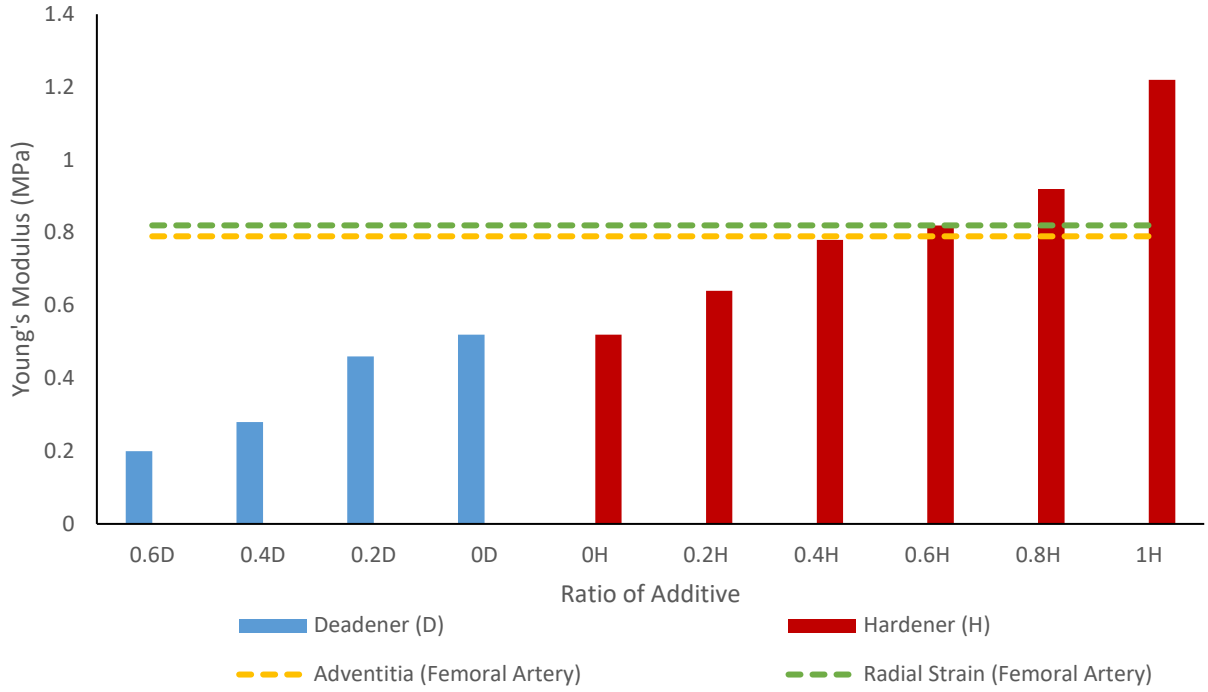

Figure 23: Tensile test results showing Young's modulus values of custom vessels with different amounts of hardener and deadener [152]. The ratio of additive is relative to the total weight of the elastomer while maintaining equal amounts of Part A and Part B. The Young's modulus of a healthy femoral artery, in terms of the adventitia and radial strain [176], is shown using dotted lines.

In the case of tissue phantoms, an increase in the amount of deadener corresponded to a softening of the material, as demonstrated by the decrease in the Young's modulus illustrated in Figure 24. With increasing hardener, the Young's modulus of the tissue phantoms rose, indicating greater hardness of the material. A normal Young's modulus for tissue found in the finger is shown in Figure 24, which ranges between 0.07 MPa and 0.2 MPa [177]. By using a ratio of 0.2 to 0.8 deadener to equal amounts of Part A and Part B, it is feasible to create tissue of a similar elasticity to that of the human finger.

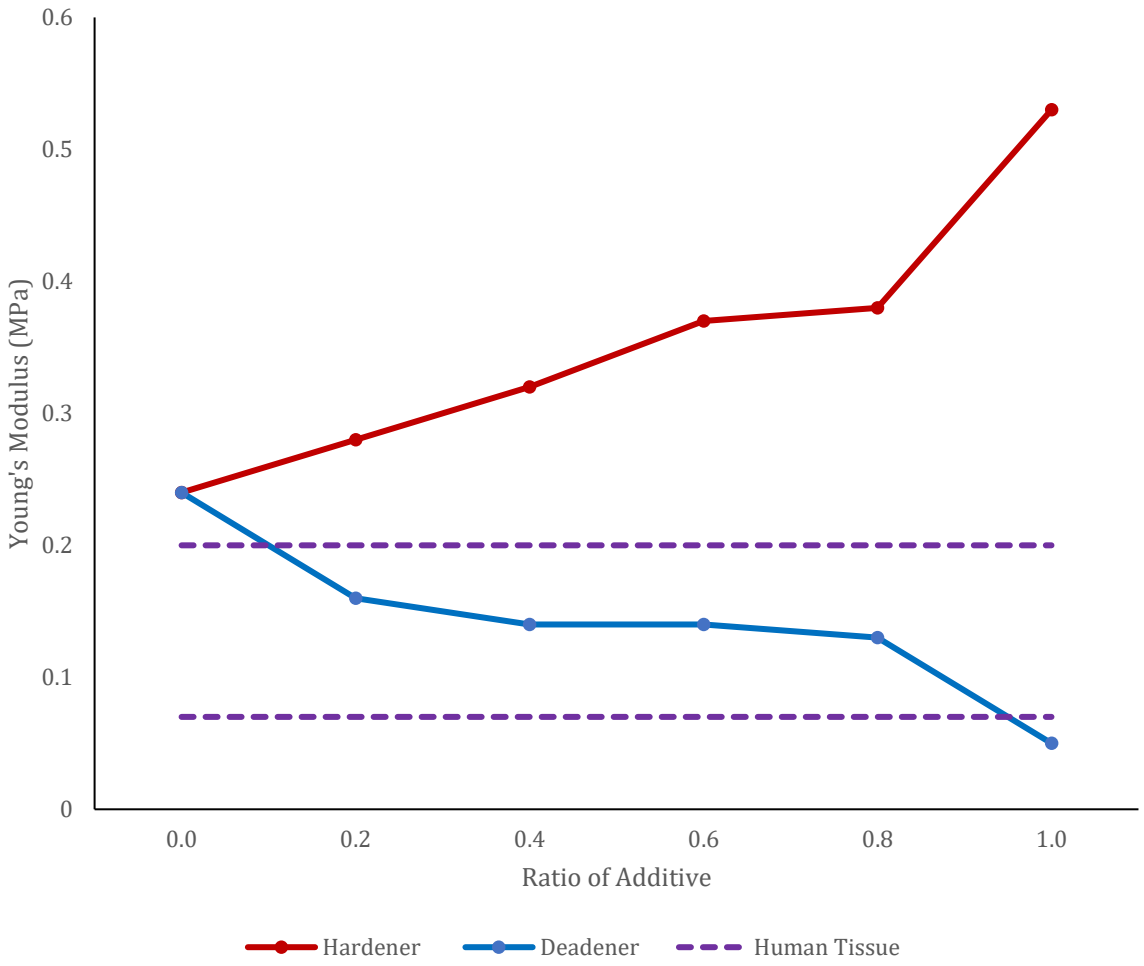

Figure 24: Compression test results showing Young's modulus values of custom tissues with different amounts of hardener and deadener [152]. Increasing hardener concentration increased Young's modulus, whereas increasing deadener concentration decreased Young's modulus. The normal range for tissue found in the human finger [177] is indicated by the dotted lines.

6.3.3 Measuring Hardness

The AD-100-OO Precision Shore Durometer (Checkline Europe, Enschede, The Netherlands) was used to assess the hardness of the cured silicone tissue from the dip pot, as depicted in Figure 25. The durometer was placed on the surface of the tissue with the footpad at a slight angle and then gently rolled to a flat position for the most accurate reading. Readings were taken from multiple sites on the tissue and averaged. This process was repeated for tissues with varying levels of retarder, deadener, and hardener. Consequently, a record was produced to observe changes in tissue hardness depending on additives.

Figure 25: Measuring the hardness of silicone tissue using a Shore-OO Durometer. Measurements were taken from multiple locations on the tissue and averaged [152].

6.3.3.1 Hardness Measurements

The hardness measurements obtained from the cured tissues with varying retarder levels using the Shore durometer are recorded in Table 8. Hardness levels remained constant as the retarder was increased from 1.5% to 3.5%, remaining between OO 47 and OO 50 Shore hardness.

Table 8: Young's modulus measurements of custom-made silicone tubing with varying levels of retarder [152].

Retarder (%)	Hardness (Shore OO Scale)
1.5%	OO 48
2.0%	OO 49
2.5%	OO 49
3.0%	OO 50
3.5%	OO 47

With increasing amounts of deadener, a reduction in tissue hardness was observed, as indicated in Table 9. Shore hardness decreased from Shore OO 48 with no deadener to Shore OO 25 at one-part deadener. On the other hand, tissue hardness, as expected, increased with hardener concentration, as shown in Table 10. At one-part hardener, the tissue stiffness increased to Shore OO 67. The change in Shore hardness with hardener and deadener and the Shore hardness found in the dorsal thigh are presented in Figure 26.

Table 9: Shore hardness of tissue as the amount of deadener is increased, showing a negative correlation. As the ratio of deadener in the mixture is increased, the tissue hardness decreases due to the softening effect of the deadener [152].

Mixture Ratio (A:B:D)	Hardness (Shore OO Scale)
1:1:0	OO 48
1:1:0.2	OO 44
1:1:0.4	OO 43
1:1:0.6	OO 39
1:1:0.8	OO 32.5
1:1:1	OO 25

Table 10: Shore hardness of tissue as the amount of hardener is increased, showing a positive correlation. As the ratio of the hardener in the mixture is increased, the tissue hardness also increases [152].

Mixture Ratio (A:B:H)	Hardness (Shore OO Scale)
1:1:0	OO 48
1:1:0.2	OO 52
1:1:0.4	OO 56
1:1:0.6	OO 61
1:1:0.8	OO 63
1:1:1	OO 67

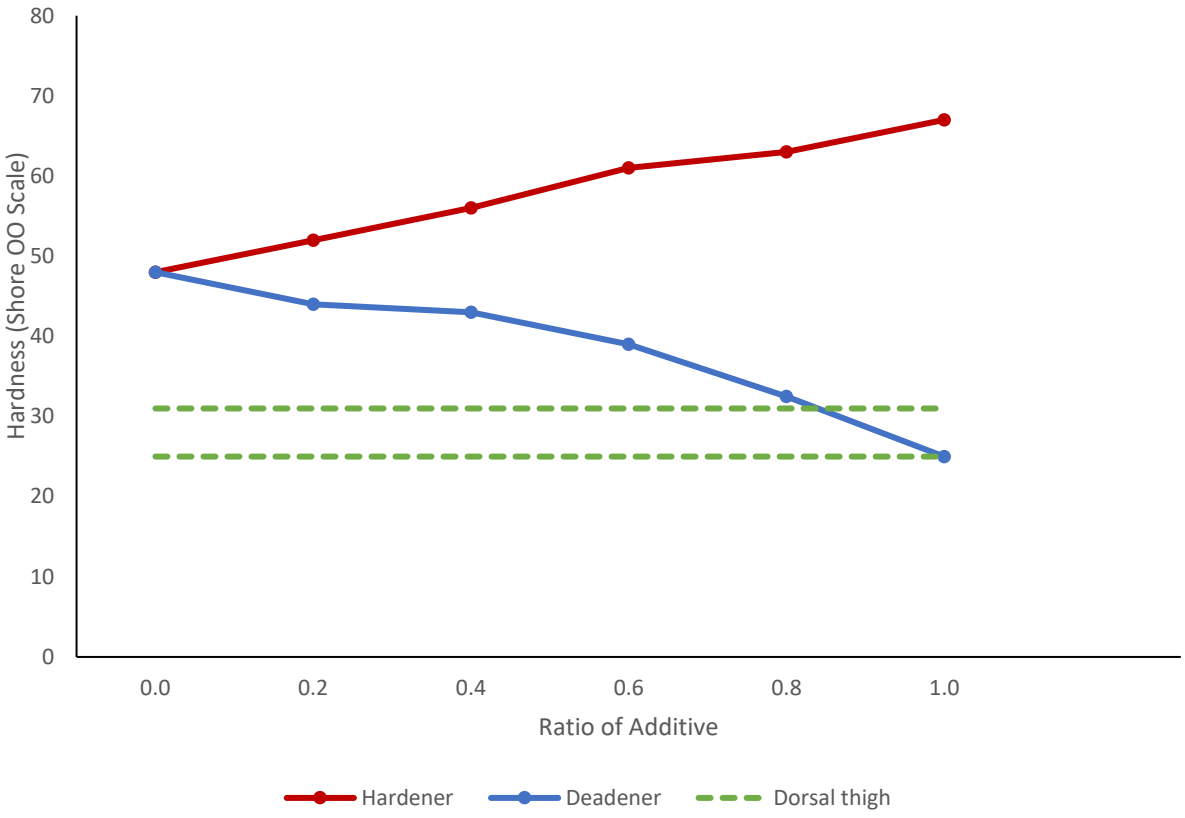

Figure 26: Change in Shore hardness with different amounts of hardener and deadener [152]. Increasing hardener concentration increased Shore hardness, whereas increasing deadener concentration decreased Shore hardness. The normal range for tissue found in the dorsal thigh [178] is indicated by the dotted lines.

In the silicone tissue, the deadener was found to make the silicone softer, as indicated by a decrease in shore hardness. Adding hardener had the opposite effect, causing the tissue to become stiffer, as shown by the increase in shore hardness. Therefore, the Young's modulus and tissue hardness are proportional, as also found by Sun et al. [179]—as the hardness increased, the Young's modulus also increased. The dorsal thigh exhibits a shore hardness ranging from shore OO 25 to shore OO 31 [178]. To replicate this, equal amounts of Part A, Part B, and deadener can be incorporated.

6.4 Obtaining PPG Signals from an In Vitro System

6.4.1 Acquisition of Photoplethysmography Signals

PPG signals were obtained from three custom vessel–tissue phantoms, each fabricated with varying additives to modify vessel elasticity, by connecting the phantoms to the in vitro system described in Chapter 5. Deadener was used as the additive in the elastic vessel at a ratio of 0.2 (10% of the total weight). For the stiff vessel, the same amount of

hardener was used. PPG signals were also recorded from a phantom with a vessel containing no additive. The PPG and pressure signals obtained from the phantoms are shown in Figure 27. This experiment was conducted in a darkened room and completed on the same day to minimise environmental influences on the recorded signals. The PPGs visually resembled human signals, featuring diastolic and systolic peaks with a dicrotic notch. There was a visual change in the PPG signals among the phantoms. As vessel stiffness increased, the amplitude of the systolic and diastolic peaks appeared to decrease, particularly in the IR signal.

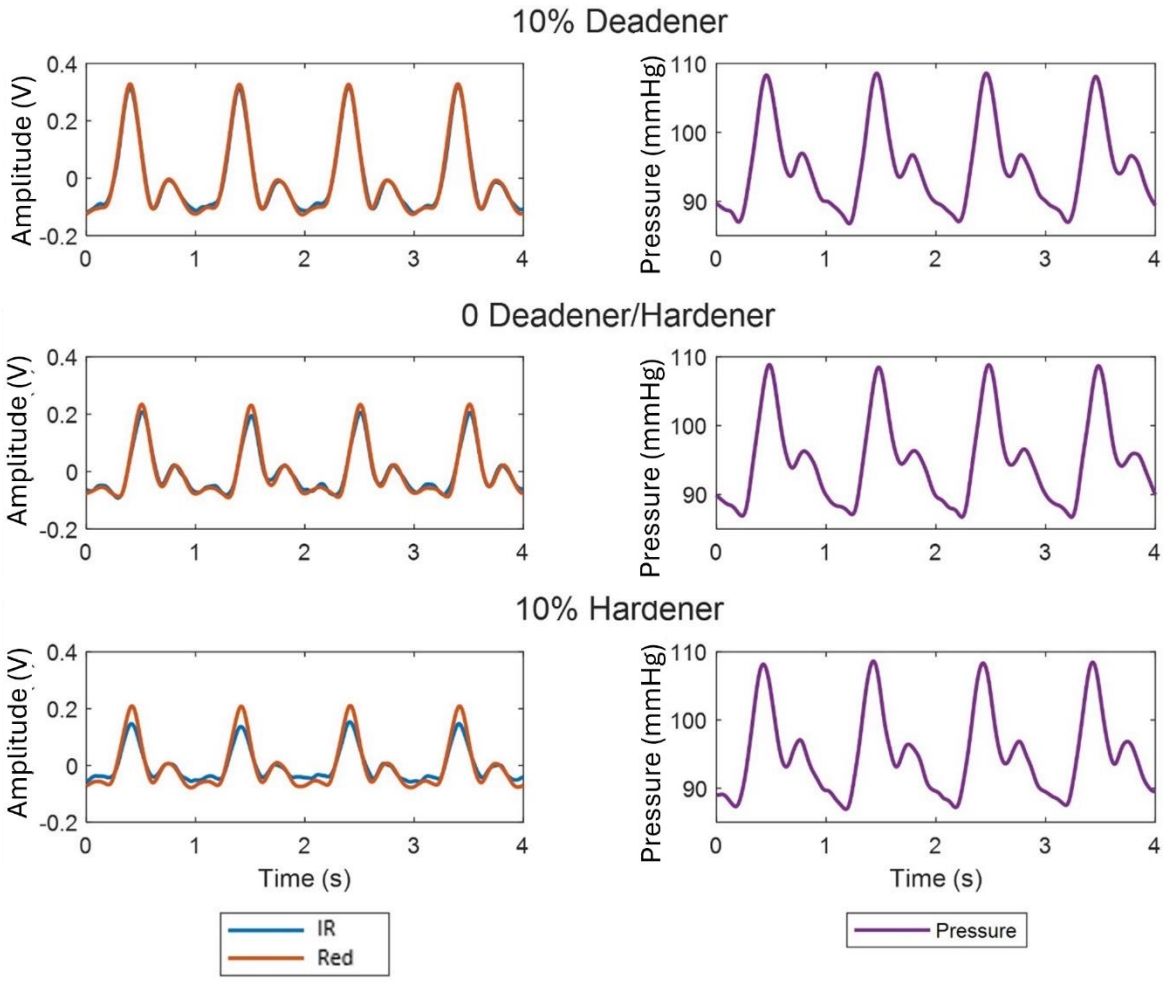

Figure 27: PPG and pressure signals recorded from custom vessel–tissue phantoms with vessels of varying stiffnesses induced by mixing different additives (hardener and deadener). The percentage of additive shown is relative to the total mixture. With increasing stiffness, the PPG amplitude decreases for both red and IR signals, while the pressure waveforms remain relatively constant [152].

Accompanying pressure signals confirmed that the morphology of the PPG wave was induced by changes in pressure. As with the PPG signals, the pressure signals obtained conformed to the expected physiological morphology. Interestingly, the varying vessel stiffness revealed a difference in the PPG morphology such as amplitude, while the pressure waveform remained constant across phantoms. This may be because the pressure sensors were placed at the end of the vessel phantom, while the PPG sensors were positioned in the middle, possibly providing greater information about volumetric changes within the vessel. While pressure waveforms serve as a secondary measure to validate the results, exploring additional methods, such as Doppler ultrasound, could provide further confirmation of the changes in volume.

6.4.2 Statistical Analysis

Statistical analysis of the recorded signals was performed using the Kruskal–Wallis test, a nonparametric one-way analysis of variance designed to evaluate differences between three or more independent groups [180]. This test serves as an extension of the Mann–Whitney U test, allowing for the comparison of multiple independent samples [181], [182].

Systolic PPG amplitude was quantified through feature extraction and presented in a box plot in Figure 28, illustrating the amplitude change among the vessel–tissue phantoms. This change was analysed for statistical significance using Kruskal–Wallis analysis, as shown in Table 11. A significant difference in amplitude was observed between the phantoms for both red and IR wavelengths ($p < 0.001$). A Dunn test was applied as a post hoc test to determine the degree of difference between each phantom, as seen in Table 12. The p-values, adjusted for multiple comparisons, suggested that the PPG amplitude of all three phantoms differed significantly ($p < 0.001$).

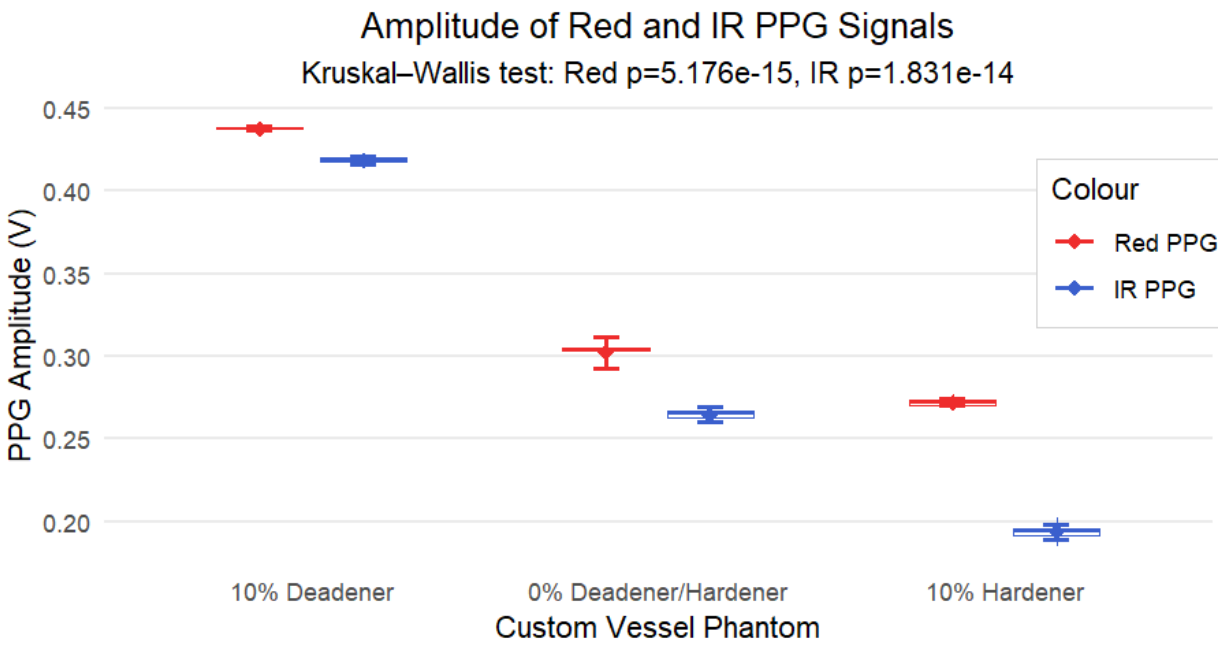

Figure 28: Box plot showing the distribution of red and IR PPG amplitude across custom phantoms with vessels of varying elasticity (10% deadener, 0% additive, and 10% hardener). Markers and error bars indicate the mean ± standard deviation. Kruskal–Wallis tests are reported for both wavelengths (red: $p = 5.176\times10^{-15}$; IR: $p = 1.831\times10^{-14}$), indicating significant differences in amplitude across the phantoms [152].

Table 11: Kruskal–Wallis analysis of red and IR PPG amplitudes from custom phantoms [152].

Comparison	Chi-Squared	Df	p-value
Red	65.789	2	5.176×10^{-15}
IR	63.263	2	1.831×10^{-14}

Table 12: Dunn test of PPG amplitudes between each custom phantom [152].

Comparison	Z	p (Unadjusted)	p (Adjusted)
0 D/H–10% D	−4.055536	5.001957×10^{-5}	1.000391×10^{-4}
0 D/H–10% H	4.055536	5.001957×10^{-5}	5.001957×10^{-5}
10% D–10% H	4.055536	5.017550×10^{-16}	1.505265×10^{-15}

6.5 Fabrication Implications and Limitations, and Considerations for Future Work

When fabricating custom vessels, some limitations were identified. Due to the delicate nature of the vessels, a ratio of deadener up to 1A:1B:0.6D was possible. It was observed that beyond this ratio, the custom vessel would adhere to the internal commercial silicone tubing being used as the form, making removal challenging. Furthermore, a minimum retarder of 1.5% should be used when the dip coater's speed is set to 40 mm/min to allow for sufficient time to pull the vessel to the maximum height. Future work could explore the impact of varying the dip coater's speed. One hypothesis suggests that increasing the speed may reduce the requirement for as much retarder, as it allows the uncured silicone to reach the maximum height quicker, thus shortening the need for a long curing time. Moreover, if the dip coater's speed is increased while using the same amount of retarder, it is anticipated that the custom vessel will reach its maximum height more rapidly, potentially providing more time for the uncured silicone to descend due to gravity, resulting in thinner custom vessels.

The results of this study were compared with those of the common femoral artery. According to Soneye et al. [183], the wall thickness of a healthy left common femoral artery is 0.55 ± 0.05 mm. The common femoral artery's vessel diameter ranged from 3.9 mm to 8.9 mm, with an average value of 6.6 mm [184]. A healthy femoral artery has been found to have a Young's modulus of 0.80 MPa, 0.79 MPa, and 0.82 MPa for the

intimate, adventitia, and radial strain, respectively [34]. From the results obtained in this experimental study, the femoral artery can be mimicked with a 1A:1B:0.6H mixture with 1.5% retarder. If commercial silicone tubing with an OD of 2.6 mm is utilised as a form, a wall thickness of 0.51 mm can be attained. The Young's modulus of 0.82 MPa is within the range for radial strain, and the diameter would be 3.96 mm, which is also within the normal range. A clogged femoral artery, known as an atherosclerotic femoral artery, has a Young's modulus of 3.6 MPa and 2.11 MPa in the adventitia and radial strain, respectively [34]. As such, to mimic an atherosclerotic femoral artery, a higher ratio of hardener must be used than 1A:1B:1H to obtain a less elastic artery with a higher Young's modulus.

Signal analysis should also be expanded upon by exploring additional parameters during PPG feature extraction. Features such as half peak width, AUC, upslope, and downslope are beneficial, as these characteristics may be indicative of arterial stiffness, providing a deeper understanding of the dynamics and mechanical properties of the custom vessels.

To extend the findings outlined in this experimental study to clinical measurements, it is crucial to assess potential influences on the PPG waveform. One such factor is sensor contact. While a secure and strong contact has proven to yield high-quality signals, peripheral vasoconstriction may result in signals of lower quality [3], [106]. In the in vitro setup, the phantoms and sensors were housed within a custom casing that prevented movement and ensured consistent contact force during readings. Another factor to consider is hydrostatic effects. The positioning of a limb in relation to the heart has an impact on arterial flow and venous return, influenced by the hydrostatic effect. The research indicated that lowering the hand below heart level results in decreased amplitudes of both alternating current (AC) and DC components of PPG, which has been attributed to venous distension. In contrast, raising the arm above heart level leads to an increase in AC and DC PPG amplitudes [185]. Therefore, it is concluded that the position of the hand is crucial in in vivo studies due to hydrostatic effects. The in vitro setup was aligned horizontally, and phantom placement was kept constant. As such, minimal hydrostatic impacts were observed.

6.6 Fabrication of Femoral Arteries

Once the vessels were mechanically characterised to determine their properties, adjustments were made to match the mechanical characteristics of human femoral arteries [152], [176]. Three custom femoral arteries were fabricated: one representing a healthy femoral artery with a Young's Modulus of 0.82 MPa, another representing an atherosclerotic femoral artery with a Young's Modulus of 2.06 MPa, and the third representing an intermediate vessel between the former two with a Young's Modulus of 1.48 MPa. The elasticity was measured using a Universal Testing System in a tensile test configuration, with the procedure set in accordance with the ASTM D412-16 [173] standard, as described in Section 6.3.2. The ID and OD of the vessels embedded in the phantom were measured at 2.95 mm and 3.96 mm, respectively. The fabrication procedure, along with the material formulation used to create the healthy, intermediate, and atherosclerotic vessels, can be found in Table 26 of the Appendix. These measurements fell within the reported literature range for the femoral artery's OD, which spans from 3.9 mm to 8.9 mm [152], [184]. To determine the compliance, vessels were cut into lengths ranging from 5 to 10.5 cm and connected to a syringe pump (kdScientific, Holliston, MA, USA) in a closed system (Figure 29). It was assumed that the vessel elasticity was uniform and homogeneous along the length. Water increments of 20 μL were pumped in to induce inflation, and the internal pressure (mmHg) was measured using a pressure transducer. The water increments were introduced progressively, increasing the pressure in the range of 0 to 160 mmHg to represent hypotensive to hypertensive conditions. During this process, images were captured using the digital microscope, as illustrated in Figure 29. Changes in diameter were measured using MATLAB (Version R2023a, 9.14, MathWorks, Natick, MA, USA), and the cross-sectional area was subsequently calculated. The compliance was determined by calculating the ratio of the change in cross-sectional area to the change in pressure ($\delta s/\delta p$) [31], [186]. A precision ruler was used as a calibration tool to ensure accurate measurements. Tissue was then created to surround these vessels, following a similar procedure as outlined in Section 6.2.3 [152], to make vessel-tissue phantoms that mimicked surrounding blood vessel tissue.

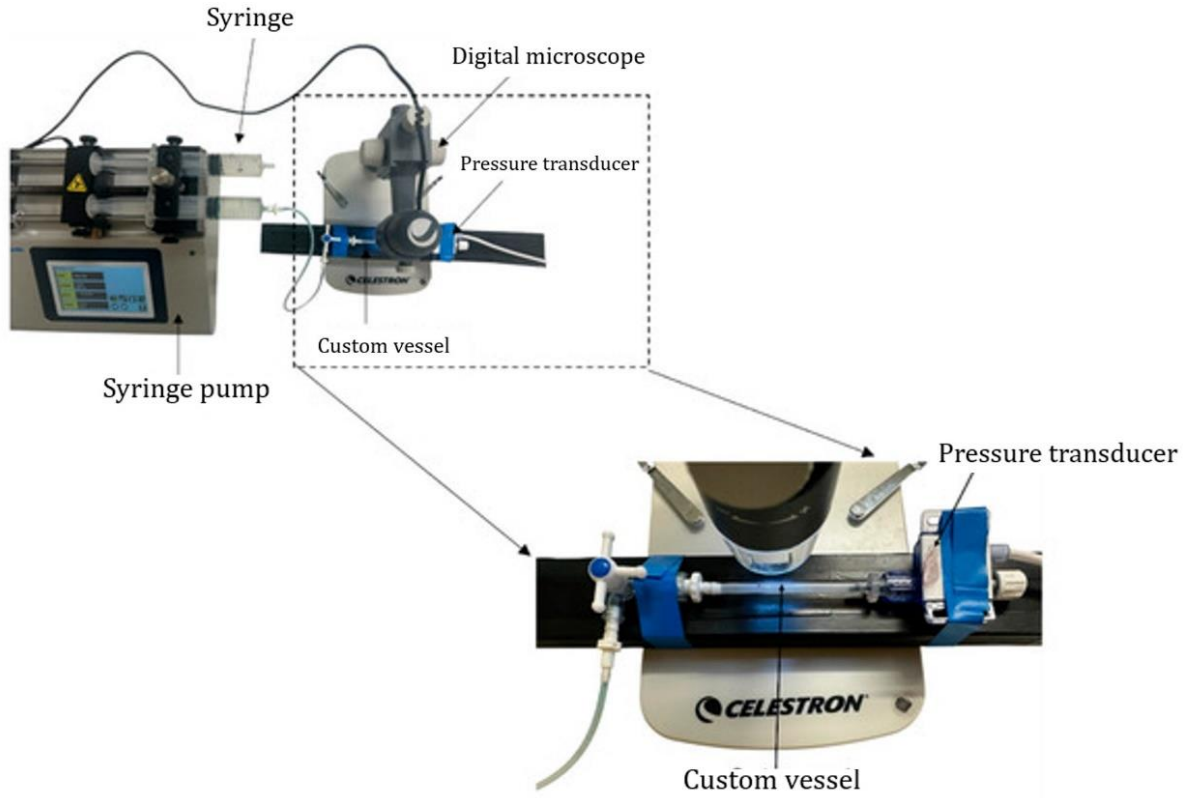

Figure 29: Setup for compliance testing [59]. The vessel was securely positioned under the digital microscope, and a syringe pump delivered 20 µL of fluid to inflate the vessel. Internal pressure was monitored using a pressure transducer. Changes in diameter were observed and measured with MATLAB. A close-up view of the vessel connection under the digital microscope has been illustrated.

6.6.1 Mechanical Characterisation

Blood vessels are believed to expand more prominently in the circumferential direction than in the longitudinal direction. While it has been reported that circumferential stretch in the superficial femoral artery changes insignificantly with age [187], accurately replicating physiological conditions in the human body remains crucial. Therefore, in this research, compliance was assessed for the healthy, intermediate, and unhealthy vessels, with the results presented in Figure 30. As vessel stiffness increased, from healthy to intermediate to unhealthy, the change in cross-sectional area progressively decreased. This indicates that stiffer vessels exhibit reduced expansion and, consequently, lower elasticity.

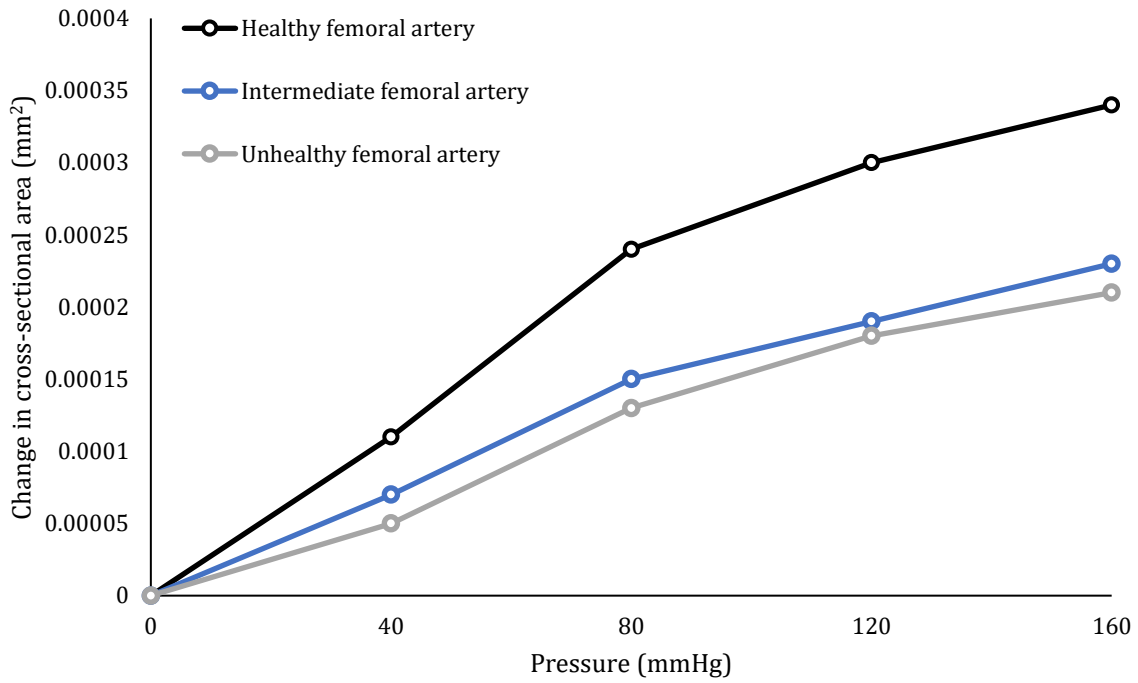

Figure 30: Mechanical properties of the femoral artery [59]. The healthy femoral artery is represented by a solid black line with white dots, the intermediate femoral artery by a solid blue line with white dots, and the unhealthy femoral artery by a solid grey line with white dots.

In cardiovascular physiology, peripheral resistance and vascular compliance are related parameters, with vessel dilation affecting peripheral resistance. Although these variables can be independently and qualitatively altered, they were held constant throughout this research. Therefore, any observed changes in resistance during the experiments were most likely attributable to changes in the phantom under investigation, where resistance would change locally.

6.7 Summary of Chapter 6

The research presented in this chapter puts forward an innovative approach to investigate the effect of arterial stiffness on PPG signals using novel vascular tissue phantoms. The fabrication process outlined in this chapter can be adapted to introduce pathologies by modifying elastomer properties to mimic both healthy and diseased vessels. The results demonstrated that the vessel wall thickness can be regulated using different retarder concentrations. Additionally, the softness and hardness of the vessels and surrounding tissue can be adjusted by adding deadener or hardener, respectively.

Mechanical testing confirmed that increasing the deadener concentrations produced softer, more elastic vessels and tissues with lower Young's modulus and Shore hardness, whereas increasing the hardener concentrations yielded stiffer vessels and tissues with higher Young's modulus and hardness. The fabrication methodology was then adapted to produce vessel–tissue phantoms replicating the mechanical properties of healthy and atherosclerotic femoral arteries, achieving elasticities consistent with values reported in the literature [152], [176].

PPG signals were recorded from three phantoms composed of vessels with varying elasticities to determine if the elasticity influenced the PPG waveform, particularly the amplitude. The softer vessel phantom was created using a ratio of 0.2 deadener (10% of total weight) and the stiffer vessel phantom was made with hardener at a ratio of 0.2 (10% of total weight). The third vessel phantom did not contain additives. Red and IR PPG signals were recorded and analysed on a cycle-by-cycle basis, which showed that as vessel stiffness increased, PPG amplitude decreased. Kruskal–Wallis analysis followed by a Dunn test found this change to be statistically significant ($p < 0.001$). This confirms the hypothesis that PPG signals can indicate changes in arterial stiffness, particularly through amplitude changes. This trend was expected, considering the physiology of blood vessels and PPG. Stiffer vessels are less elastic and therefore less able to expand when the blood pulse wave arrives at the PPG sensor. As PPG detects pulsatile changes in blood volume, and the reduced expansion results in a lower change in the volume of blood at the site, the amplitude of the signal is lower.

CHAPTER 7: INVESTIGATION OF CARDIOVASCULAR HEALTH USING PHOTOPLETHYSMOGRAPHY SENSORS IN A BILATERAL IN VITRO ARTERIAL MODEL

The content in this chapter has been adapted from my paper published at the 2023 IEEE Biosensors Conference, titled 'A Bilateral In Vitro Model for Cardiovascular Disease Investigations Using Photoplethysmography Sensors'.

The work presented in Chapter 7 was part of collaborative research aimed at ensuring the bilateral in vitro cardiovascular model could obtain high-quality PPG signals when integrating the customisable vessel–tissue phantoms into the in vitro model. Accordingly, the purpose of Chapter 7 was to verify that the in vitro system functioned correctly and produced consistent, reproducible measurements.

7.1 Introduction

The experimental work outlined in this chapter was originally inspired by the study by Allen and Murray [110], who used PPG to assess the similarity of pulse waveforms recorded from the right and left sides of the body. This approach laid the foundation for the bilateral in vitro model described in Chapter 5, which integrated two identical branches into the system, replicating the two lower limbs. This design allowed for the insertion of custom fabricated vessel-tissue phantoms, as described in Chapter 6, within each branch and enabled the simultaneous acquisition of PPG signals from both sides.

The primary objective of this experimental study was twofold: (a) to verify that the bilateral in vitro system functioned correctly and could generate high-quality PPG signals while accurately replicating human vasculature; and (b) to confirm that phantoms fabricated with identical formulations demonstrated statistically similar PPG signal features, thereby validating the reliability and reproducibility of the phantom fabrication process. These aims were motivated by findings in Chapter 6, which demonstrated statistically significant differences in PPG signals when vessels with varying properties were assessed.

Therefore, this chapter presents an evaluation of the bilateral in vitro model and its suitability for PPG-based investigations by determining the system's ability to generate consistent PPG waveforms from identical vessel-tissue phantoms. This experimental

work established the foundation for the study described in Chapter 8, which extracted features from various vessel-tissue phantoms for PWA.

7.2 Methods and Materials

7.2.1 Preparation of Identical Vessel-Tissue Phantoms

The fabrication process for producing the identical vessel-tissue phantoms followed the procedure detailed in Chapter 6. However, during the preparation of the elastomers for both the vessel and the surrounding tissue, the quantities of each component in the formulation were doubled and combined in a single batch. This method ensured that the vessels and tissue phantoms were fabricated using an identical formulation, minimising variability introduced by preparing them separately. By eliminating potential inconsistencies arising from differences in mixing, timing, or environmental factors, this approach improved the reproducibility and reliability of the vessel-tissue phantom fabrication. Additionally, to further reduce potential inconsistencies between the identical vessel-tissue phantoms, a single long vessel was fabricated during the dip-coating stage, as shown in Figure 31, and then cut in half. This ensured that both phantoms originated from the same continuous structure, thereby promoting their uniformity.

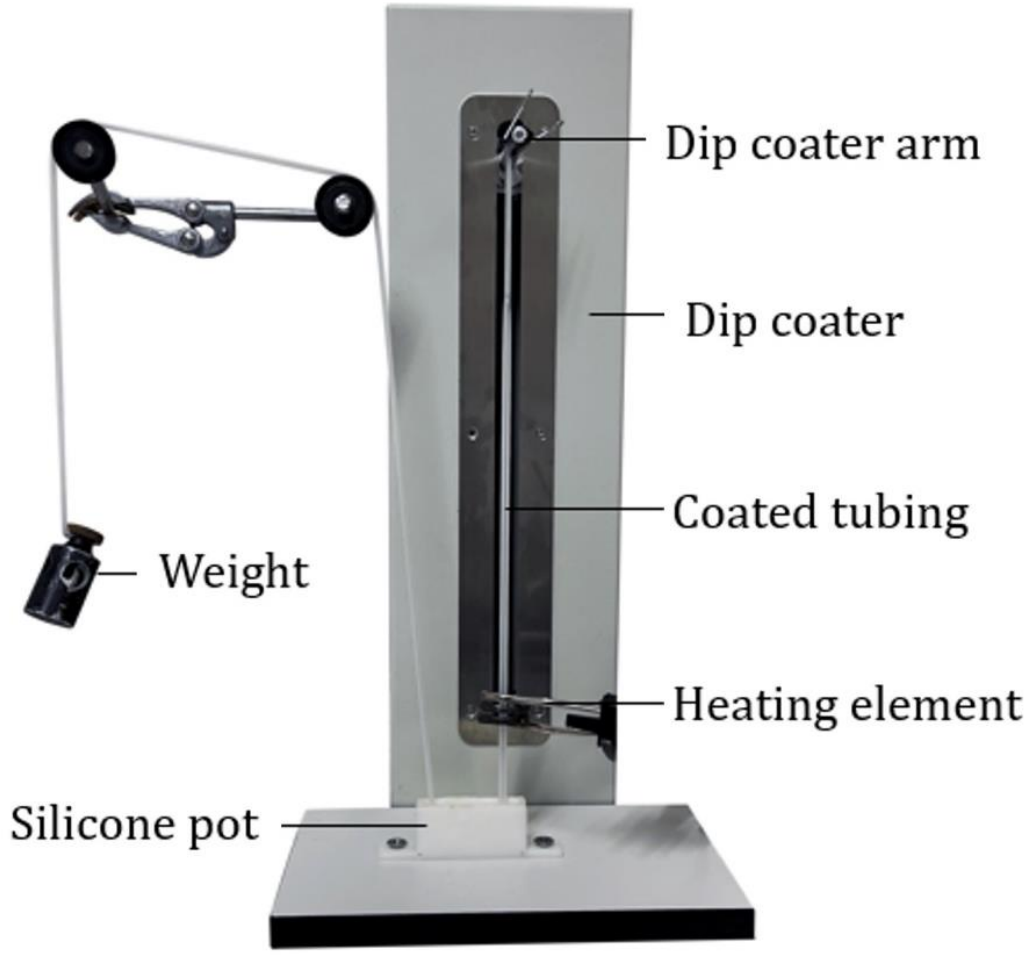

Figure 31: Image reproduced from a paper published at the 2023 IEEE Biosensors Conference [188]. The dip-coating setup, described in Chapter 6, deposits a uniform elastomer layer from the silicone pot onto the commercial silicone tubing (known as the form). The form is secured at one end to the dip coater arm and at the other to a tension weight. During coating, the dip coater arm raises the form to its highest position, creating a long, uniform elastomer coating as it passes through the heating element. After curing, the form is removed from the elastomer layer, isolating the custom fabricated vessel.

7.2.2 Bilateral Cardiovascular Model

The identical custom-fabricated vessel-tissue phantoms were positioned within each branch of the in vitro bilateral vascular model (Figure 32), as detailed in Chapter 5. This bilateral configuration enabled direct comparison between the identical phantoms. Two dual-wavelength PPG sensors, comprising both red and IR light sources, as illustrated in Figure 14, were placed directly beneath each vessel-tissue phantom. To secure the sensors in place and prevent movement, 3D-printed housings were used. This placement enabled continuous measurement of light reflected from the phantoms, allowing simultaneous acquisition and recording of PPG waveforms from both branches of the model. Four-minute recordings were acquired and segmented into 10-second windows.

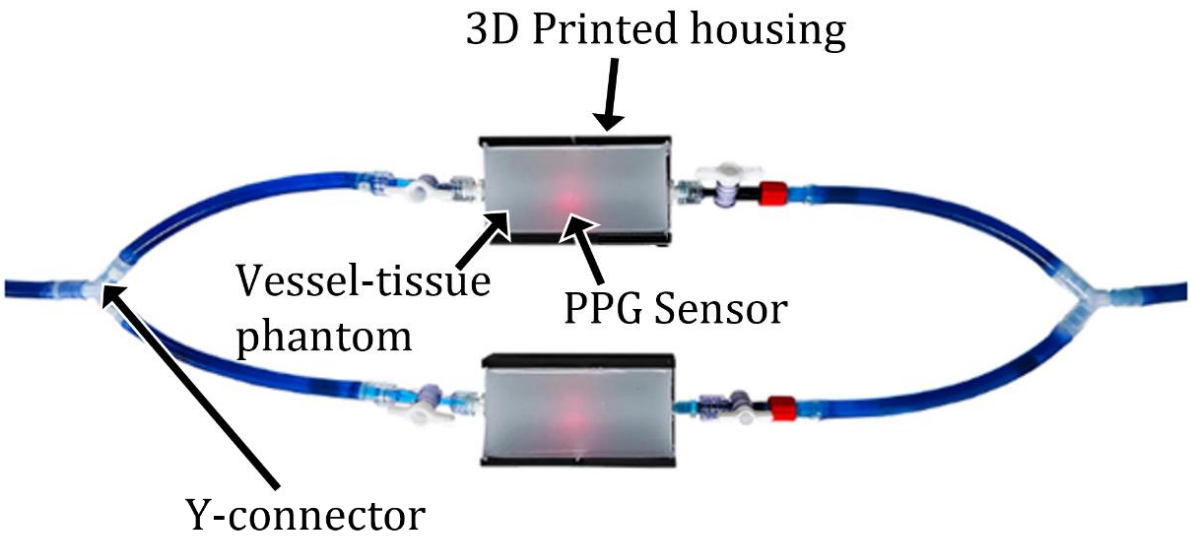

Figure 32: Image reproduced from a paper published at the 2023 IEEE Biosensors Conference [188]. The image illustrates the bilateral configuration in which the identical vessel–tissue phantoms were positioned in each branch of the system. Two dual-wavelength PPG sensors were placed beneath the phantoms to acquire reflectance-mode PPG waveforms. To secure the sensors, 3D-printed housing moulds were used.

The experimental setup used the Model 1423 PBP pulsatile pump, which does not feature an integrated reservoir for the BMF, composed of methylene blue powder dissolved in deionised water. To enable continuous fluid delivery into the system, an external reservoir was elevated above the setup to provide gravitational pressure and compensate for the absence of an in-built fluid source.

7.2.3 Feature Extraction and Statistical Analysis

Morphological features of the recorded PPG waveforms, including peak amplitude, upslope and downslope gradients, and rise and decay times, were extracted to quantitatively assess similarity between the two signals. These features represent the fundamental descriptors of PPG waveform shape [189] and were therefore selected for analysis. This analysis was conducted using a custom Python algorithm developed at RCBE [156]. The feature extraction process was based on geometrically defined points within the waveform, including the identified peaks and troughs, enabling a comparison of signal morphology across the two branches.

To establish the degree of conformity between the PPG signals obtained from the two branches, statistical analysis was conducted using the Kruskal–Wallis one-way analysis of variance. This method was used to test the null hypothesis that the extracted features

from both branches originated from the same population. Given that the vessel–tissue phantoms were fabricated using an identical silicone mixture, it was hypothesised that any observed differences between the samples would be statistically insignificant.

7.3 Results and Discussion

Using MATLAB, the PPG signals acquired from each branch of the in vitro system were filtered and visualised to assess the degree of morphological similarity between the signals produced by each vessel-tissue phantom. As illustrated in Figure 33 for the IR signal, both phantoms generated PPG waveforms with similar morphology, suggesting that the two branches of the system exhibited similar flow dynamics and light–tissue interaction characteristics. Notably, noise artefacts were observed at the systolic peaks of the signals, which may be attributed to mechanical vibrations introduced by the pumping mechanism. The use of a non-mechanical pump may help reduce such artefacts in the future. Additionally, minor differences in signal morphology could be influenced by variations in sensor performance. Although the sensors recorded simultaneously, inter-sensor variability may have introduced slight discrepancies in the acquired signals. Furthermore, the differences observed in Figure 33 for the same wavelength (IR) suggest that the bilateral branches may not be perfectly symmetrical. Minor mismatches in branch compliance may therefore be present, which could lead to differences in waveform morphology. It is also suggested that the use of BMF containing deionised water and methylene blue, which exhibits peak absorption in the red spectral region [188], may contribute to differences between the red and IR signals. It is acknowledged that the waveforms shown in Figure 33 appear less smooth than those obtained in later experiments, which may be attributable to differences in the pulsatile pumping mechanism. In later studies (Chapters 8 through 10), the PD-1100 Pulsatile Pump System was utilised; this change in pump system may therefore account for the observed differences in the acquired PPG signals.

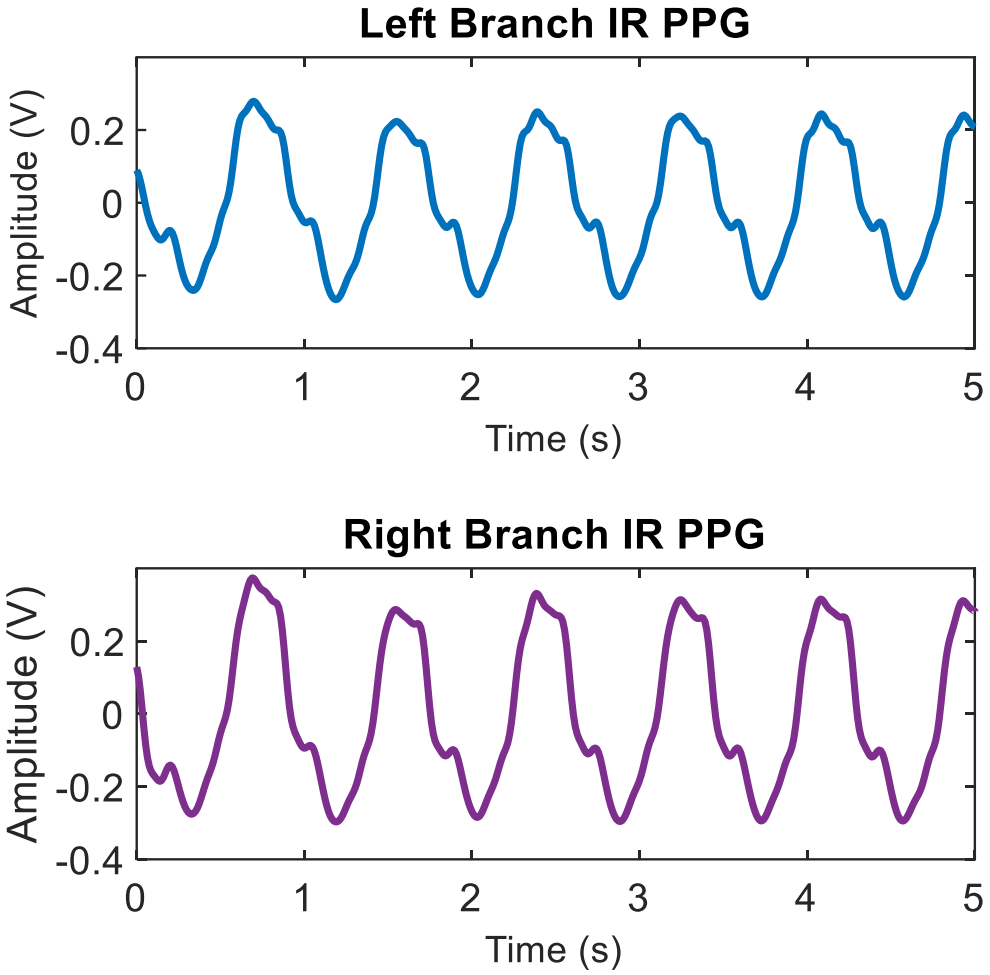

Figure 33: IR PPG signals obtained from each bilateral branch in the in vitro setup, visualised using MATLAB. Image reproduced from a study presented at the 2023 IEEE Biosensors Conference [188].

From the recorded PPG signals, five key morphological features were extracted: amplitude, upslope, downslope, rise time, and decay time. For each feature, a *p*-value was calculated using the Kruskal–Wallis one-way analysis of variance to evaluate statistical similarity between the two branches (right and left). For the IR signal, the range and distribution of values for each feature are shown in the box plots shown in Figure 34. The results indicate that both branches produced morphologically similar PPG waveforms. Specifically, the amplitude, downslope, rise time, and decay time yielded *p*-values greater than 0.05, suggesting no statistically significant difference between the two groups. Based on these findings, it can be concluded that the vessel–tissue phantoms were considered identical within the in vitro setup.

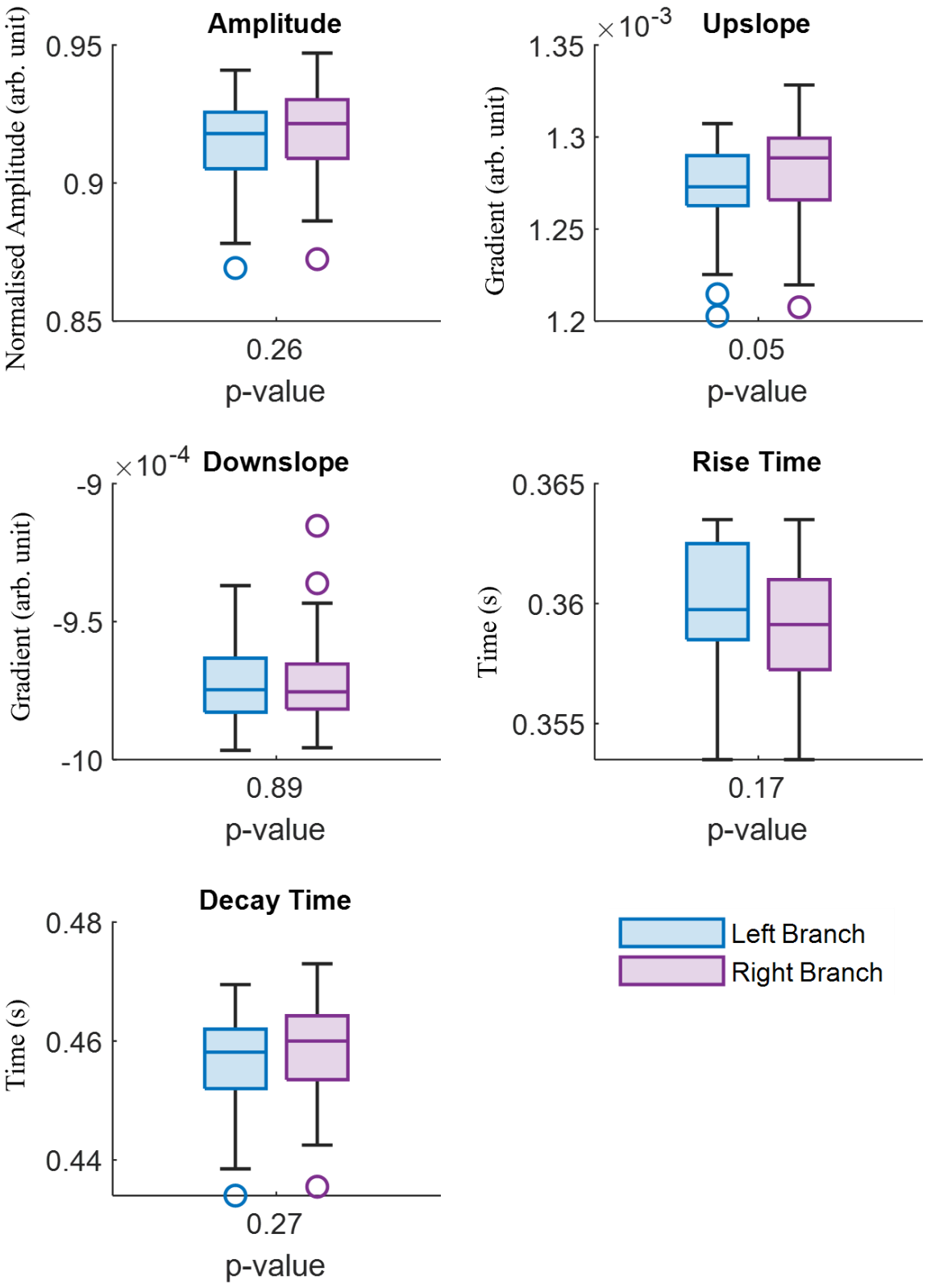

Figure 34: Kruskal–Wallis statistical analysis of IR PPG signals obtained from the two vessel-tissue phantoms (right and left branches), comparing the similarity of each extracted feature. For plots with arbitrary units, axes are labelled as arb. unit. A p-value greater than or equal to 0.05 indicates no statistically significant difference between the phantoms. The box plot taken is reproduced from a paper published at the 2023 IEEE Biosensors Conference [188].

To validate the findings, the experiment was repeated three times, as summarised in Table 13. Consistent with earlier results, the amplitude, downslope, and decay time features demonstrated statistical similarity between the two vessel–tissue phantoms. Rise time, however, was an exception, with many *p*-values below 0.05, indicating a statistically significant difference. It is suggested that inaccuracies in peak detection, potentially due to noise artefacts, contributed to errors in rise-time estimation and consequently to the observed differences.

Furthermore, when comparing signals of the same wavelength across different experimental runs, such as the red signal, variations were observed. These discrepancies may have resulted from external influences, as the experiments were conducted sequentially rather than simultaneously. Environmental factors, including fluctuations in temperature and ambient lighting, may have affected the signal recordings. Nonetheless, the *p*-values generally remained above the 0.05 threshold, supporting the conclusion of statistical similarity. Notably, these variations were less pronounced in the IR PPG signals, suggesting greater stability compared to the red signals.

Table 13: P-values corresponding to red and IR PPG signal features obtained from three repetitions of the experiment. P-values greater than or equal to 0.05 indicate statistical similarity between the two vessel-tissue phantoms. The table has been adapted from a study presented at the 2023 IEEE Biosensors Conference [188].

	Experiment 1		**Experiment 2**		**Experiment 3**	
Feature	**Red**	**IR**	**Red**	**IR**	**Red**	**IR**
Amplitude (arb. unit)	0.84	0.26	0.45	0.68	0.57	0.96
Upslope (arb. unit)	0.38	0.05	0.55	0.08	0.53	0.20
Downslope (arb. unit)	0.57	0.89	0.53	0.56	0.71	0.02
Rise time (s)	0.02	0.17	0.03	0.01	0.03	0.18
Decay time (s)	0.78	0.27	0.45	0.72	0.56	0.95

The study investigated the use of a bilateral in vitro flow rig to compare PPG signals obtained from two identical vessel–tissue phantoms. It is acknowledged that, in the current setup, both the vessel–tissue phantoms and the PPG sensors were positioned within rigid 3D-printed housings to ensure stable and repeatable sensor placement. While this configuration was necessary for experimental control, embedding vessel–tissue phantoms within rigid 3D-printed structures does not replicate human physiology. Therefore, the experiment was limited by the requirement to stabilise the sensors within the moulds. Future designs could integrate sensor housings that more closely resemble the multiwavelength sensor configuration described in Chapter 9 and Chapter 10, in which the sensor is housed without affecting the surrounding tissue boundaries.

Statistical analysis revealed that the majority of extracted features showed no significant differences between the two branches, indicating a high degree of morphological

similarity. Furthermore, in the context of expanding PPG-based vascular ageing assessments, the results suggest that clinicians should consider bilateral measurements. Previous studies have reported inter-limb differences in PPG signals among individuals with PAD, highlighting the importance of examining both limbs in clinical assessments [60]. Similarly, the bilateral in vitro configuration may serve as a useful platform for experimentally simulating and analysing asymmetrical vascular conditions under controlled settings.

7.4 Summary of Chapter 7

The experimental study presented in this chapter explored the use of the in vitro vascular model in a bilateral configuration to investigate the morphological similarity of PPG signals obtained from two identically fabricated vessel–tissue phantoms. The model was designed to simultaneously acquire signals from both branches using dual-wavelength PPG sensors. Key features, namely amplitude, upslope, downslope, rise time, and decay time, were extracted from the recorded PPG signals using a custom Python algorithm, and were statistically compared using Kruskal–Wallis analysis.

The results demonstrated that most features showed no statistically significant differences between the two branches, indicating that the vessel-tissue phantoms were largely identical. Some variability was observed in repeated experiments, especially for the red signal, which may be due to environmental factors and inter-sensor variability, as experiments were conducted sequentially. Nonetheless, the *p*-values generally exceeded 0.05, supporting the hypothesis of statistical similarity between the phantoms.

This chapter demonstrates the reliability of the bilateral in vitro model for generating comparable PPG signals from identical phantoms. The findings support its application in studying vascular symmetry, confirming the model's ability to produce similar signals from identical vessel–tissue constructs. While asymmetry was not directly examined in this study, the results suggest that the bilateral model could be valuable for future investigations into vascular asymmetry, such as differences between healthy and diseased limbs. Furthermore, the results emphasise the clinical relevance of bilateral PPG measurements, particularly where vascular ageing assessments may benefit from examining both limbs due to known inter-limb differences in conditions such as PAD.

CHAPTER 8: ARTERIAL STIFFNESS ASSESSMENT USING PHOTOPLETHYSMOGRAPHY PULSE WAVE ANALYSIS (PWA)

Most of the content in this chapter is adapted from my published paper in Scientific Reports, titled 'Arterial stiffness assessment using PPG feature extraction and significance testing in an in vitro cardiovascular system'. The material presented in Section 8.4 is adapted from my published paper in Photonics, titled 'Feasibility of Photoplethysmography in Detecting Arterial Stiffness in Hypertension'.

While some of the work presented within Chapter 8 was completed in collaboration to assess the correlation between arterial stiffness and a wide range of PPG-derived features, this thesis extended the collaborative work by identifying a subset of four features that could potentially be used to identify arterial stiffness.

8.1 Introduction

The morphology and characteristics of recorded PPG signals are commonly assessed using PWA, a technique that evaluates the shape and features of the pulse waveform [3]. A typical PPG waveform comprises a systolic peak followed by a diastolic peak, with the two separated by a distinct dicrotic notch, as illustrated in Figure 35. However, in older individuals, the diastolic peak is often diminished or absent [190], [191]. Additionally, arterial stiffness, which can result from vascular ageing, can lead to alterations in other morphological features of the waveform when compared to those observed in individuals with a younger vasculature [3].

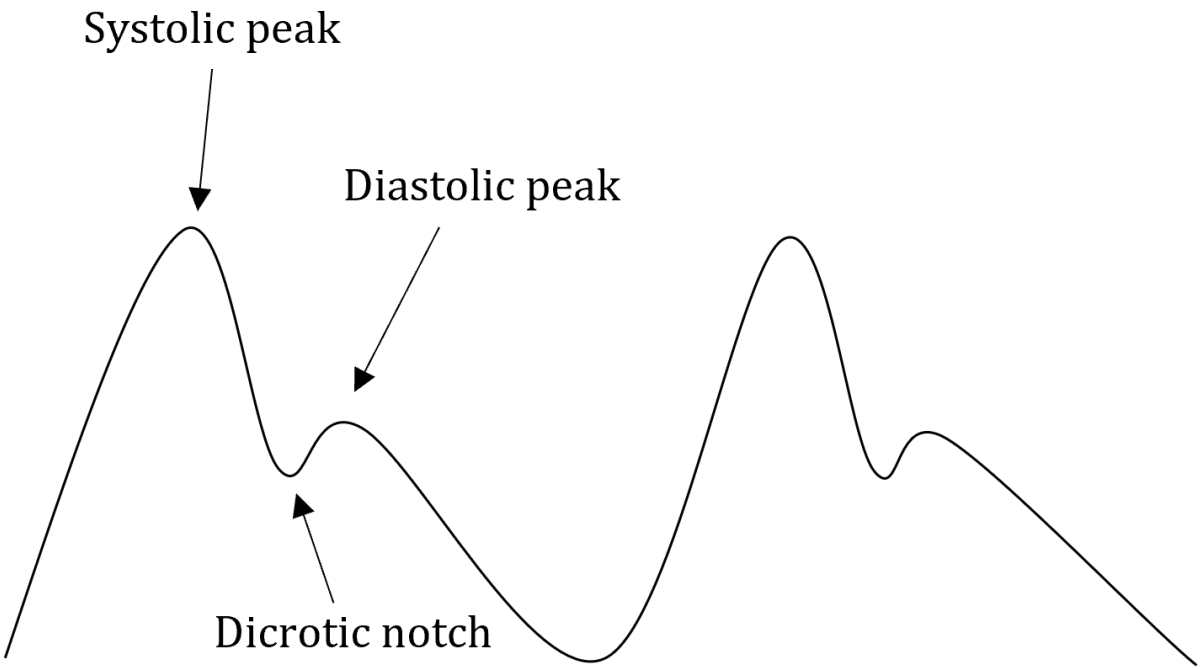

Figure 35: Representative PPG waveform illustrating the systolic peak, diastolic peak, and the dicrotic notch.

To enable future clinical application of PPG, it is essential to identify which waveform features are most strongly associated with vascular ageing, particularly arterial stiffness. This chapter employs feature extraction algorithms that focus exclusively on the systolic peak of the PPG waveform, with the aim of examining its relationship to arterial stiffness. The study utilises a range of customisable vessel–tissue phantoms designed to represent varying elastic properties, rather than simulating a specific artery. This approach enables the evaluation of PPG features across a broader spectrum of arterial stiffness levels before narrowing the focus to those most indicative of vascular ageing. Feature extraction was performed directly on the filtered PPG waveform, without reliance on its derivatives. This choice was made to ensure applicability in scenarios where SDPPG fiducial points are unreliable or absent [192].

The study presented in this chapter utilised the in vitro vascular model in a single-branch configuration to investigate the relationship between arterial stiffness and vascular ageing, as assessed through PPG signals acquired from the system. A range of pulse wave features were examined to evaluate their diagnostic potential and to determine which may be most informative for future applications of PPG-based arterial assessment, particularly in the context of controlled in vitro settings [106], [193], [194]. The experimental investigation was guided by the hypothesis that specific morphological

features of the PPG waveform would exhibit measurable sensitivity to changes in vessel stiffness. Based on the results, a subset of these features was identified and selected for further analysis in Chapter 9 and Chapter 10.

8.2 Methods and Materials

8.2.1 Vessel-Tissue Phantom Selection

Following the vessel-tissue phantom fabrication methodology outlined in Chapter 6, five vessels with varying stiffness levels were produced for this experimental study. The vessels were fabricated by mixing equal parts of Part A and Part B Gel-10, with incremental additions of hardener ranging from 5% to 20% in 5% steps. Regardless of whether a phantom is intended to mimic healthy or diseased femoral arteries, some amount of hardener is required in the Gel-10 mixture to achieve the femoral artery stiffnesses described in the literature [176]. As a result, the chosen range focused on incremental increases in hardener content to span a spectrum of elasticities. Deadener, which reduces stiffness, was not used, as it was not necessary for constructing vessels within the target stiffness range. Mechanical testing using the Universal Testing System yielded Young's Modulus values of 0.52 MPa, 0.60 MPa, 0.64 MPa, 0.78 MPa, and 0.80 MPa.

8.2.2 In Vitro Vascular Model Configuration

As described in Chapter 5, the in vitro flow model was configured to utilise only a single-branch of the bifurcation system. This configuration allowed each vessel to be inserted sequentially into the monitoring area for data acquisition. The PD-1100 Pulsatile Pump System was operated at a constant rate of 60 bpm, and the built-in reservoir was filled with a BMF composed of methylene blue powder dissolved in deionised water. A dual-wavelength PPG sensor, equipped with red (660 nm) and IR (940 nm) LEDs, was positioned beneath the vessel–tissue phantoms to acquire PPG signals. The ZenPPG system, previously detailed in Section 5.3.1 of Chapter 5, was connected to the sensor and configured with a sampling frequency of 2000 Hz [154]. Signal acquisition and real-time visualisation were carried out using LabVIEW software.

8.2.3 Feature Extraction and Statistical Analysis

Using a custom Python script developed at the RCBE [156], key features were extracted and analysed from the recorded PPG signals. These features included upslope and downslope lengths, amplitude, rise and decay times, as well as systolic and diastolic widths, among others. Each vessel recording lasted four minutes and was segmented into 10 second windows, yielding a total of 24 windows per recording. Within each window, signal features were averaged to generate a single data point, resulting in a time series of values for each feature. The extracted features, listed in Table 14, were visualised and analysed using MATLAB.

Table 14: Extracted PPG features used in this experimental study [192].

Feature	Description
AUC	Total area beneath the pulse waveform
Systolic AUC	Area under the systolic portion of the pulse
Diastolic AUC	Area under the diastolic portion of the pulse
AUC Ratio	Ratio of systolic to diastolic area
Rise Time	Duration from trough to peak
Decay Time	Duration from peak to trough
Rise-Decay Time Ratio	Ratio of decay time to rise time
Amplitude	Median pulse amplitude

Feature	Description
Upslope Length	Distance from trough to peak
Downslope Length	Distance from peak to trough
Upslope	Gradient during the rising edge
Downslope	Gradient during the falling edge
Onset-End Slope	Slope from the start to the end of the pulse
Slope Ratio	Ratio of upslope to downslope gradients
Length-Height Ratio	Pulse width-to-height ratio
Slope Length Ratio	Ratio of upslope length to downslope length
Upslope Length Ratio	Proportion of total length in the rising phase
Downslope Length Ratio	Proportion of total length in the falling phase
Start Datum Area	Area between waveform and rising tangent
End Datum Area	Area between waveform and falling tangent

Feature	Description
Datum Area Ratio	Ratio of systolic to diastolic datum areas
Maximum Start Datum Difference	Maximum distance between the PPG signal and the rising tangent
Maximum End Datum Difference	Maximum distance between the PPG signal and the falling tangent
Median Start Datum Difference	Median distance between the PPG waveform and the rising tangent
Median End Datum Difference	Median distance between the PPG waveform and the falling tangent
Pulse Width	Full width at 50% of peak amplitude
Systolic Width	Width of the systolic phase at 50% height
Diastolic Width	Width of the diastolic phase at 50% height
Width Ratio	Ratio of systolic to diastolic width
Variance	Signal dispersion from the mean
Skewness	Asymmetry of the pulse waveform
Kurtosis	Sharpness of the pulse

Feature	Description
SNR	Relative signal strength to noise
Zero-Crossing Rate	Frequency of zero-value crossings
Peak-To-Instantaneous Ratio	Change in amplitude over time

Once the features were extracted, statistical analysis was performed using cross-correlation to assess the relationship between each feature and arterial stiffness. This analysis produced Pearson correlation coefficient values, which were used to rank the features based on the strength of their linear association with arterial stiffness [195].

8.3 Results and Discussion

To examine the effects of varying arterial stiffness, red and IR PPG signals, along with their corresponding pressure waveforms, were recorded from the custom vessels. Figure 36 shows an example of the red PPG recording. The stiffer vessel, with a Young's modulus of 0.8 MPa, yielded lower systolic and diastolic amplitudes compared to the softer vessel, which had a Young's modulus of 0.6 MPa. The systolic and diastolic peak amplitudes of the softer vessel were 0.71 V and 0.21 V, respectively, whereas the stiffer vessel displayed corresponding peaks of 0.32 V and 0.13 V. The recorded pressure waveforms were consistent with the characteristics of a typical pressure pulse wave [196]. The visual representation demonstrates that the vessels fabricated using the dip-coating procedure described in Chapter 6 along with the in vitro vascular system, are capable of successfully replicating human PPG waveforms, including the systolic and diastolic peaks as well as the dicrotic notch. A greater reduction in systolic amplitude was observed compared to the diastolic peak when comparing the soft and stiff vessels. The reduction in amplitude may be explained by the physiological behaviour of blood flow and PPG signal acquisition, whereby stiffer arteries are less able to expand. As a result, a smaller change in blood

volume occurs within the monitored region, leading to a PPG signal with lower amplitude [197].

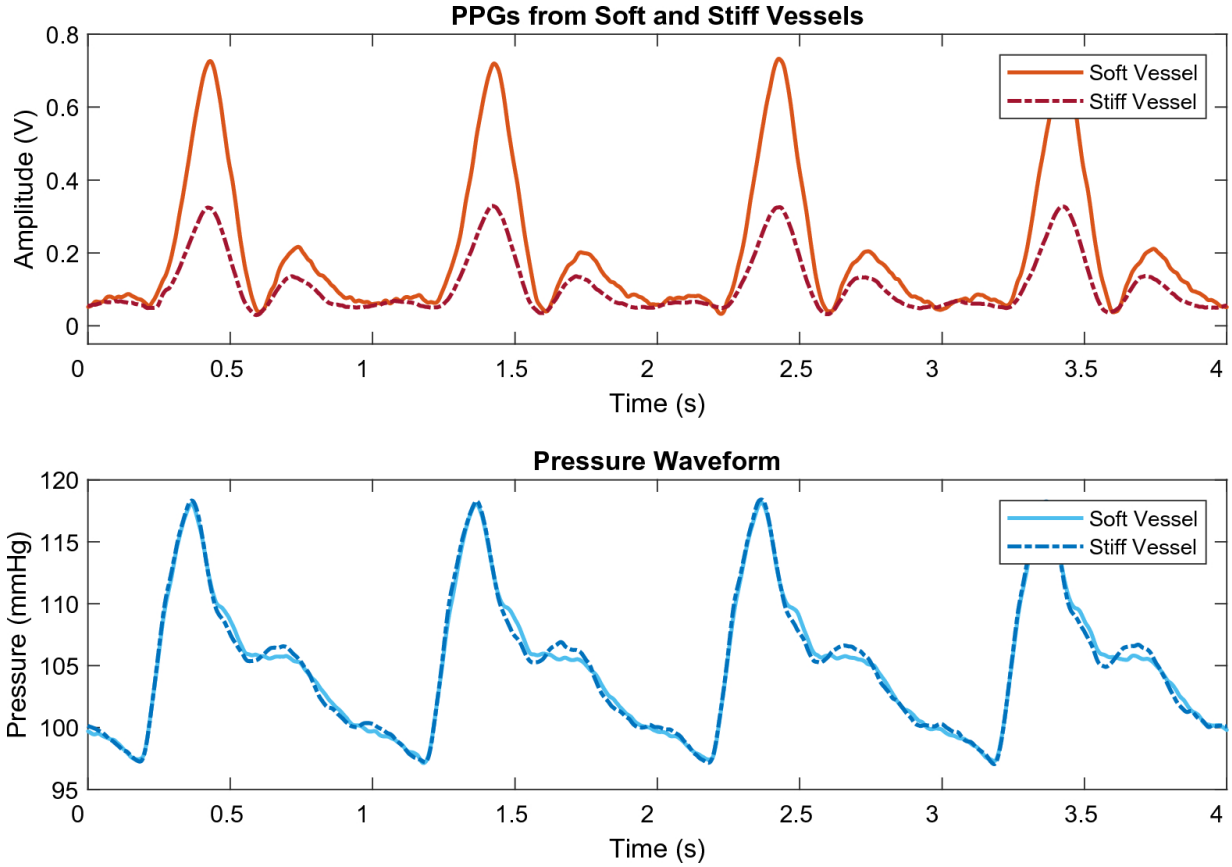

Figure 36: Red PPG signals (top) and corresponding pressure waveforms (bottom) recorded from two vessels with differing stiffness: a softer vessel with a Young's modulus of 0.6 MPa and a stiffer vessel with a Young's modulus of 0.8 MPa [192]. The stiffer vessel showed a reduced PPG amplitude relative to the softer vessel, while the pressure waveforms remained closely matched despite the difference in stiffness.

Signal features were extracted to assess additional morphological differences, including rise and decay times, upslope and downslope lengths, and pulse widths. The overall distribution and range were illustrated using box plots, as shown in Figure 37, while the mean value of each feature was calculated and visualised using line plots, as shown in Figure 38. General trends were observed from these plots. For instance, the AUC demonstrated a negative correlation with increasing arterial stiffness, while the skewness and kurtosis features showed a positive correlation for both red and IR PPG signals. As previously discussed, increased vessel stiffness is associated with a reduction in PPG amplitude. This reduction is also expected to influence other characteristics of the PPG waveform; specifically, a decrease in amplitude is typically accompanied by a corresponding reduction in the AUC and pulse width [198]. Comparing related

morphological features to identify consistent trends offers a means of validating the feature extraction algorithm. When one feature reliably predicts changes in another, such as a decrease in AUC coinciding with a reduction in pulse width, it provides evidence that the extraction algorithm is functioning as intended.

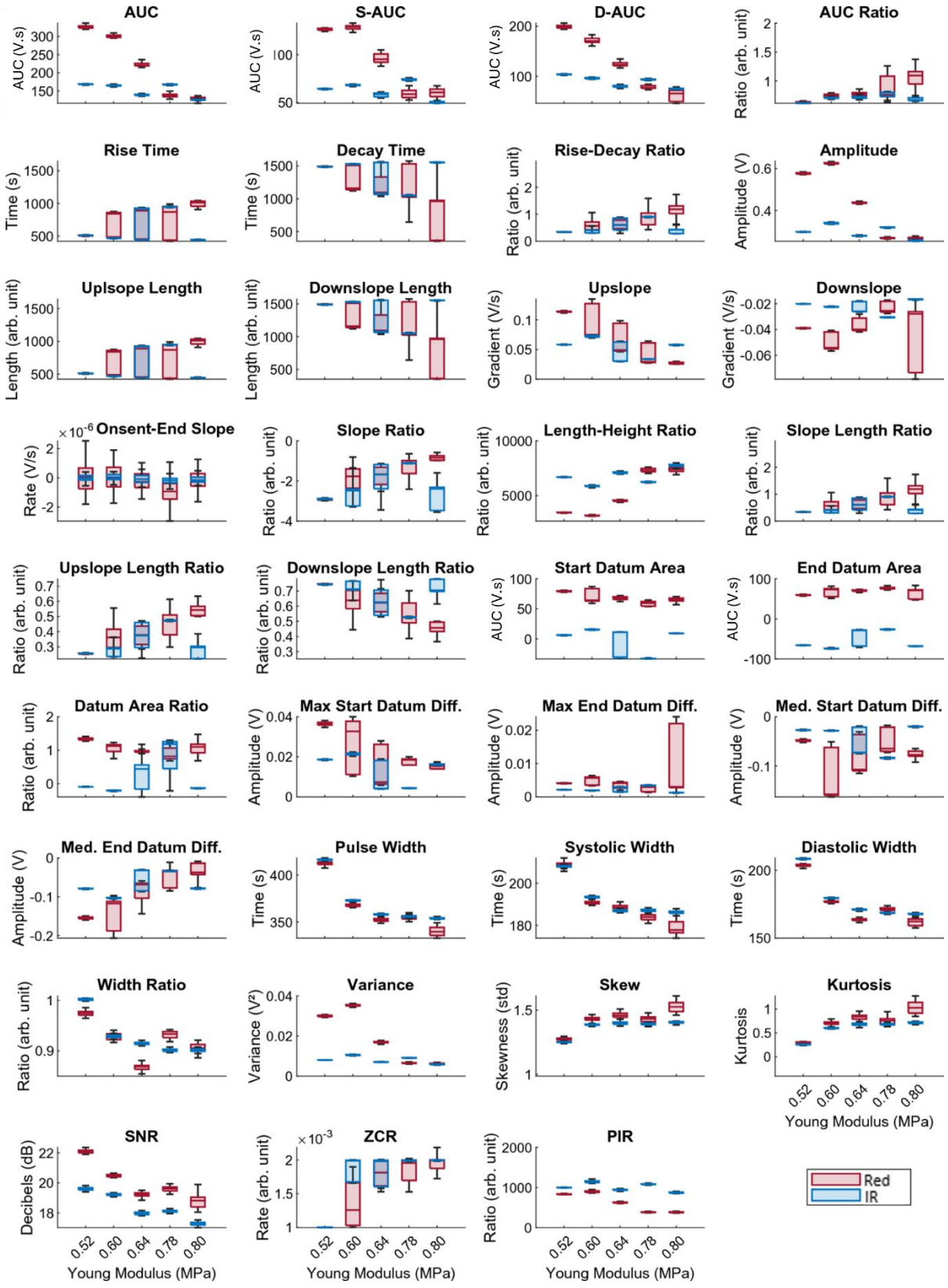

Figure 37: Distribution and range of red and IR PPG signal features across increasing vessel stiffness, presented as box plots for five vessels with Young's moduli of 0.52 MPa, 0.60 MPa, 0.64 MPa, 0.78 MPa, and 0.80 MPa [192].

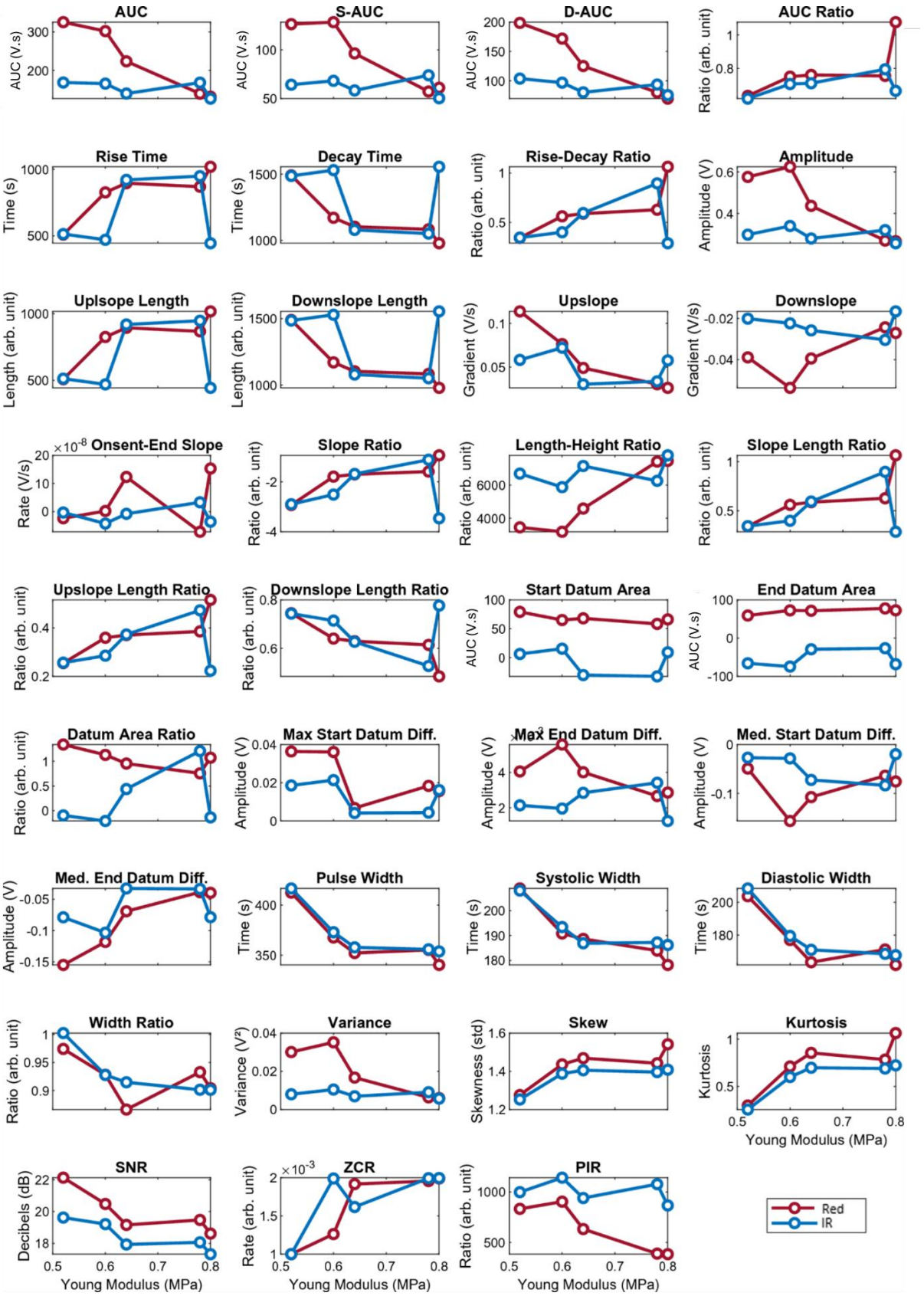

Figure 38: Trends in red and IR PPG signal features in relation to increasing arterial stiffness, measured across five vessels with Young's moduli of 0.52 MPa, 0.60 MPa, 0.64 MPa, 0.78 MPa, and 0.80 MPa. Changes in feature values are presented as line plots, showing the mean values [192].

With increasing vessel stiffness, it was anticipated that amplitude, AUC, and pulse widths (both systolic and diastolic) would decrease, reflecting a negative correlation. This trend is evident in the red PPG signal across both the line and box plots, thereby supporting the validity of the feature extraction process. In contrast, the IR signal showed a weaker correlation for amplitude and AUC, suggesting reduced sensitivity to morphological changes in these features. However, the pulse width in the IR signal followed a similar trend to that of the red signal, displaying a more pronounced negative correlation. This may indicate that the IR signal is less responsive to morphological variations, potentially due to factors such as the absorption spectra of the BMF (specifically methylene blue), the penetration depth of the wavelengths, or the placement of the PPG sensor. Further investigation is required to determine the underlying cause. Based on the box plots (Figure 37), features related to area, amplitude, and width, as well as indices such as skewness, kurtosis, and SNR, demonstrated the greatest stability. These features exhibited noticeable changes between stiffness levels while maintaining low variation within each vessel, suggesting that indices can be used in conjunction with geometrical features for more reliable arterial stiffness assessment.

To quantitatively assess the relationships between signal features and arterial stiffness, including those not immediately apparent from visual plots, the Pearson correlation coefficients were calculated. These coefficients were ranked and presented in Figure 39 for each wavelength (red and IR). Rise time was hypothesised to show a strong correlation with arterial stiffness. However, although rise time showed evidence of an association with stiffness in both the red and IR signals, this feature did not rank highly overall. Additional experiments are necessary to validate the ranking of extracted features. Nonetheless, rankings based on correlation coefficients can help identify the most reliable PPG features for assessing arterial stiffness, offering value in both in vitro and in vivo contexts. Figure 39 highlights a notable relationship between arterial stiffness and the area of PPG waveforms, with AUCs ranking highest among the red PPG features. Notably, these features are less prominent in the IR signal rankings, highlighting the benefits of using more than one PPG wavelength to enable comparative analysis, as certain wavelengths may perform better than others. In the case of the IR signal, pulse width features were more strongly correlated, suggesting that different wavelengths are influenced differently by changes in arterial stiffness. Future work should explore which

features are most strongly correlated with arterial stiffness across additional PPG wavelengths, such as green light.

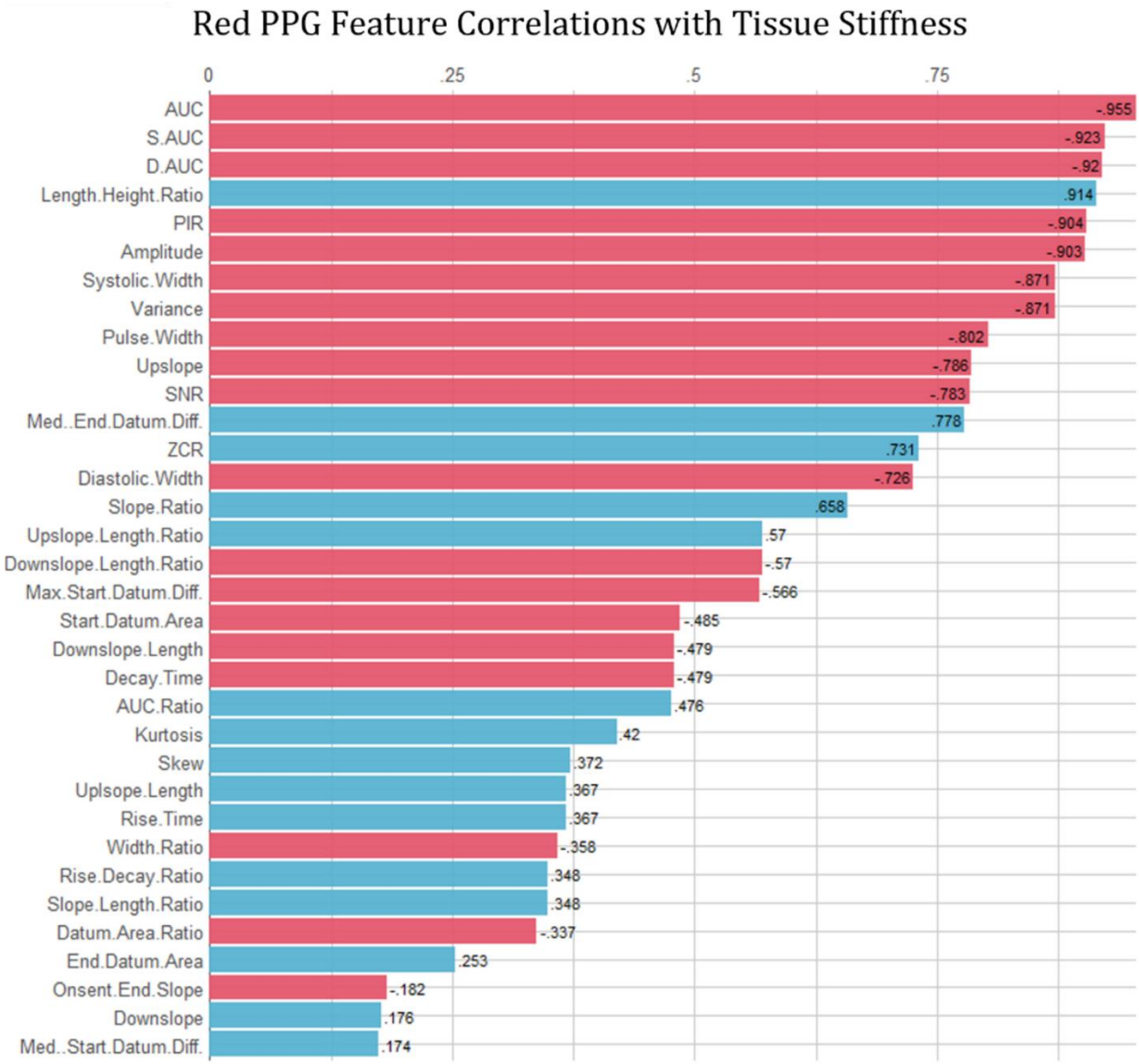

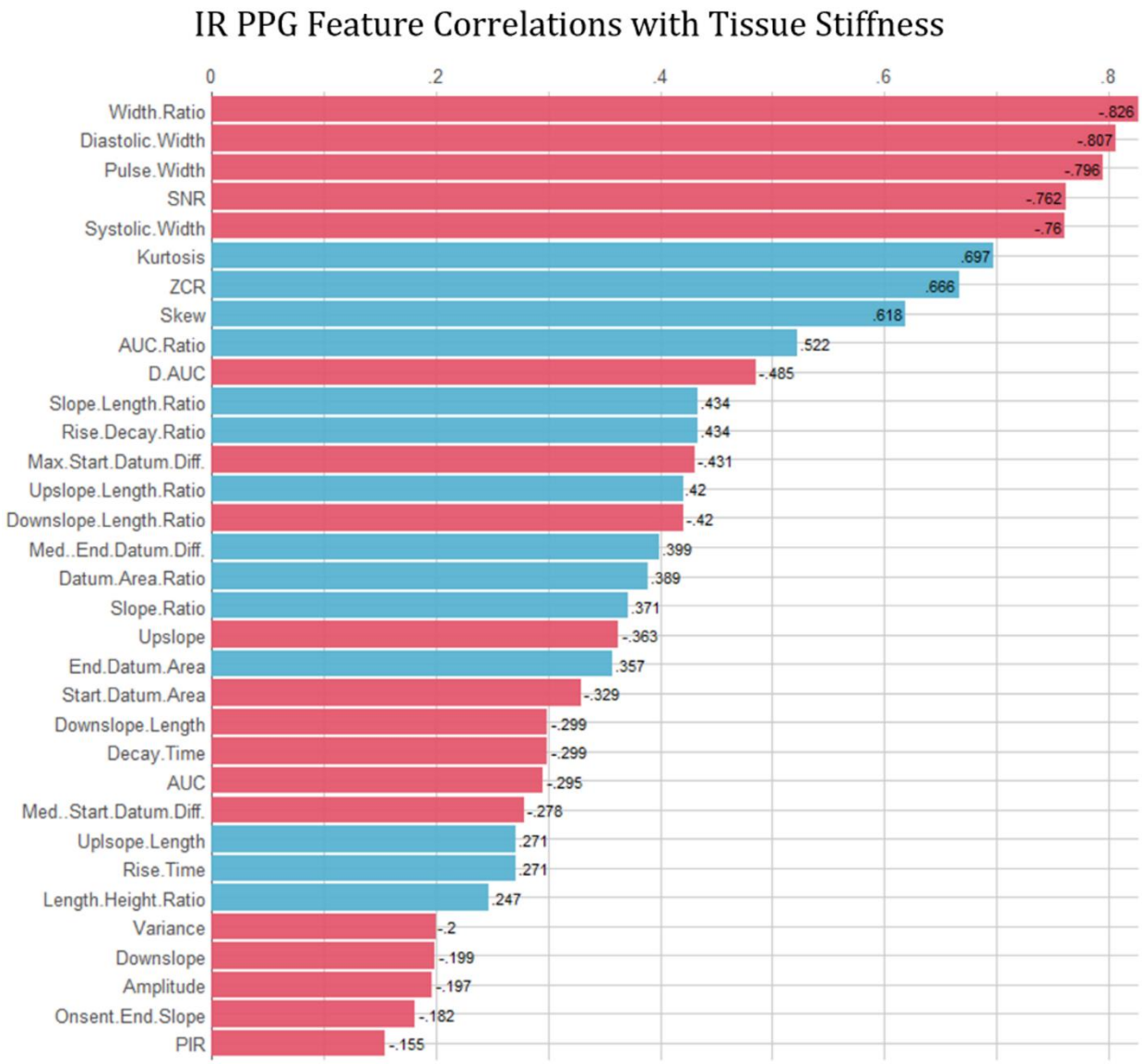

Figure 39: Extracted red and IR PPG signal features ranked by their Pearson correlation coefficient with arterial stiffness. Correlation magnitudes are presented as a screening metric to highlight candidate features for subsequent experiments. Blue bars represent positive correlations, while red bars indicate negative correlations [192].

8.4 Selection of Key Photoplethysmography Features Selected for Further Analysis

Based on the correlations between PPG features and arterial stiffness discussed in this chapter, four primary features were selected for analysis in Chapter 9 and Chapter 10. This reduced feature set was intended to test whether a small number of complementary metrics could capture stiffness-related changes in the PPG waveform, or whether additional or alternative descriptors would be required. Accordingly, the selected features were chosen to represent distinct aspects of waveform morphology: signal

magnitude (amplitude), volume-related behaviour (AUC), waveform shape (median upslope-to-downslope ratio), and waveform sharpness (median end datum difference).

The first feature, amplitude, defined as the maximum peak value of the normalised signal, was chosen (see Figure 40). With increased vessel stiffness, it is expected that the vessels will expand less, resulting in a lower volume of blood in that area. In unhealthy, stiff vessels, it is expected that more photons will be detected by the photodetector, indicating that fewer photons are absorbed. Therefore, a lower amplitude should be observed with increasing stiffness. In addition, the AUC was selected as another key feature, as shown in Figure 40. With increased vessel stiffness, a lower amplitude is anticipated, leading to a corresponding reduction in the AUC value. The third feature, the median upslope-to-downslope ratio, can be used as an indicator of vascular ageing. Figure 40 illustrates how the upslope-to-downslope ratio is calculated from the upslope and downslope lengths. A decrease in the median upslope-to-downslope ratio may suggest vascular stiffness and reduced elasticity. The more negative this ratio is, the less steep the upslope (or rising phase) becomes compared to the downslope (the falling phase). This suggests impaired elasticity and increased stiffness, as vascular ageing leads to vessels becoming less able to expand.

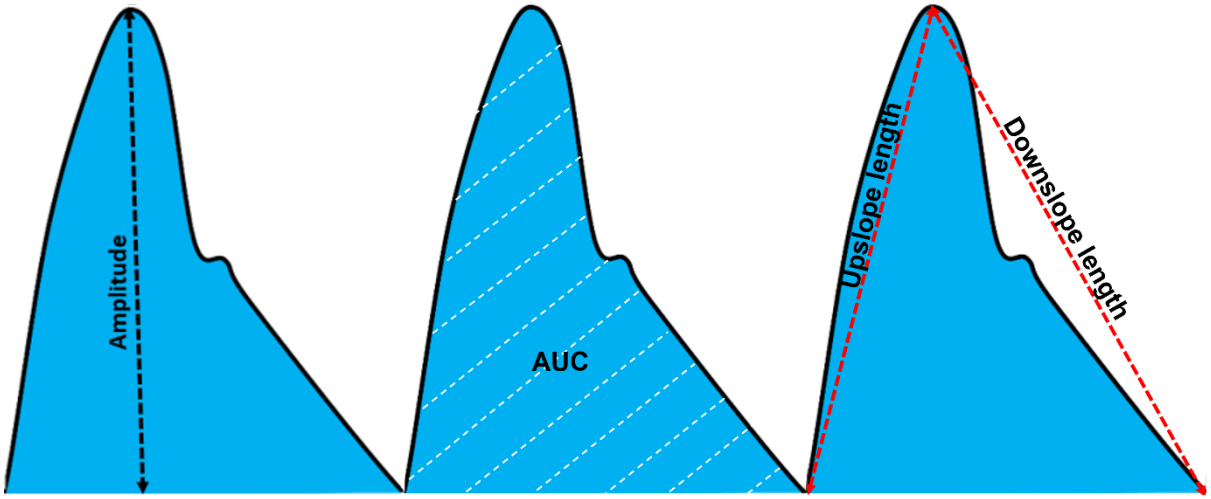

Figure 40: A PPG waveform illustrating key signal characteristics. The amplitude, represented by a dotted black line, is defined as the distance from the baseline to the maximum peak of the signal. The area under the curve (AUC) is depicted using dotted white lines. Additionally, the upslope and downslope lengths, indicated by red dotted lines, define the ascent and descent of the waveform, allowing for the calculation of the upslope-to-downslope ratio [59].

The fourth feature, the median end datum difference, examines the median length between the PPG signal and the peak-trough tangent [192]. When this value is negative, it indicates that the signal has decreased from the start to the end. An increase in this feature may suggest vascular stiffness, as it can imply that the signal has become sharper.

8.5 Summary of Chapter 8

This chapter used PWA techniques to investigate features extracted directly from filtered PPG signals, without reliance on derivatives, to determine which features were most strongly correlated with arterial stiffness. This approach is intended to guide future research towards prioritising key features in the assessment of arterial stiffness, which is a key indicator of vascular ageing.

The experimental study involved the use of custom vessels with varying elasticities, rather than vessel–tissue phantoms, to isolate and examine the direct impact of vessel stiffness on PPG signals. A dual-wavelength PPG sensor, consisting of red (660 nm) and IR (940 nm) light sources, was used to acquire signals. Features were extracted specifically from the systolic portion of the waveform to assess morphological changes across vessels of increasing stiffness.

Cross-correlation analysis was conducted between each feature and vessel stiffness, and Pearson correlation coefficients were calculated to quantify and rank the strength of these relationships.

It was found that red PPG signals demonstrated the most pronounced changes in area-related features, such as amplitude and AUC, with increasing stiffness. In comparison, IR PPG signals showed weaker correlations in area-related features while demonstrating stronger trends in pulse width-related features. These findings suggest that different wavelengths respond differently to changes in arterial stiffness. Importantly, the variation between wavelengths highlights the advantage of multi-wavelength PPG measurements, as depending on the specific morphological feature being assessed, certain wavelengths may demonstrate greater sensitivity. It may therefore be beneficial to use multiple wavelengths in parallel to optimise arterial stiffness assessment. Additional wavelengths commonly used in PPG, such as green light, should also be investigated to determine which features exhibit the strongest correlations with arterial stiffness at each wavelength.

Based on the findings, four key features were selected for further analysis in the experimental investigations presented in Chapter 9 and Chapter 10. These features were: amplitude, AUC, median upslope-to-downslope ratio, and median end datum difference. It is hypothesised that, with vascular ageing and the associated increase in arterial stiffness, amplitude, AUC, and the median upslope-to-downslope ratio will decrease, while the median end datum difference will increase.

CHAPTER 9: Feasibility of Photoplethysmography in Detecting Arterial Stiffness in Hypertension

The content in this chapter has been adapted from my paper published in Photonics, titled 'Feasibility of Photoplethysmography in Detecting Arterial Stiffness in Hypertension'.

The work presented in Chapter 9 was completed solely for the purpose of this thesis to assess the feasibility of using PPG to monitor arterial stiffness under different BP conditions.

9.1 Introduction

High BP, also referred to as hypertension, stands out as a prevalent risk factor for CVD [199]. Hypertension can be influenced by various environmental factors, including smoking and alcohol consumption, as well as by age and genetic predisposition [200]. Roughly 47% of global coronary heart diseases are linked to high BP [201], emphasising the significance of exploring the relationship between hypertension and CVD.

The study presented in this chapter builds on the vessel–tissue phantom fabrication process outlined in Chapter 6, specifically utilising the phantoms described in Section 6.6, and aims to simulate varying BP (high, normal, and low) in the controlled in vitro study (as described in Chapter 5) to examine vascular ageing. The three types of vessels, namely healthy, intermediate, and unhealthy, were introduced, with properties closely matching those of human femoral vessels. Each vessel was subjected to different BP conditions to unravel the link between PPG signal morphology and BP fluctuations during vascular ageing, with the hypothesis that stiffness related to CVDs, such as PAD, may be detectable under higher BP states.

While previous studies have used PPG to assess vascular health, many rely on in vivo data [119], [123], [125], which introduces biological variability and limits reproducibility. In contrast, this study offered a reproducible in vitro framework that allowed for the independent variation of vessel properties and BP levels. Furthermore, this study analysed fiducial points from the SDPPG to evaluate the potential utility of SDPPG in assessing arterial stiffness in the context of vascular ageing. The novelty of this work lies in its integration of physiologically realistic artificial vessels within a controlled in vitro system, allowing for the precise manipulation of BP conditions.

9.2 Methodology

9.2.1 Materials

As outlined in Chapter 6, particularly Sections 6.6 and 6.6.1, three vessel–tissue phantoms were fabricated to replicate the mechanical properties of human femoral arteries [152], [176]. The first phantom incorporated a vessel with a Young's modulus of 0.82 MPa, representing a healthy femoral artery. A second phantom was designed to mimic an atherosclerotic (unhealthy) femoral artery, with the embedded vessel having a Young's modulus of 2.06 MPa. The third, representing an intermediate stage between healthy and unhealthy states, had a vessel with a Young's modulus of 1.48 MPa.

The elastic properties of the vessels were characterised using a Universal Testing System configured for tensile testing in accordance with ASTM D412-16 [173]. As described in Section 6.6, the ID and OD of the embedded vessels were measured at 2.95 mm and 3.96 mm, respectively.

9.2.2 In Vitro Model

The phantoms were inserted into the in vitro vascular system described in Chapter 5, using the BMF fluid formulated from the ingredients detailed in Section 5.2. This fluid comprised of deionised water, Indian Ink, Wright stain, and Congo red powder. It was circulated throughout the system using a PD-1100 Pulsatile Pump operating at 66 bpm. A reflectance-mode PPG sensor (described in Section 5.3), equipped with three wavelengths (green at 530 nm, red at 655 nm, and IR at 940 nm), was positioned above the phantom to capture the signals, as shown in Figure 41, and recorded as illustrated in the example in Figure 42. This sensor was interfaced with a PPG acquisition system, operating at a sampling frequency of 2000 Hz, developed by RCBE [155]. The light intensity of the sensor was determined by the current of three LEDs integrated into the PPG sensor, which were set to 40 mA.

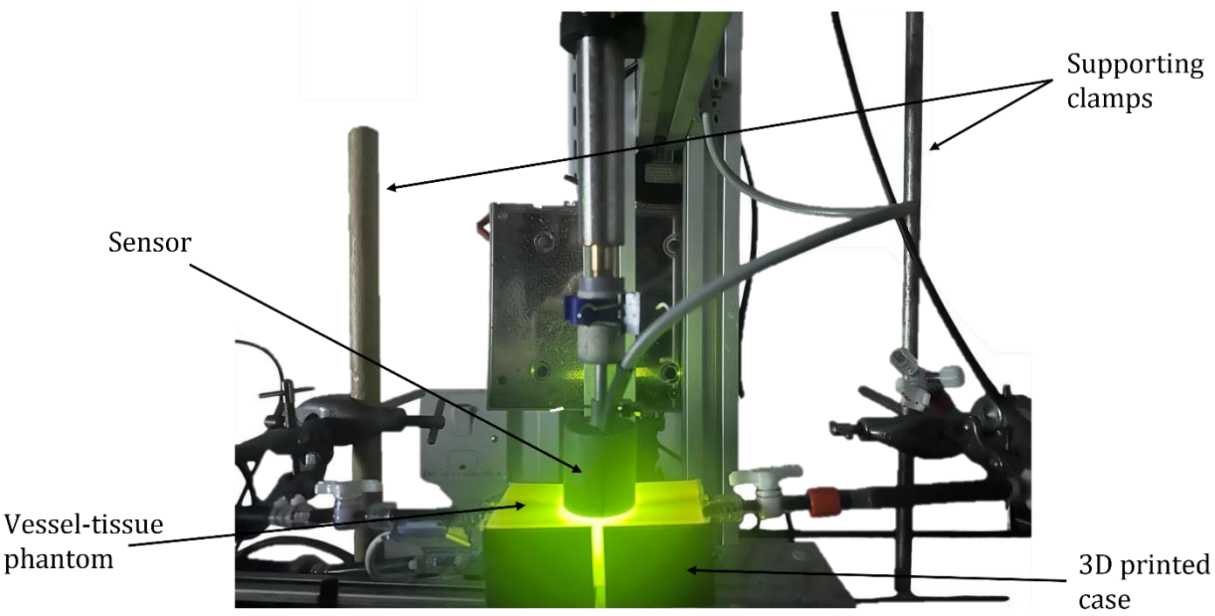

Figure 41: Reflectance sensor setup. The sensor was placed above the phantom during the experimental procedure. The vessel-tissue phantom was held securely in place using a 3D-printed case. Supporting clamps were arranged to maintain stability during the experiment. This experiment was performed using the single-branch configuration [59].

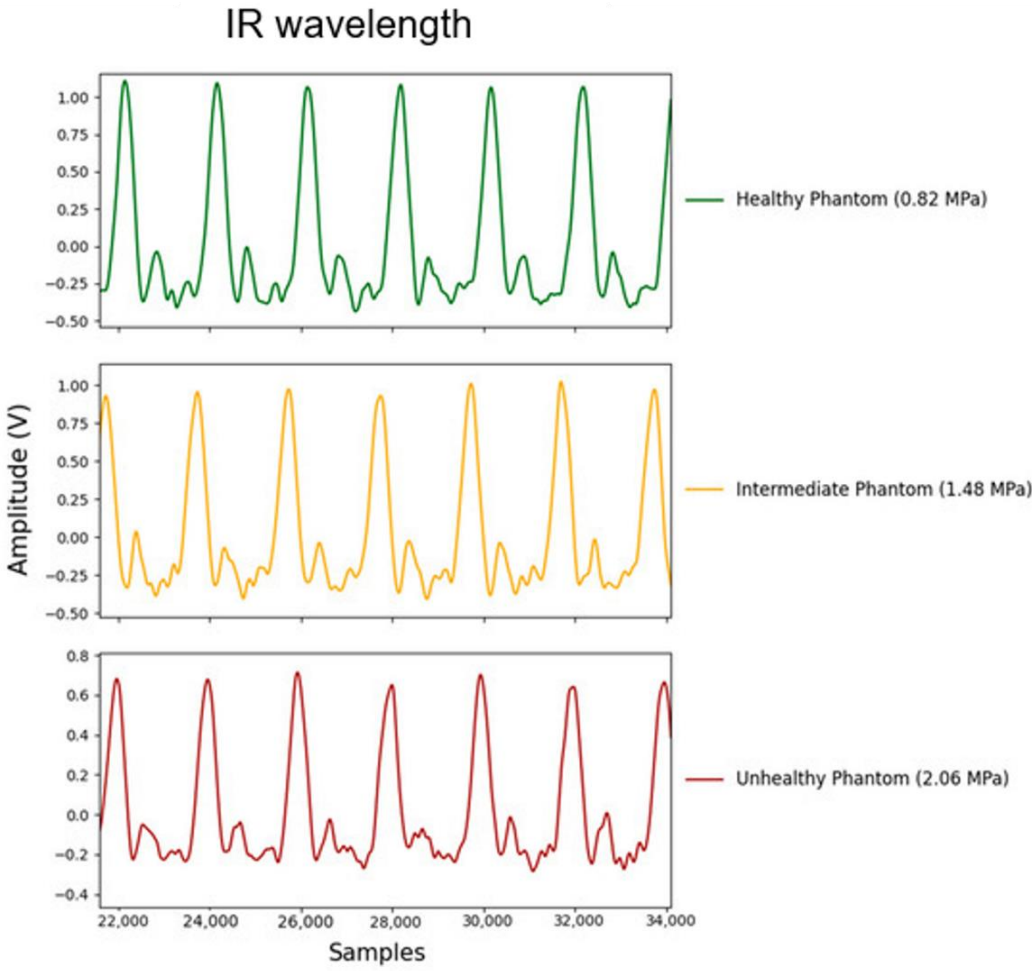

Figure 42: Recorded PPG signals from phantoms with varying Young's Moduli: 0.82 MPa, 1.48 MPa, and 2.06 MPa. Recordings were obtained under normotensive conditions using the IR wavelength [59].

9.2.3 Determining Blood Pressure Values

To stabilise the BP values, categorised as high, low, and normal, a pressure sensor was connected at the beginning of the return flow branch. Variations in BP were induced by the pulsatile pump, generating pressure waves. A clamp was placed on the return branch to modulate system pressure, allowing precise control to reach the target BP levels. The pump itself featured an adjustable resistance clamp, which was fine-tuned to maintain the desired pressure. Additionally, a second pressure sensor was positioned within the setup, before the phantom, to record pressure levels prior to the phantom. BP values ($\frac{Systolic}{Diastolic}$ mmHg) were pre-set at the beginning of each run of the protocol. The hypertensive state was defined as $\frac{148}{113}$ mmHg, the normotensive state as $\frac{121}{87}$ mmHg, and the hypotensive state as $\frac{85}{59}$ mmHg. These values were carefully adjusted to closely replicate BP ranges reported in the literature [202], [203].

9.2.4 Feature Extraction and Statistical Analysis

Once the signals were recorded, relevant features were extracted based on the selection presented in Chapter 8 Section 8.4. The extracted features included signal amplitude, AUC, median upslope-to-downslope ratio, and median end datum difference.

In this study, features extracted from vessels with varying elastic moduli (0.82 MPa, 1.48 MPa, and 2.06 MPa) were analysed to determine whether statistically significant differences existed among them, using the Kruskal-Wallis test (described in Chapter 6, Section 6.4.2), with significance defined as $p < 0.05$ [204]. The analysis aimed to determine whether the extracted features could differentiate between healthy and unhealthy vessels, and to assess the degree to which the intermediate elasticity condition aligned with either group or presented distinct features of its own.

9.2.5 Second Derivative of Photoplethysmography

Numerous studies have examined the SDPPG, illustrated in Figure 43, as a potential tool for monitoring arterial health conditions [189], [205]. Fiducial points are distinct features on the waveform that facilitate analysis. Specifically, the fiducial point *a* corresponds to the maximum peak during the systolic phase of the SDPPG. The point *b* represents the subsequent minimum peak following the *a*-peak, while *c* is identified as the next positive peak after *b*. The point *d* is characterised as the first negative peak occurring after the *c*-peak, and *e* marks the onset of the diastolic component of the waveform.

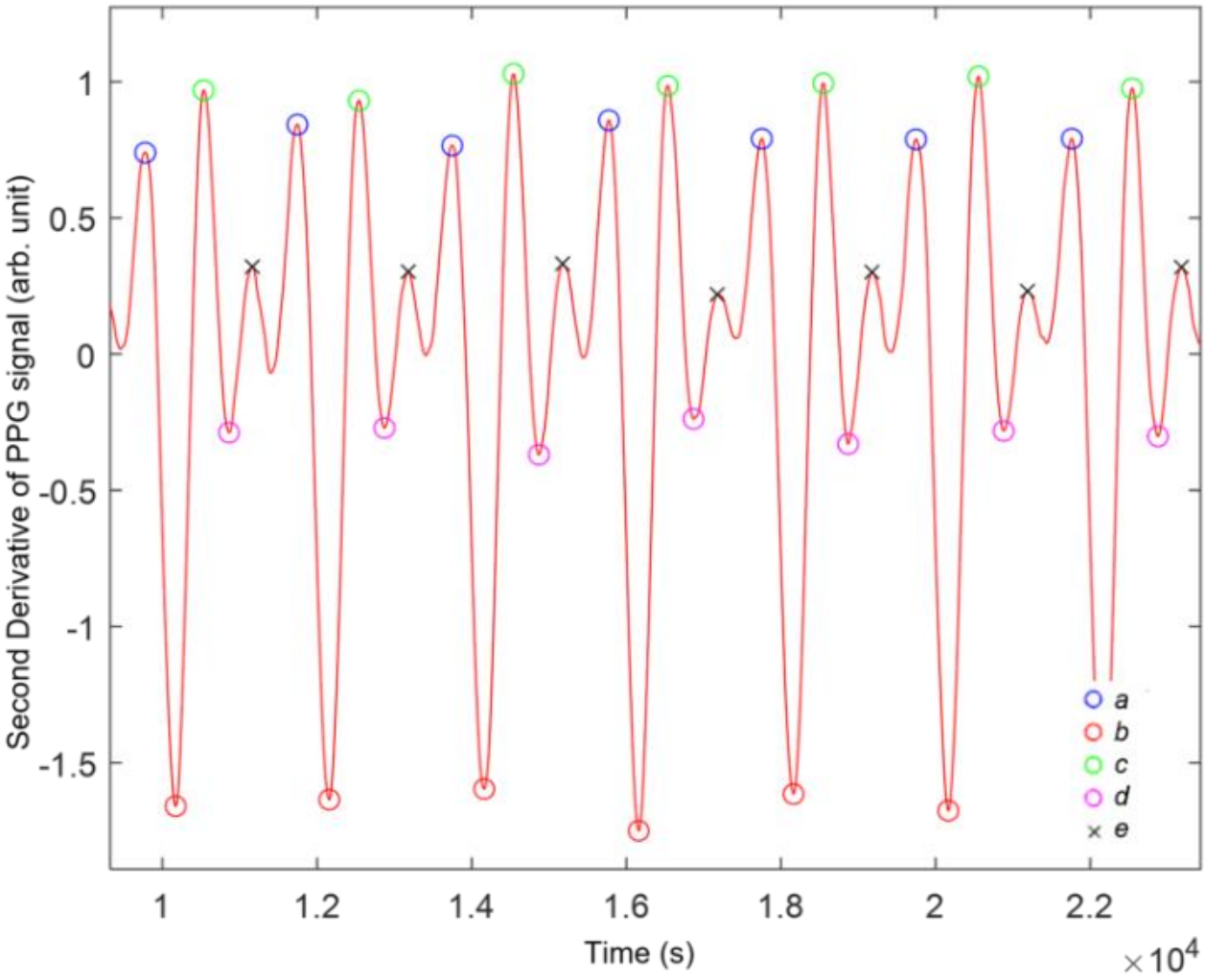

Figure 43: An example of the second derivative of the photoplethysmography signal (SDPPG) is shown, with the filtered signal depicted as a solid red line. The fiducial points (a, b, c, and d) are marked with blue, red, green, and magenta circles, respectively. The fiducial point e is represented by a black cross [59].

9.3 Results and Discussion

9.3.1 Analysis of Extracted Features

Signals were acquired from each phantom, the healthy, intermediate, and unhealthy, across three different health categories: hypertensive, normotensive, and hypotensive. A total of nine data sets were recorded for the study. Using a custom Python script (version 3.12.3) developed by RCBE [156], the key features were selected and extracted from the recorded signals.

The features for the three vessel phantoms (healthy, intermediate, and unhealthy) were extracted and presented in a box plot for the normotensive state, as illustrated in Figure 44. The four features followed expected trends, showing a progressive decrease from healthy to unhealthy vessels, with the exception of the median end datum difference, which increased as anticipated. However, the red PPG signal for the intermediate vessel exhibited an unexpectedly higher median amplitude compared to that of the healthy vessel. This deviation from the anticipated pattern, where healthier vessels typically display stronger signal responses, raises concerns about the extent to which PPG monitoring can effectively differentiate between healthy, intermediate, and unhealthy vessels. It is conceivable that PPG may be effective in distinguishing between healthy and unhealthy vessels but may be less reliable in detecting intermediate states. The IR and green PPG channels, by contrast, followed the expected trend, with healthy vessels demonstrating higher median signal values. Across all channels (red, IR, and green), unhealthy vessels showed lower signal readings, except for the median end datum difference. This pattern aligns with the expected decline in vessel elasticity, which affects both the structure and performance of the vessels [206].

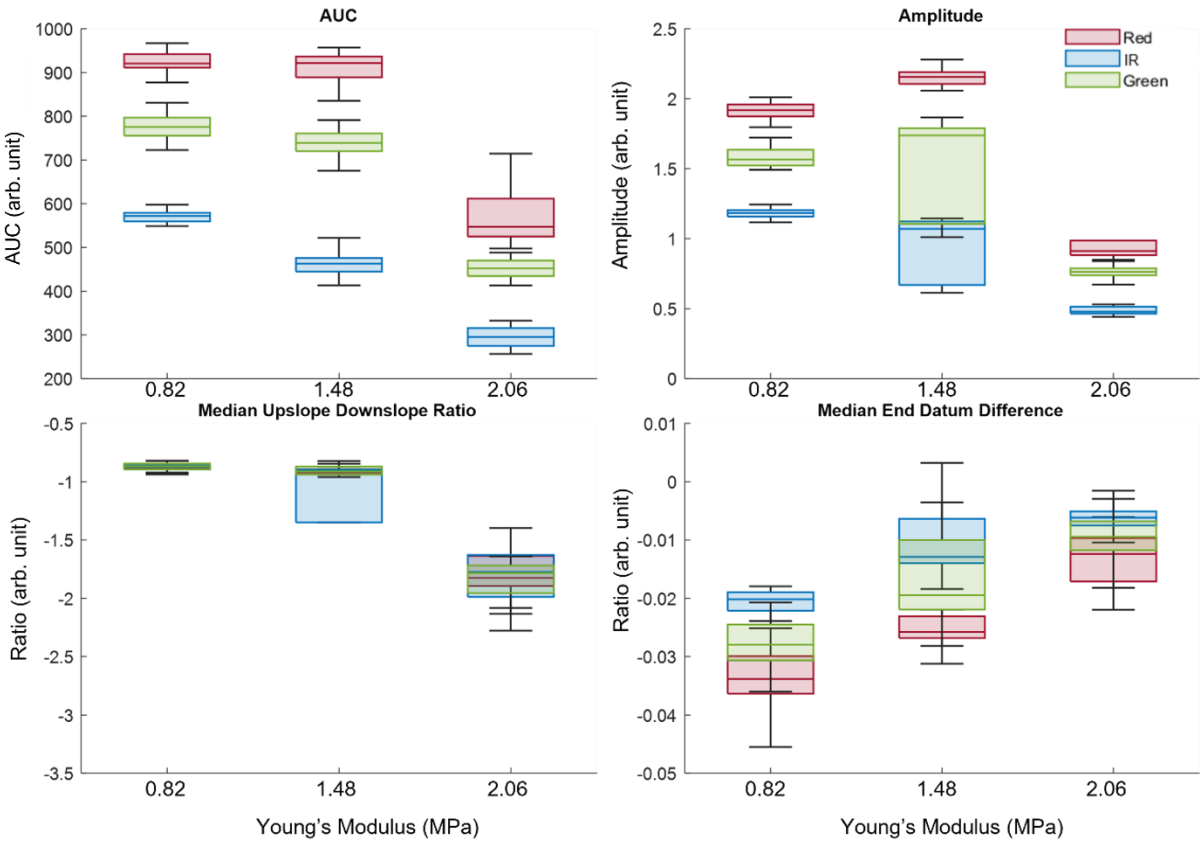

Figure 44: Box plot of the features extracted when the system was in a normotensive state, illustrating the changes in red, IR, and green signals from the phantoms, arranged in order of decreasing elasticity: from healthy (0.82 MPa), to intermediate (1.48 MPa), to unhealthy (2.06 MPa) [59].

The vessel phantoms were then placed in the hypertensive state and features were extracted, as illustrated in the box plot in Figure 45. With an increase in BP, a greater volume of blood will be present within the vessel in a given area, which can be seen with the increased AUC and amplitude. In more elastic vessels, this increase in blood volume is expected to result in greater expansion compared to stiffer, less healthy vessels. Consequently, as vessels transition from healthy to intermediate to unhealthy, the degree of expansion is anticipated to decrease. This progression is reflected in the features extracted from the PPG signal. This reduced expansion in less healthy vessels results in a lower volume of blood, meaning more photons are detected by the photodetector as fewer are absorbed.

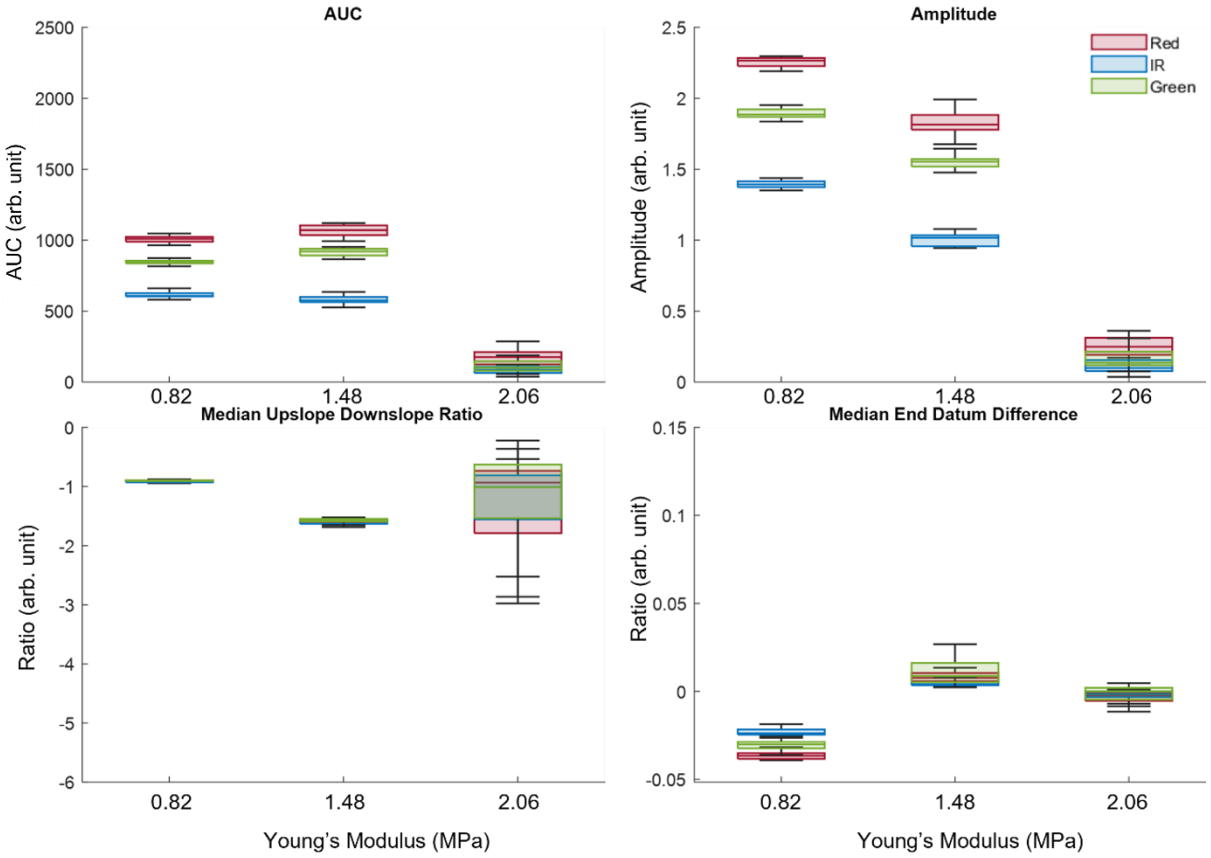

Figure 45: Box plot of the features extracted when the system was in a hypertensive state, illustrating the changes in red, IR, and green signals from the phantoms, arranged in order of decreasing elasticity: from healthy (0.82 MPa), to intermediate (1.48 MPa), to unhealthy (2.06 MPa) [59].

Unlike the features collected for high and normal BP, the characteristics associated with low BP exhibit greater variability. The box plot in Figure 46 illustrates this increased dispersion in the data set, in contrast to the more compact distributions observed in Figure 44 and Figure 45, particularly the healthy vessel. The dispersion in the elastic vessel is logical; as the vessel is more elastic, it becomes increasingly susceptible to fluctuations in expansion and contraction, which can amplify data variability. Nonetheless, an overall trend is still discernible: both the AUC and amplitude decrease with diminishing vessel elasticity. However, the extracted features raise important questions regarding the utility of PPG monitoring in patients experiencing hypotension. The variations observed in the data for healthy vessels may lead to confusion, as they overlap with data from individuals in intermediate and unhealthy states, particularly concerning the median upslope-to-downslope ratio and the median end datum difference. Consequently, employing PPG monitoring to assess vascular ageing in hypotensive patients may prove challenging. Alternative features should be extracted and explored to evaluate the feasibility of PPG monitoring in hypotensive patients.

Nevertheless, the observed variability itself may hold diagnostic significance and could potentially serve as an indicator of vascular health. However, further research in signal processing is necessary to determine whether this variability can be reliably extracted and leveraged, particularly in combination with range measures, for clinical applications.

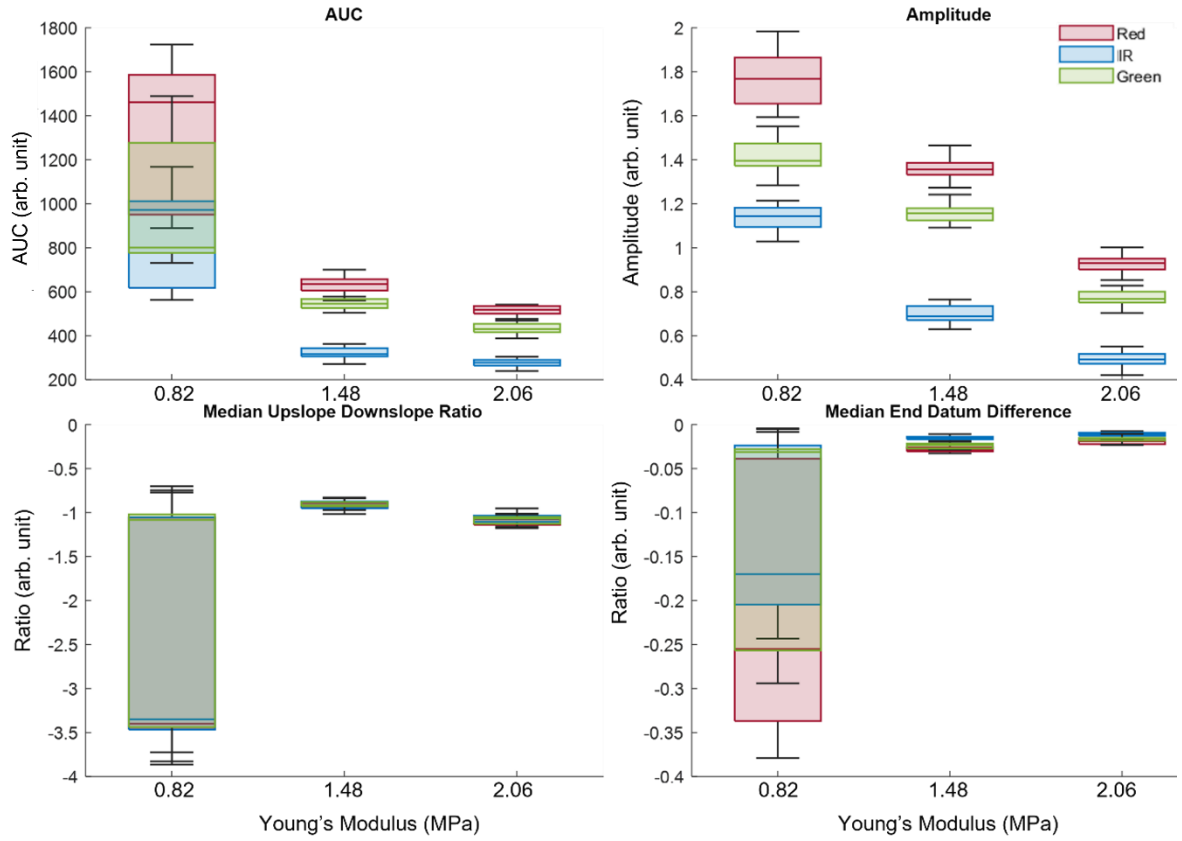

Figure 46: Box plot of the features extracted when the system was in a hypotensive state, illustrating the changes in red, IR, and green signals from the phantoms, arranged in order of decreasing elasticity: from healthy (0.82 MPa), to intermediate (1.48 MPa), to unhealthy (2.06 MPa) [59].

9.3.2 Statistical Analysis Using Kruskal–Wallis One-Way Analysis of Variance

A Kruskal–Wallis analysis was conducted to examine whether there was a statistically significant difference between the healthy and unhealthy vessels, with elasticities of 0.82 MPa and 2.06 MPa, respectively. Additionally, the analysis aimed to determine whether this statistical difference extended to the intermediate state, represented by the vessel with an elasticity of 1.48 MPa. Statistical significance was defined by *p*-values less than 0.05 [180]. The null hypothesis (H_0) for the Kruskal–Wallis test proposed that arterial stiffness has no effect on PPG morphology across different BP states. The alternative hypothesis (H_a) asserted that PPG morphology is affected by varying BP conditions depending on the level or arterial disease.

The majority of features analysed displayed statistically significant differences between healthy and unhealthy vascular states, as shown in Table 15, Table 16, and Table 17, highlighting the potential of PPG in detecting vascular ageing. Notably, however, the median upslope-downslope ratio was the exception, with a p-value of 9.86×10^{-2}, as shown in Table 16, indicating no statistical difference between the health states in the hypertensive condition. This result raises questions about the consistency and sensitivity of this feature for detecting vascular differences. However, given that this feature did exhibit statistical differences under normal and low BP, this finding may represent an anomaly. For a potential screening device, further investigation is required to determine whether the median upslope–downslope ratio should be included to enhance diagnostic accuracy. Moreover, in all BP settings (normal, high, and low), statistical differences were consistently observed between intermediate and unhealthy states, strengthening the case for PPG's utility in identifying patients in transition from intermediate to unhealthy vascular states. However, distinguishing between healthy and intermediate states proved more challenging, as amplitude and AUC did not show statistical differences in normal BP, and AUC was also not statistically different at high BP. Therefore, while PPG shows potential, further research is necessary to determine whether it can reliably differentiate intermediate states or if its primary utility lies in distinguishing between distinctly healthy and unhealthy states, where feature differences are more pronounced.

Table 15: Kruskal–Wallis p-value obtained for features extracted in normotensive state. A p-value of less than 0.05 represents a statistically significant difference. For features with a p-value equal to or greater than 0.05, the actual p-value is included in the table [59].

	Healthy–Intermediate	**Intermediate–Unhealthy**	**Healthy–Unhealthy**
AUC (arb. unit)	0.0662	$p < 0.05$	$p < 0.05$
Amplitude (arb. unit)	0.6690	$p < 0.05$	$p < 0.05$
Median Upslope–Downslope Ratio (arb. unit)	$p < 0.05$	$p < 0.05$	$p < 0.05$
Median End Datum Difference (arb. unit)	$p < 0.05$	$p < 0.05$	$p < 0.05$

Table 16: Kruskal–Wallis p-value obtained for features extracted in hypertensive state. A p-value of less than 0.05 represents a statistically significant difference. For features with a p-value equal to or greater than 0.05, the actual p-value is included in the table [59].

	Healthy–Intermediate	**Intermediate–Unhealthy**	**Healthy–Unhealthy**
AUC (arb. unit)	0.1540	$p < 0.05$	$p < 0.05$
Amplitude (arb. unit)	$p < 0.05$	$p < 0.05$	$p < 0.05$
Median Upslope–Downslope Ratio (arb. unit)	$p < 0.05$	$p < 0.05$	0.0986
Median End Datum Difference (arb. unit)	$p < 0.05$	$p < 0.05$	$p < 0.05$

Table 17: Kruskal–Wallis p-value obtained for features extracted in hypotensive state. A p-value of less than 0.05 represents a statistically significant difference. For features with a p-value equal to or greater than 0.05, the actual p-value is included in the table [59].

	Healthy–Intermediate	**Intermediate–Unhealthy**	**Healthy–Unhealthy**
AUC (arb. unit)	$p < 0.05$	$p < 0.05$	$p < 0.05$
Amplitude (arb. unit)	$p < 0.05$	$p < 0.05$	$p < 0.05$
Median Upslope–Downslope Ratio (arb. unit)	$p < 0.05$	$p < 0.05$	$p < 0.05$
Median End Datum Difference (arb. unit)	$p < 0.05$	$p < 0.05$	$p < 0.05$

9.3.3 Analysis of the Second Derivative of Photoplethysmography

The SDPPG is increasingly recognised in research as a valuable indicator for assessing vascular ageing [207], [208], [209], [210]. From the SDPPGs derived in this study, fiducial points were identified, and the ratios between these points were calculated. This analysis was conducted across different BP settings for each health status, as shown in Table 18. Studies have shown that the $\frac{b}{a}$ ratio increases with arterial stiffness, while the $\frac{c}{a}$, $\frac{d}{a}$, and $\frac{e}{a}$ ratios decrease as stiffness worsens [211], [212], [213]. In the hypertensive state, as the vessels become less healthy, the $\frac{b}{a}$ ratio rises from −2.13 to −2.06. This ratio reflects the distensibility of the vascular wall, with increased stiffness indicating diminished elasticity. In the hypertensive state, the $\frac{c}{a}$, $\frac{d}{a}$, and $\frac{e}{a}$ ratios decrease, as supported by the existing literature [213]. It was observed that the differences between these ratios across BP settings are most pronounced in the hypertensive state. In contrast, the normotensive and hypotensive states show smaller differences in these ratios between healthy and unhealthy statuses. Specifically, in the normotensive state, the $\frac{b}{a}$ ratio exhibited a slight increase of 0.01, while in the hypotensive state, no differences were observed in the $\frac{b}{a}$ ratio between healthy and unhealthy vessels. The most significant variations in the $\frac{b}{a}$ ratio

was found in the hypertensive state. Similarly, the $\frac{c}{a}$, $\frac{d}{a}$, and $\frac{e}{a}$ ratios decreased in the normotensive state as expected. In the hypotensive state, however, the $\frac{e}{a}$ ratio remained unchanged between healthy and unhealthy vessels, while the $\frac{c}{a}$ and $\frac{d}{a}$ ratios showed the expected decrease. These qualitative findings suggest that the SDPPG holds potential for identifying vascular ageing, particularly in the hypertensive state. It is important to note that previous studies have reported that SDPPG indices exhibit variations between men and women within the same age group, highlighting the importance of analysing these indices separately based on sex [207], [213], [214]. In this study, the influence of sex was not considered in the evaluation of SDPPG ratios for vascular ageing, as the experiments were conducted in vitro, and sex could not be accounted for. Despite this limitation, these preliminary findings provide valuable insight into the potential utility of SDPPGs as a tool for assessing vascular health and ageing. Further research should be conducted to refine these observations and explore the role of sex in SDPPG-based assessments.

Table 18: Ratios derived from the fiducial points of the red PPG signal for each health status and BP setting [59].

		Hypertensive				**Normotensive**				**Hypotensive**			
		$\frac{b}{a}$	$\frac{c}{a}$	$\frac{d}{a}$	$\frac{e}{a}$	$\frac{b}{a}$	$\frac{c}{a}$	$\frac{d}{a}$	$\frac{e}{a}$	$\frac{b}{a}$	$\frac{c}{a}$	$\frac{d}{a}$	$\frac{e}{a}$
Red signal	Healthy	−2.13	1.29	−0.43	0.37	−2.18	1.34	−0.41	0.38	−1.98	1.05	−0.21	0.28
	Unhealthy	−2.06	1.01	−0.44	0.36	−2.17	1.33	−0.43	0.37	−1.98	1.02	−0.22	0.28

9.4 Summary of Chapter 9

Asymptomatic PAD poses a silent risk, potentially leading to severe conditions if undetected. Integrating new screening tools could enable earlier detection. The study in Chapter 9 investigates the feasibility of PPG monitoring for assessing vascular health across different BP conditions. Custom femoral artery phantoms representing healthy (0.82 MPa), intermediate (1.48 MPa), and atherosclerotic (2.06 MPa) vessels were tested under hypertensive, normotensive, and hypotensive conditions to evaluate PPG's ability to distinguish between vascular states. Extracted features from the PPG signal, including amplitude, AUC, median upslope–downslope ratio, and median end datum difference, were analysed.

Significant differences in PPG features were observed between healthy and unhealthy vessels through Kruskal–Wallis tests, particularly amplitude, AUC, and median end datum difference, validating the feasibility of PPG for vascular health assessment. However, detecting intermediate states proved more challenging, as did differentiating between vessels in hypotensive conditions, where data variability led to overlap between healthy, intermediate, and unhealthy states. The median upslope–downslope ratio did not show a statistically significant difference between healthy and unhealthy vessels in the hypertensive condition, suggesting that alternative features may need to be considered.

The fiducial points from the second derivative of the SDPPG were analysed and studied. The $\frac{b}{a}$ ratio was most pronounced between healthy and unhealthy phantoms under hypertensive conditions (ranging from –2.13 to –2.06), suggesting a change in vascular wall distensibility. Under normotensive conditions, the difference in the $\frac{b}{a}$ ratio between healthy and unhealthy phantoms was smaller (0.01), and no meaningful difference was observed under hypotensive conditions, suggesting the reduced sensitivity of this metric at lower BPs. Ratios derived from fiducial points of the SDPPG were most pronounced in the hypertensive state.

This study highlights the potential of PPG monitoring for distinguishing between healthy and unhealthy vascular states, particularly in normotensive and hypertensive patients, offering a non-invasive means of detecting vascular ageing and atherosclerosis. Given the study design, the in vitro setup had limited ability to capture systemic vascular ageing, as

only segmental stiffness was introduced. Despite this challenge, this novel study provides insight into the use of PPG for the early detection of vascular changes under various BP settings, as well as into the use of SDPPG under hypertensive conditions.

CHAPTER 10: Multimodal Assessment of Arterial Stiffness Using Photoplethysmography and Laser Doppler Flowmetry

Most of the content in this chapter has been adapted from my paper published in npj Cardiovascular Health, titled 'Multimodal assessment of arterial stiffness using photoplethysmography and laser Doppler flowmetry'.

The work presented in Chapter 10 has been completed for the sole purpose of this thesis, with a focus on whether combining LDF with PPG would improve the differentiation of vascular health states associated with varying arterial stiffness.

10.1 Introduction

In 2021 alone, there were 648,507 recorded cases of CVD in the United Kingdom [215], remaining its position as the leading cause of death globally. Although vascular ageing cannot be prevented, early detection and the possibility of delaying its progression are of considerable clinical interest.

As outlined in Chapter 2, Section 2.3, vascular ageing is associated not only with structural and volumetric alterations but is also recognised to contribute to haemodynamic changes. As predicted by Poiseuille's Law (Equation 2), increasing arterial stiffness increases vascular resistance, thereby reducing flow rates in comparison to healthier vessels.

LDF is a technique for assessing microvascular blood flow, with growing recognition among researchers, as evidenced by the increase in publications from 1980 to 2006 [216]. The method involves illuminating the tissue surface with a laser light source (monochromatic), delivered via an optical fibre or a focused light beam. The probe, which integrates both the light-emitting and light-collecting fibres, captures a portion of the backscattered light. This scattered light, which results from interactions with moving red blood cells, is transmitted to a photodetector connected to signal processing electronics. The technique is based on the Doppler effect: when coherent laser light (operating at 785 nm ± 10 nm) interacts with moving red blood cells, it undergoes a frequency shift (Doppler broadening). The photodetector detects this broadened frequency spectrum, and the resulting signal is processed to yield a quantitative measure of blood flow, typically displayed on a fibre optic monitor [100]. LDF can capture low-speed

microvascular flows associated with nutritive capillary circulation near the skin surface, as well as flow within deeper arterioles and venules that contribute to thermoregulatory control. The LDF signal is commonly reported as flux, defined as the product of the mean blood cell speed and the concentration of moving blood cells, and is typically expressed in arbitrary perfusion units [217].

LDF has demonstrated potential as a valuable tool for the early detection of PAD, a condition marked by the progressive narrowing of arterial vessels, often resulting from wall thickening or the build-up of atherosclerotic plaques [3], [218]. Given that arterial stiffness, a consequence of vascular ageing, induces haemodynamic alterations, it is reasonable to hypothesise that changes in microvascular blood flow may also occur. This raises the question of whether vascular ageing can be indirectly monitored through such changes in blood flow, and whether LDF could serve as a viable method for its detection.

This experimental study investigates the use of LDF alongside PPG within a multimodal assessment approach. The primary aim was to monitor pulsatile changes in blood volume and blood flow using both modalities and to evaluate the feasibility of this combined approach for assessing vascular ageing. While previous research has investigated vascular health, most studies have focused on either PPG or LDF in isolation, or have relied heavily on in vivo data, which is often affected by biological variability [59], [87], [111], [219]. In contrast, this study utilised in vitro signals from both PPG and LDF probes to explore the potential for a synergistic application of these modalities. The integration of LDF with PPG may enhance discriminatory accuracy by providing insights into both volumetric and haemodynamic parameters. This multimodal approach holds promise for increasing the clinical utility of non-invasive vascular assessments, particularly where early identification of vascular ageing is critical for preventive cardiovascular care.

10.2 Methods

10.2.1 Custom Femoral Artery Phantoms

Three preconstructed vascular phantoms (Figure 47) were produced using the process outlined in Chapter 6. These phantoms were used for this study due to their mechanical similarities to human femoral arteries, as detailed in Section 6.6 and Section 6.6.1. The surrounding tissue was consistent across all phantoms; however, the embedded vessels differed in mechanical stiffness, as characterised by their respective Young's modulus.

The vessel with a Young's modulus of 0.82 MPa was designated as representative of a healthy femoral artery, while the vessel with a modulus of 2.06 MPa was used to model a diseased atherosclerotic artery. A third vessel, representing an intermediate pathological state, had a Young's modulus of 1.48 MPa.

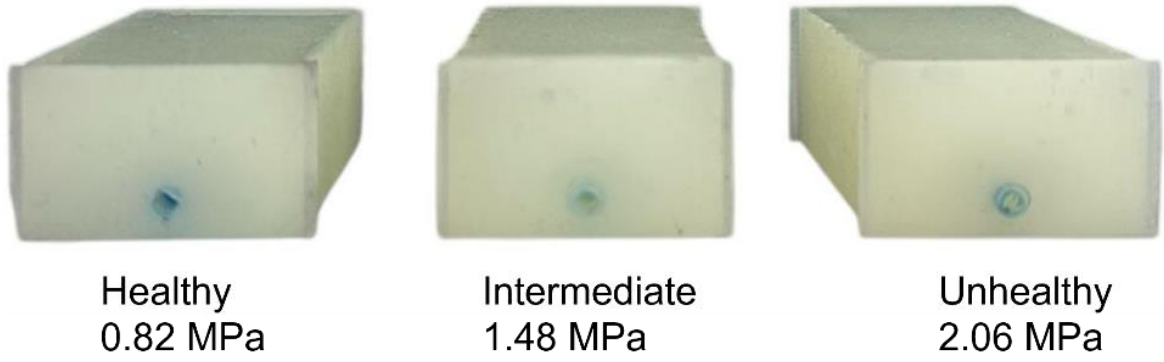

Figure 47: Fabricated vessel-tissue phantoms. The phantom on the left represents a healthy femoral artery, with a vessel characterised by a Young's modulus of 0.82 MPa. The central phantom corresponds to an intermediate pathological stage, incorporating a vessel with a Young's modulus of 1.48 MPa. The phantom on the right represents an atherosclerotic femoral artery, with a vessel modelled to have a Young's modulus of 2.06 MPa.

10.2.2 Set up of the In Vitro Cardiovascular System

As described in Chapter 5, the in vitro cardiovascular system was operated in the single-branch configuration (Figure 13), with the integration of the LDF device. The pulsatile pump (Figure 12) was set to 60 bpm.

Two formulations of BMF were evaluated to determine which offered superior performance in in vitro PPG and LDF experiments. Both BMFs were prepared at the RCBE as described in Section 5.2 and contained scattering agents. Each formulation contained Wright stain, Congo red powder, and Indian ink, with deionised water serving as the base solvent. The scattering medium was either LPFS or a laboratory-prepared intralipid, produced via oil-in-water emulsion with lecithin. The LPFS contained the non-ionic surfactant Tween 20 and OptiBind™ polystyrene microspheres that undergo Brownian motion, thereby enhancing optical scattering. This formulation was incorporated at a concentration of 0.25% of the total BMF volume. The intralipid formulation was prepared in the laboratory following a previously described method [153], incorporating a 30% oil-in-water emulsion.

10.2.3 Sensor Configuration

The LDF and PPG sensors were positioned on the custom-made phantoms, as illustrated Figure 2. The PPG sensor and LDF probe were alternated to obtain readings and prevent any optical interference between the light sources of the two devices. To avoid cross-interference, data collection was performed sequentially, with each recording lasting four minutes. The PPG sensor was connected to acquire signals at three wavelengths: green (530 nm), red (655 nm), and IR (940 nm). It was positioned above the phantom and interfaced with a PPG acquisition system operating at a sampling frequency of 2000 Hz, as described in Section 5.3.1 [155]. The LEDs which determined the light intensity of the sensor were set to 30 mA. The LDF system was connected in single-channel mode, and a skin probe was secured to the phantom. The LDF device collected tissue perfusion (Flux) data using a laser diode operating at 785 nm, with a maximum output power of 1.3 mW. The Flux smoothing time constant was set to 1.0 seconds [220].

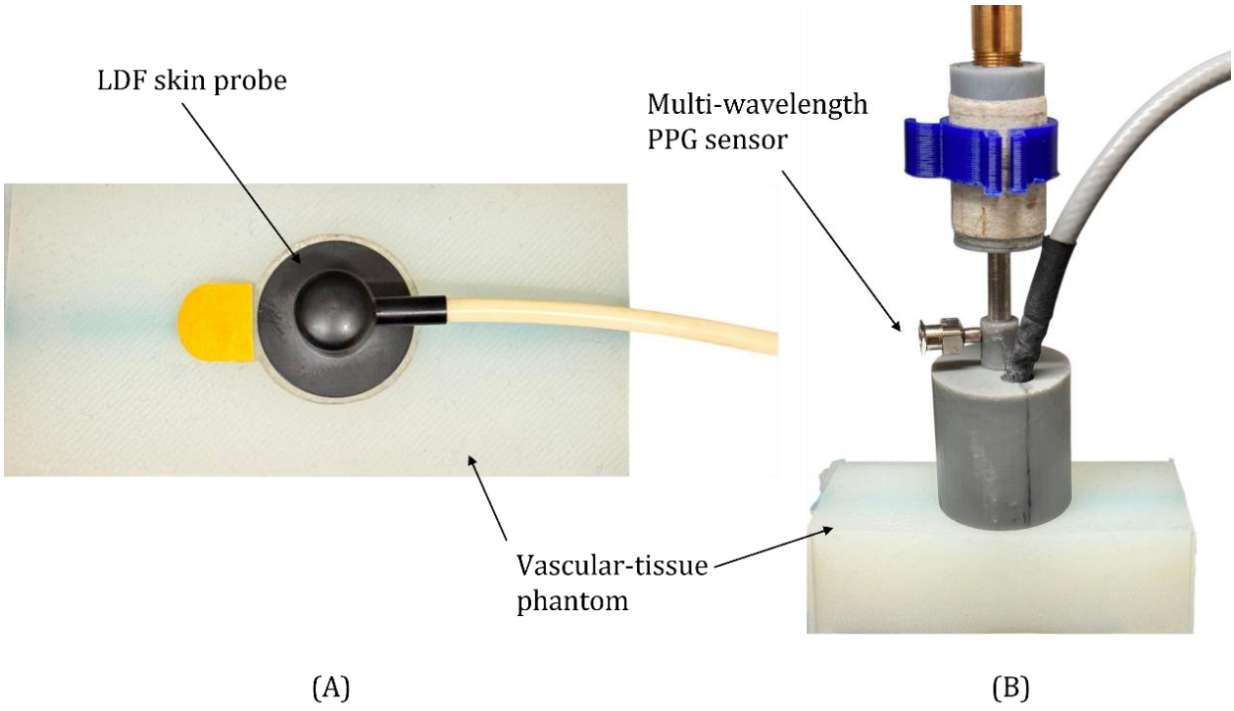

Figure 48: Configuration of the LDF (A) and PPG (B) sensors on the vessel–tissue phantom. The LDF probe was used to measure LDF-derived flux, while the PPG sensor was used to capture pulsatile blood volume changes.

Both PPG and LDF signals were acquired from each phantom condition (healthy, intermediate, and unhealthy) for each BMF, yielding a total of 12 datasets in this study.

10.2.4 Feature Extraction and Statistical Analysis

In accordance with Chapter 8, Section 8.4, four primary PPG features were selected for analysis in the present study: amplitude, AUC, median upslope-downslope ratio, and median end datum difference. These features were identified for their relevance to vascular ageing assessment and were applied in the study described in Chapter 9. They were then re-examined in the present study to extend that investigation. The rationale for selecting these specific features was to evaluate whether they alone provide sufficient sensitivity for detecting vascular ageing, or whether additional parameters may be required. As previously hypothesised in Section 8.4, ageing vessels are associated with a reduction in amplitude, AUC, and the median upslope-downslope ratio, as well as an increase in the median end datum difference when measured using PPG.

For the LDF signal, and in accordance with the literature [219], the AC and DC components were identified separately. For the AC component, the AUC and pulsatility were investigated. Signals were divided into 10 second windows, within which the mean AUC and pulsatility were calculated. This process was repeated across the entire recording to derive representative values. For the DC component, a similar approach was applied using 10 second windows to calculate mean DC flux. It was expected that, as vessels stiffen and vascular resistance increases, flow rate would decrease. The reduced flow rate was hypothesised to present a reduction in flux levels when transitioning from healthy to unhealthy vessel-tissue phantoms.

The resultant features were statistically analysed to assess whether they could discriminate between phantoms with differing vascular health statuses. Features obtained from each device were analysed using the Kruskal–Wallis test and cross-correlation analysis. These methods were chosen to assess statistically significant differences across health states for both modalities and to identify the most significant features. Demonstrating such differences in both devices would support their combined use as complementary diagnostic tools, where dual confirmation could enhance the reliability of vascular ageing assessments and potentially aid in identifying intermediate stages of vascular decline.

The Kruskal-Wallis test (described in Chapter 6, Section 6.4.2) was used to assess whether statistically significant differences existed among the groups, with a threshold

p-value of less than 0.05 [204]. Cross-correlation analysis was conducted to evaluate the relationship between each PPG feature and arterial stiffness, and the features were ranked according to their significance (as previously described in Chapter 8). The strength and direction of these relationships were quantified using Pearson correlation coefficients [221].

10.3 Results and Discussion

10.3.1 Analysis of Photoplethysmography Signals

The raw PPG signals were filtered using a second-order Chebyshev band-pass filter with a low-pass cut-off frequency of 6 Hz and a high-pass cut-off frequency of 0.5 Hz. Filtered outputs are shown in Figure 49 and Figure 50 for the intralipid-based and LPFS-based BMFs, respectively. As expected, there was a clear decrease in amplitude from the healthy to the unhealthy phantom in both BMF solutions. This decrease was less pronounced in the transition from healthy to intermediate than from intermediate to unhealthy. Although the intermediate vessel was fabricated with a Young's modulus between that of the healthy and unhealthy vessels, the corresponding change in signal amplitude between healthy and intermediate states was less evident. A notable finding was that, with the addition of intralipid to the BMF, the IR signal was of low quality, and the PPG waveform morphology was inconsistent across the health states. Although this may have been influenced by experimental noise, the red and green wavelengths produced distinguishable PPG signals. This may be explained by the fact that IR light penetrates deeper than red and green; however, the increased scattering induced by intralipid reduces the number of photons reaching the detector in a coherent, pulsatile pattern, thereby suppressing the IR signal. Intralipid, comprising lecithin and vegetable oil dispersed in an aqueous phase, forms a lipid emulsion whose droplets act as Mie scatterers. This produces strong scattering [222], thereby degrading the IR PPG signal, as deeper penetration (relative to red and green wavelengths) increases the photon pathlength; this increases the likelihood of multiple scattering events and reduces the proportion of photons reaching the detector. These findings suggest that IR measurements appear less sensitive to the intralipid BMF. Although native blood does not contain intralipid, the scattering and refractive properties introduced by intralipid in the BMF render it a useful experimental surrogate. In in vivo contexts where blood shows

optical behaviour similar to intralipid-induced changes in BMF, it is suggested that sensor probe could be adjusted to preserve signals in vivo.

In contrast, the IR signal did not appear to be diminished by the addition of LPFS to the BMF. Given that the volume of LPFS was comparatively lower than that of the intralipid formulation, it is likely that the intralipid itself contributed to the reduction in IR signal quality. Furthermore, when comparing the intralipid-based and LPFS-based BMFs, signals acquired with LPFS demonstrated greater amplitudes at the same wavelengths than those obtained with intralipid. This is likely due to the lower concentration of scattering agent present in the LPFS-based BMF, resulting in weaker overall scattering and allowing more photons to reach the detector. As such, reduced scattering produced larger signal amplitudes. Compared with intralipid, LPFS incorporates scattering microspheres that are typically near-monodisperse, resulting in more controllable and reproducible scattering properties than a polydisperse lipid emulsion (intralipid) [223]. This provides a plausible explanation for the preserved IR signals observed with LPFS relative to the intralipid-based BMF.

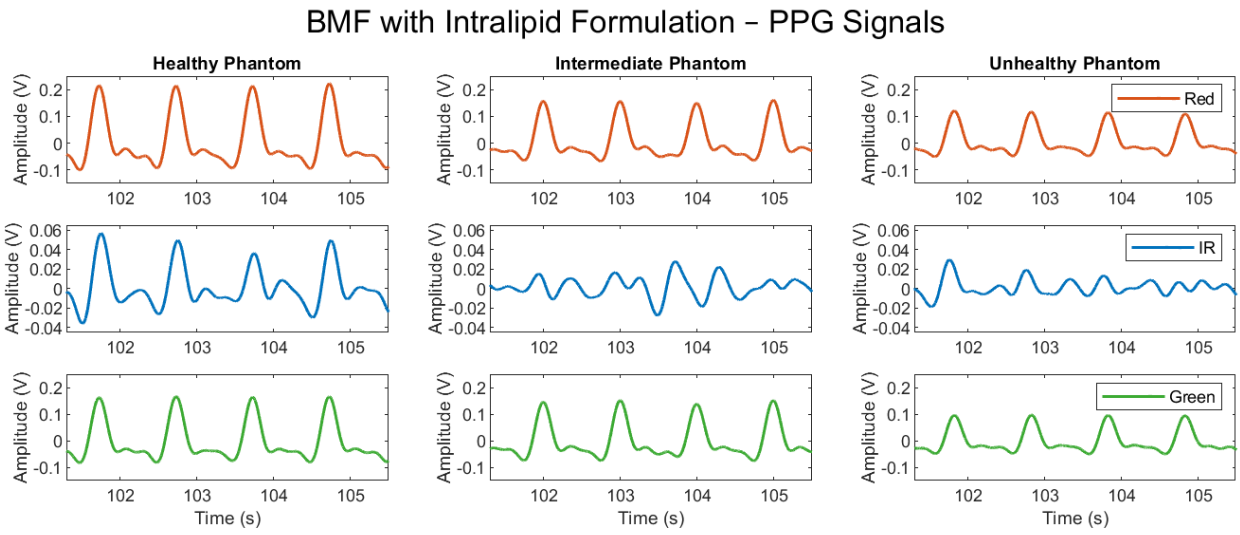

Figure 49: PPG signals acquired from healthy, intermediate, and unhealthy vessel–tissue phantoms using a multi-wavelength sensor (red, IR, and green channels). The BMF used an intralipid formulation prepared as a 30% oil-in-water emulsion.

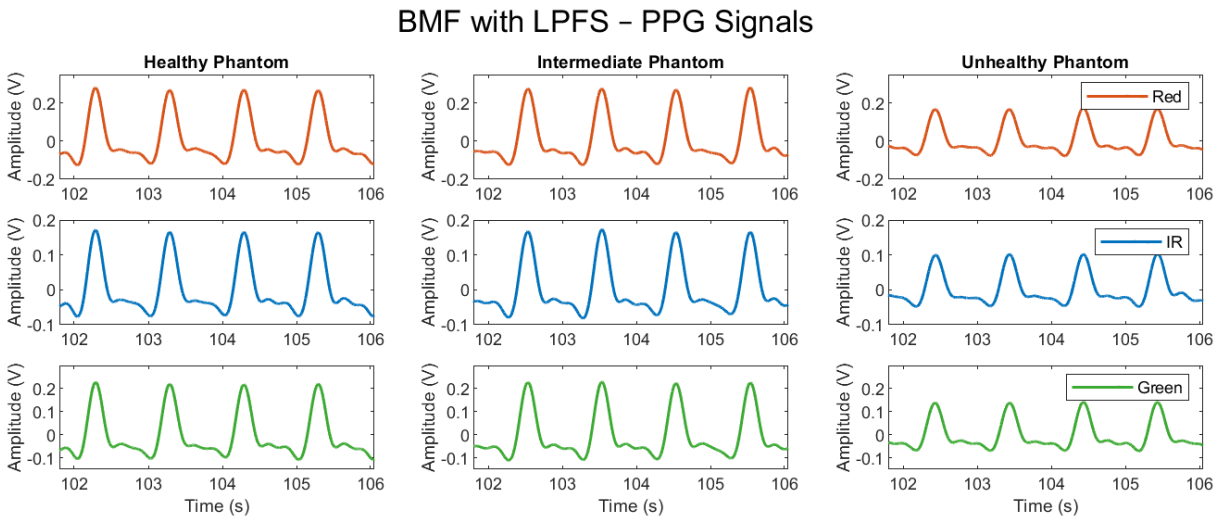

Figure 50: PPG signals acquired from healthy, intermediate, and unhealthy vessel–tissue phantoms using a multi-wavelength sensor (red, IR, and green channels). The BMF used LPFS at a concentration of 0.25% of the total volume.

The PPG features analysed were amplitude, AUC, median upslope–downslope ratio, and median end datum difference. The resulting box plot distributions of the features obtained with the intralipid-based BMF are shown in Figure 51. As expected, across the red, IR, and green wavelengths, both amplitude and AUC decreased with increasing vessel stiffness. This reflects the reduced ability of stiffer vessels to expand, which, given that PPG detects pulsatile changes in blood volume, manifests as reduced amplitude and AUC. This trend is consistent with previous findings in the absence of intralipid within the BMF (Chapter 9) [59].

However, when intralipid was introduced, the median upslope–downslope ratio did not follow the expected pattern. Although the PPG signals were morphologically consistent with expectations, the slope-derived feature appeared unstable, resulting in high variability. As this feature relies on peak detection and fiducial point identification, inaccuracies in locating these points may have contributed to variability in the slope ratios.

An expected trend was observed in the red signal for the median end datum difference, which increased with stiffness, indicating a sharper signal [59]. A similar, though less pronounced, trend was observed in the green and IR signals.

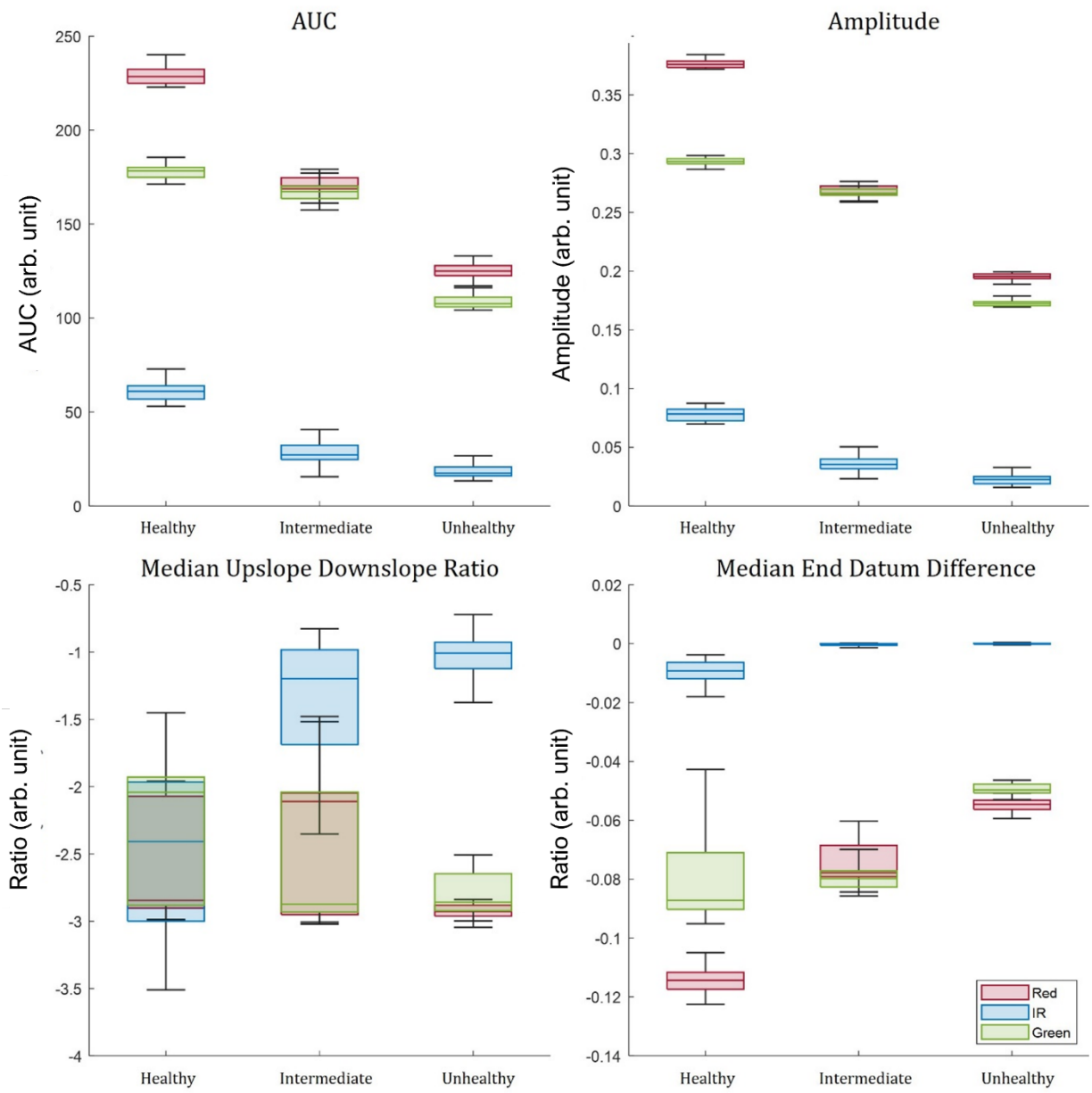

Figure 51: Box plot of the PPG features extracted from phantoms with the intralipid-based BMF, showing the red, IR, and green signals across phantoms arranged by decreasing elasticity: healthy (0.82 MPa), intermediate (1.48 MPa), and unhealthy (2.06 MPa).

When the BMF contained LPFS, the intermediate vessel–tissue phantom did not follow the expected trends for AUC and amplitude, where a progressive decrease was expected with increasing stiffness. Although a reduction was observed from the healthy, elastic vessels to the stiff, unhealthy vessels, the intermediate vessel response was closer to the healthy case and, in some instances, slightly elevated, as shown in Figure 52. This behaviour was also reported in Chapter 9 [59], where the red, IR, and green wavelengths

showed similar values between the healthy and intermediate levels for AUC, and in terms of amplitude, the red signal increased from the healthy to intermediate state.

In contrast to the intralipid-based BMF, both the median upslope–downslope ratio and the median end datum difference demonstrated increased variability across all vessel states and wavelengths. The upslope–downslope ratio is particularly sensitive to the downslope region of the PPG waveform, where the signal is more susceptible to noise and baseline drift, which can complicate accurate pulse segmentation. The introduction of LPFS increases scattering and may introduce inaccuracies in fiducial point identification, thereby affecting downslope estimation. This instability likely explains the absence of consistent trends across the stiffness levels.

Similarly, the end datum difference displayed greater variability in the LPFS-based BMF compared with the intralipid-based BMF. This was most evident in the healthy and intermediate states, although the unhealthy phantom also showed increased variability. These findings suggest that while the end datum difference may retain some discriminatory value between vessel states [59], its reliability diminishes when additional scattering agents are introduced to the BMF.

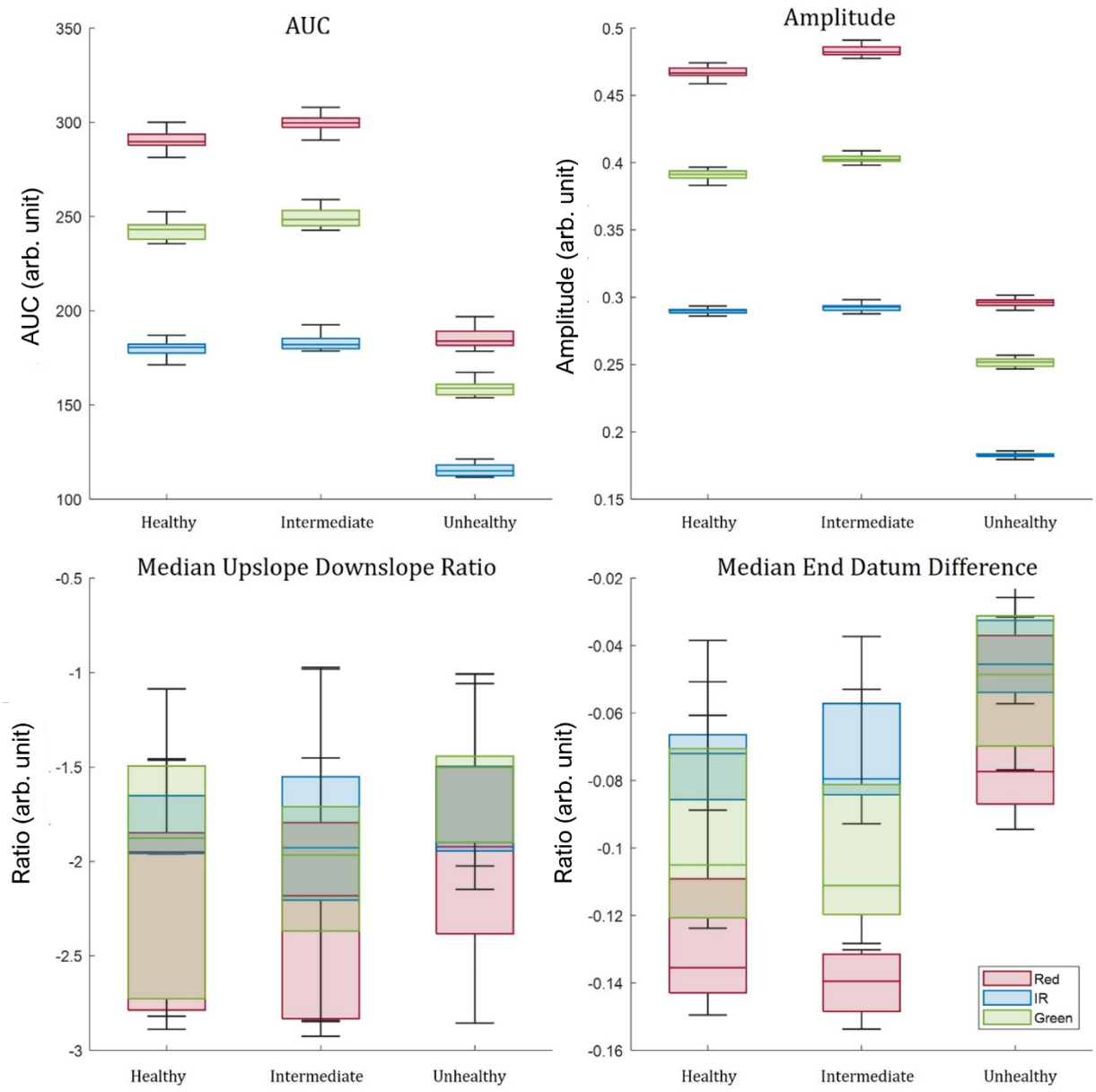

Figure 52: Box plot of the PPG features extracted from phantoms with the LPFS-based BMF, showing the red, IR, and green signals across phantoms arranged by decreasing elasticity: healthy (0.82 MPa), intermediate (1.48 MPa), and unhealthy (2.06 MPa).

10.3.2 Statistical Analysis of Photoplethysmography Waveform Features

Kruskal–Wallis analysis of the extracted PPG features was performed to evaluate whether these features could distinguish between the three vessel–tissue phantoms representing different stiffness levels. The objective was to determine whether PPG could identify differences between healthy and unhealthy vascular states, as well as detect an intermediate transitional stage. Table 19 and Table 20 present the Kruskal–Wallis results obtained for the intralipid-based BMF and LPFS-based BMF, respectively. As the aim of this research was to assess the feasibility of applying PPG as a non-invasive tool for

assessing arterial stiffness, the wavelengths were combined for simplicity. Accordingly, a single *p*-value was calculated for each feature to assess differences across stiffness levels rather than across individual wavelengths.

Table 19: Kruskal–Wallis p-values for PPG features extracted using the intralipid-based BMF. A p-value < 0.05 was considered statistically significant. For features with p-values ≥ 0.05, the exact values are reported in the table.

	Healthy–Intermediate	**Intermediate–Unhealthy**	**Healthy–Unhealthy**
AUC (arb. unit)	$p < 0.05$	$p < 0.05$	$p < 0.05$
Amplitude (arb. unit)	$p < 0.05$	$p < 0.05$	$p < 0.05$
Median Upslope–Downslope-Ratio (arb. unit)	$p < 0.05$	0.566	0.450
Median End Datum Difference (arb. unit)	$p < 0.05$	$p < 0.05$	$p < 0.05$

Table 20: Kruskal-Wallis p-values for PPG features extracted using the LPFS-based BMF. A p-value < 0.05 was considered statistically significant. For features with p-values ≥ 0.05, the exact values are reported in the table.

	Healthy–Intermediate	**Intermediate–Unhealthy**	**Healthy–Unhealthy**
AUC (arb. unit)	$p < 0.05$	$p < 0.05$	$p < 0.05$
Amplitude (arb. unit)	$p < 0.05$	$p < 0.05$	$p < 0.05$
Median Upslope–Downslope-Ratio (arb. unit)	0.541	$p < 0.05$	0.071
Median End Datum Difference (arb. unit)	0.346	0.346	$p < 0.05$

Using the intralipid-based BMF, statistically significant differences were observed between the healthy and intermediate vessel–tissue phantoms across all extracted features (as shown in Table 19). In contrast, previous work (presented in Chapter 9), where the BMF formulation did not include intralipids, reported no significant differences between the healthy and intermediate phantoms for AUC and amplitude [59]. Furthermore, while earlier results presented in Chapter 9 showed that all features yielded p-values < 0.05 when comparing the intermediate and unhealthy phantoms, as well as the healthy and unhealthy [59], the intralipid-based BMF did not demonstrate a significant difference for the median upslope–downslope ratio. This discrepancy may reflect the instability of this feature, as illustrated in Figure 51, whereby high variability was observed.

Interestingly, although the LPFS-based BMF produced higher PPG signal amplitudes compared with the intralipid-based BMF, Table 20 presented a greater number of features that were not statistically different compared with Table 19. The median upslope–downslope ratio did not demonstrate significant differences between either the

healthy and intermediate or the healthy and unhealthy phantoms, highlighting the need to explore additional features. Furthermore, although the median end datum difference identified a significant difference between the healthy and unhealthy vessel–tissue phantoms, the intermediate stage did not differ significantly from either extreme. Therefore, while the median end datum difference was able to discriminate between the two extremes of elasticity, additional features may be required to capture transitional stages if the LPFS-based BMF is to be used in future investigations.

Cross-correlation analysis was performed to quantify the relationship between extracted PPG features and vessel elasticity across wavelengths and BMFs to validate the visualised box plot patterns and support the Kruskal-Wallis analysis. Features were ranked by Pearson correlation coefficients, with a significance threshold set at $p < 0.05$. This comparison, presented in Figure 53 for the intralipid-based BMF features, and Figure 54 for the LPFS-based features. This comparison assessed whether the observed correlations were reproducible across formulations, or if the type of BMF influenced the strength of association between PPG features and vessel elasticity.

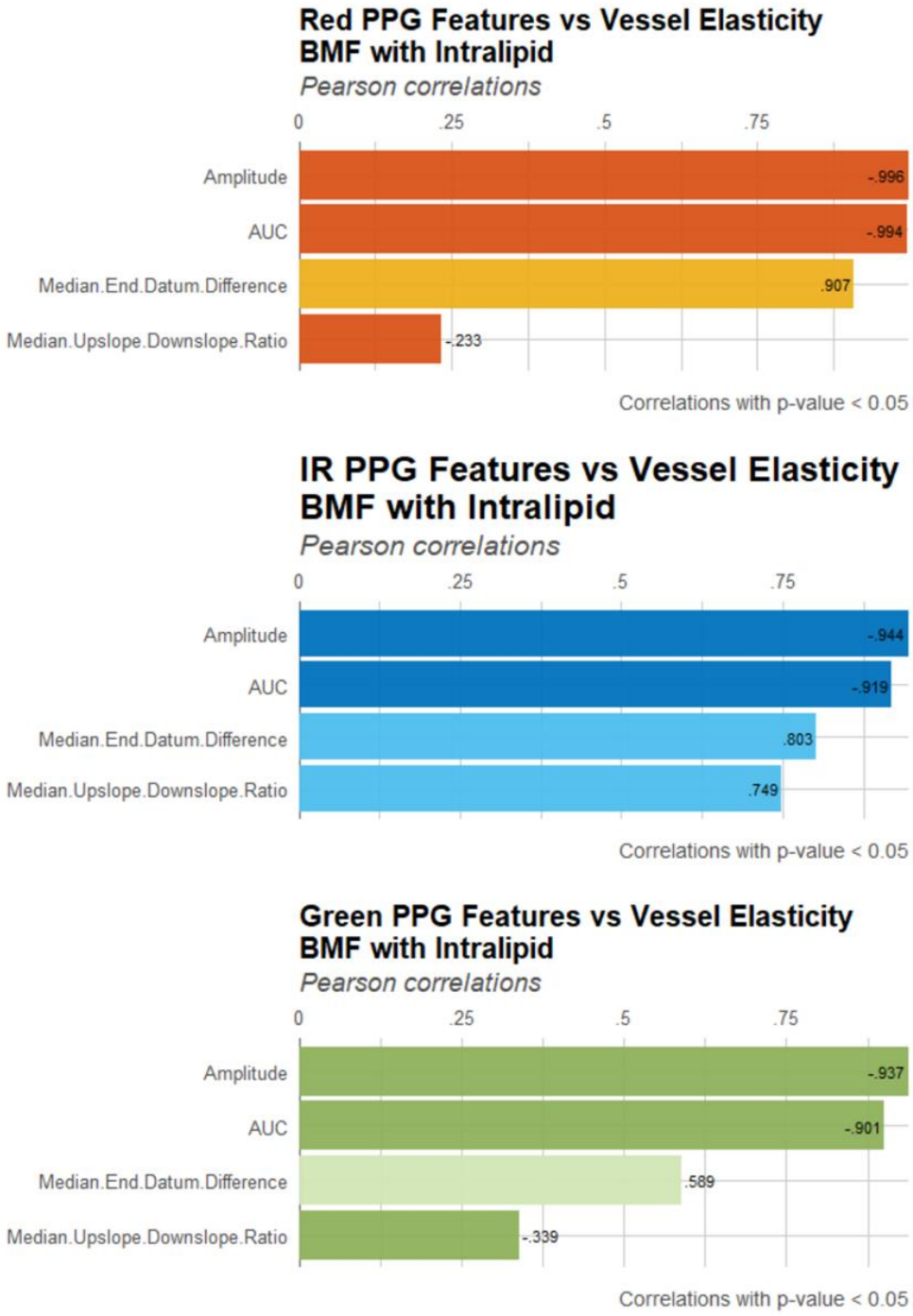

Figure 53: Correlation of PPG features with vessel elasticity using intralipid-based BMF. Pearson correlation coefficients ($p < 0.05$) are presented for amplitude, AUC, median upslope-downslope ratio, and median end datum difference across red, IR and green wavelengths.

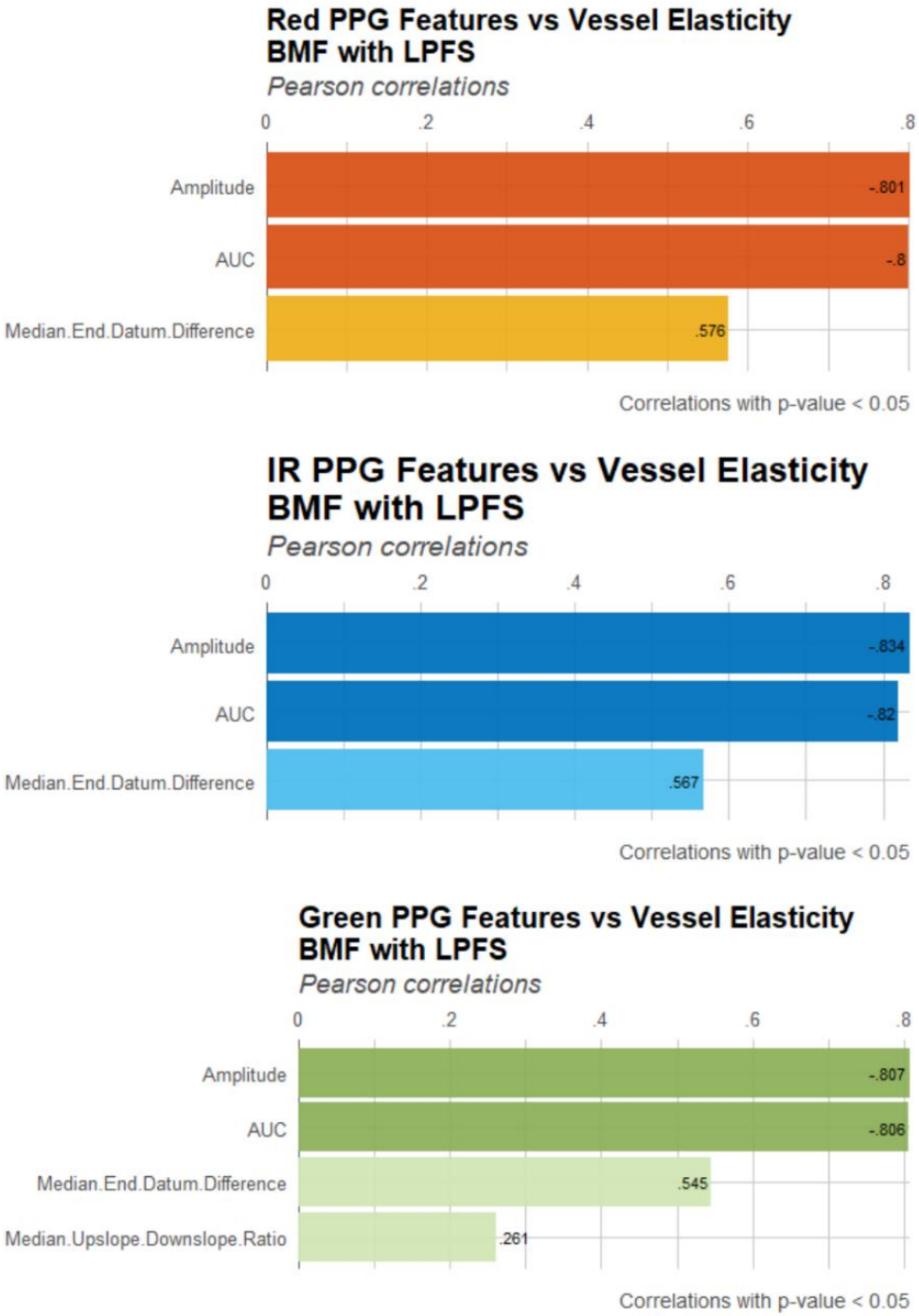

Figure 54: Correlation of PPG features with vessel elasticity using LPFS-based BMF. Pearson correlation coefficients ($p < 0.05$) are presented for amplitude, AUC, median end-datum difference, and median upslope-downslope ratio across red, IR and green wavelengths. Stronger correlations were observed using the intralipid-based BMF than the LPFS-based BMF, particularly for amplitude and AUC, while slope-derived features displayed weaker or inconsistent associations.

Comparing the two BMF formulations, intralipid consistently produced stronger correlations across all wavelengths, particularly amplitude and AUC. The LPFS formulation also demonstrated significant correlations; however, their overall strength was comparatively weaker. This suggests that intralipid functions as a more reliable optical medium for accentuating the sensitivity of PPG features to vascular elasticity.

Amplitude and AUC emerged as the most reliable indicators of vessel stiffness, exhibiting strong negative correlations consistently across wavelengths and both formulations, supporting the Kruskal-Wallis test and box plot distributions. The end datum difference also showed a consistent positive correlation, though its magnitude fluctuated between wavelengths and BMFs. The median upslope-downslope ratio was the least consistent feature, with varying correlation directions and in some cases not reaching statistical significance. This highlights the susceptibility of slope-derived features to noise and errors in fiducial point detection, which limits their utility as stiffness markers compared to those based on amplitude and area.

The cross-correlation results align with the findings from both the Kruskal-Wallis test and the box plot distributions, indicating that intralipid-based BMF provides stronger statistical validation for arterial stiffness detection using PPG-derived features. Furthermore, amplitude and AUC were consistently shown to be more reliable than datum and slope features. These PPG features could potentially be investigated alongside LDF signals to identify similar or contrasting physiological patterns.

10.3.3 Analysis of Laser Doppler Flowmetry Signals

The raw LDF signals, separated into DC components, are presented in Figure 55 for the intralipid-based BMF and the LPFS-based BMF. The DC flux is a commonly analysed parameter in the literature [219], [224], and demonstrated a relatively steady baseline across all conditions. For both formulations, the DC amplitude decreased progressively from the healthy to the unhealthy states. Previous studies have similarly reported that perfusion levels decline from healthy individuals to those with vascular pathologies [224]. Notably, the intralipid-based BMF consistently produced higher flux values compared to the LPFS-based BMF under equivalent vessel–phantom conditions. Moreover, the intralipid formulation demonstrated a more pronounced reduction in flux across the healthy, intermediate, and unhealthy states, suggesting improved

differentiation between vascular conditions. Such clearer separation may be advantageous, as larger signal variations could facilitate clinical interpretation. This difference may, however, be attributed to the higher concentration of the scattering agent present in the intralipid-based BMF relative to the LPFS-based formulation.

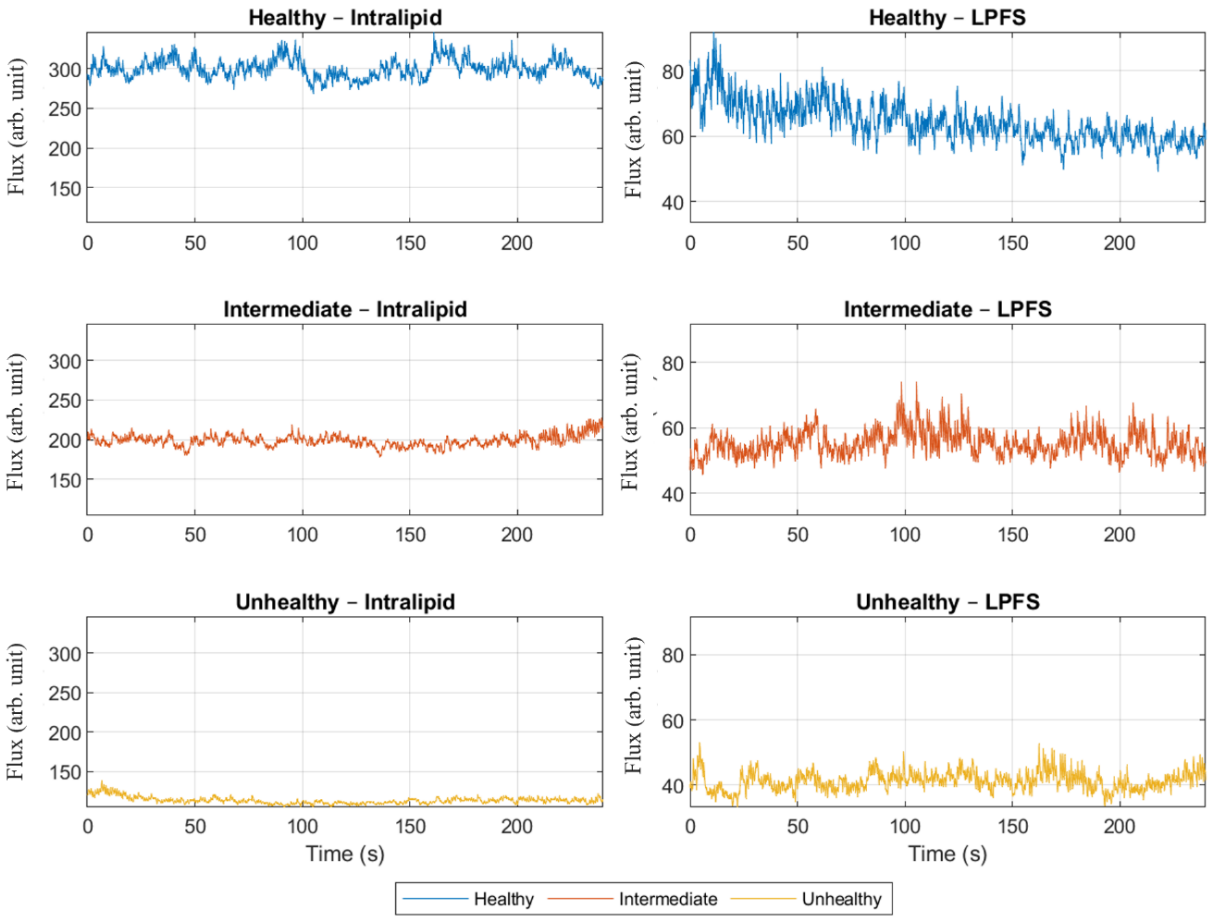

Figure 55: LDF DC flux signals acquired from healthy (blue), intermediate (orange), and unhealthy (yellow) vessel–tissue phantoms using the intralipid-based BMF (left panel) and LPFS-based BMF (right panel). The raw DC signals are displayed over the full 4-minute recording.

To investigate the potential for LDF to assess vascular ageing, alongside PPG, both DC and AC features were extracted from the acquired LDF signals, as shown in Figure 56, for the intralipid-based and LPFS-based BMF. Following previous literature for LDF DC analysis, the mean flux was calculated and plotted [219], with averages over 10-second windows. For AC, peak-to-peak pulsatility and AUC were calculated, also in 10-second windows. The DC mean flux yielded promising results, with clear differences between each health stage of the vessel-tissue phantoms. As the arterial stiffness of the vessel-tissue phantoms increased, corresponding to a decline in vascular health, flux levels decreased, consistent

with the hypothesis that stiffer vessels have lower flow rates due to increased resistance, as explained by Poiseuille's law [41]. Accordingly, the DC mean flux from the vessel-tissue phantoms reflected this pattern in both the intralipid- and LPFS-based BMFs. The intralipid-based BMF showed a greater range of flux variation between stiffness levels, likely due to the higher concentration of intralipid used.

In AC extracted LDF features, the intralipid-based BMF demonstrated greater potential for differentiating vessel stiffness. The healthy phantom showed the clearest separation from the intermediate and unhealthy states. In contrast, the PPG signals indicated that the unhealthy phantoms were the most distinct, consistent with previous findings [59]. This may be because, as the phantoms transition to stiffer states, the AC LDF features tend to saturate, making it difficult to discriminate between the intermediate and unhealthy conditions. With the LPFS-based BMF, the healthy phantom did not separate clearly, and all three phantoms produced overlapping features, despite the distinctions observed in the DC mean flux. However, it should be noted that, for the AC features, the inconsistency in the trends obtained should be further investigated. It is suggested that this inconsistency may arise from internal gain within the LDF system, or alternatively from signal saturation.

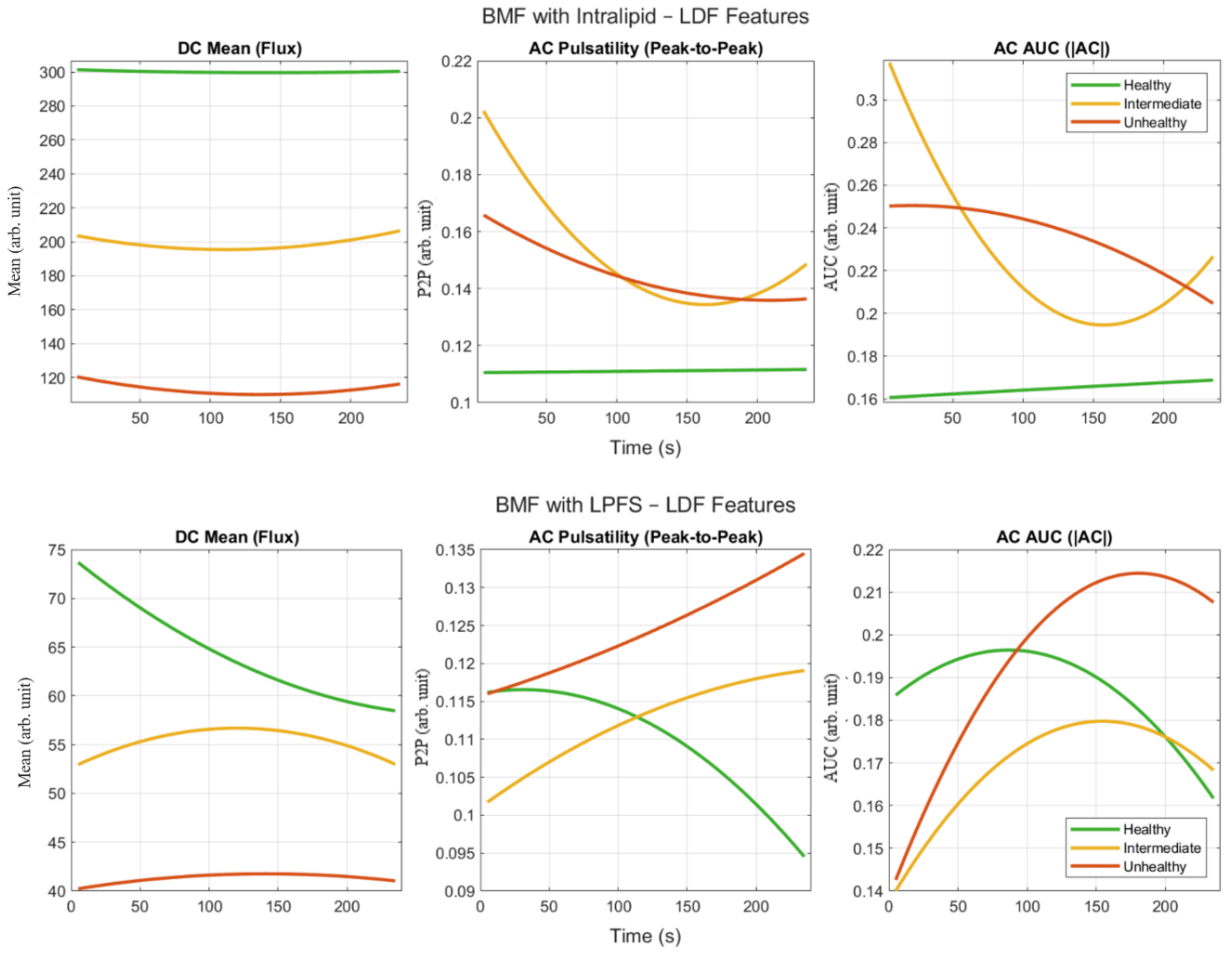

Figure 56: DC and AC features extracted from LDF signals acquired from healthy (green), intermediate (yellow), and unhealthy (orange) vessel-tissue phantoms using the intralipid-based BMF (top panel) and LPFS-based BMF (bottom panel). The extracted features are DC Mean Flux, AC Peak-to-Peak Pulsatility and AC AUC.

10.3.4 Statistical Analysis of Laser Doppler Flowmetry Features

Kruskal–Wallis analysis was conducted on the extracted AC and DC features to evaluate whether LDF could statistically differentiate between vessels of varying elasticities. The resulting *p*-values are summarised in Table 21 and Table 22 for the intralipid-based BMF and the LPFS-based BMF, respectively. As shown in Figure 56, the mean DC flux values for each vessel–phantom were clearly separated, consistent with the statistically significant differences observed ($p < 0.05$). While DC mean flux was reliably distinct across all phantoms in both formulations, the AC-derived features proved less consistent. For the intralipid-based BMF, differentiation between intermediate and unhealthy states was not significant (AUC: $p = 0.174$; pulsatility: $p = 0.312$), suggesting that the reduction in pulsatile amplitude between these two states was relatively small, resulting in overlapping values (Figure 56). Nevertheless, the intralipid-based BMF enabled clear

separation between the extremes of vessel elasticity (healthy vs unhealthy) for all features.

In contrast, the LPFS-based BMF showed non-significant differences in AUC between healthy and unhealthy states, whereas significant differences were observed between intermediate and unhealthy states ($p < 0.05$). This discrepancy may reflect differences in the scattering properties of the two formulations, which influence their sensitivity to pulsatile fluctuations. Overall, larger differences in vessel stiffness (such as between healthy and unhealthy states) were more readily distinguishable, particularly with the intralipid-based BMF, supporting its greater suitability for clinical application.

Table 21: Kruskal–Wallis p-values for LDF features extracted using the intralipid-based BMF. A p-value < 0.05 was considered statistically significant. For features with p-values ≥ 0.05, the exact values are reported in the table.

	Healthy–Intermediate	**Intermediate–Unhealthy**	**Healthy–Unhealthy**
AC – AUC (arb. unit)	$p < 0.05$	0.174	$p < 0.05$
AC – Pulsatility (arb. unit)	$p < 0.05$	0.312	$p < 0.05$
DC – Mean Flux (arb. unit)	$p < 0.05$	$p < 0.05$	$p < 0.05$

Table 22: Kruskal–Wallis p-values for LDF features extracted using the LPFS-based BMF. A p-value < 0.05 was considered statistically significant. For features with p-values ≥ 0.05, the exact values are reported in the table.

	Healthy–Intermediate	**Intermediate–Unhealthy**	**Healthy–Unhealthy**
AC – AUC (arb. unit)	$p < 0.05$	$p < 0.05$	0.635
AC – Pulsatility (arb. unit)	0.606	$p < 0.05$	$p < 0.05$
DC – Mean Flux (arb. unit)	$p < 0.05$	$p < 0.05$	$p < 0.05$

10.3.5 Summary of Findings

According to Poiseuille's law (Equation 2), aged vessels, which are less compliant with increased resistance, should demonstrate lower flow rates in comparison to young, healthy elastic vessels [41]. Consistent with this, LDF measurements in both the intralipid and LPFS setups showed that greater vessel stiffness was associated with lower flux.

The integration of LDF alongside PPG in in vitro investigations using vascular phantoms may support the assessment of vascular health. Optimising the scattering properties of the BMF is critical to achieving a formulation suitable for both modalities. In this study, two additives were investigated: intralipid and LPFS. Table 23 and Table 24 summarise the discriminatory findings between health states for the intralipid-based BMF and the LPFS-based BMF, respectively, for both PPG and LDF. This summary was based on all extracted features from PPG (AUC, amplitude, median upslope-to-downslope ratio, and median end datum difference) and for LDF, on DC mean flux only, which proved to be more robust than AC-derived features. The findings indicate that LDF helps discriminate between health states and can be used complementarily to strengthen PPG assessments of vascular health.

Table 23: Summary of discriminatory strength between health states (healthy, intermediate, and unhealthy) using intralipid-based BMF, for each modality (PPG and LDF). For LDF, only DC mean flux was included, as it proved the most robust.

	Healthy–Intermediate	**Intermediate–Unhealthy**	**Healthy–Unhealthy**
PPG	Strong discrimination strength: statistically significant differences were observed across all extracted features.	Strong discrimination strength: statistically significant differences were observed across all extracted features, apart from the median upslope-to-downslope ratio.	Strong discrimination strength: statistically significant differences were observed across all extracted features, apart from the median upslope-to-downslope ratio.
LDF	Strong discrimination strength.	Strong discrimination strength.	Strong discrimination strength.

Table 24: Summary of discriminatory strength between health states (healthy, intermediate, and unhealthy) using LPFS-based BMF, for each modality (PPG and LDF). For LDF, only DC mean flux was included, as it proved the most robust.

	Healthy–Intermediate	**Intermediate–Unhealthy**	**Healthy–Unhealthy**
PPG	Mixed discrimination strength: AUC and amplitude showed statistically significant differences, while the median upslope-to-downslope ratio and median end datum difference showed no statistically significant difference.	Strong discrimination strength: statistically significant differences were observed across all extracted features, apart from the median end datum difference.	Strong discrimination strength: statistically significant differences were observed across all extracted features, apart from the median upslope-to-downslope ratio.
LDF	Strong discrimination strength.	Strong discrimination strength.	Strong discrimination strength.

Both formulations produced LDF signals that varied with vessel stiffness, with mean flux levels decreasing as stiffness increased. Although this trend was observed in both BMFs, the intralipid-based BMF demonstrated stronger separation between vessel states and a wider range of flux values. The AC LDF features also showed clearer differentiation between vascular states with intralipid compared to LPFS.

A negative effect of intralipid was observed on the PPG signals, characterised by reduced amplitude across all wavelengths. This effect was most pronounced in the IR signals, where visual degradation of pulsatility was also evident. In contrast, these effects were not present when using the LPFS formulation, which may be related to the lower volume of LPFS used in this study compared to the higher concentration of intralipid within the BMFs. These findings suggest that while intralipid appears more advantageous for in vitro LDF investigations, its adverse impact on PPG signals should be carefully considered when combining both modalities. To optimise signal quality across both techniques, adjustment of intralipid concentrations may be required.

Analysis of the PPG signals indicated that the unhealthy phantom was more distinguishable in AUC and amplitude features compared to the healthy and intermediate phantoms. By contrast, LDF features demonstrated the greatest variation in the healthy phantom. Together, these findings support the integration of LDF with PPG for vascular assessment, enabling the capture of a wider range of health states. However, limitations remain, including the signal processing and motion artefact challenges associated with LDF [3], as well as potential cross-interference between sensors, which may be minimised by multiplexing.

10.4 Summary of Chapter 10

The study presented in Chapter 10 marks an early step towards combining LDF with PPG for the assessment of vascular ageing, with the aim of developing a multimodal approach suitable for evaluating arterial stiffness. Two scattering agents were incorporated into a BMF to evaluate both modalities: intralipid- and LPFS-based formulations. Although the intralipid-based BMF suppressed the IR component of the PPG signal, it produced larger reductions in DC flux between vascular health states compared to the LPFS-based BMF. The larger differences in flux values between healthy and diseased conditions may facilitate clearer clinical interpretation.

To minimise optical cross-interference between sensors, a sequential acquisition approach was adopted in place of simultaneous measurements. While this limited multimodal synchrony, it nonetheless established a reliable basis for evaluating the feasibility of combining LDF with PPG. The results demonstrated that amplitude and AUC were the most reliable PPG-derived features, whereas slope-based metrics showed

reduced reliability in the presence of scattering agents. A comparison of the intralipid and LPFS formulations further emphasised that optical scattering differentially influences signal quality, highlighting the importance of BMF composition in multimodal experiments.

Given that PPG reflects pulsatile changes in blood volume and LDF captures haemodynamic alterations, their combined application offers complementary discriminatory value. The larger flux variations observed with intralipid-based LDF suggest that this formulation may facilitate clearer interpretation when differentiating vascular health states. However, persistent challenges remain, including instability in slope-derived features and susceptibility of LDF to motion artefacts, which must be addressed before clinical implementation.

CHAPTER 11: DISCUSSION, CONCLUSIONS & FUTURE WORK

11.1 Discussion

11.1.1 Key findings

Although further research is required to confirm the clinical suitability of PPG for vascular ageing assessment, the findings presented in this thesis provide novel experimental evidence underscoring the potential of PPG as a low-cost, user-friendly, and non-invasive tool for this purpose. This section outlines the key findings obtained throughout the research.

Through an in vitro approach, vessel stiffness could be isolated and systematically manipulated while other variables were controlled, allowing the observed changes in PPG waveform morphology to be attributed primarily to stiffness rather than to biological variability. This controlled setting reduced confounding factors that are difficult to manage in vivo and strengthened the internal validity of the findings. The in vitro platform also enabled the incorporation of co-morbidities, such as hypertension, into the model, allowing closer replication of human physiology. In addition, because the work did not involve human participants, ethics approval was not required; this removed a major practical barrier and enabled iterative testing across a range of stiffness conditions. The controlled in vitro rig also facilitated multimodal measurements, enabling assessment of whether combining modalities could leverage complementary strengths to improve vascular characterisation beyond PPG alone. Overall, the in vitro model provided a repeatable, ethically low-burden platform to test the impact of stiffness on PPG-derived features under controlled haemodynamic conditions, thereby offering a practical testbed for mechanistic interpretation and feature screening prior to in vivo translation.

Through this work, a reproducible method was developed for fabricating silicone-based vascular tissue phantoms with tuneable mechanical properties. This work introduced a refined fabrication method, in which varying the proportions of additives, specifically retarder, deadener, and hardener, made it possible to finely control wall thickness and elasticity, thereby enabling the simulation of both healthy and diseased vessels. While high concentrations of deadener occasionally made it difficult to remove the custom vessel, the overall fabrication process, based on a dip-coating technique, was

straightforward, cost-effective, and compatible with a variety of elastomer formulations. Mechanical characterisation through tensile, compression, and hardness testing confirmed that the phantoms spanned a range of Young's modulus and Shore hardness values representative of femoral arteries and adjacent soft tissue. However, it is acknowledged that the method assumed mechanical uniformity and did not account for local inhomogeneities within the vessel wall.

Simultaneous PPG recordings from identical vessel–tissue phantoms demonstrated that the in vitro vascular model was capable of replicating vascular symmetry. The phantoms, fabricated from a single silicone batch and continuous vessel segment, produced statistically comparable PPG signals across several features, including amplitude, rise and decay times, and waveform slopes. While the bilateral setup confirmed the repeatability of the fabrication process, minor variations in signal morphology were still observed, likely attributable to inter-sensor variability or mechanical artefacts. Notably, IR PPG signals demonstrated greater stability and were less susceptible to variation across repeated measurements compared to red PPG signals, possibly due to their deeper tissue penetration.

A range of morphological features were extracted from filtered PPG signals to investigate how waveform characteristics change with increasing arterial stiffness, without relying on derivative-based metrics. Comparisons between red and IR signals revealed that certain features exhibited stronger correlations with arterial stiffness than others. Specifically, area-related features in the red wavelength were more strongly associated with stiffness, whereas pulse width–based features were more strongly correlated in the IR wavelength. Although the analysis was limited to red and IR signals, the findings support the validity of using multi-wavelength PPG sensors for arterial stiffness assessment, as feature-stiffness correlations differed between wavelengths. Visual and statistical analyses of key features including amplitude, AUC, pulse width, and metrics such as skewness, mirrored expected physiological trends, reinforcing the reliability of the in vitro model for controlled vascular ageing assessment. Based on feature rankings, four primary metrics were identified for tracking arterial stiffness in subsequent experimental studies: amplitude, AUC, median upslope-to-downslope ratio, and median end datum difference. These features were applied in both the study assessing the

feasibility of PPG in detecting arterial stiffness in hypertension and the investigation exploring a multimodal assessment of arterial stiffness using PPG and LDF.

PPG features were found to correlate with arterial health under both hypertensive and normotensive conditions. The findings indicated that specific features, particularly amplitude, AUC, and median end datum difference, differentiated significantly between healthy and unhealthy vessels at elevated BP levels. However, distinctions between intermediate vascular states were less pronounced. Under hypotensive conditions, healthy vessels displayed greater variability in PPG features, likely due to their increased elasticity compared to intermediate or stiffened vessels. This enhanced elasticity may have contributed to amplified fluctuations in vessel expansion and contraction, thereby increasing signal variability. It is suggested that variability itself could serve as a potential diagnostic indicator of vascular ageing; however, further research is needed to determine whether such variability can be reliably quantified and clinically leveraged. Additionally, changes in fiducial point ratios derived from the SDPPG provided additional insight into arterial stiffness, particularly in hypertensive conditions. At lower BP levels, however, some fiducial ratios showed minimal or no change, indicating limited sensitivity in hypotensive states.

For the first time, PPG and LDF were combined in an in vitro setting to evaluate whether their complementary sensitivities could improve vascular health assessment across two different BMF formulations. The multimodal approach demonstrated that each modality could differentiate between healthy and unhealthy vascular states, although with distinct strengths and limitations. PPG showed limited ability to distinguish between intermediate and healthy states, whereas LDF was less successful in separating intermediate from unhealthy states. The choice of scattering agent within the BMF was also found to influence modality performance; intralipid-based BMF enhanced LDF DC flux sensitivity while simultaneously suppressing the IR PPG signal, whereas LPFS-based BMF preserved PPG signal quality yet provided weaker LDF flux differentiation. The findings highlight the potential of PPG and LDF, whether used independently or in combination, as non-invasive methods for the identification of vascular stiffness and the early detection of vascular ageing.

Overall, the methods used in this work showed that the findings differed depending on the PPG wavelength, feature extraction strategy (morphological versus derivative-based metrics such as SDPPG), and measurement modality. The wavelength analysis demonstrated that stiffness sensitivity was feature-dependent, with area-related features showing stronger associations in the red channel and width-based features showing stronger associations in the IR channel. In terms of feature strategy, morphological metrics extracted from the filtered waveform differentiated vascular states, and the addition of SDPPG fiducial ratios provided complementary information most clearly under hypertensive conditions, with reduced sensitivity at lower BP. Finally, the multimodal assessment highlighted that PPG and LDF capture partly distinct physiological information; while LDF is not a direct measure of conduit-vessel stiffness and is primarily sensitive to microvascular perfusion, its ability to separate vascular states via DC flux supports further investigation into whether integrating LDF with PPG can improve vascular characterisation beyond PPG alone.

11.1.2 Challenges and Limitations

While the experimental studies presented in this thesis provide evidence that PPG could potentially be utilised for the assessment of vascular ageing, practical challenges and limitations must be acknowledged.

A limitation of the vessel–tissue phantoms was the absence of layered anatomical structure, including distinct intima, media, and adventitia layers, which may influence in vivo PPG signals. In addition, the vessel-tissue phantoms were not optically characterised. Addressing these limitations could improve the physiological relevance of future models. Nonetheless, the phantoms developed in this work provided a structure with mechanical properties closely resembling those of human vasculature and therefore yielded valuable experimental insights.

In the experimental studies described in Chapter 9 and Chapter 10, differentiating between intermediate stiffness states proved challenging. In the study presented in Chapter 9, statistical differences were observed between the intermediate and unhealthy states; however, distinguishing between the healthy and intermediate states was more difficult. Under hypotensive conditions, feature variability increased, with signal characteristics overlapping across different vessel stiffness levels. This overlap reduces

the confidence in the reliable classification of vessels according to stiffness unless further research in signal processing is undertaken to determine whether such variability can be exploited for clinical applications. The findings in Chapter 10 suggested that differentiating between the healthy and intermediate states was more challenging using PPG technology, whereas separating the unhealthy and intermediate states was more difficult using LDF technology.

A limitation observed in the multimodal study was the dependence of PPG and LDF signals on the scattering properties of the BMF. While intralipid produced clearer separation of LDF DC flux values between vascular states, it simultaneously suppressed the IR PPG signal. In contrast, the LPFS-based BMF preserved PPG signal quality yet generated weaker LDF differentiation, particularly between the intermediate and unhealthy state. These findings highlight the challenge of optimising a single BMF formulation that performs consistently well across modalities. Additionally, certain PPG features, including the median upslope–downslope ratio and the median end datum difference, demonstrated instability and high variability. Such variability raises concerns regarding their reliability and could limit their applicability for vascular ageing assessment, both in unimodal and multimodal applications.

It should also be noted that, within the in vitro setup, only regional stiffness was introduced. As a result, the research could not capture systemic vascular ageing. Nonetheless, the work provides a foundation for exploring the use of PPG in the early detection of vascular health. Despite its limitations, the in vitro model offers a controlled and repeatable environment in which vascular conditions can be simulated. Such an approach enables the isolation of variables and the validation of PPG-based metrics before their application in more complex in vivo studies or in primary care settings.

11.2 Conclusions

The research presented in this thesis demonstrates the potential of PPG to differentiate between vessels of varying arterial stiffness through PWA. The work introduces novel, customisable vessel–tissue phantoms, mechanically characterised to replicate the properties of human vasculature. Using an in vitro vascular model, these phantoms were integrated into the system, and PPG technology was employed to evaluate whether it could reliably distinguish between healthy and atherosclerotic arteries. Experiments were conducted in both bilateral and single-branch configurations to investigate the feasibility of PPG in monitoring vascular ageing, with a primary focus on arterial stiffness. Dual-modality monitoring, incorporating LDF alongside PPG, was also explored to determine whether PPG alone was sufficient or if combining modalities enhanced the assessment of vascular ageing.

11.3 Future Work

While the findings indicate that PPG holds promise for vascular ageing assessment, further research is required to validate its clinical utility at the primary care level.

Overall, future work should prioritise (i) improving the physiological relevance of the in vitro platform, (ii) reducing measurement artefacts, and (iii) strengthening sensitivity to intermediate stiffness states and low BP conditions. The in vitro platform could be further improved through optical characterisation of the vessel–tissue phantoms and BMF, including the development of skin tone–matched phantom designs to better represent in vivo optical variability. In parallel, the dataset generated by the in vitro platform could support data-driven modelling, including the evaluation of ML approaches for vascular characterisation.

Within the fabrication process of the customisable vessel–tissue phantoms, the dip-coating stage could be further investigated, particularly regarding factors influencing the mechanical properties of the phantoms. The effects of dip-coater speed and heating element temperature could be examined to reduce reliance on retarder concentration. It is hypothesised that increasing the dip-coater speed could decrease the requirement for retarder concentration, as the uncured silicone would reach the maximum coating height more rapidly. Furthermore, while this research primarily focused on femoral artery stiffening, future iterations could incorporate additional arterial pathologies, such as

plaques or calcification, to simulate more complex disease states. The phantoms could also be refined to include distinct intima, media, and adventitia layers, allowing layer-specific investigations and more closely replicating human arterial structure.

To minimise waveform artefacts, potentially caused by vibrations, the use of a non-mechanical pump could be considered as an alternative to the current pulsatile pump. Future studies should investigate whether the pump type influences signal quality. Additionally, in the experimental studies, sensor placement varied between being positioned above or below the phantom, depending on the sensor type. Further optimisation of sensor positioning and contact pressure is needed to ensure consistently high-quality signals. Setting the in vitro model in bilateral mode could also facilitate exploration of PPG's utility in detecting signal asymmetry, as may occur in conditions such as PAD. Moreover, as the experimental studies in this thesis modelled only segmental stiffness, systemic vascular ageing could not be fully captured. Future developments could expand the in vitro network to better represent systemic vascular dynamics.

Further work should also explore the wavelength sensitivity of extracted features. Chapter 8 focused exclusively on red and IR wavelengths; however, other wavelengths, such as green, may exhibit higher sensitivity for specific features. Investigating a broader wavelength range, and potentially employing multiple wavelengths in parallel, could strengthen vascular ageing assessments. Understanding how arterial stiffness–related features vary by wavelength may also inform sensor selection for wearable or clinical PPG devices. Additionally, as Chapter 8 analysed only filtered signals, future work should consider derivatives to identify the most stiffness-sensitive features, which could then be combined for clinical use.

Optimisation of PPG feature extraction for intermediate disease states and assessment of PPG performance under low BP conditions should also be prioritised. While PPG successfully distinguished between intermediate and unhealthy states, the transition from healthy to intermediate was less distinct. Introducing an additional phantom representing an incremental intermediate stage between the existing intermediate and unhealthy states could help identify the threshold at which mechanical changes become detectable. For clinical application, it is important to establish normative thresholds for

healthy and unhealthy vascular states, as well as to determine the number of intermediate states PPG can reliably identify. This may be achieved by fabricating phantoms with incremental stiffness variations. Low BP conditions in this study introduced greater variability than normotensive or hypertensive states, which may itself hold diagnostic value. Future research could investigate whether this variability can be exploited clinically, particularly through signal processing techniques. Additionally, the inclusion of the median upslope-to-downslope ratio as a clinical feature should be reassessed, given the absence of statistically significant differences between the healthy and unhealthy phantoms under hypertensive conditions and in cases where scattering agents were introduced into the BMF. The qualitative findings from Chapter 9 suggest that SDPPG may be valuable in identifying vascular ageing, particularly in hypertensive states. However, sex-related differences require further investigation to determine their impact on clinical implementation. The diagnostic utility of SDPPG for intermediate states also remains unclear and should be examined further.

Future work should explore optimising scattering concentrations within BMFs to balance performance when multiple modalities are utilised. It is suggested that intralipid concentrations be reduced to minimise IR suppression, or that LPFS levels be increased, as the present study was constrained by using lower LPFS levels than intralipid. Additional multimodal investigations at lower flow rates are also recommended; while PPG signals may be compromised under such conditions, LDF may maintain performance and reduce the risk of saturation. Furthermore, applying frequency-domain and wavelet analyses could enhance the characterisation of LDF signals in future studies. To evaluate the feasibility of LDF and PPG, individually or in combination, for point-of-care application, in vivo studies are essential, commencing with healthy participants, and progressing to patients with established vascular risk. In this research, the LDF device recorded flux via the tissue perfusion output channel; however, as flux reflects the combined influence of moving blood cell concentration and velocity, future work should, where available, analyse these components separately to aid physiological interpretation.

This research supports the potential of PPG for vascular ageing assessment, particularly in distinguishing between healthy and unhealthy vasculature. However, further work is required before clinical integration.

Appendix

A.0 Literature Search

This section provides the full set of literature search keywords and Boolean combinations used across the databases in this research.

Table 25: Full literature search keywords and logical combinations for each database.

Database	Search string
PubMed	(((vascular ageing[Title]) OR (vascular aging[Title]) OR (arterial stiffness[Title])) AND ((non-invasive[Title/Abstract]) OR (PPG[Title/Abstract]) OR (photoplethysmography[Title/Abstract]) OR (photoplethysmogram[Title/Abstract])))
Embase	(vascular ageing or vascular aging or arterial stiffness).ti. and (non-invasive or PPG or photoplethysmography or photoplethysmogram).ab.
Scopus	(TITLE (vascular AND aging) OR TITLE (vascular AND ageing) OR TITLE (arterial AND stiffness)) AND (ABS (non-invasive) OR ABS (ppg) OR ABS (photoplethysmography) OR ABS (photoplethysmogram))
Web of Science	((TI=(vascular aging) OR TI=(vascular ageing) OR TI=(arterial stiffness)) AND (AB=(non-invasive) OR AB=(PPG) OR AB=(photoplethysmography) OR AB=(photoplethysmogram)))
Cochrane Library	((TI=(vascular aging) OR TI=(vascular ageing) OR TI=(arterial stiffness)) AND (AB=(non-invasive) OR AB=(PPG) OR AB=(photoplethysmography) OR AB=(photoplethysmogram)))

A.1 Scope of Vessel-Tissue Phantoms Fabrication

This appendix provides step-by-step protocols for:

- Fabrication of silicone vessels using a precision dip-coating method
- Fabrication of vessel–tissue phantoms using 3D-printed moulds

A.2 Materials

Vessel fabrication

- PlatSil Gel-10 (Part A, Part B) (Polytek Development Corp., Easton, PA, USA)
- Retarder (Polytek Development Corp., Easton, PA, USA)
- Smith's Deadener (Polytek Development Corp., Easton, PA, USA)
- Hardener (Polytek Development Corp., Easton, PA, USA)
- Commercial silicone tubing used as internal form (Hilltop Products Limited, Warrington, UK)

Tissue fabrication

- Gel-00 (Part A, Part B) (Polytek Development Corp., Easton, PA, USA)
- 3D-printed moulds (78 mm × 25 mm × 38 mm; length × width × height)
- Metal rods (used to support the vessel during embedding)

General

- Disposable mixing cups, stirrers
- Precision scale (model: Scout, Ohaus, Parsippany, NJ, USA)
- Vacuum chamber (Applied Vacuum Engineering, Bristol, UK)

A.3 Equipment and Key Settings

- Precision Dip Coater (Qualtech Products Industry, Denver, CO, USA)
    - Withdrawal speed: 40 mm/min
    - Heating element warm-up: 3 min
    - Heating element temperature: 275 °C

A.4 Protocol 1: Fabrication of Custom Silicone Vessels (Dip-Coating)

- Weigh Part A and Part B separately using a precision scale.
- Combine Part A and Part B at 1:1 by weight.
- Add retarder to extend working time:
- 1% retarder of total mixture weight doubled pour time.
- Mix thoroughly for 3 minutes.
- If modifying stiffness, add deadener or hardener (Section A.4.4). For the final femoral artery vessels in Section A.6, deadener was not used (deadener = 0%).
- Degas in vacuum chamber for 3 minutes to remove bubbles.

A.4.1 Dip Coater Setup

- Pour degassed elastomer mixture into the silicone dip pot.
- Attach the silicone tubing "form" onto pulleys and route through heating element.
- Attach one end of the form to a tension weight and secure the other end to the dip-coater arm.
- Activate heating element for 3 minutes until 275 °C is reached.

A.4.2 Coating and Curing

- Start withdrawal at a fixed speed of 40 mm/min.
- Allow the form to pass through the heated region during withdrawal to avoid premature curing.
- Once the arm reaches its highest point, deactivate heating.
- Leave coated tubing to fully cure for 4 hours at room temperature.
- Carefully separate and remove the internal form from the cured vessel.

A.4.3 Controlling geometry and stiffness

Two independent adjustments were used:

1. *Wall thickness control (retarder-based)*
   - Internal form OD: 3 mm
   - Retarder amount varied to change wall thickness.

2. *Elasticity control (deadener/hardener-based)*
   - Internal form OD: 2.6 mm
   - Additives used to tune stiffness.

A.5 Protocol 2: Vessel–Tissue Phantom Fabrication (Embedding in Gel-00)

A.5.1 Tissue material preparation

- Weigh Gel-00 Part A and Part B at 1:1 by weight.
- Mix thoroughly for 3 minutes.
- Degas mixture in vacuum chamber until bubbles are removed (time: 3 min).

A.5.2 Moulding and Embedding

- Position the fabricated vessel horizontally within the 3D-printed mould using metal rods. Place rods 3 mm above the base of the mould.
- Pour degassed Gel-00 into the mould slowly to minimise bubble formation.
- Cure fully for 4 hours at room temperature.
- Demould to obtain vessel–tissue phantom.

A.6 Target Femoral Artery Vessels

Following mechanical characterisation, three custom femoral arteries were fabricated:

- Healthy: Young's modulus 0.82 MPa
- Intermediate: Young's modulus 1.48 MPa
- Atherosclerotic: Young's modulus 2.06 MPa

The targeted femoral artery vessels had measured dimensions of:

- ID: 2.95 mm
- OD: 3.96 mm

Table 26: Material formulation for fabricating healthy, intermediate, and atherosclerotic femoral artery vessels. Deadener/Hardener (%) is expressed as a percentage of the total mixture (Part A + Part B + additive) by weight.

Vessel type	Form OD (mm)	Retarder (%)	Deadener (%)	Hardener (%)	Young's Modulus (MPa)	ID (mm)	OD (mm)
Healthy	2.6	1.5	0	23.08%	0.82	2.95	3.96
Intermediate	2.6	1.5	0	50.00%	1.48	2.95	3.96
Atherosclerotic	2.6	1.5	0	54.55%	2.06	2.95	3.96

References

[1] ‘Cardiovascular diseases’. Accessed: Feb. 02, 2023. [Online]. Available: https://www.who.int/health-topics/cardiovascular-diseases

[2] D. Adhikary, S. Barman, R. Ranjan, and H. Stone, ‘A Systematic Review of Major Cardiovascular Risk Factors: A Growing Global Health Concern’, *Cureus*, vol. 14, no. 10, p. e30119, doi: 10.7759/cureus.30119.

[3] P. Karimpour, J. M. May, and P. A. Kyriacou, ‘Photoplethysmography for the Assessment of Arterial Stiffness’, *Sensors (Basel)*, vol. 23, no. 24, p. 9882, Dec. 2023, doi: 10.3390/s23249882.

[4] D. C. Y. Cheng, R. E. Climie, M. Shu, S. M. Grieve, R. Kozor, and G. A. Figtree, ‘Vascular aging and cardiovascular disease: pathophysiology and measurement in the coronary arteries’, *Front Cardiovasc Med*, vol. 10, p. 1206156, Nov. 2023, doi: 10.3389/fcvm.2023.1206156.

[5] J. A. Maier *et al.*, ‘Aging and Vascular Disease: A Multidisciplinary Overview’, *Journal of Clinical Medicine*, vol. 12, no. 17, Aug. 2023, doi: 10.3390/jcm12175512.

[6] J. Stewart, G. Manmathan, and P. Wilkinson, ‘Primary prevention of cardiovascular disease: A review of contemporary guidance and literature’, *JRSM Cardiovasc Dis*, vol. 6, p. 2048004016687211, Jan. 2017, doi: 10.1177/2048004016687211.

[7] T. Williams, ‘What is the future of wearable technology in healthcare?’, Digital Health Technology News. Accessed: Aug. 01, 2023. [Online]. Available: https://www.healthtechdigital.com/what-is-the-future-of-wearable-technology-in-healthcare/

[8] P. H. Charlton, P. A. Kyriacou, J. Mant, V. Marozas, P. Chowienczyk, and J. Alastruey, ‘Wearable Photoplethysmography for Cardiovascular Monitoring’, *Proceedings of the IEEE*, vol. 110, no. 3, pp. 355–381, Mar. 2022, doi: 10.1109/JPROC.2022.3149785.

[9] S. Canali, V. Schiaffonati, and A. Aliverti, ‘Challenges and recommendations for wearable devices in digital health: Data quality, interoperability, health equity, fairness’, *PLOS Digit Health*, vol. 1, no. 10, p. e0000104, Oct. 2022, doi: 10.1371/journal.pdig.0000104.

[10] S. Zanelli *et al.*, ‘Developing technologies to assess vascular ageing: a roadmap from VascAgeNet’, *Physiol Meas*, vol. 45, no. 12, p. 121001, Dec. 2024, doi: 10.1088/1361-6579/ad548e.

[11] A. Arackal and K. Alsayouri, 'Histology, Heart', in *StatPearls*, Treasure Island (FL): StatPearls Publishing, 2025. Accessed: May 29, 2025. [Online]. Available: http://www.ncbi.nlm.nih.gov/books/NBK545143/

[12] C. C. Tarniceriu *et al.*, 'The Pulmonary Venous Return from Normal to Pathological—Clinical Correlations and Review of Literature', *Medicina (Kaunas)*, vol. 57, no. 3, p. 293, Mar. 2021, doi: 10.3390/medicina57030293.

[13] R. B. Hinton and K. E. Yutzey, 'Heart Valve Structure and Function in Development and Disease', *Annu Rev Physiol*, vol. 73, pp. 29–46, 2011, doi: 10.1146/annurev-physiol-012110-142145.

[14] V. Mahadevan, 'Anatomy of the heart', *Surgery (Oxford)*, vol. 36, no. 2, pp. 43–47, Feb. 2018, doi: 10.1016/j.mpsur.2017.11.010.

[15] D. B. Tran, C. Weber, and R. A. Lopez, 'Anatomy, Thorax, Heart Muscles', in *StatPearls*, Treasure Island (FL): StatPearls Publishing, 2025. Accessed: Jun. 02, 2025. [Online]. Available: http://www.ncbi.nlm.nih.gov/books/NBK545195/

[16] Y. Cao, S. Duca, and J. Cao, 'Epicardium in Heart Development', *Cold Spring Harb Perspect Biol*, vol. 12, no. 2, p. a037192, Feb. 2020, doi: 10.1101/cshperspect.a037192.

[17] I. Rehman, A. Nassereddin, and A. Rehman, 'Anatomy, Thorax, Pericardium', in *StatPearls [Internet]*, StatPearls Publishing, 2023. Accessed: Jun. 05, 2025. [Online]. Available: https://www.ncbi.nlm.nih.gov/books/NBK482256/

[18] A. M. Smits, E. Dronkers, and M.-J. Goumans, 'The epicardium as a source of multipotent adult cardiac progenitor cells: Their origin, role and fate', *Pharmacological Research*, vol. 127, pp. 129–140, Jan. 2018, doi: 10.1016/j.phrs.2017.07.020.

[19] K. R. Kumar, R. E. Kirsch, and C. P. Hornik, '13 - Cardiovascular Physiology for Intensivists', in *Critical Heart Disease in Infants and Children (Third Edition)*, R. M. Ungerleider, J. N. Meliones, K. Nelson McMillan, D. S. Cooper, and J. P. Jacobs, Eds., Philadelphia: Elsevier, 2019, pp. 111-133.e5. doi: 10.1016/B978-1-4557-0760-7.00013-9.

[20] Z. S. Bruss and A. Raja, 'Physiology, Stroke Volume', in *StatPearls*, Treasure Island (FL): StatPearls Publishing, 2025. Accessed: Jun. 02, 2025. [Online]. Available: http://www.ncbi.nlm.nih.gov/books/NBK547686/

[21] J. King and D. R. Lowery, ‘Physiology, Cardiac Output’, in *StatPearls*, Treasure Island (FL): StatPearls Publishing, 2025. Accessed: May 01, 2025. [Online]. Available: http://www.ncbi.nlm.nih.gov/books/NBK470455/

[22] E. Mejía-Mejía, J. Allen, K. Budidha, C. El-Hajj, P. A. Kyriacou, and P. H. Charlton, ‘4 - Photoplethysmography signal processing and synthesis’, in *Photoplethysmography*, J. Allen and P. Kyriacou, Eds., Academic Press, 2022, pp. 69–146. doi: 10.1016/B978-0-12-823374-0.00015-3.

[23] R. Chaudhry, J. H. Miao, and A. Rehman, ‘Physiology, Cardiovascular’, in *StatPearls*, Treasure Island (FL): StatPearls Publishing, 2022. Accessed: Oct. 31, 2022. [Online]. Available: http://www.ncbi.nlm.nih.gov/books/NBK493197/

[24] W. D. Tucker, Y. Arora, and K. Mahajan, ‘Anatomy, Blood Vessels’, in *StatPearls*, Treasure Island (FL): StatPearls Publishing, 2025. Accessed: Jun. 03, 2025. [Online]. Available: http://www.ncbi.nlm.nih.gov/books/NBK470401/

[25] A. Taki, A. Kermani, S. M. Ranjbarnavazi, and A. Pourmodheji, ‘Chapter 4 - Overview of Different Medical Imaging Techniques for the Identification of Coronary Atherosclerotic Plaques’, in *Computing and Visualization for Intravascular Imaging and Computer-Assisted Stenting*, in The Elsevier and MICCAI Society Book Series. , Academic Press, 2017, pp. 79–106. doi: 10.1016/B978-0-12-811018-8.00004-7.

[26] M. Watson, H. Byrne, C. Macaskill, and M. Myerscough, ‘A multiphase model of growth factor-regulated atherosclerotic cap formation’, *Journal of Mathematical Biology*, vol. 81, Aug. 2020, doi: 10.1007/s00285-020-01526-6.

[27] A. J. A. Leloup, C. E. Van Hove, A. Heykers, D. M. Schrijvers, G. R. Y. De Meyer, and P. Fransen, ‘Elastic and Muscular Arteries Differ in Structure, Basal NO Production and Voltage-Gated Ca2+-Channels’, *Front. Physiol.*, vol. 6, Dec. 2015, doi: 10.3389/fphys.2015.00375.

[28] D. B. Young, ‘Venous Return’, in *Control of Cardiac Output*, Morgan & Claypool Life Sciences, 2010. Accessed: Jun. 03, 2025. [Online]. Available: https://www.ncbi.nlm.nih.gov/books/NBK54476/

[29] A. K. Verma *et al.*, ‘Skeletal Muscle Pump Drives Control of Cardiovascular and Postural Systems’, *Sci Rep*, vol. 7, no. 1, p. 45301, Mar. 2017, doi: 10.1038/srep45301.

[30] F. L. Abel and J. A. Waldhausen, 'Respiratory and cardiac effects on venous return', *American Heart Journal*, vol. 78, no. 2, pp. 266–275, Aug. 1969, doi: 10.1016/0002-8703(69)90019-2.

[31] A. Bhusal *et al.*, 'Development and characterization of silicone-based tissue phantoms for pulse oximeter performance testing', *Journal of Biomedical Optics*, vol. 29, no. Suppl 3, p. S33314, Jan. 2025, doi: 10.1117/1.JBO.29.S3.S33314.

[32] S. Iurciuc, C. Anca Maria, F. Mitu, R. Heredea, and M. Iurciuc, 'Vascular aging and subclinical atherosclerosis: Why such a "never ending" and challenging story in cardiology?', *Clinical Interventions in Aging*, vol. Volume 12, pp. 1339–1345, Aug. 2017, doi: 10.2147/CIA.S141265.

[33] S. J. Zieman, V. Melenovsky, and D. A. Kass, 'Mechanisms, Pathophysiology, and Therapy of Arterial Stiffness', *Arteriosclerosis, Thrombosis, and Vascular Biology*, vol. 25, no. 5, pp. 932–943, May 2005, doi: 10.1161/01.ATV.0000160548.78317.29.

[34] X. Xu *et al.*, 'Age-related Impairment of Vascular Structure and Functions', *Aging Dis*, vol. 8, no. 5, pp. 590–610, Oct. 2017, doi: 10.14336/AD.2017.0430.

[35] J. D. Pollock, I. V. Murray, S. J. Bordes, and A. N. Makaryus, 'Physiology, Cardiovascular Hemodynamics', in *StatPearls*, Treasure Island (FL): StatPearls Publishing, 2025. Accessed: Jun. 04, 2025. [Online]. Available: http://www.ncbi.nlm.nih.gov/books/NBK470310/

[36] T. J. LaRocca, C. R. Martens, and D. R. Seals, 'Nutrition and other lifestyle influences on arterial aging', *Ageing Research Reviews*, vol. 39, pp. 106–119, Oct. 2017, doi: 10.1016/j.arr.2016.09.002.

[37] L. K. Hill, J. J. Sollers, and J. F. Thayer, 'Resistance Reconstructed: Estimation of Total Peripheral Resistance From Computationally-Derived Cardiac Output', *Biomed Sci Instrum*, vol. 49, pp. 216–223, 2013.

[38] Y. Nguyen and V. Bora, 'Arterial Pressure Monitoring', in *StatPearls*, Treasure Island (FL): StatPearls Publishing, 2025. Accessed: Jun. 04, 2025. [Online]. Available: http://www.ncbi.nlm.nih.gov/books/NBK556127/

[39] C. L. Wells and M. Townsend, 'Chapter 14 - Management of the Acutely Ill and Medically Complex Older Patient', in *Guccione's Geriatric Physical Therapy (Fourth Edition)*, D. Avers and R. A. Wong, Eds., St. Louis (MO): Mosby, 2020, pp. 309–343. doi: 10.1016/B978-0-323-60912-8.00014-2.

[40] F. Rahman *et al.*, 'Relation of Diastolic Blood Pressure and Coronary Artery Calcium to Coronary Events and Outcomes (From the Multi-Ethnic Study of Atherosclerosis)', *Am J Cardiol*, vol. 120, no. 10, pp. 1797–1803, Nov. 2017, doi: 10.1016/j.amjcard.2017.07.094.

[41] S. Singh, L. V. Randle, P. T. Callaghan, C. J. E. Watson, and C. J. Callaghan, 'Beyond Poiseuille: Preservation Fluid Flow in an Experimental Model', *J Transplant*, vol. 2013, p. 605326, 2013, doi: 10.1155/2013/605326.

[42] T. Kiserud and G. Haugen, '58 - Umbilical Circulation', in *Fetal and Neonatal Physiology (Fifth Edition)*, R. A. Polin, S. H. Abman, D. H. Rowitch, W. E. Benitz, and W. W. Fox, Eds., Elsevier, 2017, pp. 599-611.e2. doi: 10.1016/B978-0-323-35214-7.00058-5.

[43] X. Xu *et al.*, 'Recent Progress in Vascular Aging: Mechanisms and Its Role in Age-related Diseases', *Aging Dis*, vol. 8, no. 4, pp. 486–505, Jul. 2017, doi: 10.14336/AD.2017.0507.

[44] M. Cortes-Canteli and C. Iadecola, 'Alzheimer's Disease and Vascular Aging', *Journal of the American College of Cardiology*, vol. 75, no. 8, pp. 942–951, Mar. 2020, doi: 10.1016/j.jacc.2019.10.062.

[45] Ž. Reiner, 'Arterial Stiffness—What Do We Know about It and What Do We Expect from This Biomarker?', *Journal of Clinical Medicine*, vol. 11, no. 16, p. 4843, Aug. 2022, doi: 10.3390/jcm11164843.

[46] W. Fhayli, Q. Boëté, O. Harki, A. Briançon-Marjollet, M.-P. Jacob, and G. Faury, 'Rise and fall of elastic fibers from development to aging. Consequences on arterial structure-function and therapeutical perspectives', *Matrix Biology*, vol. 84, pp. 41–56, Nov. 2019, doi: 10.1016/j.matbio.2019.08.005.

[47] D. H. Endemann and E. L. Schiffrin, 'Endothelial dysfunction', *J Am Soc Nephrol*, vol. 15, no. 8, pp. 1983–1992, Aug. 2004, doi: 10.1097/01.ASN.0000132474.50966.DA.

[48] M. Y. Henein, S. Vancheri, G. Longo, and F. Vancheri, 'The Role of Inflammation in Cardiovascular Disease', *Int J Mol Sci*, vol. 23, no. 21, p. 12906, Oct. 2022, doi: 10.3390/ijms232112906.

[49] G. Van den Bergh, B. Opdebeeck, P. C. D'Haese, and A. Verhulst, 'The Vicious Cycle of Arterial Stiffness and Arterial Media Calcification', *Trends in Molecular Medicine*, vol. 25, no. 12, pp. 1133–1146, Dec. 2019, doi: 10.1016/j.molmed.2019.08.006.

[50] L. Stoner, D. Credeur, D. R. Dolbow, and D. R. Gater, 'Vascular health toolbox for spinal cord injury: Recommendations for clinical practice', *Atherosclerosis*, vol. 243, no. 2, pp. 373–382, Dec. 2015, doi: 10.1016/j.atherosclerosis.2015.10.013.

[51] H.-L. Kim, 'Arterial stiffness and hypertension', *Clin Hypertens*, vol. 29, p. 31, Dec. 2023, doi: 10.1186/s40885-023-00258-1.

[52] I. B. Wilkinson, H. MacCallum, L. Flint, J. R. Cockcroft, D. E. Newby, and D. J. Webb, 'The influence of heart rate on augmentation index and central arterial pressure in humans', *J Physiol*, vol. 525, no. Pt 1, pp. 263–270, May 2000, doi: 10.1111/j.1469-7793.2000.t01-1-00263.x.

[53] R. Pahwa and I. Jialal, 'Atherosclerosis', in *StatPearls*, Treasure Island (FL): StatPearls Publishing, 2025. Accessed: Jun. 10, 2025. [Online]. Available: http://www.ncbi.nlm.nih.gov/books/NBK507799/

[54] R. D. Shahjehan, S. Sharma, and B. S. Bhutta, 'Coronary Artery Disease', in *StatPearls*, Treasure Island (FL): StatPearls Publishing, 2025. Accessed: Jun. 10, 2025. [Online]. Available: http://www.ncbi.nlm.nih.gov/books/NBK564304/

[55] G. Dhaliwal and D. Mukherjee, 'Peripheral arterial disease: Epidemiology, natural history, diagnosis and treatment', *Int J Angiol*, vol. 16, no. 2, pp. 36–44, 2007, doi: 10.1055/s-0031-1278244.

[56] D. Kyle *et al.*, 'Accuracy of Peripheral Arterial Disease Registers in UK General Practice: Case-Control Study', *J Prim Care Community Health*, vol. 11, p. 2150132720946148, Sep. 2020, doi: 10.1177/2150132720946148.

[57] M. R. Zemaitis, J. M. Boll, and M. A. Dreyer, 'Peripheral Arterial Disease', in *StatPearls*, Treasure Island (FL): StatPearls Publishing, 2025. Accessed: Jun. 10, 2025. [Online]. Available: http://www.ncbi.nlm.nih.gov/books/NBK430745/

[58] A. Buttolph and A. Sapra, 'Gangrene', in *StatPearls*, Treasure Island (FL): StatPearls Publishing, 2023. Accessed: Aug. 08, 2023. [Online]. Available: http://www.ncbi.nlm.nih.gov/books/NBK560552/

[59] P. Karimpour, J. M. May, and P. A. Kyriacou, 'Feasibility of Photoplethysmography in Detecting Arterial Stiffness in Hypertension', *Photonics*, vol. 12, no. 5, Art. no. 5, May 2025, doi: 10.3390/photonics12050430.

[60] M. Bentham, G. Stansby, and J. Allen, 'Innovative Multi-Site Photoplethysmography Analysis for Quantifying Pulse Amplitude and Timing

Variability Characteristics in Peripheral Arterial Disease', *Diseases*, vol. 6, no. 3, Art. no. 3, Sep. 2018, doi: 10.3390/diseases6030081.

[61] D. J. Omeh and E. Shlofmitz, 'Angiography', in *StatPearls*, Treasure Island (FL): StatPearls Publishing, 2022. Accessed: Nov. 24, 2022. [Online]. Available: http://www.ncbi.nlm.nih.gov/books/NBK557477/

[62] C. M. Sena, L. Gonçalves, and R. Seiça, 'Methods to evaluate vascular function: a crucial approach towards predictive, preventive, and personalised medicine', *EPMA J*, vol. 13, no. 2, pp. 209–235, May 2022, doi: 10.1007/s13167-022-00280-7.

[63] 'PRISMA'. Accessed: Nov. 27, 2023. [Online]. Available: http://prisma-statement.org/prismastatement/flowdiagram.aspx

[64] J. Gong *et al.*, 'Sex-specific difference in the relationship between body fat percentage and arterial stiffness: Results from Fuzhou study', *The Journal of Clinical Hypertension*, vol. 25, no. 3, pp. 286–294, 2023, doi: 10.1111/jch.14649.

[65] H. Ji *et al.*, 'Measuring the Carotid to Femoral Pulse Wave Velocity (Cf-PWV) to Evaluate Arterial Stiffness', *J Vis Exp*, no. 135, p. 57083, May 2018, doi: 10.3791/57083.

[66] E. Cantürk *et al.*, 'Changes in Aortic Pulse Wave Velocity and the Predictors of Improvement in Arterial Stiffness Following Aortic Valve Replacement', *Ann Thorac Cardiovasc Surg*, vol. 23, no. 5, pp. 248–255, 2017, doi: 10.5761/atcs.oa.17-00062.

[67] E. Lurz, E. Aeschbacher, N. Carman, S. Schibli, C. Sokollik, and G. D. Simonetti, 'Pulse wave velocity measurement as a marker of arterial stiffness in pediatric inflammatory bowel disease: a pilot study', *Eur J Pediatr*, vol. 176, no. 7, pp. 983–987, Jul. 2017, doi: 10.1007/s00431-017-2927-7.

[68] C.-S. Liu *et al.*, 'Arterial stiffness measured as pulse wave velocity is highly correlated with coronary atherosclerosis in asymptomatic patients', *J Atheroscler Thromb*, vol. 18, no. 8, pp. 652–658, 2011, doi: 10.5551/jat.7021.

[69] S. Tsuchikura *et al.*, 'Brachial-ankle pulse wave velocity as an index of central arterial stiffness', *J Atheroscler Thromb*, vol. 17, no. 6, pp. 658–665, Jun. 2010, doi: 10.5551/jat.3616.

[70] K. Yufu, N. Takahashi, F. Anan, M. Hara, H. Yoshimatsu, and T. Saikawa, 'Brachial arterial stiffness predicts coronary atherosclerosis in patients at risk for cardiovascular diseases', *Jpn Heart J*, vol. 45, no. 2, pp. 231–242, Mar. 2004, doi: 10.1536/jhj.45.231.

[71] M. R. Scudder *et al.*, 'Dual impedance cardiography: An inexpensive and reliable method to assess arterial stiffness', *Psychophysiology*, vol. 58, no. 7, p. e13772, 2021, doi: 10.1111/psyp.13772.

[72] T. Miyoshi and H. Ito, 'Assessment of Arterial Stiffness Using the Cardio-Ankle Vascular Index', *Pulse (Basel)*, vol. 4, no. 1, pp. 11–23, Jul. 2016, doi: 10.1159/000445214.

[73] S. Darroudi *et al.*, 'Multivariate linear regression to predict association of non-invasive arterial stiffness with cardiovascular events', *ESC Heart Fail*, vol. 12, no. 2, pp. 1141–1150, Apr. 2025, doi: 10.1002/ehf2.15077.

[74] J. D. de Souza-Neto, Í. M. de Oliveira, H. A. Lima-Rocha, J. W. Oliveira-Lima, and F. Bacal, 'Hypertension and arterial stiffness in heart transplantation patients', *Clinics*, vol. 71, no. 9, pp. 494–499, Jan. 2016, doi: 10.6061/clinics/2016(09)02.

[75] R. Klocke, J. Cockcroft, G. Taylor, I. Hall, and D. Blake, 'Arterial stiffness and central blood pressure, as determined by pulse wave analysis, in rheumatoid arthritis', *Ann Rheum Dis*, vol. 62, no. 5, pp. 414–418, May 2003, doi: 10.1136/ard.62.5.414.

[76] Y. Zhang *et al.*, 'Non-Invasive Assessment of Early Atherosclerosis Based on New Arterial Stiffness Indices Measured with an Upper-Arm Oscillometric Device', *Tohoku J Exp Med*, vol. 241, no. 4, pp. 263–270, Apr. 2017, doi: 10.1620/tjem.241.263.

[77] C. Vlachopoulos *et al.*, 'The role of vascular biomarkers for primary and secondary prevention. A position paper from the European Society of Cardiology Working Group on peripheral circulation: Endorsed by the Association for Research into Arterial Structure and Physiology (ARTERY) Society', *Atherosclerosis*, vol. 241, no. 2, pp. 507–532, Aug. 2015, doi: 10.1016/j.atherosclerosis.2015.05.007.

[78] M.-C. Wang, A.-B. Wu, M.-F. Cheng, J.-Y. Chen, C.-S. Ho, and W.-C. Tsai, 'Association of Arterial Stiffness Indexes, Determined From Digital Volume Pulse Measurement and Cardiovascular Risk Factors in Chronic Kidney Disease', *American Journal of Hypertension*, vol. 24, no. 5, pp. 544–549, May 2011, doi: 10.1038/ajh.2010.266.

[79] S. C. Millasseau, R. P. Kelly, K. Prasad, J. R. Cockcroft, J. M. Ritter, and P. J. Chowienczyk, 'Noninvasive Assessment of the Digital Volume Pulse: Comparison With the Peripheral Pressure Pulse', *Hypertension*, vol. 36, no. 6, pp. 952–956, Dec. 2000, doi: 10.1161/01.HYP.36.6.952.

[80] C.-S. Choy, D. Y.-J. Wang, T.-B. Chu, W.-M. Choi, and H.-Y. Chiou, 'Correlation Between Arterial Stiffness Index and Arterial Wave Pattern and Incidence of Stroke', *International Journal of Gerontology*, vol. 4, no. 2, pp. 75–81, Jun. 2010, doi: 10.1016/S1873-9598(10)70027-2.

[81] T. Naessen, G. Einarsson, D. Henrohn, and G. Wikström, 'Peripheral Vascular Ageing in Pulmonary Arterial Hypertension as Assessed by Common Carotid Artery Intima Thickness and Intima/Media Thickness Ratio: An Investigation Using Non-Invasive High-Resolution Ultrasound', *Heart, Lung and Circulation*, vol. 32, no. 3, pp. 338–347, Mar. 2023, doi: 10.1016/j.hlc.2022.10.017.

[82] Z. Li, L. Du, F. Wang, and X. Luo, 'Assessment of the arterial stiffness in patients with acute ischemic stroke using longitudinal elasticity modulus measurements obtained with Shear Wave Elastography', *Med Ultrason*, vol. 18, no. 2, pp. 182–189, Jun. 2016, doi: 10.11152/mu.2013.2066.182.wav.

[83] A. Bjällmark, B. Lind, M. Peolsson, K. Shahgaldi, L.-Å. Brodin, and J. Nowak, 'Ultrasonographic strain imaging is superior to conventional non-invasive measures of vascular stiffness in the detection of age-dependent differences in the mechanical properties of the common carotid artery', *European Journal of Echocardiography*, vol. 11, no. 7, pp. 630–636, Aug. 2010, doi: 10.1093/ejechocard/jeq033.

[84] L. Arnold *et al.*, 'Short-Term Changes in Arterial Stiffness Measured by 2D Speckle Tracking in Patients Undergoing Transcatheter Aortic Valve Implantation', *Journal of Clinical Medicine*, vol. 13, no. 1, Art. no. 1, Jan. 2024, doi: 10.3390/jcm13010222.

[85] K.-W. Kang *et al.*, 'Cardiac magnetic resonance imaging-derived pulmonary artery distensibility index correlates with pulmonary artery stiffness and predicts functional capacity in patients with pulmonary arterial hypertension', *Circ J*, vol. 75, no. 9, pp. 2244–2251, 2011, doi: 10.1253/circj.cj-10-1310.

[86] H. Ha *et al.*, 'Age-Related Vascular Changes Affect Turbulence in Aortic Blood Flow', *Front Physiol*, vol. 9, p. 36, Jan. 2018, doi: 10.3389/fphys.2018.00036.

[87] M. Sorelli, A. Perrella, and L. Bocchi, 'Detecting Vascular Age Using the Analysis of Peripheral Pulse', *IEEE Transactions on Biomedical Engineering*, vol. 65, no. 12, pp. 2742–2750, Dec. 2018, doi: 10.1109/TBME.2018.2814630.

[88] E. M. Rogers, N. F. Banks, and N. D. M. Jenkins, 'Metabolic and microvascular function assessed using near-infrared spectroscopy with vascular occlusion in

women: age differences and reliability', *Experimental Physiology*, vol. 108, no. 1, pp. 123–134, 2023, doi: 10.1113/EP090540.

[89] F. V. Melo E Silva *et al.*, 'Association of Body Composition with Arterial Stiffness in Long-lived People', *Arq Bras Cardiol*, vol. 117, no. 3, pp. 457–462, Sep. 2021, doi: 10.36660/abc.20190774.

[90] R. Perrault, A. Omelchenko, C. G. Taylor, and P. Zahradka, 'Establishing the interchangeability of arterial stiffness but not endothelial function parameters in healthy individuals', *BMC Cardiovascular Disorders*, vol. 19, no. 1, p. 190, Aug. 2019, doi: 10.1186/s12872-019-1167-3.

[91] K. Markakis *et al.*, 'Feasibility of non-invasive measurement of central blood pressure and arterial stiffness in shock', *European Journal of Clinical Investigation*, vol. 51, no. 9, p. e13587, 2021, doi: 10.1111/eci.13587.

[92] J. J. O. A. Costa *et al.*, 'Analysis of Vascular Aging in Arterial Hypertension – Population-based Study: Preliminary Results', *Artery Research*, vol. 25, no. 3–4, pp. 131–138, Dec. 2019, doi: 10.2991/artres.k.191201.001.

[93] Y. Sridhar, M. U. R. Naidu, P. Usharani, and Y. S. N. Raju, 'Non-invasive evaluation of arterial stiffness in patients with increased risk of cardiovascular morbidity: A cross-sectional study', *Indian Journal of Pharmacology*, vol. 39, no. 6, p. 294, Jan. 2007, doi: 10.4103/0253-7613.39150.

[94] H. Komine, Y. Asai, T. Yokoi, and M. Yoshizawa, 'Non-invasive assessment of arterial stiffness using oscillometric blood pressure measurement', *BioMedical Engineering OnLine*, vol. 11, no. 1, p. 6, Feb. 2012, doi: 10.1186/1475-925X-11-6.

[95] F. Hoffmann *et al.*, 'An oscillometric approach in assessing early vascular ageing biomarkers following long-term space flights', *Int J Cardiol Hypertens*, vol. 2, p. 100013, Jun. 2019, doi: 10.1016/j.ijchy.2019.100013.

[96] I. Juganaru *et al.*, 'A Non-invasive, Easy to Use Medical Device for Arterial Stiffness', *Revista de Chimie*, vol. 70, pp. 642–645, Mar. 2019, doi: 10.37358/RC.19.2.6975.

[97] M. W. Osman, M. Nath, A. Khalil, D. R. Webb, T. G. Robinson, and H. A. Mousa, 'Longitudinal study to assess changes in arterial stiffness and cardiac output parameters among low-risk pregnant women', *Pregnancy Hypertension*, vol. 10, pp. 256–261, Oct. 2017, doi: 10.1016/j.preghy.2017.10.007.

[98] J. B. Kostis, C. P. Lin, J. M. Dobrzynski, W. J. Kostis, M. Ambrosio, and J. Cabrera, 'Prediction of stroke using an algorithm to estimate arterial stiffness', *International Journal of Cardiology Cardiovascular Risk and Prevention*, vol. 11, p. 200114, Dec. 2021, doi: 10.1016/j.ijcrp.2021.200114.

[99] M. Negoita, S. Abdullateef, A. D Hughes, K. H Parker, and A. W Khir, 'Semiautomatic Vendor Independent Software for Assessment of Local Arterial Stiffness', in *Proceedings of the 2018 Computing in Cardiology Conference*, Maastricht, Dec. 2018. doi: 10.22489/CinC.2018.218.

[100] J. Micheels, B. Aisbjorn, and B. Sorensen, 'Laser doppler flowmetry. A new non-invasive measurement of microcirculation in intensive care?', *Resuscitation*, vol. 12, no. 1, pp. 31–39, May 1984, doi: 10.1016/0300-9572(84)90056-X.

[101] A. N. Obeid, N. J. Barnett, G. Dougherty, and G. Ward, 'A critical review of laser Doppler flowmetry', *Journal of Medical Engineering & Technology*, vol. 14, no. 5, pp. 178–181, Jul. 2009, doi: 10.3109/03091909009009955.

[102] J. Hong, M. Nandi, P. H. Charlton, and J. Alastruey, 'Noninvasive hemodynamic indices of vascular aging: an in silico assessment', *American Journal of Physiology-Heart and Circulatory Physiology*, vol. 325, no. 6, pp. H1290–H1303, Dec. 2023, doi: 10.1152/ajpheart.00454.2023.

[103] J. Allen and P. A. Kyriacou, 'Editorial: Advances in basic and applied research in photoplethysmography', *Front Physiol*, vol. 15, p. 1415049, May 2024, doi: 10.3389/fphys.2024.1415049.

[104] J. Park, H. S. Seok, S.-S. Kim, and H. Shin, 'Photoplethysmogram Analysis and Applications: An Integrative Review', *Frontiers in Physiology*, vol. 12, 2022, Accessed: Feb. 27, 2023. [Online]. Available: https://www.frontiersin.org/articles/10.3389/fphys.2021.808451

[105] P. A. Kyriacou and S. Chatterjee, '2 - The origin of photoplethysmography', in *Photoplethysmography*, J. Allen and P. Kyriacou, Eds., Academic Press, 2022, pp. 17–43. doi: 10.1016/B978-0-12-823374-0.00004-9.

[106] J. M. May, E. Mejía-Mejía, M. Nomoni, K. Budidha, C. Choi, and P. A. Kyriacou, 'Effects of Contact Pressure in Reflectance Photoplethysmography in an In Vitro Tissue-Vessel Phantom', *Sensors*, vol. 21, no. 24, Art. no. 24, Jan. 2021, doi: 10.3390/s21248421.

[107] M. Wang, Z. Li, Q. Zhang, and G. Wang, 'Removal of Motion Artifacts in Photoplethysmograph Sensors during Intensive Exercise for Accurate Heart Rate Calculation Based on Frequency Estimation and Notch Filtering', *Sensors (Basel)*, vol. 19, no. 15, p. 3312, Jul. 2019, doi: 10.3390/s19153312.

[108] E. von Wowern, K. Källén, and P. Olofsson, 'Arterial stiffness in normal pregnancy as assessed by digital pulse wave analysis by photoplethysmography – A longitudinal study', *Pregnancy Hypertension*, vol. 15, pp. 51–56, Jan. 2019, doi: 10.1016/j.preghy.2018.11.002.

[109] E. von Wowern, G. Östling, P. M. Nilsson, and P. Olofsson, 'Digital Photoplethysmography for Assessment of Arterial Stiffness: Repeatability and Comparison with Applanation Tonometry', *PLOS ONE*, vol. 10, no. 8, p. e0135659, Aug. 2015, doi: 10.1371/journal.pone.0135659.

[110] J. Allen and A. Murray, 'Similarity in bilateral photoplethysmographic peripheral pulse wave characteristics at the ears, thumbs and toes', *Physiol. Meas.*, vol. 21, no. 3, p. 369, Aug. 2000, doi: 10.1088/0967-3334/21/3/303.

[111] D. G. Brillante, A. J. O'sullivan, and L. G. Howes, 'Arterial stiffness indices in healthy volunteers using non-invasive digital photoplethysmography', *Blood Pressure*, vol. 17, no. 2, pp. 116–123, Jan. 2008, doi: 10.1080/08037050802059225.

[112] I. Jannasz *et al.*, 'Relationship between the Central and Regional Pulse Wave Velocity in the Assessment of Arterial Stiffness Depending on Gender in the Geriatric Population', *Sensors (Basel)*, vol. 23, no. 13, p. 5823, Jun. 2023, doi: 10.3390/s23135823.

[113] M. Tąpolska *et al.*, 'Arterial Stiffness Parameters Correlate with Estimated Cardiovascular Risk in Humans: A Clinical Study', *International Journal of Environmental Research and Public Health*, vol. 16, no. 14, Art. no. 14, Jan. 2019, doi: 10.3390/ijerph16142547.

[114] H. Chen, F. Fan, Z. Ye, Z. Liang, X. Qin, and Y. Zhang, 'Photoplethysmography-Derived Arterial Stiffness Index Delivered Greater Cardiovascular Prevention Value to Non-Elderly: A Retrospective Cohort Study Based on UK Biobank', *The Journal of Clinical Hypertension*, vol. 27, no. 5, p. e70058, 2025, doi: 10.1111/jch.70058.

[115] G. Tanaka *et al.*, 'A novel photoplethysmography technique to derive normalized arterial stiffness as a blood pressure independent measure in the finger vascular

bed', *Physiol. Meas.*, vol. 32, no. 11, p. 1869, Oct. 2011, doi: 10.1088/0967-3334/32/11/003.

[116] B. Djurić, K. Žikić, Z. Nestorović, D. Lepojević-Stefanović, N. Milošević, and D. Žikić, 'Using the photoplethysmography method to monitor age-related changes in the cardiovascular system', *Front Physiol*, vol. 14, p. 1191272, Jul. 2023, doi: 10.3389/fphys.2023.1191272.

[117] M. Huotari, N. Yliaska, V. Lantto (Emer), K. Määttä, and J. Kostamovaara, 'Aortic and arterial stiffness determination by photoplethysmographic technique', *Procedia Chemistry*, vol. 1, no. 1, pp. 1243–1246, Sep. 2009, doi: 10.1016/j.proche.2009.07.310.

[118] H. Hellqvist *et al.*, 'Overnight stiffness index from finger photoplethysmography in relation to markers of cardiovascular risk and vascular ageing', *Heart Vessels*, Mar. 2025, doi: 10.1007/s00380-025-02537-3.

[119] S. M. Zekavat *et al.*, 'Genetic Association of Finger Photoplethysmography-Derived Arterial Stiffness Index With Blood Pressure and Coronary Artery Disease', *Arteriosclerosis, Thrombosis, and Vascular Biology*, vol. 39, no. 6, pp. 1253–1261, Jun. 2019, doi: 10.1161/ATVBAHA.119.312626.

[120] E. J. Sharkey *et al.*, 'Innovative multi-site photoplethysmography measurement and analysis demonstrating increased arterial stiffness in paediatric heart transplant recipients', *Physiol. Meas.*, vol. 39, no. 7, p. 074007, Aug. 2018, doi: 10.1088/1361-6579/aac76a.

[121] C.-C. Wei, 'Developing an Effective Arterial Stiffness Monitoring System Using the Spring Constant Method and Photoplethysmography', *IEEE Transactions on Biomedical Engineering*, vol. 60, no. 1, pp. 151–154, Jan. 2013, doi: 10.1109/TBME.2012.2207384.

[122] Y.-J. Park, 'Association between blood glucose levels and arterial stiffness marker: comparing the second derivative of photoplethysmogram and cardio-ankle vascular index scores', *Front Endocrinol (Lausanne)*, vol. 14, p. 1237282, Sep. 2023, doi: 10.3389/fendo.2023.1237282.

[123] L. A. Bortolotto, J. Blacher, T. Kondo, K. Takazawa, and M. E. Safar, 'Assessment of vascular aging and atherosclerosis in hypertensive subjects: second derivative of photoplethysmogram versus pulse wave velocity', *American Journal of Hypertension*, vol. 13, no. 2, pp. 165–171, Feb. 2000, doi: 10.1016/S0895-7061(99)00192-2.

[124] P. Jeyashree, K. Dilara, K. Maruthy, and K. Dhamodhini, 'Comparison of Arterial Stiffness among Prehypertensive and Normotensive Subjects using Photo Pulse Plethysmography: A Pilot Study', *Journal of Clinical and Diagnostic Research*, vol. 18, no. 3, pp. CC01–CC04, Mar. 2024, doi: https://doi.org/10.7860/JCDR/2024/67377.19131.

[125] O. Korneeva and O. Drapkina, 'PP.33.08: Arterial stiffness parameters in obese hypertensive patients using different statin-based regimens and fixed antihypertensive combination.', *Journal of Hypertension*, vol. 33, p. e431, Jun. 2015, doi: 10.1097/01.hjh.0000468731.83210.fd.

[126] O. Drapkina and V. Ivashkin, 'Improving in arterial stiffness parameters by pulse-wave analysis in obese patients', *Atherosclerosis*, vol. 235, no. 2, pp. e156–e157, Aug. 2014, doi: 10.1016/j.atherosclerosis.2014.05.447.

[127] O. Drapkina, 'Rosuvastatin significantly improves arterial stiffness parameters by pulse-wave analysis in high risk patients with arterial hypertension and dyslipidemia', *Atherosclerosis*, vol. 235, no. 2, p. e95, Aug. 2014, doi: 10.1016/j.atherosclerosis.2014.05.252.

[128] W. K. Lefferts, E. C. Lefferts, B. A. Hibner, K. J. Smith, and B. Fernhall, 'Impact of acute changes in blood pressure and arterial stiffness on cerebral pulsatile haemodynamics in young and middle-aged adults', *Experimental Physiology*, vol. 106, no. 7, pp. 1643–1653, 2021, doi: 10.1113/EP089319.

[129] P. Salvi *et al.*, 'Comparative study of methodologies for pulse wave velocity estimation', *J Hum Hypertens*, vol. 22, no. 10, Art. no. 10, Oct. 2008, doi: 10.1038/jhh.2008.42.

[130] D. Djeldjli, F. Bousefsaf, C. Maaoui, F. Bereksi-Reguig, and A. Pruski, 'Remote estimation of pulse wave features related to arterial stiffness and blood pressure using a camera', *Biomedical Signal Processing and Control*, vol. 64, p. 102242, Feb. 2021, doi: 10.1016/j.bspc.2020.102242.

[131] K. de S. Kock, J. B. F. da Silva, and J. L. B. Marques, 'Comparison of the ankle-brachial index with parameters of stiffness and peripheral arterial resistance assessed by photoplethysmography in elderly patients', *J Vasc Bras*, vol. 18, p. e20180084, doi: 10.1590/1677-5449.180084.

[132] T. Murakami, K. Asai, Y. Kadono, T. Nishida, H. Nakamura, and H. Kishima, 'Assessment of Arterial Stiffness Index Calculated from Accelerated

Photoplethysmography', *Artery Research*, vol. 25, no. 1–2, pp. 37–40, Dec. 2019, doi: 10.2991/artres.k.191120.001.

[133] C. F. Clarenbach *et al.*, 'Comparison of photoplethysmographic and arterial tonometry-derived indices of arterial stiffness', *Hypertens Res*, vol. 35, no. 2, Art. no. 2, Feb. 2012, doi: 10.1038/hr.2011.168.

[134] L. Dall'Olio *et al.*, 'Prediction of vascular aging based on smartphone acquired PPG signals', *Sci Rep*, vol. 10, no. 1, Art. no. 1, Nov. 2020, doi: 10.1038/s41598-020-76816-6.

[135] H. Shin, G. Noh, and B.-M. Choi, 'Photoplethysmogram based vascular aging assessment using the deep convolutional neural network', *Sci Rep*, vol. 12, no. 1, Art. no. 1, Jul. 2022, doi: 10.1038/s41598-022-15240-4.

[136] J. Park and H. Shin, 'Vascular Aging Estimation Based on Artificial Neural Network Using Photoplethysmogram Waveform Decomposition: Retrospective Cohort Study', *JMIR Med Inform*, vol. 10, no. 3, p. e33439, Mar. 2022, doi: 10.2196/33439.

[137] K. P. Abrisham, K. Alipour, B. Tarvirdizadeh, and M. Ghamari, 'Neural network models for predicting vascular age from PPG signals: A comparative study', *IET Wireless Sensor Systems*, vol. 15, no. 1, p. e12103, Dec. 2024, doi: 10.1049/wss2.12103.

[138] Y. Chen, X. Yang, R. Song, X. Liu, and J. Zhang, 'Predicting Arterial Stiffness From Single-Channel Photoplethysmography Signal: A Feature Interaction-Based Approach', *IEEE Journal of Biomedical and Health Informatics*, vol. 28, no. 7, pp. 3928–3941, Jul. 2024, doi: 10.1109/JBHI.2024.3383234.

[139] J. O. Olmedo-Aguirre, J. Reyes-Campos, G. Alor-Hernández, I. Machorro-Cano, L. Rodríguez-Mazahua, and J. L. Sánchez-Cervantes, 'Remote Healthcare for Elderly People Using Wearables: A Review', *Biosensors*, vol. 12, no. 2, Art. no. 2, Feb. 2022, doi: 10.3390/bios12020073.

[140] C. Reeves, A. Islam, and T. Gentry, 'The State of Health and Care of Older People, 2023'. Accessed: Nov. 30, 2023. [Online]. Available: https://www.ageuk.org.uk/globalassets/age-uk/documents/reports-and-publications/reports-and-briefings/health--wellbeing/age-uk-briefing-state-of-health-and-care-july-2023-abridged-version.pdf

[141] C. Lian *et al.*, 'Robust and Remote Photoplethysmography Based on Smartphone Imaging of the Human Palm', *IEEE Transactions on Instrumentation and Measurement*, vol. 72, pp. 1–11, 2023, doi: 10.1109/TIM.2023.3264041.

[142] L. Zhao *et al.*, 'Remote photoplethysmography (rPPG) based learning fatigue detection', *Appl Intell*, vol. 53, no. 23, pp. 27951–27965, Dec. 2023, doi: 10.1007/s10489-023-04926-5.

[143] G. Casalino, G. Castellano, and G. Zaza, 'Evaluating the robustness of a contact-less mHealth solution for personal and remote monitoring of blood oxygen saturation', *J Ambient Intell Human Comput*, vol. 14, no. 7, pp. 8871–8880, Jul. 2023, doi: 10.1007/s12652-021-03635-6.

[144] D. Perpetuini *et al.*, 'Multi-Site Photoplethysmographic and Electrocardiographic System for Arterial Stiffness and Cardiovascular Status Assessment', *Sensors*, vol. 19, no. 24, Art. no. 24, Jan. 2019, doi: 10.3390/s19245570.

[145] P. H. Charlton *et al.*, 'Assessing hemodynamics from the photoplethysmogram to gain insights into vascular age: a review from VascAgeNet', *Am J Physiol Heart Circ Physiol*, vol. 322, no. 4, pp. H493–H522, Apr. 2022, doi: 10.1152/ajpheart.00392.2021.

[146] T. C. Margain, E. Powell, A. Clark, and A. Bush, 'Phonocardiography based pulse wave velocity system for non-occlusive assessment of arterial stiffness', *Front. Cardiovasc. Med.*, vol. 12, Jan. 2025, doi: 10.3389/fcvm.2025.1481836.

[147] J. R. Hydren *et al.*, 'Delineating the age-related attenuation of vascular function: Evidence supporting the efficacy of the single passive leg movement as a screening tool', *Journal of Applied Physiology*, vol. 126, no. 6, pp. 1525–1532, Jun. 2019, doi: 10.1152/japplphysiol.01084.2018.

[148] J. R. Gifford and R. S. Richardson, 'CORP: Ultrasound assessment of vascular function with the passive leg movement technique', *Journal of Applied Physiology*, vol. 123, no. 6, pp. 1708–1720, Dec. 2017, doi: 10.1152/japplphysiol.00557.2017.

[149] J.-P. Sirkiä, T. Panula, and M. Kaisti, 'Investigating the impact of contact pressure on photoplethysmograms', *Biomedical Engineering Advances*, vol. 7, p. 100123, Jun. 2024, doi: 10.1016/j.bea.2024.100123.

[150] P. Karimpour, R. Ferizoli, J. M. May, and P. A. Kyriacou, 'Custom Silicone Vessels for In Vitro Investigations on Vascular Ageing using Photoplethysmography', in *2024 46th Annual International Conference of the IEEE Engineering in Medicine and*

Biology Society (EMBC), Jul. 2024, pp. 1–4. doi: 10.1109/EMBC53108.2024.10781560.

[151] T.-J. Whang, H.-Y. Huang, M.-T. Hsieh, and J.-J. Chen, 'Laser-Induced Silver Nanoparticles on Titanium Oxide for Photocatalytic Degradation of Methylene Blue', *Int J Mol Sci*, vol. 10, no. 11, pp. 4707–4718, Nov. 2009, doi: 10.3390/ijms10114707.

[152] P. Karimpour, R. Ferizoli, J. M. May, and P. A. Kyriacou, 'Customisable Silicone Vessels and Tissue Phantoms for In Vitro Photoplethysmography Investigations into Cardiovascular Disease', *Sensors*, vol. 24, no. 5, Art. no. 5, Jan. 2024, doi: 10.3390/s24051681.

[153] V. Fritz, P. Martirosian, J. Machann, R. Daniels, and F. Schick, 'A comparison of emulsifiers for the formation of oil-in-water emulsions: stability of the emulsions within 9 h after production and MR signal properties', *MAGMA*, vol. 35, no. 3, pp. 401–410, 2022, doi: 10.1007/s10334-021-00970-9.

[154] K. Budidha, V. Rybynok, and P. A. Kyriacou, 'Design and Development of a Modular, Multichannel Photoplethysmography System', *IEEE Transactions on Instrumentation and Measurement*, vol. 67, no. 8, pp. 1954–1965, Aug. 2018, doi: 10.1109/TIM.2018.2810643.

[155] J. M. May, 'Investigation Of Fontanelle Photoplethysmographs And Oxygen Saturations In Intensive Care Neonates And Infants Utilising Miniature Photometric Sensors', Thesis (Doctoral), City University London, 2013.

[156] G. Bradley, *Enantiodromis/PPGExtract*. (Aug. 16, 2023). Python. Accessed: Aug. 24, 2023. [Online]. Available: https://github.com/Enantiodromis/PPGExtract

[157] C. Johnson, R. Baugh, C. Wilson, and J. Burns, 'Age related changes in the tunica media of the vertebral artery: implications for the assessment of vessels injured by trauma', *J Clin Pathol*, vol. 54, no. 2, pp. 139–145, Feb. 2001, doi: 10.1136/jcp.54.2.139.

[158] K. L. Hansen and J. F. Carlsen, 'New Trends in Vascular Imaging', *Diagnostics (Basel)*, vol. 11, no. 1, p. 112, Jan. 2021, doi: 10.3390/diagnostics11010112.

[159] M. G. Miglis, 'Chapter 12 - Sleep and the Autonomic Nervous System', in *Sleep and Neurologic Disease*, M. G. Miglis, Ed., San Diego: Academic Press, 2017, pp. 227–244. doi: 10.1016/B978-0-12-804074-4.00018-2.

[160] Q. Gao *et al.*, '3D printed multi-scale scaffolds with ultrafine fibers for providing excellent biocompatibility', *Materials Science and Engineering: C*, vol. 107, p. 110269, Feb. 2020, doi: 10.1016/j.msec.2019.110269.

[161] P. Datta, B. Ayan, and I. T. Ozbolat, 'Bioprinting for vascular and vascularized tissue biofabrication', *Acta Biomaterialia*, vol. 51, pp. 1–20, Mar. 2017, doi: 10.1016/j.actbio.2017.01.035.

[162] J. Schöneberg *et al.*, 'Engineering biofunctional in vitro vessel models using a multilayer bioprinting technique', *Sci Rep*, vol. 8, no. 1, Art. no. 1, Jul. 2018, doi: 10.1038/s41598-018-28715-0.

[163] X.-Y. Du, Q. Li, G. Wu, and S. Chen, 'Multifunctional Micro/Nanoscale Fibers Based on Microfluidic Spinning Technology', *Advanced Materials*, vol. 31, no. 52, p. 1903733, 2019, doi: 10.1002/adma.201903733.

[164] J. Nie *et al.*, 'Vessel-on-a-chip with Hydrogel-based Microfluidics', *Small*, vol. 14, no. 45, 2018, doi: 10.1002/smll.201802368.

[165] Q. Liang *et al.*, 'Coaxial Scale-Up Printing of Diameter-Tunable Biohybrid Hydrogel Microtubes with High Strength, Perfusability, and Endothelialization', *Advanced Functional Materials*, vol. 30, no. 43, 2020, doi: 10.1002/adfm.202001485.

[166] L. Zhou, Y. Li, Q. Tu, and J. Wang, 'A 3D printing mold method for rapid fabrication of artificial blood vessels', *Colloids and Surfaces A: Physicochemical and Engineering Aspects*, vol. 662, p. 130952, Apr. 2023, doi: 10.1016/j.colsurfa.2023.130952.

[167] M. Nomoni, J. M. May, and P. A. Kyriacou, 'Novel Polydimethylsiloxane (PDMS) Pulsatile Vascular Tissue Phantoms for the In-Vitro Investigation of Light Tissue Interaction in Photoplethysmography', *Sensors*, vol. 20, no. 15, Art. no. 15, Jan. 2020, doi: 10.3390/s20154246.

[168] H. Lan, A. M. Al-Jumaily, A. Lowe, and W. Hing, 'Effect of tissue mechanical properties on cuff-based blood pressure measurements', *Medical Engineering & Physics*, vol. 33, no. 10, pp. 1287–1292, Dec. 2011, doi: 10.1016/j.medengphy.2011.06.006.

[169] J. J. Chruściel, 'Modifications of Textile Materials with Functional Silanes, Liquid Silicone Softeners, and Silicone Rubbers—A Review', *Polymers*, vol. 14, no. 20, Art. no. 20, Jan. 2022, doi: 10.3390/polym14204382.

[170] Accessed: Jan. 25, 2023. [Online]. Available: https://polytek.com/content/pdf/technicalbulletin/Polytek_TB_PlatSilGels_5-5-2021.pdf

[171] M. Nomoni, J. M. May, and P. A. Kyriacou, 'Fabricating Novel PDMS Vessels for Phantoms in Photoplethysmography Investigations', in *2020 42nd Annual International Conference of the IEEE Engineering in Medicine & Biology Society (EMBC)*, Jul. 2020, pp. 4458–4461. doi: 10.1109/EMBC44109.2020.9176476.

[172] R. Jafary, S. Armstrong, T. Byrne, A. Stephens, V. Pellegrino, and S. D. Gregory, 'Fabrication and Characterization of Tissue-Mimicking Phantoms for Ultrasound-Guided Cannulation Training', *ASAIO J*, vol. 68, no. 7, pp. 940–948, Jul. 2022, doi: 10.1097/MAT.0000000000001593.

[173] ASTM International, *Test Methods for Vulcanized Rubber and Thermoplastic Elastomers-Tension*, ASTM D412-16, West Conshohocken, PA, United States., 2021. doi: 10.1520/D0412-16.

[174] ASTM International, *Standard Test Methods for Rubber Properties in Compression*, ASTM D575-91, West Conshohocken, PA, United States., 2024. doi: 10.1520/D0575-91R24.

[175] S. Bastida, J. I. Eguiazábal, M. Gaztelumendi, and J. Nazábal, 'On the thickness dependence of the modulus of elasticity of polymers', *Polymer Testing*, vol. 17, no. 2, pp. 139–145, Apr. 1998, doi: 10.1016/S0142-9418(97)00042-1.

[176] J. Brum, G. Balay, D. Bia, and N. Benech, 'Improvement of Young Modulus Estimation by Ultrasound Using Static Pressure Step', Jan. 2010, doi: 10.1016/j.phpro.2010.01.141.

[177] C. Oprişan, V. Cârlescu, A. Barnea, G. Prisacaru, D. N. Olaru, and G. Plesu, 'Experimental determination of the Young's modulus for the fingers with application in prehension systems for small cylindrical objects', *IOP Conf. Ser.: Mater. Sci. Eng.*, vol. 147, no. 1, p. 012058, Aug. 2016, doi: 10.1088/1757-899X/147/1/012058.

[178] V. Falanga and B. Bucalo, 'Use of a durometer to assess skin hardness', *Journal of the American Academy of Dermatology*, vol. 29, no. 1, pp. 47–51, Jul. 1993, doi: 10.1016/0190-9622(93)70150-R.

[179] W.-J. Sun, S. Kothari, and C. C. Sun, 'The relationship among tensile strength, Young's modulus, and indentation hardness of pharmaceutical compacts', *Powder Technology*, vol. 331, pp. 1–6, May 2018, doi: 10.1016/j.powtec.2018.02.051.

[180] E. Theodorsson-Norheim, 'Kruskal-Wallis test: BASIC computer program to perform nonparametric one-way analysis of variance and multiple comparisons on ranks of several independent samples', *Computer Methods and Programs in Biomedicine*, vol. 23, no. 1, pp. 57–62, Aug. 1986, doi: 10.1016/0169-2607(86)90081-7.

[181] E. Whitley and J. Ball, 'Statistics review 6: Nonparametric methods', *Critical Care*, vol. 6, no. 6, p. 509, Sep. 2002, doi: 10.1186/cc1820.

[182] V. Bewick, L. Cheek, and J. Ball, 'Statistics review 10: Further nonparametric methods', *Crit Care*, vol. 8, no. 3, pp. 196–199, 2004, doi: 10.1186/cc2857.

[183] M. A. Soneye, A. J. Adekanmi, M. O. Obajimi, and A. Aje, 'Intima-Media Thickness of Femoral Arteries and Carotids among an Adult Hypertensive Nigerian Population: A Case–Control Study to Assess their Use as Surrogate Markers of Atherosclerosis', *Ann Afr Med*, vol. 18, no. 3, pp. 158–166, 2019, doi: 10.4103/aam.aam_57_18.

[184] K. S. Spector and W. E. Lawson, 'Optimizing safe femoral access during cardiac catheterization', *Catheterization and Cardiovascular Interventions*, vol. 53, no. 2, pp. 209–212, 2001, doi: 10.1002/ccd.1150.

[185] M. Hickey, J. P. Phillips, and P. A. Kyriacou, 'Investigation of peripheral photoplethysmographic morphology changes induced during a hand-elevation study', *J Clin Monit Comput*, vol. 30, no. 5, pp. 727–736, Oct. 2016, doi: 10.1007/s10877-015-9761-0.

[186] T. Matsumoto, D. Baker, L. V. d'Uscio, G. Mozammel, Z. S. Katusic, and J. M. van Deursen, 'Aging-Associated Vascular Phenotype in Mutant Mice With Low Levels of BubR1 | Stroke', vol. 38, doi: 10.1161/01.STR.0000257967.86132.01.

[187] M. Jadidi, S. A. Razian, M. Habibnezhad, E. Anttila, and A. Kamenskiy, 'Mechanical, Structural, and Physiologic Differences in Human Elastic and Muscular Arteries of Different Ages: Comparison of the Descending Thoracic Aorta to the Superficial Femoral Artery', *Acta Biomater*, vol. 119, pp. 268–283, Jan. 2021, doi: 10.1016/j.actbio.2020.10.035.

[188] R. Ferizoli, P. Karimpour, J. M. May, and P. A. Kyriacou, 'A Bilateral In Vitro Model for Cardiovascular Disease Investigations Using Photoplethysmography Sensors', *IEEE Biosensors Conference 2023*.

[189] D. Castaneda, A. Esparza, M. Ghamari, C. Soltanpur, and H. Nazeran, 'A review on wearable photoplethysmography sensors and their potential future applications in

health care', *Int J Biosens Bioelectron*, vol. 4, no. 4, pp. 195–202, Aug. 2018, doi: 10.15406/ijbsbe.2018.04.00125.

[190] K. S. Hong, K. T. Park, and J. M. Ahn, 'Aging Index using Photoplethysmography for a Healthcare Device: Comparison with Brachial-Ankle Pulse Wave Velocity', *Healthc Inform Res*, vol. 21, no. 1, pp. 30–34, Jan. 2015, doi: 10.4258/hir.2015.21.1.30.

[191] A. Grabovskis, Z. Marcinkevics, U. Rubins, and E. Kviesis-Kipge, 'Effect of probe contact pressure on the photoplethysmographic assessment of conduit artery stiffness', *JBO*, vol. 18, no. 2, p. 027004, Feb. 2013, doi: 10.1117/1.JBO.18.2.027004.

[192] R. Ferizoli, P. Karimpour, J. M. May, and P. A. Kyriacou, 'Arterial stiffness assessment using PPG feature extraction and significance testing in an in vitro cardiovascular system', *Sci Rep*, vol. 14, no. 1, Art. no. 1, Jan. 2024, doi: 10.1038/s41598-024-51395-y.

[193] M. Nomoni, J. M. May, and P. A. Kyriacou, 'A Pulsatile Optical Tissue Phantom for the Investigation of Light-Tissue Interaction in Reflectance Photoplethysmography', in *2019 41st Annual International Conference of the IEEE Engineering in Medicine and Biology Society (EMBC)*, Berlin, Germany: IEEE, Jul. 2019, pp. 3204–3207. doi: 10.1109/EMBC.2019.8857036.

[194] H. Njoum and P. A. Kyriacou, 'In vitro validation of measurement of volume elastic modulus using photoplethysmography', *Med Eng Phys*, vol. 52, pp. 10–21, Feb. 2018, doi: 10.1016/j.medengphy.2017.11.011.

[195] L. L. Bernardo, *laresbernardo/lares*. (Nov. 29, 2023). R. Accessed: Dec. 12, 2023. [Online]. Available: https://github.com/laresbernardo/lares

[196] D. Chambers, C. Huang, and G. Matthews, 'Arterial pressure waveforms', in *Basic Physiology for Anaesthetists*, 2nd ed., Cambridge University Press, 2019, pp. 155–157.

[197] M. Cecelja and P. Chowienczyk, 'Role of arterial stiffness in cardiovascular disease', *JRSM Cardiovascular Disease*, vol. 1, no. 4, pp. 1–10, Jul. 2012, doi: 10.1258/cvd.2012.012016.

[198] H. Shin, 'XGBoost Regression of the Most Significant Photoplethysmogram Features for Assessing Vascular Aging', *IEEE Journal of Biomedical and Health Informatics*, vol. 26, no. 7, pp. 3354–3361, Jul. 2022, doi: 10.1109/JBHI.2022.3151091.

[199] F. D. Fuchs and P. K. Whelton, 'High Blood Pressure and Cardiovascular Disease', *Hypertension*, vol. 75, no. 2, pp. 285–292, Feb. 2020, doi: 10.1161/HYPERTENSIONAHA.119.14240.

[200] R. M. Carey, P. Muntner, H. B. Bosworth, and P. K. Whelton, 'Prevention and Control of Hypertension: JACC Health Promotion Series', *J Am Coll Cardiol*, vol. 72, no. 11, pp. 1278–1293, Sep. 2018, doi: 10.1016/j.jacc.2018.07.008.

[201] C. M. Lawes, S. V. Hoorn, and A. Rodgers, 'Global burden of blood-pressure-related disease, 2001', *The Lancet*, vol. 371, no. 9623, pp. 1513–1518, May 2008, doi: 10.1016/S0140-6736(08)60655-8.

[202] J. S. Shahoud, T. Sanvictores, and N. R. Aeddula, 'Physiology, Arterial Pressure Regulation', in *StatPearls [Internet]*, StatPearls Publishing, 2023. Accessed: Oct. 16, 2024. [Online]. Available: https://www.ncbi.nlm.nih.gov/books/NBK538509/

[203] D. B. Camasão and D. Mantovani, 'The mechanical characterization of blood vessels and their substitutes in the continuous quest for physiological-relevant performances. A critical review', *Mater Today Bio*, vol. 10, p. 100106, Mar. 2021, doi: 10.1016/j.mtbio.2021.100106.

[204] J. Concato and J. A. Hartigan, 'P values: from suggestion to superstition', *Journal of Investigative Medicine*, vol. 64, no. 7, p. 1166, Aug. 2016, doi: 10.1136/jim-2016-000206.

[205] M. Elgendi, 'On the Analysis of Fingertip Photoplethysmogram Signals', *Current Cardiology Reviews*, vol. 8, no. 1, p. 14, Feb. 2012, doi: 10.2174/157340312801215782.

[206] M. A. Almarshad, M. S. Islam, S. Al-Ahmadi, and A. S. BaHammam, 'Diagnostic Features and Potential Applications of PPG Signal in Healthcare: A Systematic Review', *Healthcare*, vol. 10, no. 3, Art. no. 3, Mar. 2022, doi: 10.3390/healthcare10030547.

[207] K. Takazawa *et al.*, 'Assessment of Vasoactive Agents and Vascular Aging by the Second Derivative of Photoplethysmogram Waveform', *Hypertension*, vol. 32, no. 2, pp. 365–370, Aug. 1998, doi: 10.1161/01.HYP.32.2.365.

[208] H. J. Baek, J. S. Kim, Y. S. Kim, H. B. Lee, and K. S. Park, 'Second Derivative of Photoplethysmography for Estimating Vascular Aging', in *2007 6th International Special Topic Conference on Information Technology Applications in Biomedicine*, Nov. 2007, pp. 70–72. doi: 10.1109/ITAB.2007.4407346.

[209] R. Mohamad Rozi, S. Usman, M. A. Mohd Ali, and M. B. I. Reaz, 'Second derivatives of photoplethysmography (PPG) for estimating vascular aging of atherosclerotic patients', in *2012 IEEE-EMBS Conference on Biomedical Engineering and Sciences*, Dec. 2012, pp. 256–259. doi: 10.1109/IECBES.2012.6498064.

[210] K. Q. Yousef, U. Rubins, and A. Mafawez, 'Photoplethysmogram second derivative review: Analysis and applications', *Sci. Res. Essays*, vol. 10, no. 21, pp. 633–639, Nov. 2015, doi: 10.5897/SRE2015.6322.

[211] N. Gayapersad, S. Rocke, Z. Ramsaroop, A. Singh, and C. Ramlal, 'Beyond Blood Pressure and Heart Rate Monitoring: Towards a Device for Continuous Sensing and Automatic Feature Extraction of Cardiovascular Data', in *2016 8th International Conference on Computational Intelligence and Communication Networks (CICN)*, Dec. 2016, pp. 261–265. doi: 10.1109/CICN.2016.58.

[212] M. Z. Suboh, R. Jaafar, N. A. Nayan, N. H. Harun, and M. S. F. Mohamad, 'Analysis on Four Derivative Waveforms of Photoplethysmogram (PPG) for Fiducial Point Detection', *Front Public Health*, vol. 10, p. 920946, Jun. 2022, doi: 10.3389/fpubh.2022.920946.

[213] J. Choi and M.-G. Park, 'Variations in the Second Derivative of a Photoplethysmogram with Age in Healthy Korean Adults', *International Journal of Environmental Research and Public Health*, vol. 20, no. 1, p. 236, Dec. 2022, doi: 10.3390/ijerph20010236.

[214] Y. Iketani, T. Iketani, K. Takazawa, and M. Murata, 'Second Derivative of Photoplethysmogram in Children and Young People', *Japanese Circulation Journal*, vol. 64, no. 2, pp. 110–116, 2000, doi: 10.1253/jcj.64.110.

[215] British Heart Foundation (BHF), 'Heart and Circulatory Disease Statistics 2024'. Oct. 16, 2024. [Online]. Available: https://www.bhf.org.uk/-/media/files/for-professionals/research/heart-statistics/bhf-cvd-statistics-compendium-2024-v3.pdf?rev=c72e2593b0ac4f2b999ad2f5999d8c07&hash=7DCC7E6832AA9495B0F5E720357DB9FB

[216] V. Rajan, B. Varghese, T. G. van Leeuwen, and W. Steenbergen, 'Review of methodological developments in laser Doppler flowmetry', *Lasers Med Sci*, vol. 24, no. 2, pp. 269–283, Mar. 2009, doi: 10.1007/s10103-007-0524-0.

[217] A. P. Shepherd, *Laser-Doppler Blood Flowmetry*. in Developments in Cardiovascular Medicine Ser, no. v. 107. New York, NY: Springer, 1990.

[218] T. Ishii *et al.*, 'Laser Doppler blood flowmeter as a useful instrument for the early detection of lower extremity peripheral arterial disease in hemodialysis patients: an observational study', *BMC Nephrology*, vol. 20, no. 1, p. 470, Dec. 2019, doi: 10.1186/s12882-019-1653-y.

[219] M. Hickey, J. P. Phillips, and P. A. Kyriacou, 'The effect of vascular changes on the photoplethysmographic signal at different hand elevations', *Physiol. Meas.*, vol. 36, no. 3, p. 425, Feb. 2015, doi: 10.1088/0967-3334/36/3/425.

[220] 'Tissue blood flow and temperature monitoring with moorVMS-LDF', Moor Instruments Ltd, Issue 9_1. [Online]. Available: https://www.moor.co.uk

[221] V. A. Profillidis and G. N. Botzoris, 'Chapter 5 - Statistical Methods for Transport Demand Modeling', in *Modeling of Transport Demand*, V. A. Profillidis and G. N. Botzoris, Eds., Elsevier, 2019, pp. 163–224. doi: 10.1016/B978-0-12-811513-8.00005-4.

[222] K. Horie, K. Toda, T. Nakamura, and T. Ideguchi, 'Bidirectional quantitative scattering microscopy', *Nat Commun*, vol. 16, no. 1, p. 9712, Nov. 2025, doi: 10.1038/s41467-025-65570-w.

[223] C. Berkland, K. (Kevin) Kim, and D. W. Pack, 'Fabrication of PLG microspheres with precisely controlled and monodisperse size distributions', *Journal of Controlled Release*, vol. 73, no. 1, pp. 59–74, May 2001, doi: 10.1016/S0168-3659(01)00289-9.

[224] A. Goltsov *et al.*, 'Bifurcation in Blood Oscillatory Rhythms for Patients with Ischemic Stroke: A Small Scale Clinical Trial using Laser Doppler Flowmetry and Computational Modeling of Vasomotion', *Front Physiol*, vol. 8, p. 160, Mar. 2017, doi: 10.3389/fphys.2017.00160.